OPEN AND CONFINED SPRAY FLAMES

by

YEHIA HUSSEIN ELBANHAWY

Thesis Submitted for the Degree of
Doctor of Philosophy
in the Faculty of Engineering
University of London
and
for the Diploma of Membership
of Imperial College

1979

To

my Wife, Nadia

my Parents, Mr. and Mrs. H. Elbanhawy

ABSTRACT

Measurements of local flame properties, including droplet velocity, temperature and species concentrations, are presented for a range of unconfined and confined kerosene spray flames. The operating conditions for the unconfined flame experiments comprised different values of the fuel mass flow rate and the combustion air swirl. The increase in swirl caused an increase in the turbulent mixing with consequently higher evaporation rate and increased combustion intensity. The reduction in the fuel mass flow rate also caused an increase in the combustion intensity, particularly in the near-nozzle region, which is influenced by the increase in the evaporation rate, due to the reduction in the mean droplet diameter, and by the overall air-fuel ratio which is closer to stoichiometric.

In the confined flame experiments, six flames were studied which corresponded to different values of the spray mean-droplet diameter and the combustion air swirl. The results indicated that, for both the high and low swirl flames, the increase in the mean diameter caused a reduced combustion intensity in the region downstream the spray plane and at large radii of the combustion chamber. The results obtained for the flames with different air swirl, but with the same mean droplet diameter, revealed that the reduction in swirl was associated with a reduced chemical reaction rate within the initial part of the flame and close to the centreline. The reduced combustion intensity in the central part of the flame was more significant for the lowest degree of swirl used and this was related to the simultaneous reduction in droplet evaporation and quenching of chemical reaction by the comparatively high velocity of the air stream surrounding the atomizer.

A method for the calculation of the local properties of

spray flames has been developed and its capabilities and limitations appraised by comparing calculated results with measurement. The mathematical formulation comprises the application of Eulerian conservation equations to the gas phase and Lagrangian equations of droplet motion and thermal balance to a finite number of droplet-size ranges representing the size distribution within the spray. The latter is coupled with a droplet-tracking technique which allows the determination of droplet location and properties within the flow field. The spray combustion model assumes that the evaporating droplets act as distributed point-injectors of fuel vapour within the flame and that the combustion rate of fuel vapour is controlled by the turbulent mixing between the air and fuel streams. A two-equation turbulence model and a four-flux radiation model are also used. Calculations were performed for four spray flame geometries including the present confined flame geometry. The experimental and predicted results are shown to be in a good qualitative agreement albeit with finite discrepancies. The magnitude of the discrepancies and the relative importance of the sources of uncertainties in the modelling assumptions were found to be dependent on the flow features of each flame.

ACKNOWLEDGEMENTS

It gives me great pleasure to express gratitude to all persons who have helped me in one way or another during the research for this thesis. Unfortunately, it is possible only to mention some of them.

First, I wish to acknowledge with gratitude the guidance, advice and constructive criticism provided by my supervisor, Professor J. H. Whitelaw, throughout my research at Imperial College. His critical assessment at all stages of the work was very valuable in bringing the research to a fruitful conclusion.

I am indebted to Dr. A. Melling, a former colleague at Imperial College, for his advice and freely given help in the initial stages of my work and, in particular, for introducing me to the technique of velocity measurements by Laser Doppler anemometer.

The support of the departmental technical staff was vital to the research program; Messrs. O. Vis, J. Pilmer, F. Bell, J. Laker and R. Church were particularly helpful in the experimental part of the work.

Many thanks are also due to Miss E. Archer and the Mechanical Engineering library staff, to Mr. G. Tindall and the staff of the Reprographics Section and to Miss S. Chambers and Miss J. Davies for their frequent help and support throughout my research work.

My colleagues made the everyday college life most interesting and pleasant. My thanks are due to all of them and, in particular, to Mr. H. Moneib, Mr. M. Noseir, Mr. M. Habib, Mr. M. Enayat and Mr. A. Taylor for many valuable discussions.

The financial support of the Ministry of Defence is acknowledged. The rotating cup atomizer used in this work was kindly lent by the National Gas Turbine Establishment, Pyestock.

My thanks to Mrs. H. A. Bastin who had the patience to go through every typing detail with great skill.

Finally, I would like to take this opportunity to extend my deepest gratitude to my family for their support and encouragement throughout my career.

CONTENTS

NOMENCLATURE

A_j	Surface area of the thermocouple junction (m^2)
A_w	Surface area of the combustor wall (m^2)
B	Dimensionless transfer number, Equation (3.5.5)
c_p	Specific heat under constant pressure (J/kg ^oK)
c_c	Ratio of actual area of fuel flow to nozzle area (0.3 - 0.6)
c_t	A coefficient to account for loss of angular momentum
C_D	Drag coefficient
C_1, C_2, C_μ	Turbulence model constants, Table (3.2)
C_{g_1}, C_{g_2}	Combustion model constants, Table (3.2)
d	Diameter of thermocouple junction (m)
D	Diameter (m)
DISC	Disc diameter, test case 3, Table (3.3) (m)
DUCT	Duct diameter, test case 3, Table (3.3) (m)
D_{32}	Sauter mean droplet diameter (μm)
D_{30}	Mass median droplet diameter (μm)
f	Mixture fraction, Equation (3.4.4)
g	The variance of the mixture fraction, Equation (3.4.8)
h	Specific total enthalpy (J/kg)
h_c	Heat transfer coefficient (J/m^2 kg ^oK)
H_{fu}	Fuel heat of reaction (J/kg fuel)
i	Stoichiometric oxygen to fuel ratio
I_b	Total blackbody radiant intensity (W/m^2)
K_w	Thermal conductivity of thermocouple wire (J/m ^oK kg)
K_R	Radiation view factor
k	Kinetic energy of turbulence (m^2/s^2)
	Thermal conductivity (J/m ^oK kg)

k_e	Evaporation rate constant under stagnant conditions
k_{ef}	Evaporation rate constant under forced convection
$k_{\lambda a}$, $k_{\lambda s}$	Absorption and scattering coefficients for the wave length, λ (m^{-1})
ℓ	Characteristic length scale (m)
L	Fuel latent heat of vaporization (J/kg)
$\dot{m}$	Mass flow rate (kg/s)
m	Mass fraction
m_p	Mass of droplet (kg)
n_1	Number of tangential ports in atomizer
dn	Number of droplets in the size range D_p - $D_p + dD_p$
n	Total number of droplets
p	Pressure (N/m^2)
r	Radial distance (m)
R	Radius of combustion chamber (m)
Re_ℓ	Reynolds number of droplet relative to gases
R_j	Nozzle exit radius (m)
R_i	Swirl chamber radius (m)
R_p	Radius of tangential port in swirl chamber (m)
S	Generation and/or destruction source term, gas field
S_d	Droplet source term
T	Temperature (^oK)
T_{sat}	Liquid fuel saturation temperature (^oK)
t	Time
T_w	Wall temperature (^oK)
T_i	Inner temperature of suction pyrometer shield (^oK)
U	Axial velocity component (m/s)
u'	Fluctuating axial velocity component (m/s)
u_x	Droplet axial velocity at exit from atomizer (m/s)

u_t	Droplet tangential velocity at exit from atomizer (m/s)
V	Radial velocity component
W	Tangential velocity component
X	Axial distance (m)
Y	Radial position (m/s)

Greek Symbols

Γ	Exchange coefficient
Δt	Time step (s)
δ_{ij}	Dirac delta function ($\delta_{i=j} = 1$, $\delta_{i\neq j} = 0$)
ε	Dissipation rate of turbulent kinetic energy
ε_t	Emissivity of thermocouple wire
ε_w	Emissivity of wall
ε_{sh}	Emissivity of suction pyrometer shield
λ	Wave length (m)
μ	Viscosity (kg/m.s)
ν	Kinematic viscosity (m^2/s)
$\overline{\nu}_D$	Mean Doppler frequency (Hz)
$\tilde{\nu}_D$	rms of Doppler frequency
ρ	Density (kg/m^3)
σ	Stefan-Boltzmann constant ($W/m^2\ {}^oK^4$)
Φ	General dependent variable
ϕ	Half the intersection angle between the two laser beams (^{o})

Subscripts

eff	Effective (including the effects of turbulence)
end	End of time step
fu	Fuel
g	Gas

h	Enthalpy
i, j	Components in Cartesian tensor notation
lam	Laminar
ox	Oxidant
p	Droplet, particle
pr	Products of combustion
r	Relative
st	Stoichiometric condition
s.p.	Suction pyrometer
start	Start of time step
T	Turbulent
v	Vapour
α	Chemical species
Φ	General dependent variable

Superscripts

$\overline{}$	Time averaged
$'$	Fluctuating component
$\hat{}$	Instantaneous

CHAPTER 1

INTRODUCTION

1.1 Problem Considered

The investigation reported in this thesis is concerned with confined and unconfined spray flames with special emphasis on the interaction between the fuel spray and the surrounding combustion air. The study has two main parts; the first is experimental where measurements were obtained in both types of flames, under a wide range of operating conditions, in order to determine and quantify the influence of the spray-combustion air interaction on the flame properties. In the second part, a mathematical model for the fuel spray, which accounts for the various exchange processes between the spray and its surroundings, was developed and embodied in an available calculation method to allow the prediction of the local properties in spray flames. The method is evaluated by comparison with experimental data, including those of the present study.

It is known that combustion characteristics of gaseous diffusion or premixed flames are controlled by the relative importance of the chemical kinetics and mixing between fuel and oxidant. In liquid fuelled flames, spray characteristics including evaporation rate, droplet size and velocity are determined by the conditions at the fuel nozzle and the interaction between the spray and the surrounding air and can act as additional combustion-rate controlling parameters. Quantification of the extent to which the spray contributes to the overall combustion process represents a major goal in the current combustion research work. The practical relevance is made clear by the example of the gas-turbine combustor where fuel-air loading, combustor pressure and the degree of preheat vary considerably from idle to full power conditions with consequent variations in the

spray characteristics. With current restrictions on pollutant emission levels and the need for more efficient combustion, the importance of quantifying the influence of these variations on the combustion process is obvious. Direct measurements, to determine and quantify these influences, are, therefore, desirable and urgently required as are more economical and precise calculation methods.

1.2 Previous and Related Work

In the first part of this section, previous experimental investigations relevant to the present study are reviewed. Available calculation methods, which can be adapted to predict spray flames, are outlined and discussed in the second part of this section.

1.2.1 Experimental Investigations

A prerequisite for the understanding of spray combustion, and its application to the design of efficient combustion equipment, is knowledge of the evaporation and burning characteristics of single or simplified arrangements of droplets. This topic has been the subject of a large number of experimental and theoretical studies, see for example Law (1976), Natarazan et al (1975), Ohta et al (1975), Rudinger (1975), Williams (1973), Twardus et al (1978), Chiu et al (1977) and Samson et al (1978a, 1978b). These studies emphasised the importance of the droplet size, its relative velocity to the surrounding gas, properties and concentration of both the droplets and gases and the interaction between the droplets themselves.

Investigations of the detailed structure of spray flames were performed in parallel to the above studies. These include the work of Onuma et al (1975, 1977) for a range of confined spray flames, Chigier et al (1973, 1974) and Styles et al (1977) for unconfined flames emerging from burners with pressure and twin-fluid atomizers,

and Tuttle et al (1976, 1973) and Mellor (1973) for simulated and actual gas turbine combustors. The results of these studies indicated that the contribution to the overall combustion process of droplet burning with individual envelope flames is insignificant in most cases and that, in the combustion process, a liquid fuel spray feeds a diffusion type flame which surrounds the spray boundaries.

The experimental studies of Komiyama et al (1977), Tuttle et al (1976) and Beèr (1962) were mainly concerned with the influence of the spray characteristics on the flame behaviour.

Komiyama et al (1977) studied the importance of droplet evaporation in the overall fuel-air mixing process in a range of confined spray flames and indicated that where the characteristic time of evaporation is much less than the jet mixing time, the details of the evaporation process are not important and the jet length scale and kinetic energy govern the mixing process as for gaseous flames. On the other hand, when the characteristic times are comparable, the initial fuel-air mixing rate is determined by the evaporation characteristics of the fuel droplets and the kinetic energy of the jet. These conclusions were deduced from cross-sectional-averaged oxygen concentrations and no details of the other flame properties were reported.

Tuttle et al (1976) reported detailed temperature and concentration measurements in a disc-stabilized confined flame under a range of fuel-air loading conditions. Related changes in the droplet size, evaporation rate and penetration were found to have a large influence on the local properties and pollution characteristics of the flames studied. In general, the heterogeneous processes, due to the fuel spray, were found to increase in importance in going from low to high fuel and air flow rates. It is, however, likely that the experimental results of this study are influenced by the

simultaneous variation in both the fuel and air operating conditions which allowed an indirect quantification of the influences of the fuel spray on the flame behaviour.

Beèr (1962) reported measurements of temperature and species concentration in heavy fuel oil spray flames obtained in the IJ muiden furnace of the International Flame Research Foundation. The mean droplet size of the spray, which was varied between 89 μm and 113 μm, affected both the flame propagation and the burnout of carbon in the flame under otherwise unchanged aerodynamic conditions. However, the experimental results also suggest that the extent of these effects decreases with the increase in the turbulent mixing rates close to the fuel atomizer.

It is apparent from this review of the experimental studies that, although different aspects of spray combustion have been considered, information of the quantitative influence of spray characteristics on flame behaviour is relatively sparse and covers a limited range of spray flames. It is, therefore, the aim of the present experimental study to provide more quantitative information for both unconfined and confined kerosene fuel-spray flames. The operating conditions and the quantities measured are selected in a way which avoids some of the deficiencies pointed out in the above review of related studies.

1.2.2 Calculation Methods

The first attempts to treat the problems of spray flames theoretically were mainly concerned, as for the case of the experimental studies, with the behaviour of single isolated droplets. The laws governing the aerodynamic, thermal, evaporation and combustion behaviour of a droplet were developed and examined by several investigators. The outcome of these studies in the form of

expressions describing the various exchange processes of mass, heat and momentum between the droplet and its surroundings were extensively reported in the literature. A presentation of the details of these studies is beyond the scope of the present review and the reader is referred to the reviews by Williams, (1965), Williams (1973), Chigier et al (1977) and Ioannides et al (1978). It must be, however, mentioned that some of these expressions have been used in the present work and specific comments will be made in the text. Attempts to provide analytical descriptions of groups of droplets have been reported recently by Samson et al (1978a, 1978b) and Chiu et al (1977). However, in all of these treatments explicit or implicit statistical hypotheses are used to permit the deduction of the group behaviour from some known properties of single droplets.

The above basic studies were associated with the development of simple global, performance oriented mathematical models for the more complex practical spray flames. In these simple models, different approaches were used; in one case the details of the gas flow were over-simplified and attention was concentrated on the droplet behaviour, see for example Lambiris et al (1967), El Shirbini (1969) and Mellor (1976). Other approaches simulate the combustion space by a group of chemical reactors of various types (e.g. partially or well-stirred reactors) in series and/or parallel, see Fletcher et al (1971), Mosier et al (1973) and Prior et al (1978). The influences of the fuel droplets on the combustion process were included in a simple way without coupling the gas and droplet fields.

Only recently have attempts been made to consider the details of both the fuel spray and the surrounding gases in order to predict the local flow properties in spray flames. The main mathematical burden associated with these methods is related to the modelling of the discontinuous liquid-phase, the coupling between

the liquid and gas phases and the modelling of the combustion process which requires consideration of the spray characteristics. Since these methods are of immediate relevance to the present work, the following parts provide a detailed review of the different approaches.

The problem of predicting the local flow properties in situations where a spray of droplets is injected in a turbulent gas-field has been investigated by Crowe (1974), Crowe et al (1977), Abou Ellail (1974) and Sharma (1977); Eulerian conservation equations were applied to the gas-phase with the assumption of insignificant influence of local flow discontinuities induced by the presence of droplets in the gas-phase. Lagrangian equations of droplet-motion and thermal balance equations were applied to a finite number of droplet size ranges representing the size distribution within the spray. The interaction between the two phases was accounted for by considering the droplets as sources of mass, heat and momentum to the gas-field. This approach was used by the above investigators for the prediction of non-reacting spray flows with very limited comparisons with experimental data to assess its accuracy. However, it has been used more recently by Lockwood and Syed (1977) for the prediction of coal fired furnaces but, again, without validation against experimental data. The approach is apparently simple and economic of both computer storage and time, see Ioannides et al (1978).

A different approach was developed by Williams, (1965) who modelled the spray through a conservation equation (spray equation) for a statistical distribution function, defined as the number of droplets per unit droplet diameter and velocity, and spatial volume. The influence of the spray on the gas field was considered through source terms, representing different exchange processes, included in the conservation equations of the gas field. The main

difficulty associated with this approach lies in the solution of the final set of equations which have an integro-differential character. Application of the method, but with drastic simplifying assumptions, was described by Gupta et al (1978), Gany et al (1976) and Westbrook (1977). A similar approach was also used by Spalding (1970) and Ganesan et al (1979). Evaluation of this approach against experimental data was not reported in these studies.

Harlow et al (1975), Gosman et al (1976) and Spalding (1977) used the continuum formulation of the conservation equations, for both phases, to predict local gas and particle properties in a range of flow geometries. Fluid properties, which vary rapidly on a scale comparable with the particle spacing, were replaced by smoothed variables obtained by averaging over regions large compared with the particle spacing but small compared with the complete system. The resulting equations, therefore, describe the motion of the fluid and particles as though they were inter-penetrating continua, see for example Spalding (1977). There is much argument in the literature concerning the validity of the continuum assumption under different spray flow conditions, see Hinze (1971), and the modelling of turbulent stress tensor for the liquid or solid phase. Assessment of the procedure by applying it to simple two phase flow problems is, therefore, required in addition prior to its application to the more complex spray flows, see for example Baghdadi (1979).

Examination of this brief review of the available methods suggests that all are still in their development stages and that very few applications to predict reacting spray flames were reported. Another deficiency is that validation against experimental data has not been attempted by most investigators. However, the first approach of Crowe (1974) is potentially more suitable for direct adaptation to predict spray flames with the least amount of

development and modifications.

The mathematical approach employed in the present work is based on that used by Crowe (1974) but is extended here to allow for the prediction of reacting sprays. Based on the available experimental evidence for the structure of spray flames, see Subsection 1.2.1, the spray combustion model adopted here assumes that the evaporating droplets act as distributed point-injectors of fuel vapour within the flame and that the combustion rate of the fuel vapour can be treated in a way similar to that used for the prediction of gaseous flames, see for example Spalding (1976).

1.3 The Main Contributions of the Present Study

Measured values of droplet mean axial velocity, the rms of the corresponding fluctuations, mean gas temperature and droplet number density are presented for a range of unconfined swirling and non-swirling spray flames. The experimental results allowed the effects of air swirl and fuel mass flow rate and, therefore, of spray properties, on the flame behaviour to be determined and quantified.

Detailed temperature, droplet mean velocities, wall-temperature and concentration measurements were performed in a cylindrical combustion chamber equipped with a rotating cup-atomizer capable of producing a near-monosized spray. The latter allowed the spray mean droplet diameter to be varied without altering the fuel and air operating conditions. The experimental program was arranged to examine the influence of the mean-droplet diameter on the flame properties under two different turbulent mixing rates. The interaction between the near-monosized spray and the surrounding combustion air was also examined for three levels of air swirl.

A method for the calculation of the local properties of

spray flames is presented and its capabilities and limitations appraised by comparing calculated results with measurements obtained for four different spray flame geometries, including those referred to above.

1.4 Outline of the Thesis

The remainder of the thesis is presented in three chapters. The following chapter provides a detailed description of the experimental work. Measurement techniques are presented together with an assessment of their accuracy. The results for both the unconfined and confined flame experiments are reported and discussed and brief concluding remarks are given for each.

Chapter 3 is concerned with the theoretical work and is arranged to provide a statement of the equations solved and the boundary conditions used. The turbulence, combustion, spray and radiation models are described, assumptions indicated and the numerical scheme used to solve the equations presented. The calculation procedure is then appraised by comparison with measurement results from four test cases. The chapter ends with brief concluding remarks.

Finally, Chapter 4 summarizes the main conclusions of the present work and provides suggestions for future work.

In addition to the four chapters, the thesis also includes five appendices. The first two provide supplementary details of the fuel nozzles and air swirlers used in the experiments. The third appendix provides a simplified analytical analysis of the velocity characteristics of fuel droplets. The experimental results of gas temperature and species concentrations, obtained for the confined flame experiments, are presented and discussed, in the text, in the compressed contour form and the corresponding radial profiles are

given in Appendix IV for reference purposes. The last appendix, Appendix V, comprises a paper entitled "Combustion-driven oscillations in a small tube". It described experimental work, performed largely by the author, in the early stages of his research and is appendicised because its topic is not directly relevant to those of this thesis.

CHAPTER 2

EXPERIMENTAL STUDY

2.1 Introduction

The experimental study, reported in this chapter, comprised two main parts: the first was concerned with unconfined and the second with confined spray flames. For the unconfined flame experiments, a combined swirl/air-assisted atomizer was located concentrically inside a secondary air duct and the kerosene spray flames fired vertically upwards. The burner operating conditions, including combustion air swirl and fuel mass flow rate, were varied and droplet velocity information was obtained with a Laser Doppler anemometer. Related changes in the flame properties were interpreted from the velocity characteristics of the droplets. Sample measurements of droplets number distribution and gas temperature also contributed.

Experiments were then conducted with kerosene spray flames inside a cylindrical combustion chamber. A rotating-cup atomizer, capable of producing different mean-droplet diameters for a certain mass flow rate, was used in this case and the combustion air was supplied through an interchangeable swirler. The main emphasis in this case was placed on the effects of the mean-droplet diameter on the combustion characteristics which were interpreted from the detailed measurements of temperature, species concentrations and droplet velocity. The influence of the degree of swirl of the combustion air on flame properties was also considered.

The contents of this chapter are arranged as follows. Measurement techniques are described in Section 2.2 together with an assessment of accuracy for each. Details of the unconfined and confined flame experiments are presented in Sections 2.3 and 2.4 respectively

with a discussion of the experimental results and concluding remarks in each case.

2.2 Measurement Techniques

This section provides a description of the measurement techniques used during the present study. Emphasis is given to the reasons for the choice of each particular technique and to the assessment of its accuracy under the present experimental conditions. The measurements made use of a water-cooled suction pyrometer, a water-cooled stainless steel sampling probe and a Laser Doppler anemometer and these instruments are described in detail in the following subsections. Temperature measurements in the unconfined flame experiments were obtained with a bare wire thermocouple which needed no further description.

2.2.1 Temperature Measurements

Gas temperature measurements have been obtained by the suction pyrometer probe shown in Fig. 2.1. The thermocouple was shielded and the gases sucked past it. These features of the suction pyrometer emerged after consideration of the different error sources associated with gas temperature measurements by a bare wire thermocouple of comparatively large diameter (> 100 μm), see for example Khalil (1975), Land et al (1956), Moffat (1963), Chedaille et al (1972) and Bradley et al (1968). Under conditions typical of those encountered in flames the radiation and conduction heat losses from the thermcouple represent the main error sources. The true gas temperature can, in principle, be obtained by correcting the measured values either through experimental techniques, see for example Odidi (1974), Holderness et al (1969) and Attya (1979), or through the simultaneous solution of equations describing heat transfer modes between the thermocouple bead and surroundings, see Sato

et al (1975), Khalil (1975), Bradley et al (1968) and George et al (1956). Apart from the practical difficulties associated with such techniques, they are subject to uncertainties relating to the calculation of the convective heat transfer coefficient and the calculation of the radiant heat transfer (e.g. wire emissivity, surrounding temperatures, etc.), see for example Chedaille et al (1972), Moffat (1963) and Khalil (1975).

The radiation and conduction errors can be largely reduced by using fine-wire thermocouples of the type described by Ballantyne et al (1977), Odidi (1974), Moneib (1979) and Yoshida et al (1978). However, due to the small diameter of the thermocouple (around 40 μm) its life-time is very short, especially when measuring high temperatures, see Moneib (1979). This and the other practical difficulties relating to the probe-handling precluded the use of these fine-wire thermocouples in the present study.

In the suction pyrometer, the shielding of the thermocouple junction significantly reduces the radiant heat transfer (by increasing the temperature of the junction surroundings) and the suction of gases through the pyrometer increases the convective heat transfer to a level which, in a properly designed probe, compensates for any radiation or conduction losses. The suction of gases also increases the convective heat transfer to the shield with a consequent increase in its temperature and a further reduction in bead radiation.

The extent to which the temperature measured by a suction pyrometer represents that of the gas depends mainly on the geometric details and operating conditions, see Land et al (1956), Khalil (1975), George et al (1956), Terbush (1962) and Chedaille (1972). These can be summarized as: number of shields, their material and geometry, suction velocity, bead position inside the shield and the flow conditions affecting the convective heat transfer to the shield. Khalil (1975)

and Chedaille et al (1972) have indicated that the accuracy of the suction pyrometer can be better than 10%.

The suction pyrometer used in the present study encloses a thermocouple made from platinum : 13% rhodium-platinum wires of diameter 300 μm and had a bead diameter of approximately 400 μm. The bead was enclosed in a stainless-steel shield of 6 mm outer diameter, 2 mm thickness and 15 mm length and was positioned 2 mm from the entry section of the shield. Gases were sucked through the pyrometer at a rate of 20 ℓ/min. The outer diameter of the suction pyrometer, Fig. 2.1, was 6 mm. Standard compensation wires for platinum : 13% rhodium-platinum thermocouple were used to connect the pyrometer to the measuring equipment, Fig. 2.2, which include a D.C. amplifier, DISA Type 52B30 integrator and Solartron DVM respectively.

Wall-temperature measurements have been obtained in the present work by Chromel-Alumel thermocouples fixed to the combustion chamber walls as indicated in Fig. 2.2. Conduction error has been minimized by using a small diameter wire, 0.2 mm, and by increasing the length of the supporting cylindrical steel pieces as shown in Fig. 2.2, see Moffat (1963), Bradley et al (1968) and Chedaille et al (1972).

For one case, in the unconfined flame experiments, gas temperature measurements were obtained, see Section 2.3.3, by a platinum : 13% rhodium-platinum bare wire thermocouple. The wire diameter was 300 μm and the bead diameter was approximately 400 μm. In this case no corrections have been applied for the heat losses by conduction and radiation.

2.2.2 Assessment of the Accuracy of Temperature Measurements by the Suction Pyrometer

The suction rate of gases through the present pyrometer was

adjusted to a value which provided suction rate-independent temperature measurements. This level was obtained by locating the probe at different points within the flame and recording the variation of temperature with suction. Fig. 2.3 shows a sample of the resulting curves for two points having temperatures 1765 ^{o}K and 1350 ^{o}K. The measured temperature is plotted against the suction velocity, calculated from the following expression and assuming constant pressure flow of gases through the pyrometer:-

$$U_{s.p.} = \frac{V'_{p.t.}}{A} = \frac{1}{A} \cdot V_m \cdot \frac{T_{p.t.}}{T_m} \qquad (m/s)$$

where V' is the volumetric flow rate, T the temperature and A the probe tip area. The subscripts p.t. and m refer to conditions at probe tip and the volumetric flow rate measuring device.

Fig. 2.3 indicates that, for the high temperature point, a relatively higher suction rate is necessary to reach the constant-temperature portion of the pyrometer characteristics curve. This increase in suction velocity (convective heat transfer) compensates for the increase in radiation associated with high gas temperature.

The suction rate, determined from the above procedure, was kept constant during measurements and it is likely that errors in the measured temperature values can stem either from variations in this rate due to probe blockage by the deposition of carbon-particles or from the need to alter this level to account for the changes in the convective heat transfer induced by variations in gas properties. The former was minimized by frequent cleaning of the probe tip by blowing compressed air through the suction tube. An assessment of the error induced by the latter is extremely difficult, but it can be removed by using a high suction rate.

Preliminary temperature measurements with the present suction pyrometer indicated dependence of the measured values on the thermocouple bead position inside the shield which is in agreement with the results of Terbush (1962) and Khalil (1975). For example, moving the bead approximately 2 mm to either side of the position of maximum recorded temperature was found, in one case, to be associated with approximately 6% reduction in the recorded value. The bead position, corresponded to the maximum recorded temperature, was kept constant during subsequent measurements. The error induced by slight movement of the bead resulting, for example, by the need to clean the probe during measurements, can be as large as - 2.0%. The negative sign is due to the increase in radiation upon moving the bead towards the probe tip and the cooling of gases, by the probe cooling system when the bead moves away from the tip.

The following simplified analysis allows the quantification of the errors associated with conduction losses, radiation between the thermocouple junction and shield and radiation between the junction and parts of the wall seen by it. The implication of variations in shield temperature and suction velocity to the resulting error are also considered. Fig. 2.4a shows the heat transfer modes associated with the suction pyrometer. The present analysis, however, concentrates only on the heat transfer to and from the thermocouple junction as indicated in Fig. 2.4b. The heat transfer associated with the shield is by-passed by assuming different values for the shield temperature. The energy balance equation for the junction can be written as:-

$$h_c \cdot A_j (T_g - T_{s.p.}) = \varepsilon_t \cdot \varepsilon_{sh.} \cdot \sigma \cdot A_j (T_{s.p.}^4 - T_i^4) + K_R \cdot \varepsilon_t \cdot$$

$$\cdot \varepsilon_w \cdot \sigma \cdot A_j (T_{s.p.}^4 - T_w^4) + \frac{K_w \cdot A_w}{\chi} (T_{s.p.} - T_m) \qquad (2.2.1)$$

and, therefore:-

$$(T_g - T_{s.p.}) = \frac{\varepsilon_t \cdot \varepsilon_{sh} \cdot \sigma}{h_c} (T_{s.p.}^4 - T_i^4) + \frac{K_R \cdot \varepsilon_t \cdot \varepsilon_w \cdot \sigma}{h_c} (T_{s.p.}^4 - T_w^4) +$$

$$+ \frac{K_w \cdot A_w}{\chi \cdot A_j \cdot h_c} (T_{s.p.} - T_m)$$

Available data for platinum-platinum-rhodium thermocouples, see Moffat (1963) and Sato et al (1975), indicate that wire emissivity, ε_t, ranges from 0.18 to 0.55 and thermal conductivity from 40 to 60 Kcal/hr m ^oC. The higher values are used in the present analysis, since they represent the worst conditions for radiation and conduction. Wall and shield emissivities, ε_w and $\varepsilon_{sh.}$, are taken as 1 and 0.9 respectively. The heat transfer coefficient is calculated from the following correlation for the heat transfer to a thermocouple bead placed parallel to the flow direction, see Moffat (1963):-

$$N_{Nu} \cong 0.094\ N_{Re}^{0.674} \quad \text{where } N_{Nu} = \frac{h_c \cdot d}{k} \text{ and } N_{Re} = \frac{\rho_d \cdot U}{\mu}$$

The gas temperature is calculated for presumed values of suction pyrometer readings, temperature of shield inner wall, suction velocity, wall and thermocouple support temperatures. Details of the presumed values and calculated gas temperature are given in Table 2.1. The calculated values of the percentage error, due to conduction and radiation, shown in Table 2.1, indicate that it ranges between 6.0% (for $T_{s.p.}$ = 1600 ^oK) and 2.5% (for $T_{s.p.}$ = 800 ^oK). These values give approximate magnitudes for the errors associated with the suction pyrometer and it is unlikely that large modifications to them can result from the uncertainties in the presumed values and the heat transfer

coefficient correlation.

It is clear from Table 2.1 that the contribution of conduction losses to the resulting error is small, especially for the higher temperature point. The results of Bradley et al (1968) and Sato et al (1975) indicate that conduction error can be minimized by keeping the temperature of the thermocouple wire-portion adjacent to the junction as high as possible. Thus, small temperature gradients will be assured close to the junction. In the present suction pyrometer, this was achieved by projecting the junction a small distance from the supporting ceramic tube (the junction was still enclosed by the shield) and by increasing the length of the shield to minimize the cooling effects of the probe cooling water. Therefore, it is expected that the influence of conduction losses on the accuracy of the present measurements is relatively small.

The suction pyrometer shield acts, from the point of view of heat transfer, as a large-diameter bare-wire thermocouple and consequently its temperature is expected to be lower than both the thermocouple bead and surrounding gases. The extent to which the shield temperature differs from that of the gas or bead varies, as in the case of a bare-wire, with gas properties (convection), the temperature level of the gas (radiation) and the shield dimensions (convection and radiation). The calculated gas temperatures, shown in Table 2.1 for different shield temperatures, indicate that the percentage total error increases with the reduction in the shield temperature. However, the extent to which the error increases is small, for example, increasing the temperature difference from 100 ^{o}K to 800 ^{o}K causes a 4.15% increase in the error. Fig. 2.5 shows the calculated error against the temperature difference for suction pyrometer readings of 1600 ^{o}K and 800 ^{o}K. The results show that the sensitivity of the error to a

reduction in the shield temperature is appreciably reduced for the low temperature case. Again, although the calculations are based on presumed values, they give a good indication of the error trends with variation in the shield temperature.

The calculated results of the influence of suction velocity, see Table 2.1 and Fig. 2.6, confirm the experimental results presented in Fig. 2.3 but suggest a lower sensitivity to the resulting error with variations in suction velocity.

The view factor, K_R, for radiation between the thermocouple junction and the combustion chamber wall, for the present suction pyrometer, depends on the position of junction inside the shield and the distance between the probe tip and opposite wall. The latter varies during radial temperature measurements within the combustion chamber. The calculated values of Table 2.1, Case 3 and 8, give an indication of the resulting error. For the higher temperature, an increase in K_R from 0.3 to 0.5 causes a corresponding increase in the percentage error from 7.5% to 10.23%. However, it must be mentioned that, for the present suction pyrometer, the radiation view factor, K_R, is significantly smaller than 0.3 and, therefore, this source of error has a negligible influence on the accuracy of the present measurements.

Catalytic effects associated with temperature measurements by platinum-based thermocouples have been observed by many investigators, and related errors in the measured temperature profiles may be avoided by using non-catalytic coatings for the thermocouple bead, see for example Odidi (1974), Bradley et al (1968). In the present work, facilities for such coating techniques were not available, and it is speculated that the increase in gas residence-time at the probe tip, due to the high suction velocity, might reduce the associated errors, see also Tine (1961).

Probe measurements in combusting-flows are usually associated with uncertainties in the measured quantities due to the expected thermal and aerodynamic interference between the probe and surrounding gases. The degree of interference increases with probes which use suction of gases through the probe, see Bilger (1977), Tine (1961) and Yanagi (1977). In the present work, interference effects caused by the probe body were minimized by reducing the probe dimensions (ratio of probe to combustion chamber diameter was 6/150). Visual observation and wall temperature measurements indicated that the introduction of the probe into the combustion chamber had no effects on flame stability and overall combustion characteristics.

Although probe-cooling-water flow rate was minimized and the difference between the inlet and outlet water temperatures was of the order of 10 ^{o}C, it is possible that a distortion to the temperature profiles can be caused by the probe cooling effect. The suction of gases through the pyrometer also increases the possibility of such distortion. However, symmetry checks for the temperature profiles, presented in Appendix AIV, indicated that the differences between the measured values on both sides of the flame centre-line were around 6.0% and implied small distortion.

The suction of gases at velocities different from the local gas velocities (non-isokinetic condition) introduces a further complication due to the possibility of segregation effects associated with measurements in regions of large density fluctuations (e.g. high-suction velocity gives a bias towards gas pockets of high temperature, low density), see Tine (1961) and Bilger (1977). It is clear that quantification of the errors induced by the above factors of profiles-distortion and segregation effects is difficult but their contribution to the total error in the present work is expected to decrease in the

downstream direction of the combustion chamber. In these regions, the temperature profiles are more uniform and the high intensity of combustion precludes the existence of gas pockets of large density variations.

The temperature values measured by the present suction pyrometer are subject to a source of uncertainty relating to the type of averaging produced by the probe. It stems mainly from the fluctuating nature of the various properties within the present turbulent and combusting flow. In the following analysis, the relation between the averaged temperature produced by the probe and the time-averaged gas temperature will be presented and discussed. In general, the temperature attained by a thermocouple element at any instant of time is determined from the energy balance between different heat transfer modes, i.e.:-

$$(\hat{T}_g - \hat{T}_t) \cdot \hat{h}_c \cdot \alpha_1 = \alpha_2 (\hat{T}_t^4 - \hat{T}_w^4) + \alpha_3 (\hat{T}_t - \hat{T}_m) + \frac{d\hat{T}_t}{dt} \cdot \alpha_4 \qquad (2.2.2)$$

where α_1, α_2, α_3 and α_4 are constants determined by the thermocouple geometry and properties, see Equation (2.2.1).

The gas temperature, $\hat{T}_g$, and the heat transfer coefficient, $\hat{h}_c$, can be decomposed into a mean and a fluctuating component, i.e.:-

$$\hat{T}_g = \overline{T}_g + T_g' \qquad \text{and} \qquad \hat{h}_c = \overline{h}_c + h_c'$$

and if the thermocouple diameter is comparatively large the thermocouple temperature can be expressed as:-

$$\hat{T}_t = \overline{T}_t$$

where the overbar denotes the ensemble averaging (time averaging in this case).

The averaged form of the above equation can be written as:-

$$\alpha_1 \cdot \overline{T}_g \cdot \overline{h}_c + \alpha_1 \cdot \overline{T_t' \cdot h_c'} - \alpha_1 \cdot \overline{T}_t \cdot \overline{h}_c = \alpha_4 \cdot \cancel{\frac{d\overline{T}_t}{dt}}^{0} +$$

$$+ \alpha_2 (\overline{T}_t^4 - \overline{T}_w^4) + \alpha_3 (\overline{T}_t - \overline{T}_m)$$

i.e.:-

$$\overline{T}_t = \overline{T}_g + \frac{\overline{T_g' \cdot h_c'}}{\overline{h}_c} - \frac{\alpha_2 (\overline{T}_t^4 - \overline{T}_w^4)}{\alpha_1 \cdot \overline{h}_c} - \frac{\alpha_3 (\overline{T}_t - \overline{T}_m)}{\alpha_1 \cdot \overline{h}_c}$$

The last two terms in the RHS of the equation represent the radiation and conduction corrections to the measured values. By adding them to $\overline{T}_t$ and considering the resulting value as $\overline{T}_m$, the measured averaged value of temperature, it follows that:-

$$\overline{T}_m = \overline{T}_g + \frac{\overline{T_g' \cdot h_c'}}{\overline{h}_c} \qquad (2.2.3)$$

It is, therefore, evident that the measured averaged temperature differs from the true time-averaged gas temperature. The above equation can be rewritten as:-

$$\overline{T}_m = \frac{\overline{T}_g \cdot \overline{h}_c + \overline{T_g' \cdot h_c'}}{\overline{h}_c} = \frac{\overline{T_g \cdot h_c}}{\overline{h}_c}$$

and the thermocouple readings are considered to be averaged through this

relation, see Bilger (1977).

It is speculated that the thermocouple will read the time averaged temperature if a fine-wire (around 30 μm) is used in the measurements since, in this case, the heat transfer coefficient, $\overline{h}_c$, will be large (due to its dependence on wire diameter) and Equation 2.2.3 will be modified to take the form:-

$$\overline{T}_m = \overline{T}_g + \frac{\overline{T_g'h_c'} - \overline{T_t'h_c'}}{\overline{h}_c} \qquad (2.2.4)$$

and the two correlation terms are anticipated to be of comparable magnitude. In part confirmation, Moneib (1979) has indicated that the use of 15 - 20 and 40 μm diameter fine thermocouples, for the measurements of mean temperature in a gaseous diffusion flame, produced similar results. The same result was also obtained by Attya (1979) for mean temperature measurements in unconfined spray flames using 40 and 80 μm diameter wires. This suggests that the correlation term in Equation (2.2.4) is negligible compared to $\overline{T}_g$. Attya (1979) also made a comparison between the results obtained with a suction pyrometer, similar to the present one, and fine-wire thermocouples of 40 and 80 μm diameter (corrected experimentally for radiation losses) and indicated that the overall error, resulting from all sources, associated with the suction pyrometer ranges between 50 - 200 ^{o}K in temperatures of 1000 - 1600 ^{o}K. It can, therefore, be anticipated that, for the present suction pyrometer, the deviation of the measured values from the time averaged gas temperature, due to the above-mentioned source, will be small (in the range of 1.0 - 2.0%).

The contents of this subsection can be summarized as follows. The error sources associated with present suction pyrometer are mainly

due to:-

(i) The probe operating conditions (suction velocity and position of thermocouple element inside the shield).

(ii) Probe-gas interference effects.

(iii) The type of averaging produced by the probe.

The first error source was analysed and the results suggest that it can lead to an under-estimation of the temperature by around 4 - 6%. The second and third sources are more difficult to quantify but the preceeding discussion indicates that they range between 2 - 5%.

2.2.3 Concentration Measurements

Samples for the measurements of carbon dioxide, carbon monoxide and oxygen species concentration were withdrawn from different points within the present combustion chamber, using a stainless-steel water-cooled probe, see Fig. 2.7. The sampling tube had an inner diameter of 1.55 mm and was surrounded by a water cooling arrangement comprising two concentric tubes of 4.04 and 6.0 mm diameter respectively. The slender-nosed probe tip had a diameter of 4 mm at the measuring point. The samples were analysed on-line using an infra-red analyser (Holger & Watts model SC/F) for CO and CO_2, and a paramagnetic analyser (Beckman, model E2) for oxygen. Fig. 2.8 shows a schematic diagram for the sampling system. The unburned hydrocarbon vapours and H_2O were condensed and removed from the sampling line and consequently the reported results of the present measurements are based on dry-analysis. At some points within the combustion chamber the CO-concentration

exceeded the upper-range of the infra-red analyser, 5%, and the sample was diluted by nitrogen addition as indicated in Fig. 2.8.

Due to the complexity of the aerodynamics of the present flow configuration (highly swirling flames with recirculating zones) no attempt was made to use sampling probes employing the isokinetic sampling principle (sampling velocity equals gas velocity). Probes of this type were described by Tine (1961), Kent et al (1973), Vranos et al (1969) and Bowman (1977). They indicated that sampling errors caused by the suction of gases through the probe (profiles-distortion and segregation effects in regions of large density fluctuations) can be minimized by keeping the suction velocity equal to that of the gas at the measuring point. However, Tine (1961) has demonstrated large uncertainties in the practical methods used to ensure isokinetic conditions, even in a simple flow configuration. More details about this point will be given in the next subsection 2.2.4.

The high rate of soot formation associated with liquid-fuelled flames and the sample flowrate requirements for the present CO and CO_2 analysers (around 1.5 ℓ/min) precluded the use of sampling micro probes, see Fristorm et al (1965). The main advantage of these probes is the insignificant flow perturbation caused by the probe, see Yanagi (1977), Tine (1961) and Fristorm et al (1965).

Quenching of chemical reactions at the probe tip has been achieved, in the present work, by water-cooling as indicated in Fig. 2.7. Experience with the present suction pyrometer (similar in design to the sampling probe) have shown that a significant drop in the gas temperature occurs over a short distance along the probe tip (a typical value was a drop of 600 ^{o}K over 15 mm). The sampling flow rate, for the present measurements, corresponds to suction velocities ranging between 45 and 85 m/s, depending on the gas temperature. A rough estimate for the

quenching rate can be obtained if the temperature drop is assumed to be similar to that observed for the suction pyrometer, i.e.:-

$$\text{Quenching rate} = \frac{dT_o}{dt} = \Delta T/(X/V) = \frac{600}{\left(\frac{15 \times 10^{-3}}{60}\right)} = 2.4 \times 10^6 \ ^oK/s$$

where X is the distance corresponding to the temperature drop ΔT and V is the suction velocity ($\simeq$ 60 m/s). The quenching rate can also be estimated from the following expression, see Ramshaw (1968):-

$$\frac{dT_o}{dt} = \frac{4h\ (T_o - T_w)}{c_p \ . \ p \ . \ D}$$

where h is the heat transfer coefficient inside the suction tube, T_o and T_w are the gas and probe tip wall temperature respectively. Assuming a gas temperature of 1500 ^oK, wall temperature of 900 ^oK and a heat transfer coefficient of 200, calculated from the correlation:-

$$N_{Nu} \simeq 0.029 \times N_{Re}^{0.8}$$

the quenching rate, dT_o/dt, is calculated to be 1.95×10^6 $^oK/s$. These estimated values are in close agreement with those quoted by Ramshaw (1968) for similar probes.

2.2.4 Assessment of the Accuracy of Concentration Measurements

The factors influencing the accuracy of concentration measurements can be normally grouped into two categories. The first, includes those resulting from probe-gas interference, quenching of chemical reaction

and catalytic effects within the probe. The second, includes factors associated with the sample handling and analysis.

In the present work, it is unlikely that sampling errors, induced by inefficient quenching or catalytic effects, contribute significantly to the overall accuracy of measurements. The quenching rates estimated in the previous section can be considered sufficiently high especially for measurements in turbulent flames, see Bilger (1977). This has been also confirmed during the measurements where changes in the probe cooling-water flow rate were found to have a negligible effect on the measured concentrations. Tine (1961) indicated that cooling the sampling tube compensates for and probably overcomes any increase in reaction rate due to catalytic effects. Unlike in the present case, catalytic effects can be very important in connection with nitrogen-oxides measurements.

Fristorm et al (1965), Yanagi (1972a, 1972b and 1977) and Tine (1961) considered, both experimentally and theoretically, the problem of probe effects on the concentration profiles in laminar flames, where probe-gas interference can be significant. Probe effects, for simplified conditions, were mainly related to the probe size and its operating conditions (e.g. suction velocity). For example, the distortion of the profiles decreased with the probe size and with the application of isokinetic sampling. In turbulent combusting flows, sampling errors, other than those caused by profile distortion due to the probe body and the suction of gases through it, can possibly stem from segregation effects of the type described previously, Section 2.2.2, especially when sampling under non-isokinetic conditions, see Bilger (1977) and Tine (1961). The fluctuating nature of the measured quantities and the large variations in flow conditions from point to point within a turbulent flame, render it difficult to quantify such probe interference effects. However, a

estimate of the errors can be arrived at from redundant information. These include, repeatability of measurements, observed influences of suction rate on measured quantities and symmetry and atom-balance checks.

In the present measurements, the sampling flow rate was kept constant and, therefore, the departure from the isokinetic sampling condition varies with the gas velocity and temperature (suction velocity). To assess the implication of this effect for accuracy, measurements of species concentration corresponding to different suction rates were obtained for several points within the combustion chamber. No general trend for the direction of variation in the measured values with suction rate was obtained, however, the sensitivity of measurements to changes in suction rate decreases with downstream locations in the flame. This is probably due to the more uniform distribution of concentration profiles at these regions.

Figs. AIV.23 - 25, see Appendix AIV, illustrate the degree of repeatability of the present CO, CO_2 and O_2 concentration measurements. The results show comparatively large discrepancies at the upstream region of the flame, especially at points where nitrogen-dilution of the sample was used. At this region, the average repeatability was estimated as approximately ± 6% of reading. This value is reduced for downstream regions of the flame (around ± 3%). Also shown in Appendix AIV, is a sample of the symmetry checks, see Section 2.4, where measurements were obtained at both sides of the geometrical centreline of the combustion chamber. Apart from the position uncertainty of the present measurements (estimated as ± 2 mm), it can be seen that the measured values on both sides agree to within ± 5%.

The calibration of the infra-red analyser for CO and CO_2 species measurements has been carried out in the present work by using

standard gas-cylinders filled with a mixture of 12% CO_2, 4% CO and 84% N_2. The tolerance specified by the supplier was ± 5% and implies a corresponding uncertainty in the measured values. The accuracy of the analyser was specified as ± 0.5%. The accuracy of the paramagnetic oxygen analyser was also specified as ± 0.5% of full scale reading (25% O_2) but it is likely to increase in the present work to ± 1% as no corrections for background gases were incorporated. Nitrogen and oxygen gases were used to calibrate the analyser and the tolerance of the supplied cylinders was ± 6%.

At points within the combustion chamber, where dilution of the sample was necessary to allow measurements of CO concentration, the species concentration of the original mixture was calculated from the following expression:-

$$Y_o\% = Y_m\% \cdot \frac{V_t'}{V_1'}$$

where $V_t' = V_1' + V_2'$ and V_1' volume flow rate of the original mixture, V_2' volume of nitrogen, Y_o concentration of any species in the original mixture and Y_m concentration of species measured with nitrogen addition. It is clear that two measured volume flow rates are involved in calculating the composition of the original mixture. Consequently, any uncertainties in the measured values will be reflected in the calculated concentrations. During the present measurements, CO_2 and O_2 concentrations were obtained with and without nitrogen addition and the accuracy of the dilution procedure was found to be around 7%.

The measured values of species concentrations obtained in the present work are subject to a source of uncertainty, similar to that described in Subsection 2.2.2, which relates to the influence of the

fluctuations in the various properties on the type of averaging produced by the probe. During the sampling process, the instantaneous mass conservation of a species, i, can be represented by:-

$$C_{i_m} \cdot M_{tot.} = \hat{C}_{i_t} \cdot \hat{M}_{tot._t}$$

where C_i is the mass concentration of species i, $M_{tot.}$ is the total mass flow rate of the sample and the subscripts m and t refer to the measuring point and the probe tip respectively. By decomposing C_{i_t} and $M_{tot.}$ to $C_{i_t} = \overline{C}_{i_t} + C_i'$ and $M_{tot.} = A\left(\rho U_s + (\rho U_s)'\right)$ and taking the average for the above expression, it follows that:-

$$\overline{C}_{i_m} \cdot \overline{\rho U_s} = \overline{C}_{i_t} \cdot \overline{\rho U_s} + \overline{C_{i_t}' \cdot (\rho U_s)'} \qquad (2.2.5)$$

i.e.:-

$$\overline{C}_{i_m} = \overline{C}_{i_t} + \frac{\overline{C_{i_t}' \cdot (\rho U_s)'}}{\overline{\rho U_s}} \qquad (2.2.6)$$

which again indicates that the measured mean values are not the true time averaged values at the point of measurement. In effect, the probe produces an averaging according to the expression 2.2.6, i.e.:-

$$\overline{C}_{i_m} = \frac{\overline{C}_{i_t} \cdot \overline{\rho U_s} + \overline{C_{i_t}' (\rho U_s)'}}{\overline{\rho U_s}} = \frac{\overline{C_{i_t} (\rho U_s)}}{\overline{\rho U_s}}$$

If U_s is assumed constant the averaging will reduce to the density averaging form usually known as "Favre averaging", i.e.:-

$$C_{i_m} = C_{i_t} + \frac{\overline{C_{i_t}' \cdot \rho'}}{\bar{\rho}} \qquad (2.2.7)$$

It is apparent that the difference between the time averaged mass fraction and the measured values is dependent on the density-mass fraction correlation and the gas averaged density. If interest lies in measuring the time averaged mass fractions the correlation term in Equation (2.2.7) represents an error. However, it is clear that assessment of its magnitude is difficult. This point has been recognised by several investigators, see for example Bilger (1977) and Jones (1979) and the approach to get round it is to regard the measurements as averaged through Equation (2.2.7). This approach has been adopted in the present study and, therefore, the results are free from this source of error. The experimental results of the present chapter will be used in the validation study of the calculation procedure to be described in Chapter 3. Fortunately, the results of the calculations are considered as density-averaged quantities.

The preceeding discussion of the factors influencing the accuracy of concentration measurements suggest that the uncertainties associated with quenching of chemical reaction and catalytic effects within the probe are insignificant. Those associated with probe-gas interference effects are more difficult to quantify but a rough estimate of the errors can be extracted from the repeatability of measurements, observed influences of suction velocity and symmetry checks. The repeatability of measurements was found to be in the range of ± 3 - 6% and symmetry checks indicated an uncertainty of around ± 5%. The instrumentation errors are small and are anticipated to be within ± 2%. The uncertainties associated with the sample dilution with nitrogen to allow CO measurements at some points were found to be significant and can be as high as ± 6 - 7%. The measured concentrations are recongised

as density-weighted averages and, therefore, errors arising from the fluctuating nature of the present flow do not contribute to the overall accuracy of measurements.

2.2.5 Velocity Measurements - Laser Doppler Anemometer

Velocity measurements were carried out with a Laser Doppler anemometer operating in the fringe-mode with an argon ion laser (spectra physics model 164, wave length = 488 nm and maximum power around 2 w). An acousto-optic (Bragg) cell was used to provide both beam splitting and frequency shifting of 21.0 MHz between the two beams, see Durão et al (1975). The optical arrangement and signal processing equipment were different for the unconfined and confined flame measurements and, therefore, are discussed separately in the following parts together with related comments on flow conditions.

(a) Unconfined Flame Measurements

The anemometer was set-up for the forward scatter mode of operation as indicated in Fig. 2.9, see also Durst et al (1976). The laser power was approximately 80 mw and a 300 mm focal length lens was used to focus and cross the beams at a half angle of 6.58 degrees. The resulting relationship between velocity and Doppler frequency was 2.136 ms^{-1}/MHz. Forward scattered light was collected and focussed onto a photomultiplier (EMI model 9815 B) with a lens of 150 mm focal length. This arrangement allowed a measuring control volume of approximate diameter and length 0.152 and 2.1 mm respectively, see Melling (1975), Durão (1976) and Durst et al (1976).

Doppler signals detected by the photomultiplier were processed by a digital spectrum analysis system that has been described by Durão et al (1976). The system employed a conventional spectrum analyser

(Hewlett Packard model 8552A/8553B), sweep generator and a digital counter with an electronic typewriter. The probability density function of Doppler frequency (p.d.f.) was obtained from the digital output of this arrangement and the velocity data, mainly the mean and the rms values, were calculated from the first two moments $\bar{\nu}_D$ and $\tilde{\nu}_D$, using the relationships, see Durst et al (1976) and Durão (1976):-

$$\bar{U} = \lambda^* \, (\bar{\nu}_D - \nu_S)$$

and:-

$$\tilde{u} = \lambda^* \, (\tilde{\nu}_D)$$

where ν_S is the frequency shift of the Bragg cell and λ^* is the Doppler frequency/velocity conversion factor (fringe spacing) defined as:-

$$\lambda^* = \frac{\lambda}{2 \sin \phi}$$

$\bar{\nu}_D$ and $\tilde{\nu}_D$ were found from the measured p.d.f., $P(\nu_i)$, after normalization to unit area, with the equations:-

$$\bar{\nu}_D = \sum_{i=1}^{N} \nu_i \cdot P(\nu_i)$$

and:-

$$\tilde{\nu}_D = \left[\overline{(\nu_D - \bar{\nu}_D)^2}\right]^{1/2} = \left[\sum_{i=1}^{N} (\nu_i - \bar{\nu}_D)^2 \cdot P(\nu_i)\right]^{1/2}$$

The use of Laser Doppler anemometry in this set of measurements

allowed velocity measurements in the initial flame region and up to approximately 250 mm downstream. Measurements were not possible in the immediate vicinity of the fuel nozzle, i.e. $X \leq 30$ mm, as the very dense assembly of droplets attenuated the Doppler signal. The droplet velocities, especially at the near-nozzle locations, were influenced by their size and injection velocity, gas and droplet properties and processes of collision and break-up. The anemometer measured the droplet velocity which were the same as the gas velocity only when the droplets were sufficiently small. For values of $x/D \lesssim 2$, the measured mean velocities were probably significantly different from the gas velocity and, as indicated by Appendix AIII, the rms quantities were significantly influenced by the range of droplet diameters.

The time-averaged number of droplets passing through the Laser Doppler anemometer control volume was also measured in the present case using an electronic counter connected to the delayed output of the oscilloscope. The threshold level of the oscilloscope was kept constant during any axial or radial traversing measurements and provided a constant base for the counting procedure. However, the measured values are influenced by possible variation in signal amplitude due to particle size and velocity and an uncertainty of about 2.0% is expected, see Durão (1976) and Durão et al (1979).

(b) Confined Flame Measurements

The backward-scatter mode of the Laser Doppler anemometer was used in this set of measurements as indicated by the arrangement of Fig. 2.10, see also Durst et al (1976). Due to the low intensity of the scattered light in the backward direction, the laser power was increased in this case to approximately 600 mw. The transmitting optical components include the acousto-optic Bragg cell and 300 mm

focal length lens. The separation distance between the two beams was 70.5 mm with a resulting crossing angle of 13.4 degrees and a frequency/velocity conversion factor of 2.091 ms^{-1}/MHz. The receiving optical components comprised two parallel mirrors (45^{o} to the laser beam direction), a lens of 150 mm focal length, and a photomultiplier (EMI model 7815 B). The arrangement allowed control volume dimensions of 1.97 mm and 0.148 mm length and diameter respectively with a magnification factor of 3 in the light collecting arrangement.

The signal processing is similar to that described in connection with the unconfined flame experiment but, in this case, a micro-processor was interfaced with the spectrum-analyser, as described by Durão et al (1978). On-line digital processing of the spectrum analyser output was then possible and provided a direct display of the p.d.f. of Doppler frequency and values of the mean velocity and variance of velocity fluctuations. The evaluation procedure for the velocity data, described previously, were embodied in the software of the micro-processor.

Droplet velocity measurements were obtained for the range of confined flames described in Section 2.4.2 and were only confined to the spray region, see Fig. 2.27. The measurements extended to distances as close as 5 mm from the fuel atomizer. At locations away from the spray boundaries velocity measurements were not possible due to the significantly reduced number and size of fuel droplets at these locations, as influenced by their high evaporation and combustion rates. Measurements with and without a narrow-bandwidth optical filter indicated that background flame radiation had no influence on the quality of the Doppler signals.

Isothermal air flow velocity measurements within the combustion chamber were also obtained to aid the understanding of the main aero-dynamic features of the flow. They were also used in the validation study of the calculation procedure described in Chapter 3. Silicone-oil

seeding particles were used in connection with this set of isothermal velocity measurements, see Melling (1975) and Durst et al (1978).

2.2.6 Assessment of the Accuracy of Velocity Measurements

The velocity measurements in the present work were subject to errors associated with determining Doppler frequency from the spectrum analyser and converting it to velocity. There is a systematic error from the evaluation of the Doppler frequency/velocity conversion factor λ^* defined as:-

$$\lambda^* = \frac{\lambda}{2 \sin \phi}$$

Since λ is known without significant error, the error in λ^* was introduced in the measurements of ϕ. With careful measurements, ϕ was known in the present work to an accuracy of around ± 0.5%. The frequency range of the spectrum analyser was set up manually and, therefore, reflected an uncertainty in the centre frequency value of the sweeping filter of approximately ± 0.02 MHz. This precision was acceptable except for mean Doppler frequencies near the shifting frequency, ν_S = 21 MHz, where the mean velocity was near zero. For example, if $\overline{\nu}_D$ = 22 MHz, the error in $\overline{\nu}_D$ is only ± 0.091% but $\overline{U}$ has an error of ± 2%. However, frequent checks with a high-precision frequency oscillator indicated that the average error in $\overline{\nu}_D$ was in general lower than this value. The uncertainty in the frequency measurements by the spectrum analyser associated with its filter bandwidth was estimated, according to the present frequency range, as 0.7%.

The mean frequency, $\overline{\nu}_D$, and the corresponding rms value of fluctuations, $\tilde{\nu}_D$, (used in calculating the velocity values) were derived from the p.d.f. of Doppler frequency and as a result of the digital

method used to develop the p.d.f. a consequent error can stem from their estimation from a finite sample size, see Melling (1975) and Yanta (1973). Intuitively, the estimation should be improved as the number of particles, N, used to derive $\bar{\nu}_D$ and $\tilde{\nu}_D$ is increased. When the p.d.f., $P(\nu_D)$, was derived from measurements with a counter, Yanta (1973) evaluated the 95% confidence limit errors in determining the true mean Doppler frequency, μ, and the rms value, σ, from the formulae:-

$$e_\mu = \left| \frac{\bar{\nu}_D - \mu}{\mu} \right| \cong \frac{2}{\sqrt{N}} \frac{\tilde{\nu}_D}{\bar{\nu}_D}$$

$$e_\sigma = \left| \frac{\tilde{\nu}_D - \sigma}{\sigma} \right| \simeq \sqrt{\frac{2}{N}}$$

Table 2.2 presents a sample of turbulence information, corresponding to the unconfined-flame velocity measurements of run 3, see Table 2.3. The values of e_μ and e_σ are shown to be small and it is unlikely that these values will be greatly influenced by the finite number of frequency intervals used to build-up the Doppler frequency p.d.f. as indicated by Clare et al (1976).

In turbulent reacting flows, the variations in refractive index with position and time can lead to dispersion of the laser light and movement of the focal region in space and in time. This can result in reduced signal quality, reduced number of signals per unit time and a larger control volume than would apply in a non-reacting flow. During the present measurements, in particular the unconfined-flame case, this effect was considered; the receiving optical components were removed and the two laser beams were projected onto a screen positioned at a long distance from the control volume. Observation of the two beams movement indicated negligible effect of the refractive index variations and this

was probably due to the small dimensions of the flame, see Khalil (1975) and Durão (1976). For the confined flame measurements this effect was considered to be negligible due to the comparatively small distances over which the measurements were performed.

Durão et al (1976) indicated that the averaging characteristics of the photomultiplier can lead to a variation of the signal amplitude with velocity and tend to bias the velocity p.d.f. towards lower velocities. An opposite bias effect can also stem from the greater probability of detecting particles whose velocity exceeds the average fluid velocity, see for example Dimotakis (1976), McLaughlin et al (1973). The magnitude of the error in mean velocity due to both biasing effects depends largely, as indicated in a recent work by Durão et al (1979), on the sampling arrangement; if the sampling time of the signal processing equipment is greater than the time scale of the particle arrival rate, the magnitude of the correction to the measured values reduces to a negligible level. The signal processing arrangements used in the present work operate with a sufficiently large sampling time and, therefore, biasing errors were considered insignificant.

2.3 Unconfined Flames

This section provides a description of the first part of the experimental study concerning the unconfined flame experiments. The experimental set up, and program, are presented in Subsections 2.3.1 and 2.3.2 respectively. The experimental results are presented and discussed in the different parts of Subsection 2.3.3. The section ends up with brief concluding remarks.

2.3.1 Experimental Set-Up

Two burners were used in the unconfined flame experiments as

shown in Fig. 2.11. The fuel nozzle, for both burners, was of the combined swirl/air-assist type as indicated in Appendix AI, where the geometrical details and the atomization characteristics of the fuel nozzle are given. The burners were used in their vertical position and flame stability was assisted by a disc as indicated. However, the stability of flames emerging from burner A was achieved mainly through the use of both swirl in the combustion air stream and the quarl exit which created a recirculation zone downstream of the burner. Fig. 2.12 shows the supply systems for the fuel, combustion and atomization air. Two air swirlers have been used in the experiments, both have straight vanes which are inclined 60 and 45 degrees to the direction of the air flow. Details of the swirl number calculations for both swirlers are given in Appendix AII.

2.3.2 Experimental Program

Spray characteristics in liquid fuelled flames depend mainly on the exchange rates of mass, heat and momentum between the fuel spray and the surrounding combustion air. These exchange rates are determined by the size and velocity distribution of droplets at the atomizer exit, their relative velocity to the gas velocity, properties and concentration of gases and droplets, and the interaction between the droplets themselves. The effects of these factors on the behaviour of spray flames can be studied through variations in the fuel nozzle and combustion air operating conditions. The present experimental program concentrates on the influence of the combustion air swirl and fuel mass flow rate on the behaviour of unconfined kerosene spray flames. Flame characteristics are interpreted from the measured droplet velocities, mean temperature and droplet number distribution.

The operating conditions for all the flames considered in this

part of the study are given in Table 2.3. Measurements of droplet mean axial velocity and the rms of the corresponding fluctuations were obtained for two flames with swirler vane angles of 60 and 45 degrees (runs 3 and 4 respectively). These are presented and discussed in Section 2.3.3a together with the results of the flame of run 5, which was obtained without secondary combustion air. Fuel mass flow rate was also varied and velocity results obtained for flames with a constant degree of swirl (runs 1, 2 and 3); temperature values were also recorded in one case (run 2). The results for these flames and those for the flame of run 6, including the droplet number distribution, are described and discussed in Section 2.3.3b.

2.3.3 Presentation and Discussion of the Results

(a) Combustion Air Degree of Swirl

Visual observation of the three flames used to investigate the effects of the combustion air swirl (runs 3, 4 and 5, see Table 2.3) showed that the flame with higher degree of swirl, run 3, was slightly lifted and much shorter than the other two flames and had a larger average diameter (approximate length = 600 mm and diameter = 200 mm). The two flames of runs 4 and 5 were stable but lifted about 80 mm above the fuel nozzle. It was generally observed that, while chemical reaction concentrated at the spray boundaries within the initial flame region, it proceeded across the whole flame diameter with downstream distance.

The distributions of the time-averaged mean axial velocity, rms of the corresponding fluctuations and turbulence intensity along the flame centreline are shown in Fig. 2.13 for the two flames corresponding to runs 3 and 4; the results for run 5, with no secondary combustion air, are shown on the same figure for comparison. Radial distributions of mean velocity, rms of velocity fluctuations and the corresponding

intensity at different x/D values (x ≡ axial distance and D ≡ diameter of stabilization disc = 50 mm) are shown on Fig. 2.14 for runs 3 and 4.

The axial velocity of run 3 rises rapidly to a maximum which is followed by a steep decrease over a short axial distance. The initial high velocity values are probably caused by the acceleration of the droplets, especially smaller diameter droplets, due to the high-velocity atomization air at the fuel nozzle. Further downstream, where lower gas velocities exist, the drag forces acting on the droplets tend to reduce their velocities. At about x/D = 1.4 the decay of velocity begins to slow down and further downstream a nearly constant velocity is observed; this can be interpreted as a result of chemical reaction which is enhanced due to increased turbulent mixing and evaporation rates associated with high air swirl. Apart from the decrease in the drag force associated with droplet evaporation and combustion, see for example Ingebo (1962) and Williams (1965), chemical reaction causes an increase in the gas mean temperature and velocity with a consequent further reduction in the drag force. It can also be interpreted from Fig. 2.13 that the higher swirl increases the spreading rate of the fuel jet with reduced droplet concentration at the flame centreline and close to the burner; this allowed the velocity measurements in this upstream region.

The measured velocity values for run 4 indicate that, up to x/D = 2.2, the effect of the drag forces and the spreading rate of the spray jet on the decay of the centreline velocity overcomes the reverse effects of chemical reaction. Further downstream, droplet evaporation associated with lower gas velocity and higher heat transfer rates allowed local fuel/air ratios which are more conducive to combustion with resulting gradual increase in the measured velocity.

The increase in spreading rate of the fuel jet with swirl is

clearly demonstrated by comparing the measured velocity values for run 5, with no secondary combustion air, with those for runs 3 and 4. A gradual decrease of the comparatively high axial velocity is shown for the initial region of the flame, up to x/D = 2.6, followed by a slow increase due to chemical reaction which is concentrated around the flame centre-line because of lower turbulent mixing and jet spread. The high velocity values of run 5 may also be attributed to the larger diameters of droplets, associated with the absence of swirling air, which are unlikely to be affected greatly by the drag forces. It is also unlikely that the difference in the overall air-fuel ratio between run 5 and runs 3 and 4 is responsible for the observed high velocities of run 5; as shown in Table 2.3, the input air-fuel ratio for runs 3 and 4 is 8.95 and a lower value is expected for run 5 with a consequent reduction in the combustion intensity (stoichiometric air-fuel ratio is around 15).

The rms of velocity fluctuations and the corresponding intensity distributions of Fig. 2.13 show that, for the flames corresponding to runs 3, 4 and 5, relatively high values are attained at near-nozzle locations. These are associated with the spread of the droplet-size distribution and with processes of droplet collisions and break-up, the difference in injection velocity for different droplets and the turbulent gas flow. To demonstrate the influence of the spread in the size distribution, the velocities of droplets with different diameters were calculated along the flame centreline, see Appendix AIII; the results show, qualitatively that the spread in velocity, induced by the size spread, contributes significantly to the observed fluctuations. The size distribution measurements of Styles et al (1977) confirm the existence of a large spread in the droplet size distribution at the initial spray region for an approximately similar atomizer. It is clear from Fig. 2.13 that the locations of the maximum intensity and rms values shift towards

the fuel nozzle with increase in the combustion air swirl. This may be attributed mainly to the increase in the spreading rate and the early commencement of combustion with swirl.

The radial mean velocity profiles for runs 3 and 4, see Fig. 2.14, confirm the expected larger spread of the fuel spray for the higher-swirl flame, e.g. radial profiles at x/D = 1.4. They also confirm the onset of combustion for run 3 at shorter distances from the burner; this is indicated by the generally higher velocities and, to a first approximation, the ability to measure axial velocity at large radii in the flame of run 4 which implies the existence of a sufficient number of fuel droplets.

Radial profiles of the rms of velocity fluctuations, presented in Fig. 2.14 for runs 3 and 4, indicate the existence of relatively high rms values around the flame centreline and at radii corresponding to inflection points in the mean velocity profiles. The latter probably stem from instabilities caused by mean-flow inflection. The high values around the centreline are due mainly to the turbulence effects of the fuel spray previously mentioned and the spread in the droplet size distribution. It was generally observed during the measurements that a higher droplet concentration exists in the vicinity of the centreline and this will be further illustrated by the droplet number density measurements of run 6. The high rms values around the centre-line for run 3 are flattened out with downstream distances where they begin to be mainly influenced by the mean velocity gradients. The results for run 4 do not show the same trend which suggests that higher swirl increases the fuel spray spreading and evaporation rates.

(b) Fuel Mass Flow Rate

The mean axial velocity, rms of corresponding fluctuations and

intensity measured along the flame centreline are plotted on Fig. 2.15 for the three flames of runs 1, 2 and 3. Different fuel mass flow rates were used in these three flames while secondary combustion air mass flow rate and degree of swirl were maintained constant, see Table 2.3. Radial profiles of axial velocity, rms values and intensity are shown in Figs. 2.16 and 2.14 for runs 2 and 3 respectively. Flame centreline gas temperature is given in Fig. 2.17 and corresponding radial profiles in Fig. 2.18 for run 2.

The use of a combined swirl/air assist fuel nozzle implies that a decrease in the fuel flow rate results in a spray with a narrower spreading angle and a smaller mean-droplet size. The former effect is due to the decrease in the fuel angular momentum while the latter is due to increased momentum interaction between the atomizing air and fuel droplets, see for example Styles et al (1977) and Fraser et al (1957). It should be noted that this is only the case under operating conditions where the air assist dominates the swirl atomization action of the fuel nozzle. The comparatively low fuel mass flow rates used in the present study favour these conditions. An estimate of the Sauter-mean diameter of the initial droplet-size distribution for the flames of runs 1, 2 and 3 was obtained from the drop size correlation for twin-fluid atomizers reported by Fraser et al (1957). The estimated Sauter-mean diameters were 58, 70 and 85 μm for runs 1, 2 and 3 respectively. Visual observation showed that intense-combustion, short and soot free (blue) flames are obtained by reducing the fuel mass flow rate.

The results of Fig. 2.15 show only quantitative differences between the measured centreline axial velocities with a common trend of increased velocity values with decrease in the fuel mass flow rate. The decrease in the mean diameter of the droplet-size distribution increases the evaporation rate with the consequent effect of increased possibility

of the occurrence of combustion near to the fuel nozzle. This is one of the reasons for the comparatively higher axial velocity values for runs 1 and 2. Moreover, the presence of smaller droplets at near nozzle locations with their lower inertia/drag ratio and higher velocities (Chigier et al, 1974), result in higher velocity values. This is clearly demonstrated in Fig. 2.15.

Table 2.3 shows that the inlet air/fuel ratios for the flames of runs 1, 2 and 3 are 20.04, 14.3 and 8.95 respectively. This suggests that, for runs 1 and 2 with expected higher evaporation rates, the local air/fuel ratios are closer to stoichiometric with intense combustion and comparatively shorter flame lengths. Also, as a consequent effect, radiation heat transfer rates are insignificant with consequently higher temperatures and velocities within the flame. The differences in the axial velocity values for runs 1, 2 and 3, Fig. 2.15, are largely due to these two factors.

The centreline rms of velocity fluctuation measurements for runs 2 and 3, Fig. 2.15, illustrate again the existence of high rms regions near to the fuel nozzle. These are influenced by effects of the fuel spray on turbulence and the onset of chemical reaction. Points of inflection in the mean velocity profiles occur around $x/D = 1.0$ for the three flames and they correspond to the high rms values ($\tilde{u} \geq 6.0$ m/s). At small x/D values spray atomization, droplet break-up and collision and the spread in the droplet-size distribution cause an increase in the rms values. Temperature measurements for run 2, see Fig. 2.17, also indicate a sudden increase in temperature at around $x/D = 1.1$, due to the commencement of combustion and consequently an increase in the rms values is expected. The increase in the centreline rms velocity, with reduced fuel mass flow rate indicated in the upstream region by Fig. 2.15, may be attributed to the increase in the combustion intensity,

which has a larger effect on the velocity of smaller droplet diameters, and the expected reduction in the fuel spray spreading angle. The turbulence intensity along the centreline for runs 1, 2 and 3 varies from around 0.3 at near-nozzle locations to 0.23 at downstream regions.

Radial profiles of axial velocity and intensity for runs 2 and 3, Figs. 2.16 and 2.14, confirm the reduction in the spreading angle of the fuel spray and the increase in the combustion intensity as a result of reducing the fuel mass flow rate. Steep axial velocity gradients are shown to occur at smaller radii for run 2. The radial rms profiles for run 2 again indicate high values around the centreline and are qualitatively similar to those of run 3. Turbulence intensities in excess of 100% are shown at the flame boundaries on Figs. 2.14 and 2.16.

The centreline temperature distribution for run 2, Fig. 2.17, indicates a sudden increase in the mean temperature at around $x/D = 1.1$ which corresponds to the onset of combustion. Downstream of the initial flame region, where the main combustion processes take place at the spray boundaries, turbulent mixing of fuel vapour and air allows chemical reaction to proceed across the whole flame diameter. This is illustrated in Fig. 2.17 where a gradual increase in the measured temperature occurs with downstream distances. The radial temperature profiles of Fig. 2.18 confirm this explanation, the maximum temperature occurs on the centreline for distances downstream of $x/D = 3$ and further upstream the maxima occur off the centreline. The general trend of the measured temperature profiles confirms the reported temperature measurements of Onuma et al (1975, 1977) and Styles et al (1977).

The flame of run 6, with the burner geometry B, was used to obtain measurements of the time-averaged number of droplets passing through different points within the flame. The distribution of the normalized average number of droplets along the flame centreline is

shown in Fig. 2.19. It is clear that the number of droplets decreases very steeply in the initial region of the flame, due to droplet evaporation/combustion and spreading of the spray. This accords with physical descriptions for the structure of spray flames, see for example Chigier et al (1973, 1977), Onuma et al (1975, 1977) and Tuttle et al (1976).

Radial profiles for the number of droplets, normalized by the centreline values, are shown on Fig. 2.20, and clearly illustrate the spreading process of the fuel spray. The spray emerging from the fuel nozzle has a Gaussian-like droplet-number distribution with its maximum located at the centreline of the spray. The steep gradients in the radial profiles at near-nozzle locations, $x \leq 100$ mm, are consistent with a combustion process which is mainly concentrated at the spray boundaries.

The centreline axial velocity, the rms of the velocity fluctuations and the corresponding intensity distributions for run 6 are shown in Fig. 2.21 and the corresponding radial profiles on Fig. 2.22. The distributions have the same features as those of run 5 with no secondary combustion air. It can be seen from Fig. 2.21 that a slow increase in the centreline velocity is observed at around $x = 110 - 120$ mm and may indicate the beginning of chemical reaction. The maximum gradient of the droplet-number profile, Fig. 2.19, occurs also at about $x = 100$ mm and suggests that reaction zones within the flame are characterised by large gradients in the droplet-number density distributions.

2.3.4 Concluding Remarks

The following more important conclusions may be extracted from the discussion of the experimental results presented in the previous

Subsection:-

1. An increase in the degree of swirl from 0.45to 0.77was found to increase the centreline mean velocity by approximately 40%, Fig. 2.13. and this was related to the increased heat release rate associated with enhanced chemical reaction. Apart from the increase in turbulent mixing with swirl, the evaporation rate also increased and allowed intense chemical reaction to start shortly downstream of the fuel nozzle. The radial velocity profiles also showed an increase in the flame jet spreading rate with swirl and confirmed the increase in the combustion intensity.

2. A reduction in fuel mass-flow rate resulted in an increase in the centreline mean velocity, particularly in the near-nozzle region with corresponding shift in the rms of velocity fluctuations and the corresponding intensity maxima towards the nozzle. This is associated with the earlier onset of combustion as the overall air-fuel ratio approaches stoichiometric and the evaporation rate increases due to preferential evaporation of smaller droplet diameters.

3. High rms values of velocity fluctuations were recorded coincident with initial spray regions and inflections in the mean velocity profiles. The former are due partly to the effects of droplet collision, break-up, difference in injection velocity for different droplets and the turbulent gas flow and partly to the spread in velocity associated with the range of droplet sizes.

4. In the initial flame region, chemical reaction is concentrated at the spray boundaries while, further downstream, it proceeds towards the

flame centreline. This is demonstrated by mean-temperature profiles which show that the maximum temperature occurs on the centreline for downstream regions and off the centreline for upstream regions.

2.4 Confined Flames

The contents of this section are arranged to provide the details of the confined flame experiments of the present study. The experimental set-up and program are first presented in Subsections 2.4.1 and 2.4.2 respectively followed by the presentation and discussion of the experimental results in Subsection 2.4.3. A more general discussion of the results is presented in Subsection 2.4.4 and the concluding remarks for this part of the study are given in Subsection 2.4.5.

2.4.1 Experimental Set-Up

The experimental arrangement for the confined flame measurements is shown in Fig. 2.23. It consists mainly of the test section (cylindrical combustion chamber) and systems for supplying fuel (kerosene), combustion and cooling air. All systems were equipped with the necessary controlling devices as indicated in Fig. 2.23. The combustion air entered the test section (157 mm diameter) through an axial guide vane-cascade swirler assembled coaxially with the fuel atomizer which projects 50 mm inside the test section, see Fig. 2.24. The dimensions and the calculated swirl numbers for the three air swirlers used in the present work are given in Appendix II. The kerosene fuel was delivered to the combustion chamber through a rotating cup-atomizer capable of producing sprays with mono-dispersed controlled droplet size. Variations in the spray mean-droplet diameter were, therefore, possible without altering the fuel mass flow rate. Details of the atomizer are given in Appendix I. The fuel atomizer was air-cooled as shown in Fig.

2.24.

Tapping points of 7 mm diameter, drilled along one side of the combustion chamber, were used to insert probes for temperature and concentration measurements, see Section 2.2. Along the other side, a slot of 30 x 300 mm fitted with quartz observation windows was used to facilitate velocity measurements with the Laser Doppler anemometer.

2.4.2 Experimental Program

Detailed measurements of temperature, volume concentrations of CO, CO_2 and O_2, droplet velocities and wall temperature were obtained for six flames corresponding to the operating conditions summarized in Table 2.4. For the first three flames (runs 1, 2 and 3) the spray mean-droplet diameter was varied from 33 to 47 and 96 μm and a constant combustion air swirler angle of 60^o was used. The latter was then varied to 30^o and two other flames (runs 5 and 6) corresponding to 47 and 96 μm mean diameter were obtained. As indicated in Table 2.4, the kerosene fuel and air mass flow rates were constant for all flames. The results, therefore, allowed the study of the influence of the mean diameter on the combustion characteristics of spray flames with two levels of turbulent mixing. The flames corresponding to runs 2, 4 and 5 provided data concerning the effects of the combustion air swirl on the fuel spray and the resulting flame properties. Isothermal velocity measurements within the combustor were also obtained for reference purposes. The operating conditions for these velocity measurements correspond to those of runs 7 and 8.

2.4.3 Presentation and Discussion of the Results

The experimental results obtained for the range of confined spray flames considered in the present work are presented and discussed

in this subsection. The measured values of temperature and volume concentrations of CO_2, CO and O_2 species are presented in the form of contour maps; the corresponding radial profiles at different locations along the combustion chamber are given, for reference purposes, in Appendix A.IV. Contour plots are preferred since, in spite of the comparatively small number of measurement locations, they show more clearly the changes in flame properties associated with different flames which were not easily detected in the radial profiles. The results of the isothermal axial velocity measurements are first presented and discussed, Subsection 2.4.3.1, as they indicate the general aerodynamic features of the flow field. This is followed in Subsection 2.4.3.2 by the results obtained for the three flames corresponding to different spray mean-droplet diameter. The effects of the combustion air swirl on flame properties are then described in Subsection 2.4.3.3. Finally, and after presenting the results of the 30^{o} swirler flame in Subsection 2.4.3.3, the influence of the mean-droplet diameter is, again, considered but in connection with this low swirl flame.

2.4.3.1 Isothermal Velocity Measurements

The isothermal axial velocity distributions (runs 7 and 8) of Fig. 2.25 serve to illustrate the main features of the aerodynamic flow field, in particular, within the upstream part of the combustion chamber where processes of fuel spray-air interaction take place under combusting conditions. It is clear from Fig. 2.25 that the axial velocity profiles exhibit two recirculation zones; one surrounds the centreline and the other is close to the wall. For the high swirl case, Fig. 2.25a, the central recirculation zone is developed close to the air entry section,

for example, negative velocities of around 3 m/s can be seen at x/D = 0.057 and R/D < 0.4. For larger x/D values, the zero-velocity location moves radially outward and the recirculation zone covers a significant portion of the combustion chamber radius, R/D < 0.75. The results also show a corresponding movement of the points of maximum positive velocity towards larger radii. The steep velocity gradients, which can be observed at the recirculation zone boundaries, are associated with a large increase in the velocity fluctuations as indicated in the radial profiles of the rms of fluctuation, Fig. 2.26a. The wall recirculation zone is hardly detected for this high swirl case; negative velocities near the wall were only measured at x/D = 0.057. This is probably due to the high spreading rate of the air stream caused by the large angular momentum imposed on it by the swirler (60^{o} vane angle).

The radial profiles for the 30^{o}-swirler case, Fig. 2.25b, show a significant reduction in the dimensions of the central recirculation zone; it starts at x/D around 0.398 and extends only to R/D $\cong$ 0.2. This is caused by the reduction in the angular to axial momentum ratio (swirl number) which also allowed the development of a wall-recirculation zone. The latter can be seen, Fig. 2.25b, up to x/D = 0.494. Due to the more uniform spreading of the air stream, positive axial velocity values were measured at a greater number of points within the combustion chamber compared to those of the 60^{o}-swirler case. The maximum velocity values are also lower and range between 11.5 m/s, x/D = 0.127, and 8.5 m/s, x/D = 0.494, and are located at R/D around 0.5.

2.4.3.2 Spray Mean-Droplet Diameter

Flame Structure

The experimental results obtained for the three flames of runs 1, 2 and 3, together with visual observation, allowed the formulation of a physical description of the flame structure common to the three flames.

The basic flame structure is shown in Fig. 2.27. The high swirl of the combustion air created a recirculation zone which can be seen in Fig. 2.25a to surround the fuel atomizer. The spray sheet penetrated through this reverse flow zone and as a result, small droplets and fuel vapour were recirculated towards the combustion air exit. Across the shear layer, which encloses the recirculation zone, the high turbulent mixing rates and the comparatively high temperature of the recirculated gas allowed chemical reaction to proceed with a high intensity. This region extends to the fuel spray region and there the resulting high temperature increases the droplets evaporation and tends to stabilize another flame which covers the region downstream of the fuel spray. For reasons of simplicity, the above-mentioned two regions of intense combustion will be referred to, in the following presentation and discussion of the results, as the shear-layer and the main-flame regions respectively.

The contour maps of temperature and CO_2, CO and O_2 species concentrations are shown, for the three flames, in Figs. 2.28, 2.29, 2.30 and 2.31 respectively. The temperature distributions confirm the above description of the flame structure. High temperature values, around 1200 ^{o}K, are observed at the shear-layer flame region ($R/D \simeq 0.6 - 0.8$ and $x/D \simeq 0.1 - 0.3$) and higher values are recorded, $\simeq$ 1400 ^{o}K, within the main-flame stabilized by it. Although the temperature contour maps for the three flames indicate the same general trend, quantitative differences exist in the temperature values and in the relative dimensions of these high intensity-combustion zones. It can also be seen from the corresponding concentration contour plots of CO_2, CO and O_2 that these flame regions are generally associated with high concentration gradients, low oxygen values and high CO_2 and/or CO concentrations. The comparatively high CO and CO_2 values measured upstream of the fuel spray confirm that significant amounts of fuel

vapour and, probably, small droplets are swept backward towards the combustion air entry section. The radial profiles of the droplet mean axial velocity and the corresponding rms values are shown, for the three flames, in Fig. 2.32. Measurements were obtained at different axial locations concentrated in the very thin spray region. It is clear that the reverse velocity of the gases causes a steep reduction in the droplet velocity on moving radially outward. Although the mean velocity for most of the points is positive, the turbulence intensity values and the low mean velocities suggest that some droplets are moving with a negative axial velocity. This, again, suggests that small droplets are entrained by the recirculating gas flow near the atomizer. The preceeding general description of the three flames is followed in the next part of this section by a detailed discussion of the experimental results.

The Shear-Layer Flame Region

The temperature contour maps, Fig. 2.28, show that the shear layer flame region, $x/D = 0.1 - 0.3$ and $R/D \cong 0.6 - 0.8$, is characterised by high temperature values (1200 - 1300 ^{o}K) and steep gradients with corresponding occurrence of high-intensity combustion. This can also be deduced from the CO_2 and CO concentration maps, Figs. 2.29 and 2.30, which show CO_2 and CO values of around 9 - 11% and 11 - 9% respectively and again associated with steep gradients. Common to the three flames, the oxygen concentration contours of Fig. 2.31 also show small O_2 values (around 1%) coincident with this region. Close inspection of the CO_2 and CO contour lines indicates that the relative values of the measured CO_2 to CO concentrations across the inner side of the shear layer region increase with the initial mean droplet diameter (runs 1 through 3). It is also clear that the gradients of the CO_2 concentrations are less steep for the smaller mean diameter flames. This tendency of the increased

formation reaction of CO_2 with the increase in mean droplet diameter can be directly related to the corresponding reduction in the spray evaporation rate. The reduction in the evaporation rate is evidenced by the results obtained for the flame of run 3 which show comparatively high O_2 and low CO concentrations at a large number of points especially within the downstream region of the flame. The corresponding reduction in the amount of fuel vapour recirculated towards the combustion air entry section causes an increase in the local air/fuel ratio in a direction which, to some extent, allows complete combustion of the fuel.

The Central Recirculation Zone and the Near-Spray Region

The temperature and concentration contour maps, Figs. 2.28 - 2.31, show that the gradients of the measured quantities, within the upstream part of the recirculation zone, $x/D < 0.3$, are generally less steep than those observed on the other side of the shear-layer region. The temperature values vary only between 1000 - 1300 ^{o}K and comparatively large zones of nearly constant species concentrations can also be seen. The measured values within the recirculation zone are influenced by both the shear-layer reactions and the recirculated gases from downstream locations of the flame. The significantly small O_2 concentrations (1%) which are coupled with high CO and CO_2 values (9 - 11% and 11 - 9% respectively) indicate that the recirculation zone is characterised by extremely fuel-rich mixtures with the implication that large quantities of the fuel vapour, that evaporate close to the spray, are swept back to the recirculation zone.

The temperature contour lines for the three flames indicate that the transition from large to small spray mean droplet diameter is associated with an increase in the measured values at locations close to the fuel spray, $x/D \simeq 0.3$ and $R/D \simeq 0.3 - 0.6$. A similar increase in CO

values can also be seen in Fig. 2.30. The CO_2 contour lines of Fig. 2.29, on the other hand, show a slight reduction in the measured values with the decrease in the mean-droplet diameter. The trend of these changes in temperature and species concentrations implies an increase in the combustion intensity with the reduction of the mean-droplet diameter. This can be attributed to the increase in the evaporation rate associated with small droplets and to the comparatively higher temperature of the recirculated gases from downstream locations of the flame. The former provided more fuel for combustion while the latter enhanced the reaction rate of the fuel-air mixture. The increase in the evaporation rate shifts the fuel-air mixture ratio towards the fuel-rich limit and consequently a significant amount of the fuel is only partially oxidized to CO.

The Region Adjacent to the Atomizer Cooling Air Exit

The observed bending of the temperature and concentration contour lines at around $x/D \cong 0.35$ and $R/D \simeq 0.2$ is caused by the cooling and dilution effects of the atomizer cooling air. It is clear that the extent to which the measured profiles are influenced by the cooling air decreases with the reduction in the spray mean droplet diameter. This is probably due to the high temperature and species concentration levels associated with smaller diameter flames. At $x/D \simeq 0.3$ and $R/D = 0.3$ the O_2 contour lines of Fig. 2.31 show a larger percentage of the atomizer cooling air being recirculated backwards as the spray mean droplet diameter is reduced. It is likely that the increase in the fuel richness, at locations downstream of the atomizer, reduces the possibility of further reaction for a significant amount of the atomizer-cooling air.

The Boundaries and the Central Part of the Main-Flame Region

The fuel vapour and droplets that do not react within the recirculation zone or across the shear-layer flame region continue to move downstream, $x/D > 0.3$, where further evaporation, mixing with the combustion air and chemical reaction proceed along the outer and central parts of the combustion chamber (main-flame region). It is this fuel, convected from the spray region, that gives rise to the observed relative maxima in the CO concentration, Fig. 2.30, at $R/D \cong 0.3 - 0.4$ for the flame of run 3 and at R/D around 0.4 - 0.6 for the two flames of runs 1 and 2. Partial oxidation of the fuel vapour to CO is dominant at this region due to the fuel-richness of the combustible mixture. The increase in the spray evaporation rate with small droplets is also evident from the gradual increase in the measured CO concentrations as the mean droplet diameter is reduced. For example, at x/D values downstream of 0.2, the maximum recorded CO concentrations were 9% - 10% and 11% for runs 3, 2 and 1 respectively.

Along the outer boundaries of the main-flame region, $x/D > 0.3$, turbulent mixing of the fuel vapour and the surrounding combustion air allowed chemical reaction to proceed with a high intensity which can be interpreted from the steep temperature and concentration gradients observed in Figs. 2.28 - 2.31. For the flame of run 3, this region extends only from $x/D = 0.3$ to 0.8 at a radial position starting at $R/D = 0.8$ to 0.5. The results of runs 1 and 2 show this region extending from $x/D = 0.3$ to 1.4 at $R/D = 0.8$ (run 1) and from $x/D = 0.3$ to 1.1 at $R/D \simeq 0.75$ (run 2). The temperature contour lines, Fig. 2.28, show that the measured values along this high-intensity-combustion region are comparatively high for the three flames, around 1500 ^{o}K. These high values are influenced by the oxidation reaction of the fuel vapour to both CO and CO_2 which is evidenced by the high recorded CO and CO_2

concentrations in this region (around 2 - 10% and 10 - 12% respectively). It is clear that the increase in the mean droplet diameter is associated with a shifting of the main flame boundaries towards smaller radii of the combustion chamber. It is significant, however, for the flame of run 3. For example, the temperature contour lines for run 3 show a reduction in the measured values at locations downstream of $x/D = 0.4$ and at large radii of the combustion chamber, $R/D \cong 0.7$. This low temperature region is associated with high O_2 concentrations, 6 - 10%, and comparatively low CO and CO_2 levels, $CO_2 \simeq 8 - 5\%$ and $CO \simeq 1.5\%$, and consequently indicates a reduced combustion intensity. For this flame, the slow evaporation of its comparatively large droplets provides a small amount of the fuel vapour at the near-spray region and, therefore, the dilution and quenching of chemical reaction effects of the surrounding high velocity air stream increase in importance with a consequent reduction in the combustion intensity. The expected large concentrations of the unburned hydrocarbons in this region of the flame were confirmed during the concentration measurements for this run by the high accumulation rates of condensed fuel vapour experienced in the sampling system. The combustion of this unburned fuel, at further downstream locations of the flame is also unlikely due to the large reduction in the temperature. The droplet mean axial and tangential velocity components, presented in Figs. 2.32 and 2.33 respectively for the three flames, indicate that the increase in the mean droplet diameter is associated with a reduction in the injection velocity. This is mainly a result of the method of the fuel spray atomization adopted in the present work (rotating cup atomizer). It is likely that the resulting short penetration distances contribute to the above-mentioned shifting of the main-flame boundaries.

The temperature contour lines, Fig. 2.28, show the main-flame

region to be dominated by high temperature values, which for the three flames reach a maximum of around 1500 - 1600 ^{o}K. The maximum temperature values can be seen, in general, located off the combustion chamber centreline. These high temperatures are caused by the continuing oxidation reactions of the fuel vapour which is indicated in Figs. 2.29 and 2.30 by the comparatively high CO and CO_2 values and by the significant reduction in the oxygen concentrations. Within the upstream part of the main-flame, $x/D \lesssim 0.5$, and due to the fuel-richness caused by the large amounts of fuel vapour transported from the spray region, the CO concentration shows its maximum values which range between 9 and 11% for the flames of runs 3 through 1 respectively. The CO concentrations decrease steadily with downstream location and towards the centreline as oxidation and dilution rates exceed the formation and vaporization rates. It is, however, clear from Fig. 2.30 that the decay rate of CO decreases with the reduction in the mean droplet diameter which is probably due to the initial higher CO-formation rates. The CO_2 contour lines, on the other hand, show a corresponding increase in the measured values with downstream distances. The maximum recorded CO_2 concentrations for the three flames were around 10.5% (run 3) and 12% (runs 1 and 2).

The observed increase in the O_2 concentrations at the far downstream locations of the three flames ($x/D > 0.8$ (run 3), $x/D > 1.1$ (run 2) and $x/D > 1.4$ (run 1)) is mainly due to the comparatively large amount of air being transported from the near-wall region of the flame as indicated by the bending of the contour lines towards the combustion chamber centreline. The consequent dilution and quenching effects result in a reduction in both the measured values and gradients of temperature and CO_2 which can be seen in Figs. 2.28 and 2.29 at the same locations. It is also clear from the temperature contour lines that the increase in the initial mean-droplet diameter is associated with a

shortening of the main-flame region. This can be attributed to the corresponding reduction in the amount of fuel vapour that participated in chemical reaction.

Wall-Temperature Distribution

Fig. 2.34 shows the wall-temperature distributions for the three flames of runs 1, 2 and 3. In general, the three flames have the same trend, within the initial part of the flame ($x/D < 1.3$ (run 1), $x/D < 1.1$ (run 2) and $x/D < 0.7$ (run 3)), the wall-temperature increases rapidly to a maximum value which ranges between 640, 610 and 480 ^{o}K for runs 1, 2 and 3 respectively. This is followed by a gradual reduction in the measured values with downstream distance. The observed steep rise in the wall-temperature, within the upstream part of the combustion chamber, is mainly due to the high-combustion intensity at both the shear-layer region and the main-flame boundaries as indicated previously. It is clear, however, that with the reduction in the mean-droplet diameter of the spray, the wall-temperature attains a significantly higher value and the axial position of the maximum value shifts towards downstream locations of the combustion chamber. This is in agreement with the previously observed shifting of the high-temperature flame boundaries towards the combustion chamber wall and the increase in the flame length associated with small fuel droplets. This, again, confirms that, for small droplets and due to the consequent increase in the evaporation rate, a greater amount of the fuel vapour participates in the combustion process with a corresponding increase in the intensity of chemical reaction over a significant part of the combustion chamber. The decrease in the wall temperature with down-stream locations of the combustor is attributed to the reduction in the combustion intensity at these regions of the three flames as indicated previously.

2.4.3.3 Combustion Air Swirl

The experimental results of the three flames of runs 2, 4 and 5, which are used to study the influence of the combustion air swirl, are presented and discussed in the following parts of this subsection. The droplet mean velocity measurements are first presented and followed by the results of the 45^{o} and 30^{o} swirler flames. The wall-temperature measurements for the three flames are described in the final part of this subsection.

(a) The Droplet Mean Velocity

Fig. 2.39 shows the radial profiles of droplet mean axial velocity at different locations in the near-spray region of the three flames of runs 2, 4 and 5. Close to the atomizer wall, $R/D \cong 0.3$, the droplet mean velocity attains high values which are influenced by the high velocity of the cooling air surrounding the atomizer. On moving radially outward, the mean velocity decreases significantly as a result of the drag forces acting on the droplets and as the measurement locations coincide with the upstream low-velocity boundaries of the spray. The measured profiles indicate that the droplets moving in the downstream part of the spray have comparatively higher velocities. This could be interpreted as a result of the variation in injection velocity associated with different droplets. Fig. 2.40 shows samples of the velocity probability distributions at points close to the atomizer wall and it is clear that there is a range of droplet velocities at the point of injection. The increase in the droplet velocity associated with the reduction in the combustion air swirl (runs 2 through 5) and the less steep gradients observed in the radial direction imply that the spray angle decreases for lower degrees of swirl. For the 30^{o} swirler case, droplet velocity measurements were possible at locations far

downstream of the fuel spray, for example up to x/D = 0.487, and indicate that droplets penetrate a longer distance into the combustion chamber with the implication of a lower evaporation rate.

(b) The 45^{o} Swirler Flame

The temperature and concentration contour maps for run 4, Figs. 2.35B - 2.38B, show that the basic flame structure is very similar to that of run 2 which has been described in the previous subsection.

The Central Recirculation Zone

The high CO and CO_2 values, both around 8% at R/D ≃ 0.5 and x/D < 0.35, indicate that fuel (either small droplets or vapour) is swept by the recirculating gas flow backwards towards the combustion air entry section. However, these CO and CO_2 values are lower than those observed in the contour maps of run 2 and are associated with slightly higher O_2 concentrations. This indicates a reduction in the amount of fuel vapour recirculated backwards and can be interpreted as a result of the reduced strength of the central recirculation zone due to the smaller degree of swirl.

The Shear-Layer Flame Region

The shear layer flame region can be easily identified in the temperature contour map, at 0.1 < x/D < 0.4 and R/D ≃ 0.5 - 0.8, where steep gradients and high temperature values, with a maximum of 1400 ^{o}K, can be seen. This is associated with steep concentration gradients where CO and CO_2 values increase across the shear-layer by approximately an order of magnitude with a significant reduction in O_2 concentrations. It is also clear, from both the temperature and concentration contour maps, that the shear-layer flame zone is shifted radially inward in

comparison to that of the 60^{o} swirler flame. This result is in agreement with the reduction in the spreading angle of the combustion air stream associated with lower degrees of swirl which can be deduced from the isothermal axial velocity profiles of Fig. 2.25.

The Main-Flame Region

The general outline of the main-flame region, $x/D > 0.4$ and $R/D < 0.75$, is detectable in all three species and temperature contour maps, Figs. 2.35B - 2.38B. The temperature, CO and CO_2 concentrations increase appreciably across the flame boundaries, $R/D \simeq 0.75$, and a corresponding reduction in the O_2 concentrations can also be observed. It is clear, however, that the temperature values within the upstream part of the main-flame, $x/D < 0.9$, are generally lower than those obtained for the 60^{o} swirler flame and are associated with comparatively slower CO and CO_2 destruction and formation rates respectively. For example, while the CO_2 contour lines for the 60^{o} swirler flame show an increase in the measured values to a maximum of around 12% shortly downstream of the fuel atomizer those for the 45^{o} swirler flame show this maximum value to be reached at the far downstream region of the flame, $x/D \simeq 0.9$. It can also be observed that the maximum temperature, at any axial location within this upstream zone of the flame, (1300 - 1500 ^{o}K) is recorded off the combustion chamber centreline at around $R/D \simeq 0.5$. The CO_2 contour lines show relative maxima at nearly the same radial locations while the CO concentration, on the other hand, peaks close to the centreline and consequently indicates insignificant further oxidation to CO_2.

It is evident from the above results that the decrease in the combustion air swirl results in a reduction in the intensity of chemical reaction through the initial zone of the main-flame and, in particular,

at small radii of the combustion chamber. This is mainly due to the lower turbulent mixing rates associated with the smaller degree of swirl flame. The near-centreline region of the flame is greatly influenced by the reduction in mixing as small amounts of oxygen are transported to it, from the wall and the downstream regions of the flame. This is clearly shown by the O_2 contour map of Fig. 2.38b.

The gradual reduction in the CO concentrations and the increase in the CO_2 and temperature values which can be seen in the contour maps of the 45^o swirler flame at x/D values higher than 1.0 indicates that further oxidation of CO and other unburned hydrocarbons continues along the downstream part of the main-flame where the oxygen concentrations are sufficiently high for chemical reactions to proceed with a high intensity. It is also clear that the temperature and CO_2 values are comparatively higher than those observed for the 60^o swirler flame which shows that the reduction in swirl causes an increase in the flame length.

(c) The 30^o Swirler Flame

The Flame Structure

The temperature and concentration contour maps of run 5 (30^o swirler), Figs. 2.35C - 2.38C, show the extent to which the interaction between the fuel spray and the surrounding combustion air can influence the flame behaviour. Close inspection of the contour lines in connection with the isothermal axial velocity profiles, Fig. 2.25, and with the results of runs 2 and 4 suggests that the basic flame structure is similar to that of runs 2 and 4, see Section 2.4.3.1 and Fig. 2.27. Fig. 2.41 shows a physical description of the flame structure corresponding

to run 5. It is clear that the difference between that flame and those of runs 2 and 4 is that flame stabilization for the former takes place close to the wall-recirculation zone whereas for the other two flames, it occurs at the central-recirculation zone. In agreement with this description, the isothermal axial velocity profiles of Fig. 2.25 show the boundaries of the wall-recirculation zone to be roughly coincident with the flame region shown in Figs. 2.35C and 2.36C at $x/D < 0.4$ and $R/D \simeq 0.7 - 0.9$ where the temperature and CO_2 values are comparatively high with the implication of high intensity combustion. The relative maxima shown in the temperature and concentration maps at further downstream locations $x/D > 0.5$ and at R/D around 0.85 also confirm the existence of the main flame region which is ignited by the shear-layer flame zone.

The Central Part of the Flame

It is clear in Figs. 2.35C - 2.38C that the temperature, CO_2 and CO values within the central part of the flame, $R/D < 0.45$, are generally much lower than those observed for runs 2 and 4 whereas the O_2 concentrations are much higher. This reduction in the combustion intensity is mainly influenced by the dilution and quenching effects of the high velocity air stream surrounding the atomizer and by the low droplet evaporation rate caused by the consequent reduction in temperature at this region. The high velocity of air close to the atomizer is clearly indicated in the isothermal velocity profiles of Fig. 2.25. During droplet velocity measurements by the Laser Doppler anemometer, the reduction in the evaporation rate for this flame was evidenced by the detection of comparatively large number of fuel droplets at locations extending larger distances away from the fuel nozzle. For example, droplet velocity measurements were possible up to $x/D = 0.487$,

see Fig. 2.39.

The Wall Region

Within the wall recirculation zone, $x/D < 0.4$, the concentration contour maps show comparatively high O_2 concentrations (around 8%) and low CO_2 and CO values (6% and 3% respectively) which implies that either a small amount of the fuel has been swept backward by the recirculating gas or the oxidation rates of the fuel vapour is not sufficiently high. It is, however, unlikely that the latter has a significant influence as the high turbulent mixing rates at this region, which are associated with a high temperature and a low gas velocity, would favour the occurrence of intense combustion. The former, on the other hand, may stem from different factors including the slow evaporation of the fuel droplets, the narrow spray angle associated with this flame and the entrainment of a large number of droplets by the high velocity air stream surrounding the atomizer. The reduction in the spray angle implies that most of the droplets would penetrate the wall-recirculation zone near to the re-attachment point where the negative gas velocities are comparatively low and consequently a smaller amount of the fuel will be recirculated.

The recorded gas temperatures and the CO, CO_2 and O_2 concentrations reveal that the spreading of the main-flame region is much lower than that observed for the higher swirl flames of runs 2 and 4. This result appeared to be consistent with the anticipated reduction in the turbulent mixing rates for this low swirl flame. Inspection of the concentration levels of O_2, CO_2 and CO throughout the main-flame region, ($O_2 \simeq 12\%$, $CO_2 \simeq 5\%$ and $CO \simeq 0.5\%$) indicates, again, that a comparatively small amount of the fuel has been convected to it from the spray zone. This could be attributed, as previously mentioned, to the slow droplet evaporation rate and the entrainment of a large number of

droplets by the air stream surrounding the atomizer. The consequent reduction in the flame length is evidenced by the gradual decrease in the measured temperature values which start at x/D of around 0.9.

(d) Wall-Temperature Distribution

Fig. 2.42 shows the wall-temperature distribution for the three flames of runs 2, 4 and 5. The distribution for the 45^{o} swirler flame is shown to be similar to that of the higher swirl flame although the temperature values are slightly lower. The less steep reduction in the wall-temperature, along the downstream part of the combustion chamber, which can be seen associated with the 60^{o} swirler flame is probably due to the increase in the heat transfer coefficient as influenced by the higher gas velocity at the near-wall region. The significant increase in the wall-temperature for the 30^{o} swirler flame is consistent with the internal temperature distributions discussed previously which showed the maximum flame temperatures to be located close to the wall. For example, the maximum wall temperature, around 770 ^{o}K, is recorded at $x/D \simeq 0.8$ in agreement with the position of the high-temperature main-flame region, see Fig. 2.35C. The fast decay rate in the wall-temperature with downstream distances of the flame, $x/D > 0.9$, also confirms the previously mentioned observation of the short length of the main-flame region.

2.4.3.4 Spray Mean-Droplet Diameter (Low Swirl Flames)

In a previous subsection (2.4.3.2), the influence of the spray mean-droplet diameter on the flame properties was considered in connection with a highly swirling flame (60^{o} swirler vane angle). The study is extended in the present subsection to cover flames with a lower combustion air swirl (30^{o} swirler vane angle). Temperature measurements were obtained for the flame of run 6 (96 μm mean-droplet diameter) and

compared with the results of run 5 (47 μm mean-droplet diameter). Fig. 2.43 shows the temperature contours for the two flames. They show that the general features for the 96 μm diameter flame are in agreement with the basic flame structure described in the previous section (2.4.3b) for the smaller diameter flame. As indicated in Fig. 2.43, the central part of the two flames is dominated by comparatively low temperature values with the implication of a reduced combustion intensity throughout this region. The latter is influenced, as previously mentioned (Section 2.4.3b),by the dilution and quenching effects of the high-velocity air stream surrounding the atomizer. The contour lines also show that the temperatures recorded for the flame of run 6 are, however, much lower than those of run 5. For example, a drop in the measured values of at least 250 ^{o}K can be easily detected at a large number of points within this zone. This further reduction in the rate of chemical reaction is probably caused by the slower evaporation rate associated with the comparatively large fuel droplets of this flame. With the expected low turbulent mixing rates, in this region of the two flames, it is likely that the relative importance of the droplet evaporation will increase.

It can also be observed in Fig. 2.43 (run 6) that, although the shear layer flame region is not as well defined as in previous cases, comparatively high temperature values were recorded at points coincident with the wall recirculation region, $x/D < 0.4$. The less steep temperature gradients observed there, and the reduction in the measured values in comparison to those of run 5, are evidence of the low combustion intensity in this region. Again, this can be explained by the slow evaporation rate of the larger fuel droplets of this flame. The contour lines also reveal that the chemical reaction rates within the main flame region ($x/D > 0.4$, $R/D \simeq 0.85$) are influenced by the slow evaporation of the droplets and by the reduction in the combustion intensity throughout

the shear layer flame zone. The temperatures recorded in this region are, in general, lower than those obtained for run 5 by at least 200 ^{o}K and a fast decay in the temperature with downstream distances of the flame can also be observed.

2.4.4 Discussion

Comparison of the flame structure described in the previous section with flame models developed for several spray combustion arrangements revealed strong similarities. For example, the basic picture of the liquid fuel spray feeding a diffusion type flame surrounding a region of reverse flow has been observed in different cases. These include, apart from the present work, the confined disc stabilized flame of Tuttle et al (1976), the unconfined disc configuration of Chigler and co workers (1973, 1977) and the Allison J-33 combustor of Tuttle et al (1973) and Mellor (1973). In agreement with the present work, the experimental results obtained within these different flames indicate the existence of two reaction zones. A shear layer flame was found to extend along the recirculation zone boundaries and was noted to be due to mass transfer from smaller fuel droplets. A more extensive flame zone was observed to begin in the region where the larger fuel droplets penetrate through the shear layer and into the air stream.

Also in agreement with the present work, Tuttle et al (1973, 1976) found the near-spray region to be dominated by high CO concentrations, see for example Fig. 2.30, which indicated that CO formation takes place rapidly upon injection of the fuel. This is mainly due to the initial fast oxidation reactions of the hydrocarbons and the comparatively slower CO oxidation reaction, see for example Caretto (1976), Jones (1979) and Bowman (1975). In addition, the comparatively low temperatures and O_2 concentrations observed within the flame region enclosed by the shear

layer (high swirl flames, Figs. 2.28 and 2.31) were also revealed in the experimental results of Chigier et al (1973, 1974, 1977), Styles et al (1977) and Tuttle et al (1976). It was also observed by Tuttle et al (1976) that if the mixing across the shear layer is too rapid, CO concentrations show maximum values. This was interpreted as a result of reaction quenching by the colder high velocity air stream. It is likely that this would explain the high CO values, around 10%, recorded close to the shear layer region in connection with the high swirl flames, see Fig. 2.30.

The results presented in the previous section, in addition to their direct practical relevance, provide clues which assist understanding of physical processes involved in spray combustion systems. As indicated, it was generally observed that an increase in the spray mean-droplet diameter is associated with a reduction in the intensity of chemical reactions at a large number of points within the combustion chamber. The results were explained, mainly by reference to the relative importance of the droplets evaporation in controlling the combustion process. Following the arguments put forward by Mellor (1976), Tuttle et al (1976) and Komiyama et al (1977), droplet evaporation would only have an influence on the combustion process if a time, characteristic of the turbulent mixing between fuel and air, is comparable to that which characterize droplets evaporation. It is implicitly assumed that the combustion processes within a spray flame resemble those of turbulent diffusion flames and, therefore, smaller influences of chemical kinetics are anticipated.

By analogy to the Damkholar's number, see for example Bilger (1976), a ratio of the characteristic time scale of turbulence and droplets evaporation can be formed to give an indication of the combustion rate controlling parameter, i.e.:-

$$D_s = \frac{t_{turb.}}{t_{evp.}}$$

The characteristic time scale of turbulence can be given approximately by, see for example Launder et al (1972), Reynolds (1974) and Komiyama (1977):-

$$t_{turb.} \simeq \ell_m / u'$$

where u' is the rms turbulent velocity fluctuations and ℓ_m is a characteristic length scale of turbulent mixing. From the "d^2 law" of droplet evaporation, see for example Mellor (1976) and Spalding (1953), the characteristic time of droplet evaporation can be taken roughly as:-

$$t_{evp.} \cong d_i^2 / k_e ,$$

where d_i is the initial droplet diameter and k_e is the evaporation rate constant (for more details, see Section 3.5). It is clear that for $D_s \ll$ O (1), droplet evaporation would have a greater influence on the combustion rate.

To examine whether the observed influences of the spray mean droplet diameter, see Sections 2.4.3.2 and 2.4.3.4, are consistent with the above physical explanation, an order of magnitude calculation of the two time scales was performed for conditions appropriate to the present flames. In the calculation of the turbulence time scale, the velocity fluctuations were taken from the isothermal axial velocity measurements. At locations close to the fuel atomizer, $\sqrt{\overline{u'^2}}$ was in the order of 2 m/s, see Fig. 2.26a (60^o swirler case). An order of magnitude for ℓ_m was estimated from the results of the numerical calculation procedure, described in Chapter 3, which was used to predict the aerodynamic flow

field inside the present combustion chamber. Use was made of the following two expressions given by Launder et al (1972):-

$$\ell_m = \ell / C_\mu^{1/4}$$

where ℓ is a characteristic length scale defined by the following expression and C_μ is a constant of 0.09:-

$$\ell = C_\mu \cdot \frac{k^{3/2}}{\varepsilon}$$

where k is the turbulent kinetic energy and ε its rate of dissipation. From the predicted values of k and ε (60^o swirler case), ℓ_m was estimated as ℓ_m = 0 (5) mm. Therefore, $t_{turb.}$ = 0 (2.5) ms. An estimated average value for the evaporation constant, k_e, see Chapter 3 and Spalding (1953) and Williams (1973), was found as $k_e \simeq 0.0096 \times 10^{-4}$ m^2/s. For the three mean droplet diameters used in the present work, (33 μm, 47 μm and 96 μm), the characteristic evaporation time ranges between $t_{evp.} \simeq 1.3$ - 9.4 ms. It is clear, therefore, that the parameter D_s has values which are of the order or less than unity: the lower values correspond to the large droplet diameters. Consequently, it is anticipated that droplet evaporation for the present flames would have an increasing influence on reaction rates with increase in the mean droplet diameter. The above estimates for the time scales were mainly based on the results of the high swirl flames of runs 1, 2 and 3. It is expected, however, that the main conclusion will hold equally for the lower swirl flames (runs 5 and 6) where the increase in $t_{turb.}$ with the reduction in swirl will be balanced by a corresponding increase in $t_{evp.}$. The latter stems mainly from the decrease in the evaporation rate constant as

influenced by the low temperature values observed near the atomizer, see Fig. 2.43.

The main results of the present work, concerning the effect of the mean droplet size of the spray, are in agreement with those of Beèr (1962) which showed that the variation of the mean droplet diameter between 89 μm and 113 μm had a significant effect on both the flame propagation and also upon the burnout of carbon in the flame. It must be noted, however, that a heavy fuel oil was used in Beer's work whereas a light kerosene fuel was used in the present work. This indicates that the fuel spray can modify the combustion characteristics of the flame regardless of the fuel type. On the other hand, Komiyama et al (1977) indicated a small influence of droplet mean diameter on the fuel-air mixing process in a pressure atomized kerosene spray flame. This result was interpreted from a cross-section averaged oxygen concentration measurements with the assumption that radial variations in oxygen concentrations were small beyond about half a burner diameter downstream of the injection plane. The analysis of the present experimental data was, however, based on the detailed distribution of the measured values. It is believed that the use of cross-sectional averaging would not reflect accurately the local conditions in the flow and can lead to uncertainties in the consequent deductions.

It is of interest to note that the operating conditions for a range of combustion equipment, e.g. the combustion chamber of a gas turbine, after burners, etc., include high pressure operation and preheating of the combustion air and/or the liquid fuel. In the present work, air and fuel were supplied to the combustion chamber at room temperature and the combustion was under atmospheric pressure. It is likely that the above factors, apart from their direct influence on the reaction rates, will modify the evaporation characteristics of the fuel

droplets. The implications for the conclusions of the present work, in particular those concerning the influence of the mean droplet diameter, are still to be determined. It is anticipated, however, that the general trends will be correct with quantitative modifications to the extent of the influences which, more likely, will be smaller.

2.4.5 Concluding Remarks

For the range of spray flames considered in the present study, the flame structure comprised two main reaction zones. One coincided with the boundaries of the recirculation zone while the other extended downstream of the fuel spray. For the high swirl cases, flames were stabilized on the central recirculation zone while low swirl flames (30^{o} swirler) were stabilized on the wall recirculation zone.

The influence of the mean-droplet diameter on the combustion characteristics of spray flames has been examined in the present study under two levels of turbulent fuel-air mixing rates. The main conclusion was that the evaporation characteristics of the fuel spray, as determined by the mean diameter, together with turbulent mixing, controlled the chemical reaction rates. An increase in mean diameter, in the high swirl cases, was associated with a reduction in the combustion intensity at the region downstream of the fuel spray plane and, in particular, at large radii. The reduction in the chemical reaction rates was explained as a result of interacting contributions of slow evaporation, and dilution and quenching effects of the cold, high-velocity air stream near the wall. It was also found that

the CO concentrations, at the upstream part of the flame, increased with the reduction in the mean-diameter and this was attributed to the larger amount of fuel evolved in this region. The results obtained with the 30^{o} swirler flame showed the same trend of the reduction in the combustion intensity with the mean diameter. However, as the details of the flame were different from the above case, the influences associated with the increase in diameter were more significant at the central part of the flame.

The experimentally observed influences of the mean droplet diameter were examined by order of magnitude estimates of the characteristic time scales of turbulent mixing and droplet evaporation processes. It was found that their values are comparable and that the time scale of droplet evaporation increases with the mean droplet diameter. Thus, the evaporation characteristics can modify the chemical reaction processes within the flames studied especially with larger droplets.

The comparison between the results obtained for the two flames with 45^{o} and 60^{o} swirler indicated that the reduction in swirl led to a reduced chemical reaction rate within the initial part of the flame and close to the centre-line. This was deduced from the temperature values, which were around 100 - 300 ^{o}K lower, and from the comparatively slower CO and CO_2 destruction and formation rates respectively. It was also found that chemical reactions, for the low swirl flame, were concentrated at the region coincident with the expected path of the fuel vapour and droplets from the spray zone. The combustion intensity also increased at the far downstream part of the flame as the fuel-air mixture conditions favoured intense combustion.

The reduction in the swirler angle beyond 45^{o} (30^{o} swirler

flame) was found to cause the main reaction zones to move to the near wall region where the flame was stabilized. The central recirculation zone nearly vanished for this case and the high-velocity air stream surrounding the atomizer caused a quenching of the chemical reaction throughout the central part of the flame. The temperature values were at least 250 ^{o}K less than those observed for the high-swirl flames. The reduction in the combustion intensity was accelerated by the simultaneous reduction in the droplet evaporation rate which, coupled with the entrainment of a large number of droplets by the air flow around the atomizer, reduced the amount of fuel burned out at the near-wall region and within the combustor in general. It is concluded, therefore, that the fuel-air mixture conditions close to the fuel injection point play a significant role in determining the overall combustion efficiency.

TABLE 2.1

ANALYSIS OF RADIATION AND CONDUCTION ERROR FOR SUCTION PYROMETER

No	T_w °K	T_m °K	K_R	$T_{s.p.}$ °K	T_i °K	$U_{s.p.}$ m/s	T_g °K	Components of Error °K			% Total Error
								Conduction	Rad. to Wall	Rad. to Shield	
1	400	300	0.3	1600	1500	350	1681.06	21.85	34.710	24.500	4.820
2	400	300	0.3	1600	1300	350	1717.40	21.85	34.710	60.840	6.830
3	400	300	0.3	1600	1200	350	1730.27	21.85	34.710	73.710	7.500
4	400	300	0.3	1600	1000	350	1747.86	21.85	34.710	91.300	8.450
5	400	300	0.3	1600	800	350	1757.66	21.85	34.710	101.100	8.969
6	400	300	0.3	1600	1300	300	1730.27	24.24	38.510	67.500	7.500
7	400	300	0.3	1600	1300	250	1747.26	27.41	43.530	76.320	8.430
8	400	300	0.5	1600	1200	350	1782.35	21.85	86.790	73.710	10.231
9	400	300	0.3	800	700	250	818.56	11.10	3.210	4.250	2.270
10	400	300	0.3	800	600	250	821.33	11.10	3.210	7.020	2.597
11	400	300	0.3	800	300	250	824.41	11.10	3.210	10.100	2.958
12	400	300	0.3	800	600	200	824.78	12.90	3.730	8.150	3.000
13	400	300	0.3	800	600	150	830.09	15.66	4.529	9.905	3.625

$T_{s.p.}$: reading of suction pyrometer °K
T_m : thermocouple mount temperature °K
$U_{s.p.}$: suction velocity m/s
T_g : gas temperature
T_w : wall temperature °K
K_R : view factor
T_i : temperature of shield inner wall °K

TABLE 2.2

SAMPLE OF TURBULENCE PROPERTIES AND ERRORS IN DOPPLER SPECTRA, RUN 3

x/D	$\bar{\nu}_D$ MHz	$\tilde{\nu}_D$ MHz	Skewness $\overline{u^3}/(\overline{u^2})^{3/2}$	Flatness $\overline{u^4}/(\overline{u^2})^2$	e_μ	e_σ	N
0.6	35.85	4.61	- 0.0279	3.1100	0.0066	0.0151	8802.0
1.0	33.80	3.31	0.1693	2.9320	0.0036	0.0100	19951.0
2.2	30.10	2.33	0.0018	2.9067	0.0064	0.0177	6397.0
3.0	30.40	2.15	- 0.1500	2.7039	0.0124	0.0380	1362.0

$\bar{\nu}_D$, $\tilde{\nu}_D$: mean and rms Doppler frequency, MHz

e_μ : error in mean frequency

e_σ : error in rms frequency

N : number of detected signals

TABLE 2.3

OPERATING CONDITIONS, UNCONFINED FLAME EXPERIMENTS

Run No.	$\dot{m}_{air} \times 10^3$	$\dot{m}_{fuel} \times 10^3$	A/F	$\dot{m}_{atom} \times 10^3$	ΔP_{fuel}	Swirler Vane Angle (^{o})	SMD μm	Remarks
1	11.9	0.600	20.04	0.35	0.27	60.0	58	
2	11.9	0.856	14.30	0.35	0.41	60.0	70	Temperature measurements
3	11.9	1.370	8.95	0.35	0.82	60.0	85	
4	11.9	1.370	8.95	0.35	0.82	45.0	85	
5	-	1.370	-	0.35	0.82	-	85	
6	-	1.890	-	0.30	0.68	-	105	Droplet no. density measurements, burner B

$\dot{m}_{air}$: combustion air mass flow rate, kg/s

$\dot{m}_{fuel}$: fuel mass flow rate, kg/s

$\dot{m}_{atom}$: atomization air mass flow rate, kg/s

A/F : inlet air/fuel ratio

ΔP_{fuel} : pressure difference across fuel nozzle, bar

SMD : Sauter mean diameter, μm

TABLE 2.4

OPERATING CONDITIONS, CONFINED FLAME EXPERIMENTS

Run No.	$\dot{m}_{air} \times 10^2$ kg/s	$\dot{m}_{fuel} \times 10^3$ kg/s	Swirler Vane Angle (^{o})	N_{rpm}	D_i mm	$\dot{m}_{atom} \times 10^3$ kg/s	Measurements of:-
1	5.56	1.32	60	44000	33	2.29	T, CO, CO_2, O_2 wall-temperature droplets axial and tangential velocity
2	5.56	1.32	60	30000	47	2.29	
3	5.56	1.32	60	12600	96	2.29	
4	5.56	1.32	45	30000	47	2.29	T, CO, CO_2, O_2 wall-temperature droplets axial velocity
5	5.56	1.32	30	30000	47	2.29	
6	5.56	1.32	30	12600	96	2.29	Temperature
7	5.56	-	60	-	-	2.29	Isothermal mean axial velocity
8	5.56	-	30	-	-	2.29	

$\dot{m}_{air}$: combustion air mass flow rate, kg/s

$\dot{m}_{fuel}$: fuel mass flow rate, kg/s

N : rotational speed of fuel atomizer, rpm

D_i : spray mean droplet diameter

$\dot{m}_{atom}$: atomizer-cooling air mass flow rate, kg/s

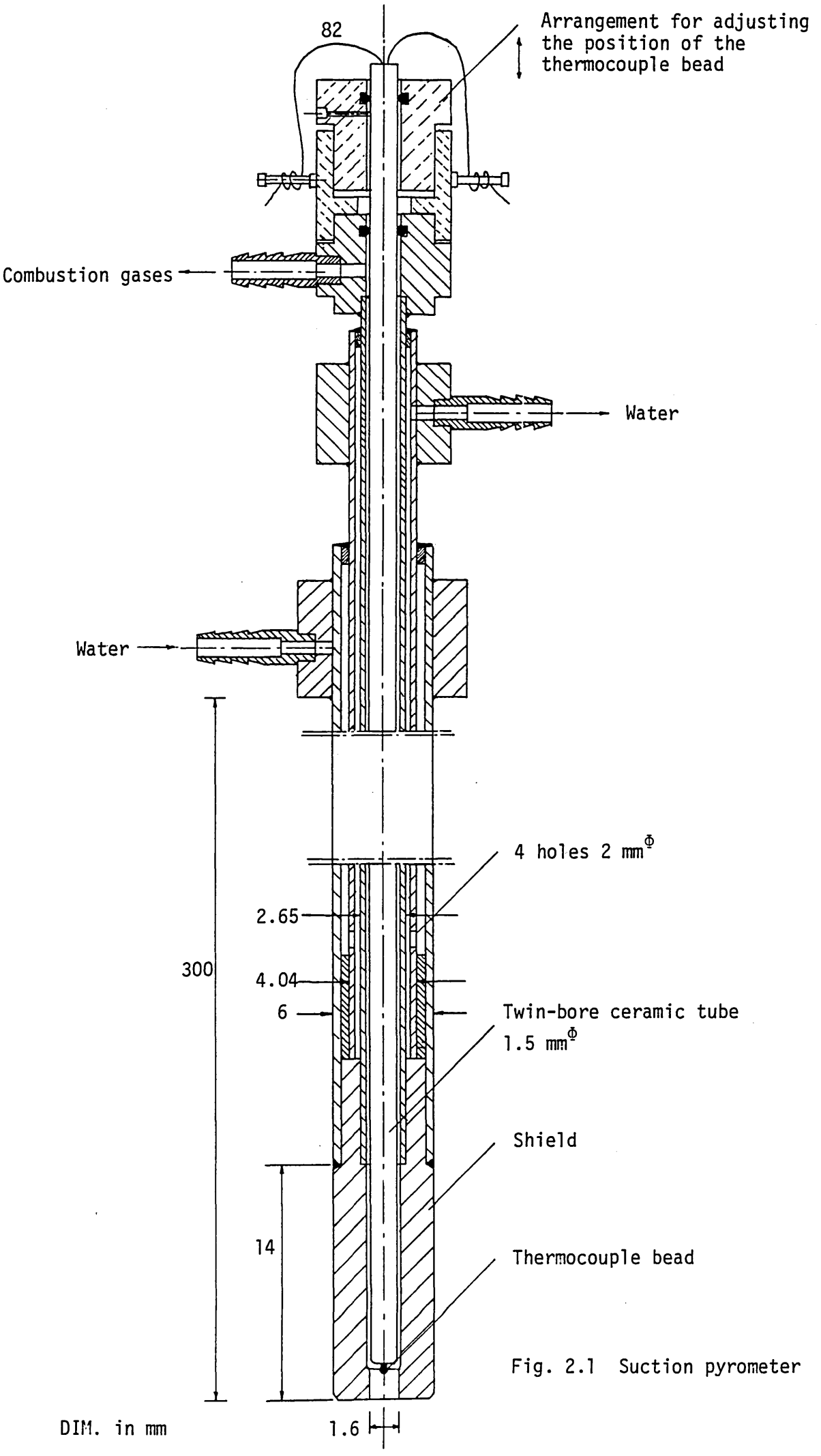

Fig. 2.1 Suction pyrometer

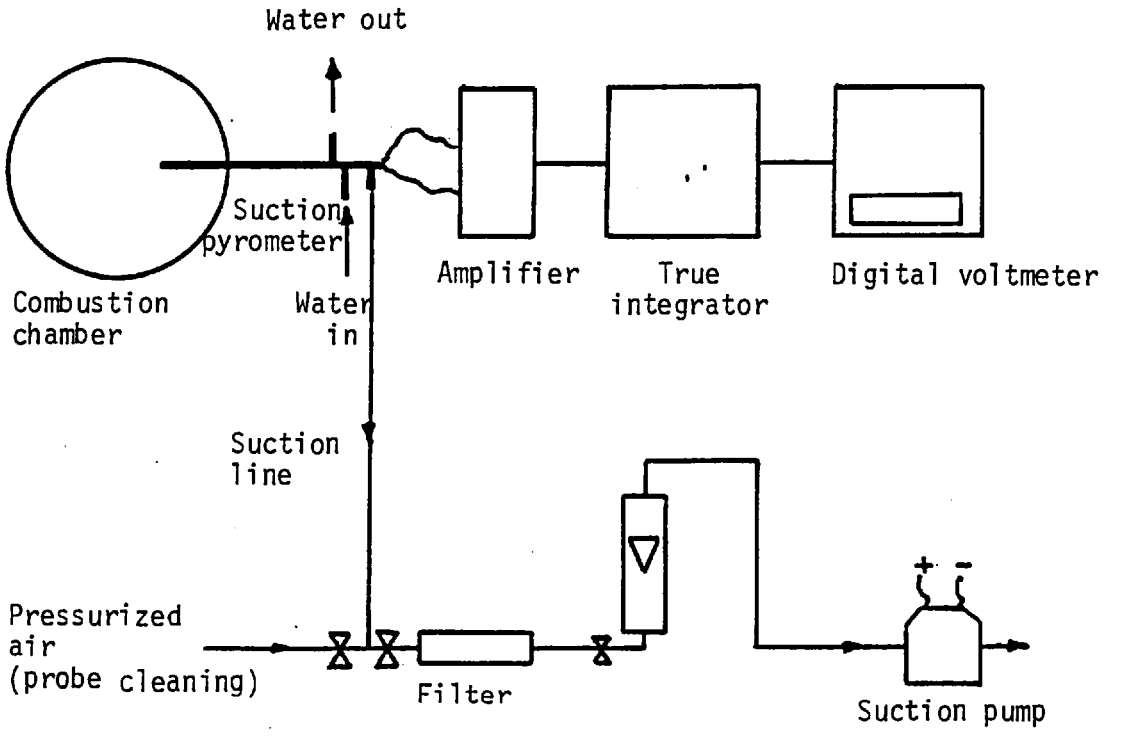

(a)

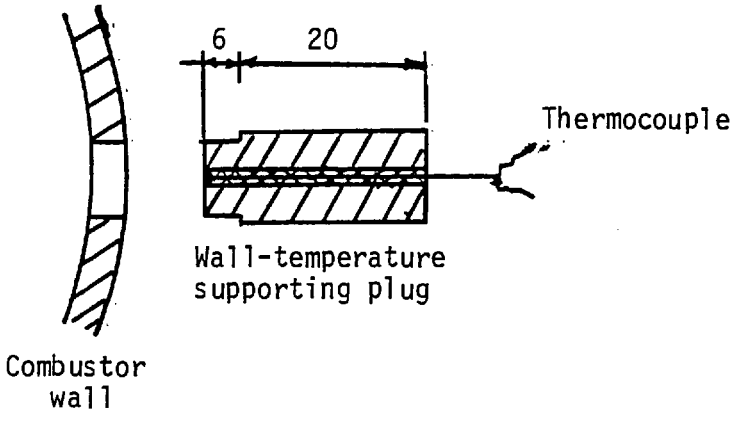

(b)

Fig. 2.2 (a) Measuring equipment for temperature measurements by the suction pyrometer

(b) Arrangement for wall-temperature measurements

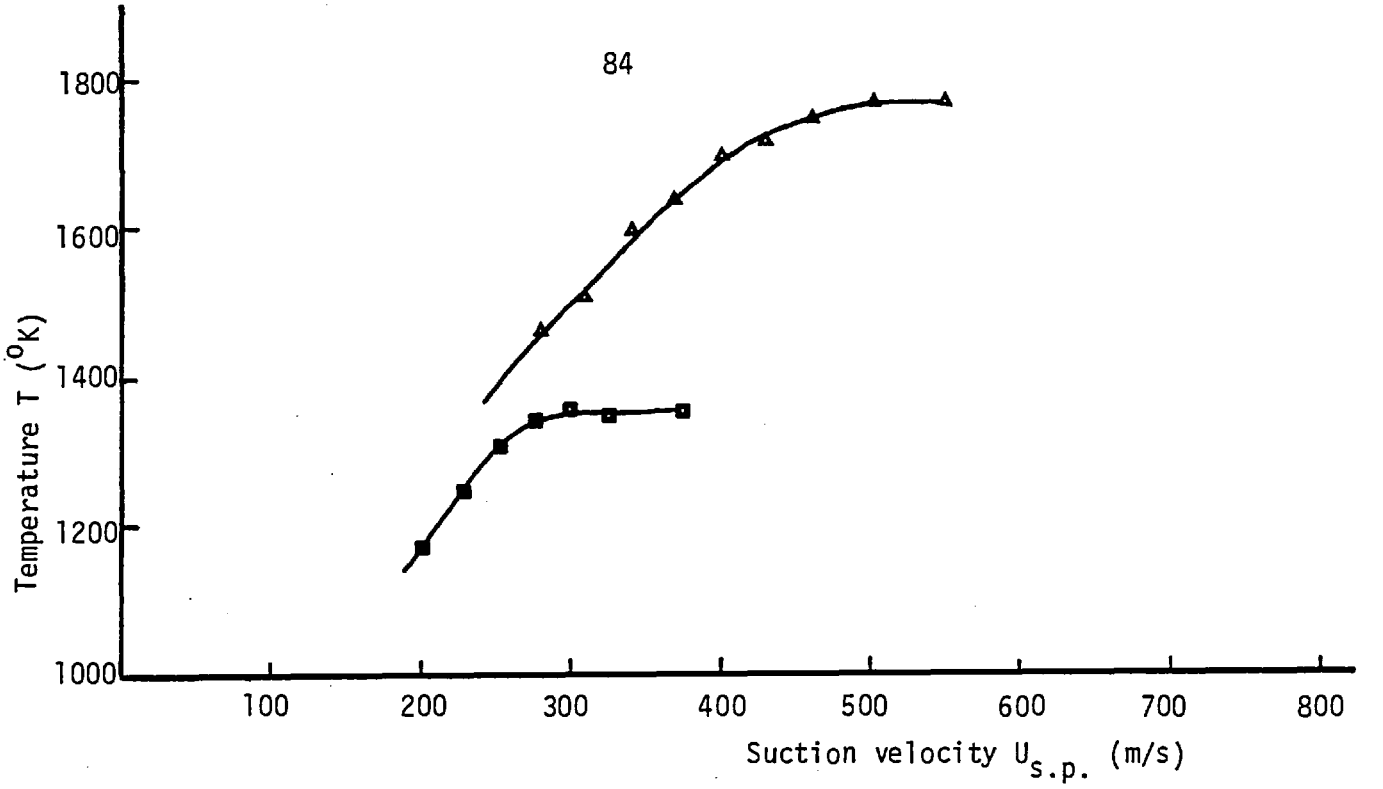

Fig. 2.3 Variation of temperature with suction velocity

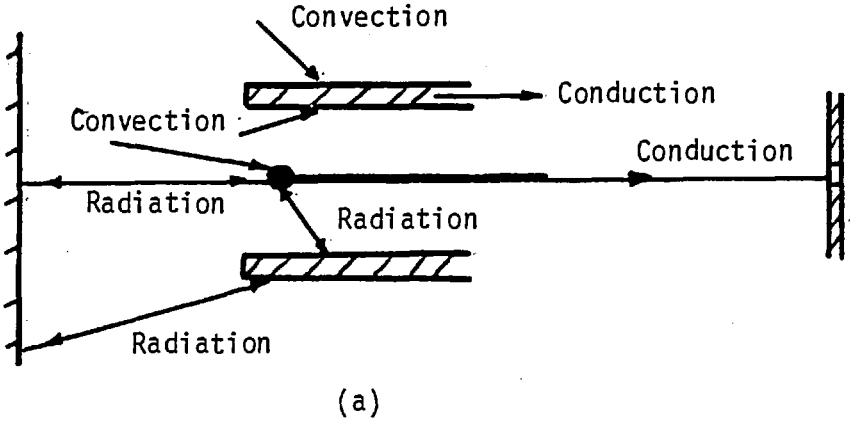

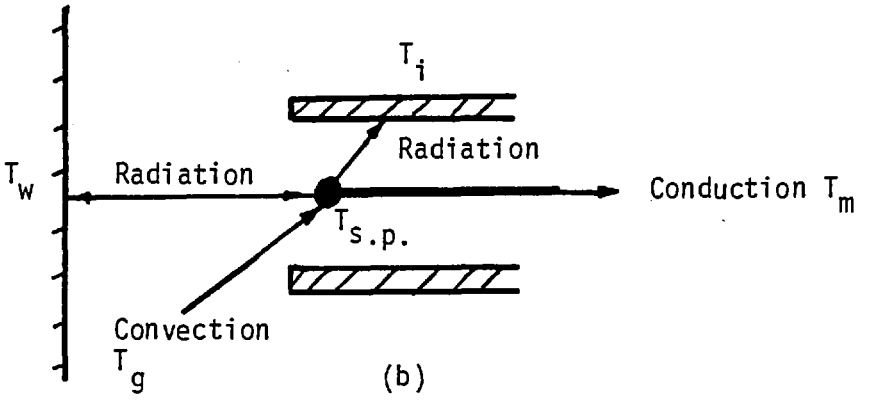

Fig. 2.4 (a) Heat transfer modes associated with the suction pyrometer

(b) Heat transfer to and from thermocouple junction

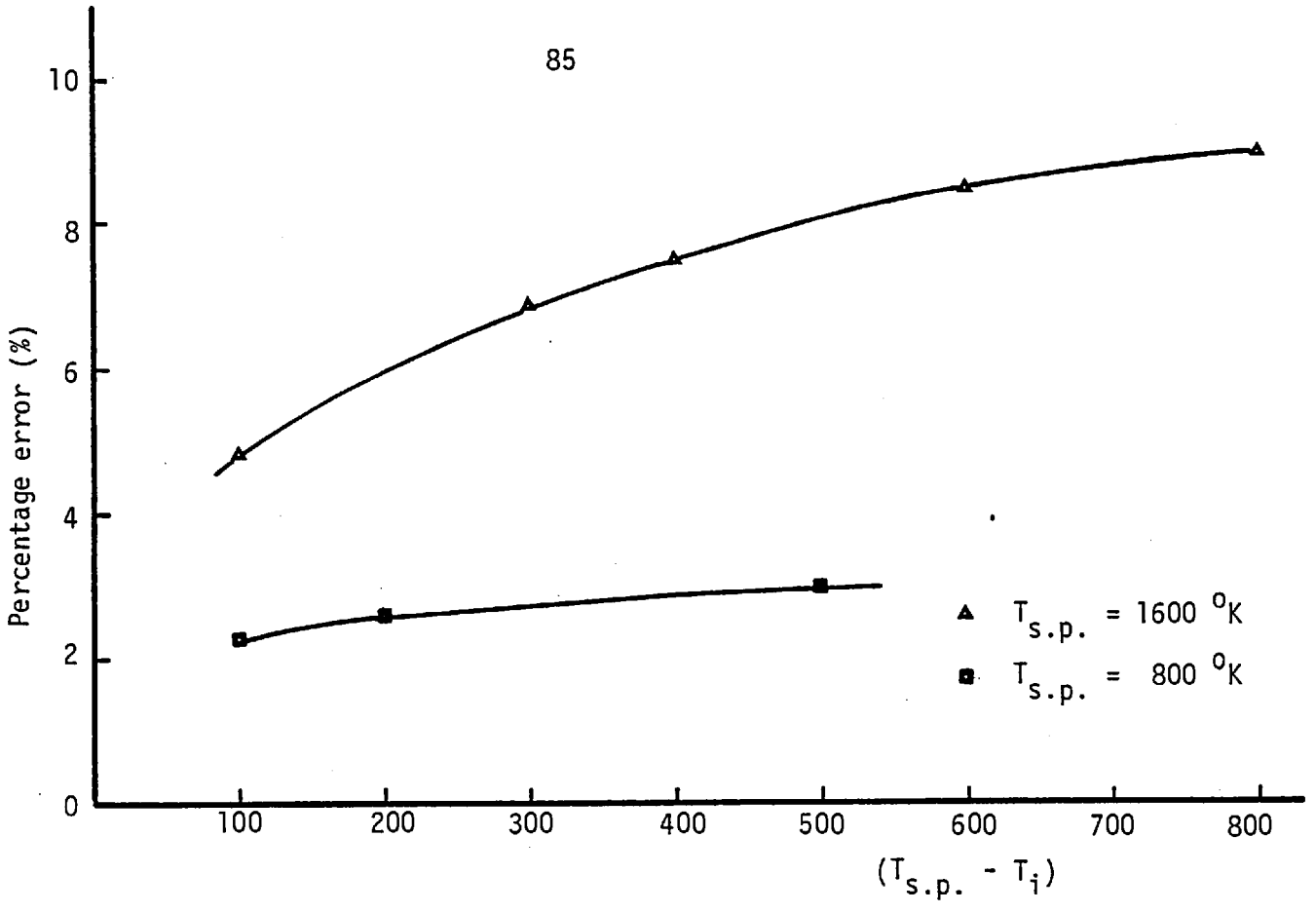

Fig. 2.5 The variation of the percentage temperature error with temperature difference between junction and shield (calculated)

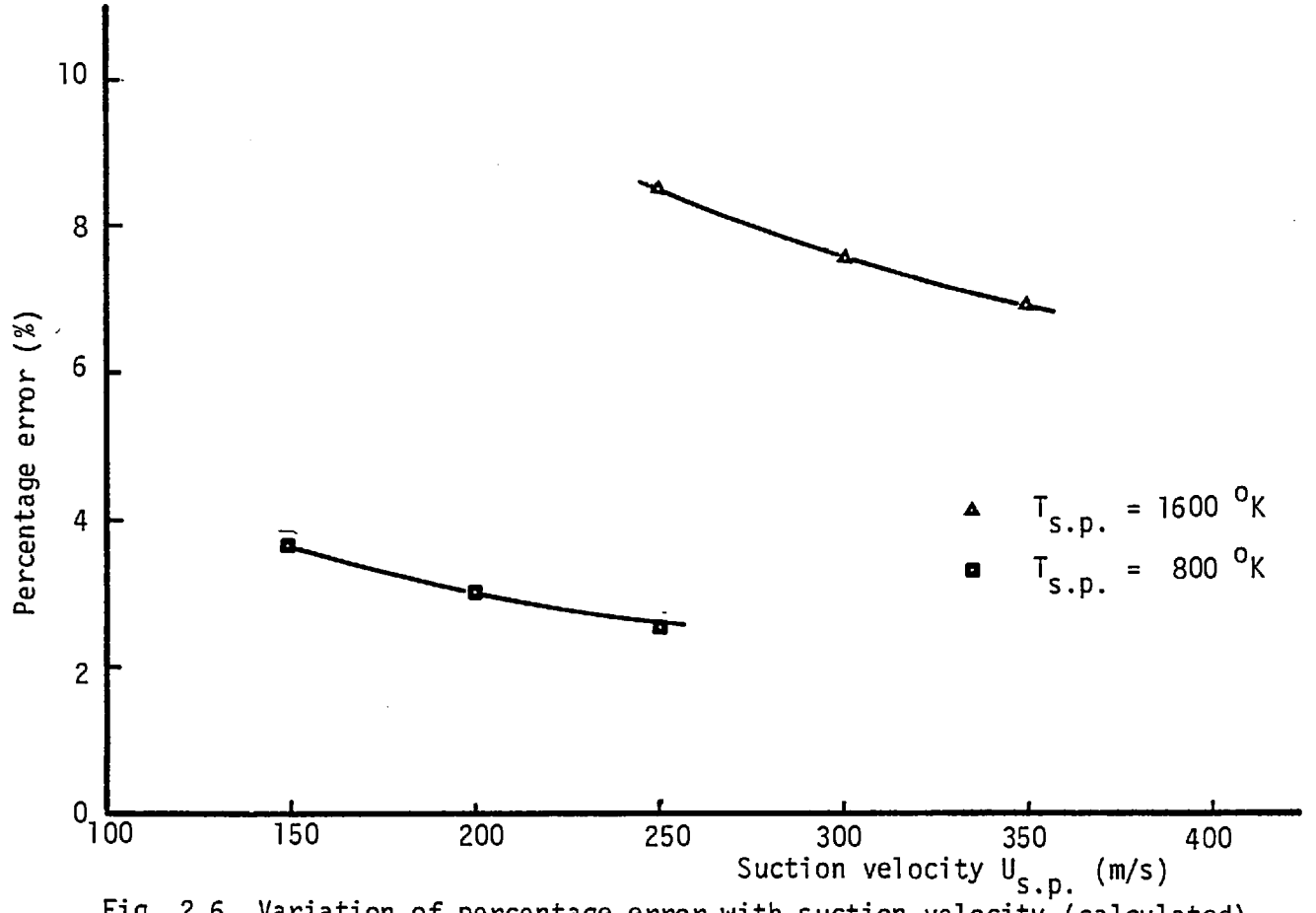

Fig. 2.6 Variation of percentage error with suction velocity (calculated)

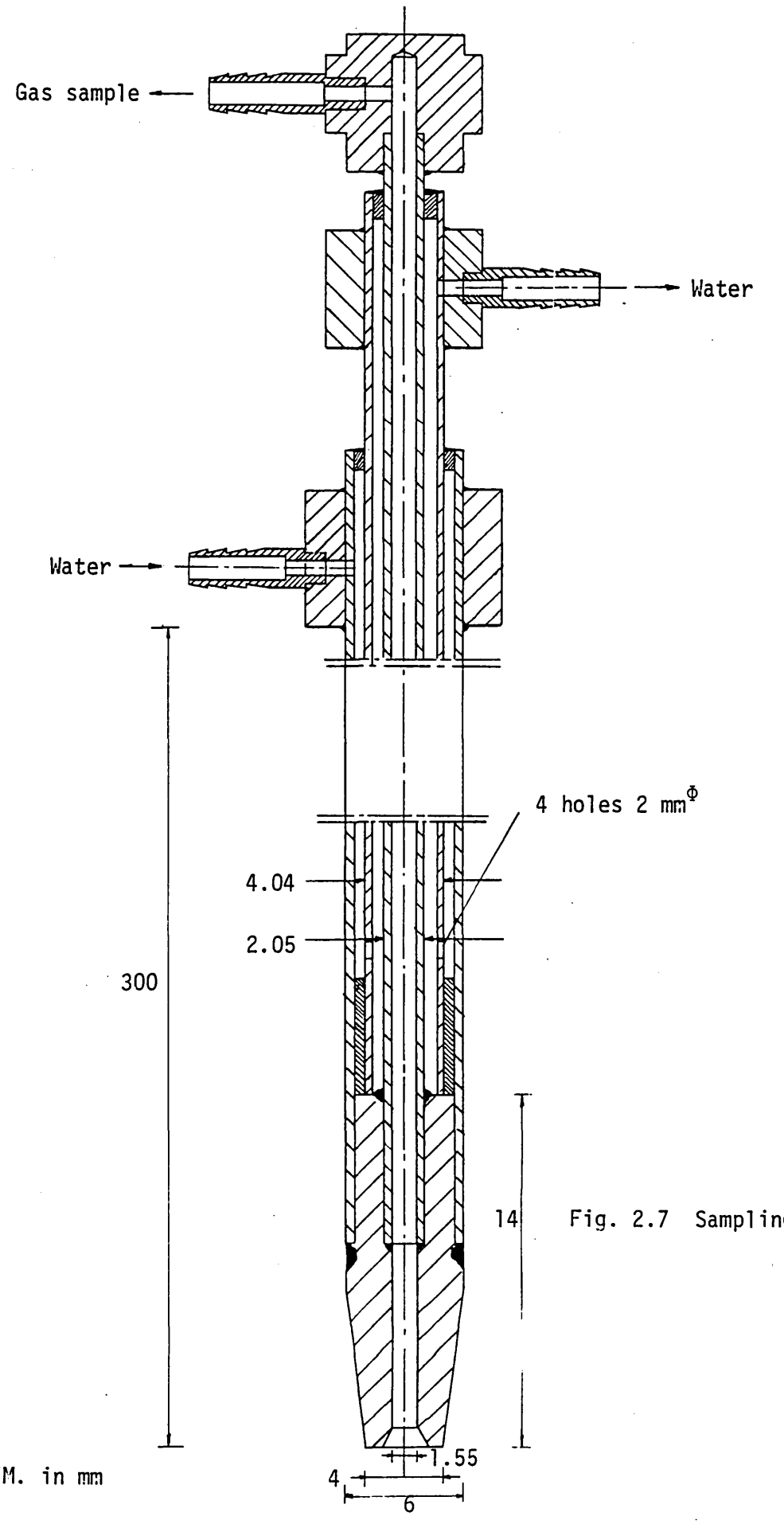

Fig. 2.7 Sampling probe

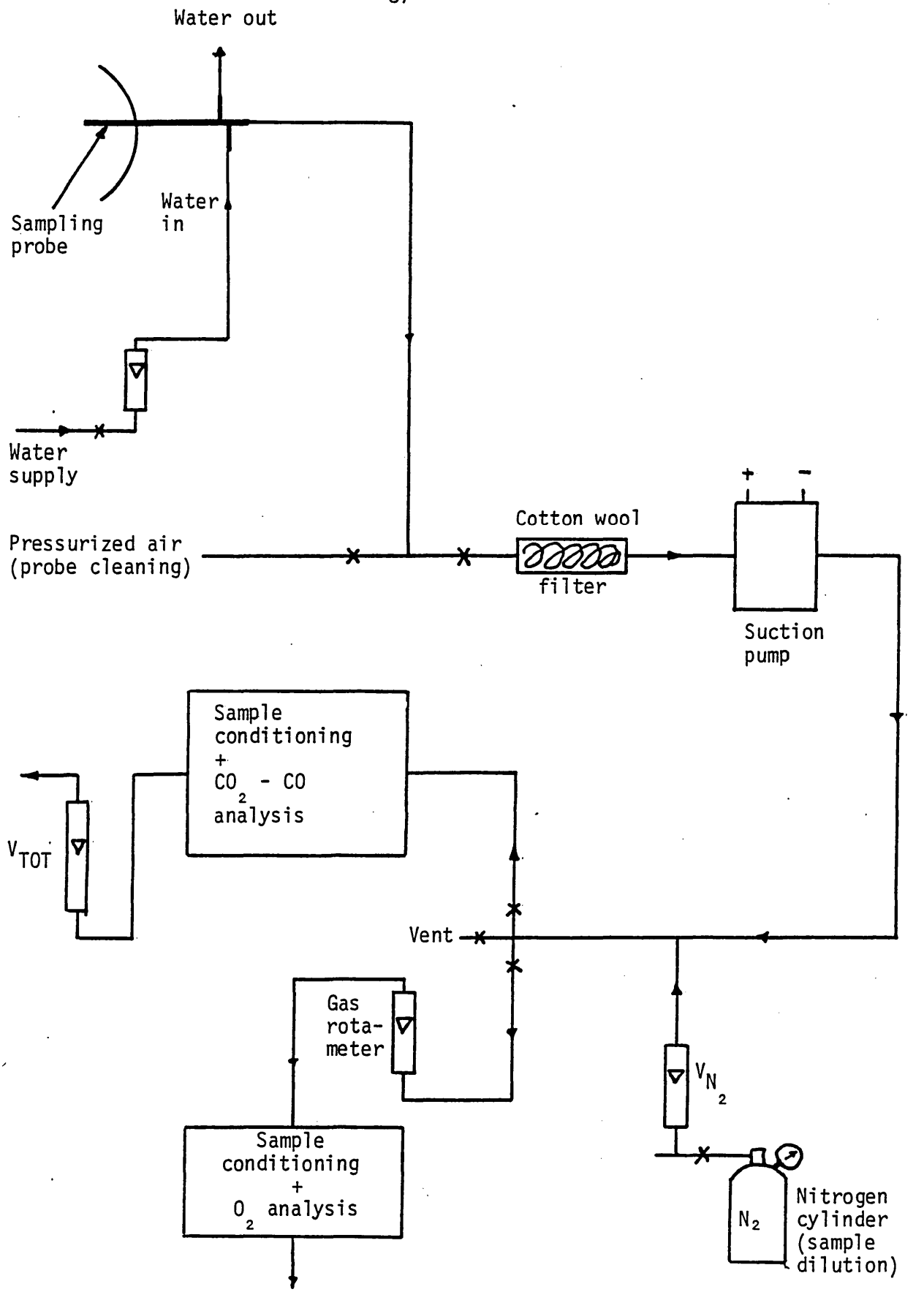

Fig. 2.8 Schematic diagram for sampling system

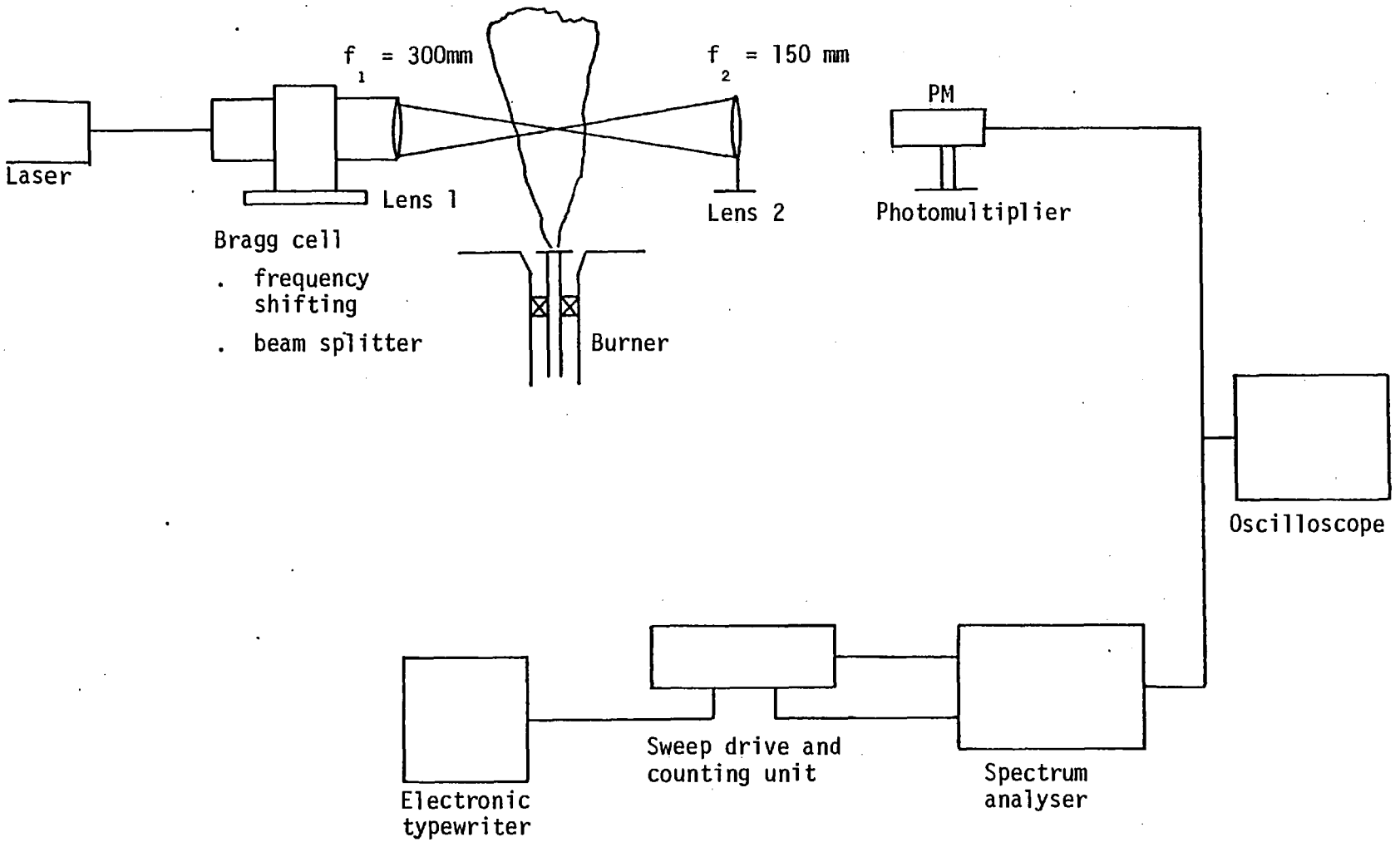

Fig. 2.9 Optical and signal processing arrangements for LDA, unconfined flames

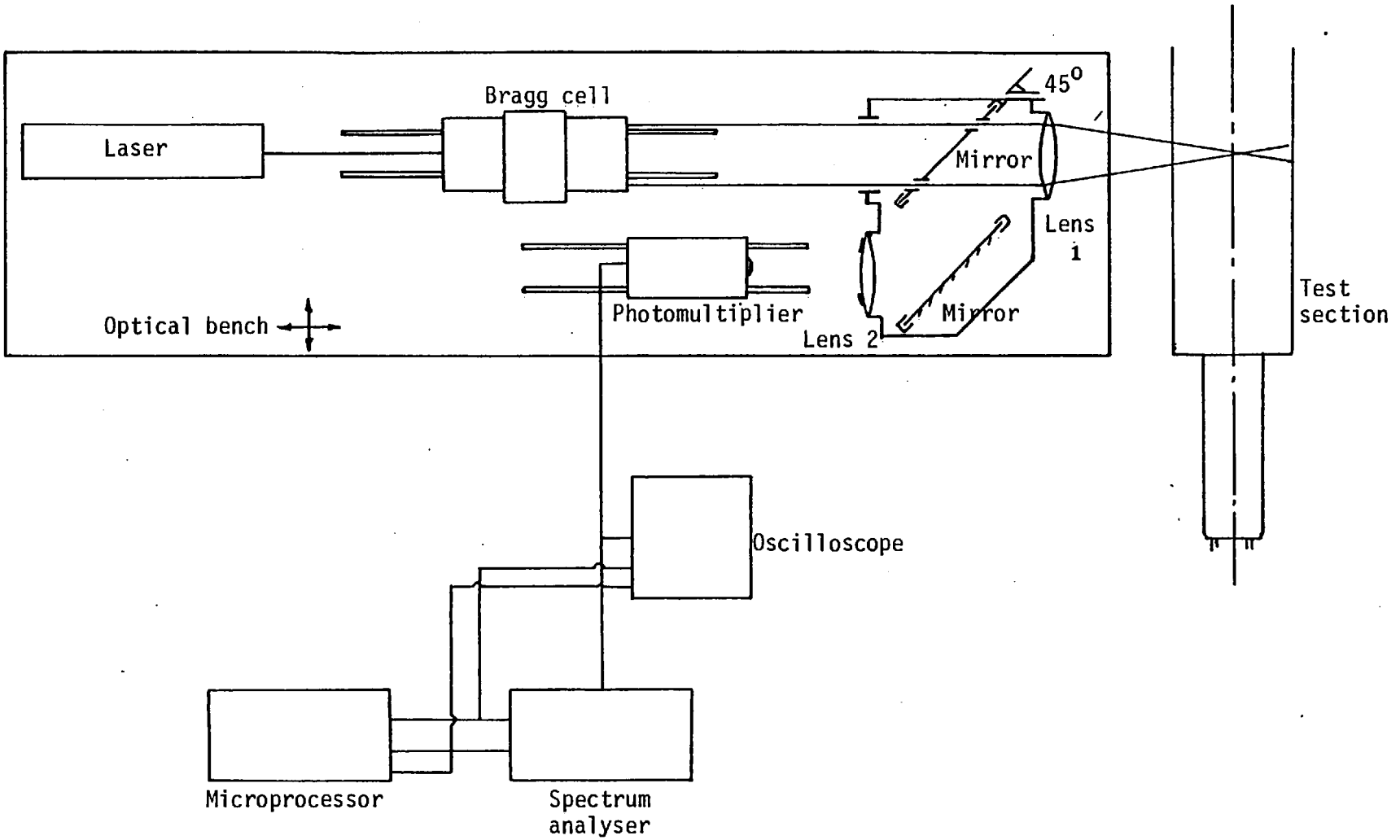

Fig. 2.10 Optical and signal processing arrangements for LDA, confined flames

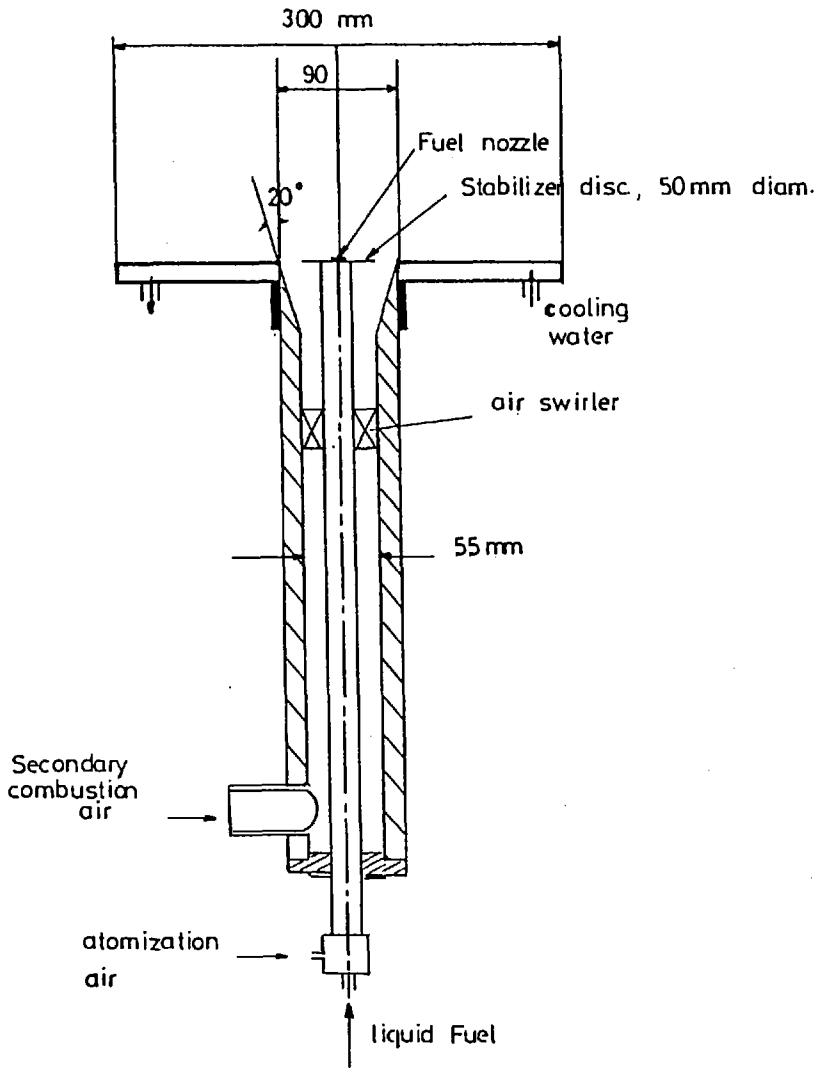

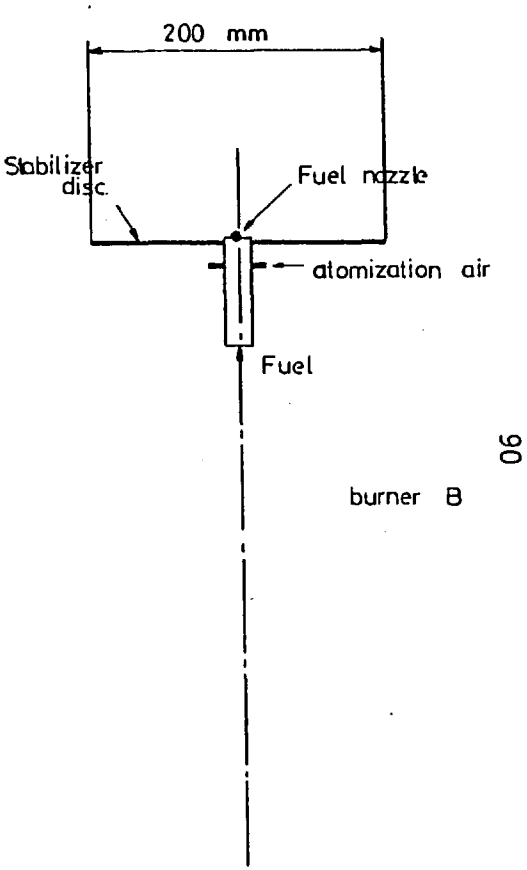

Fig. 2.11 Burner configurations, unconfined flames

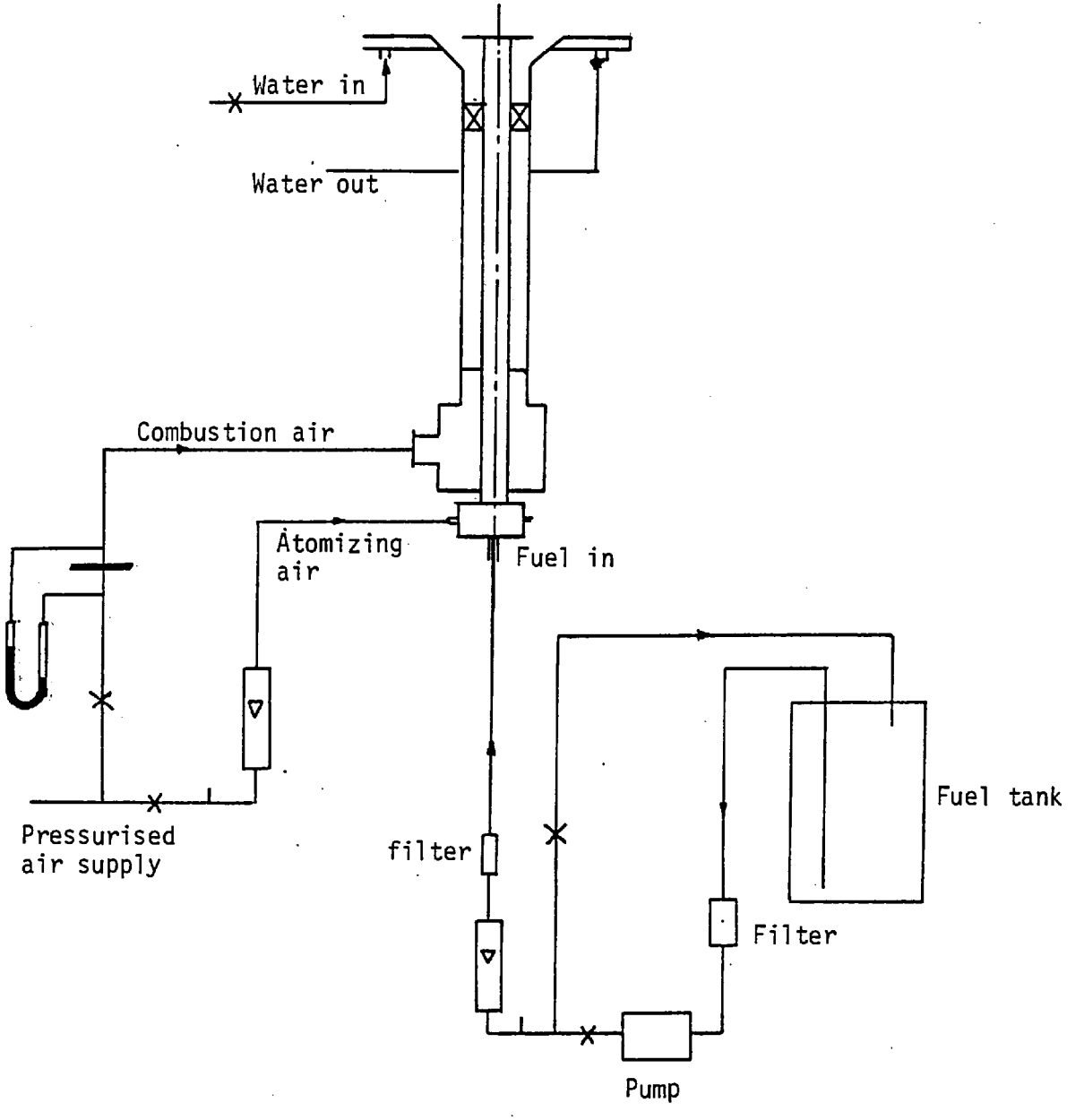

Fig. 2.12 Supply system for air and fuel, unconfined flames

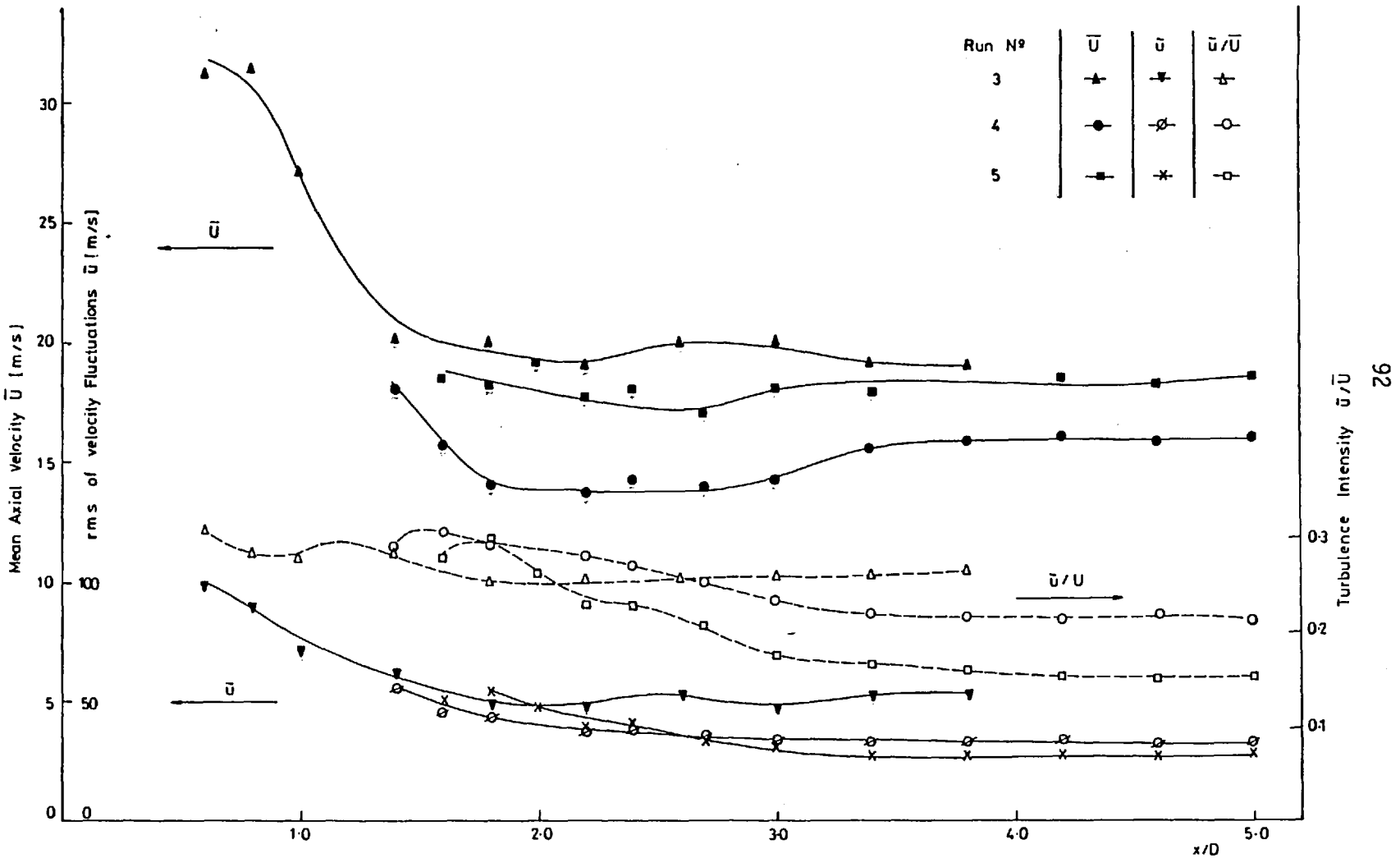

Fig. 2.13 Centreline distributions of mean velocity, rms of fluctuations and turbulence intensity - runs 3, 4 and 5

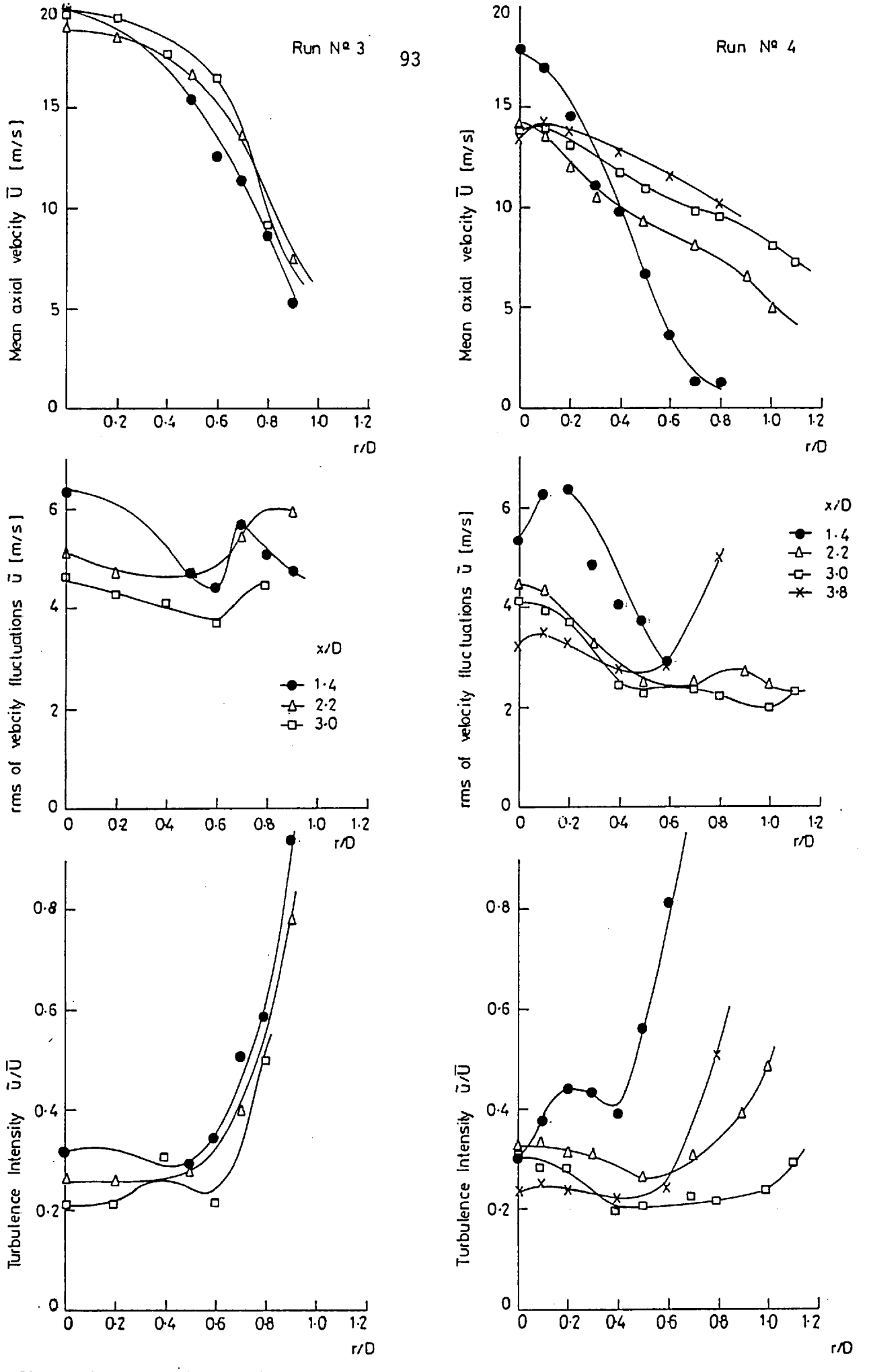

Fig. 2.14 Radial profiles of mean velocity, rms of fluctuation and turbulence intensity - runs 3 and 4

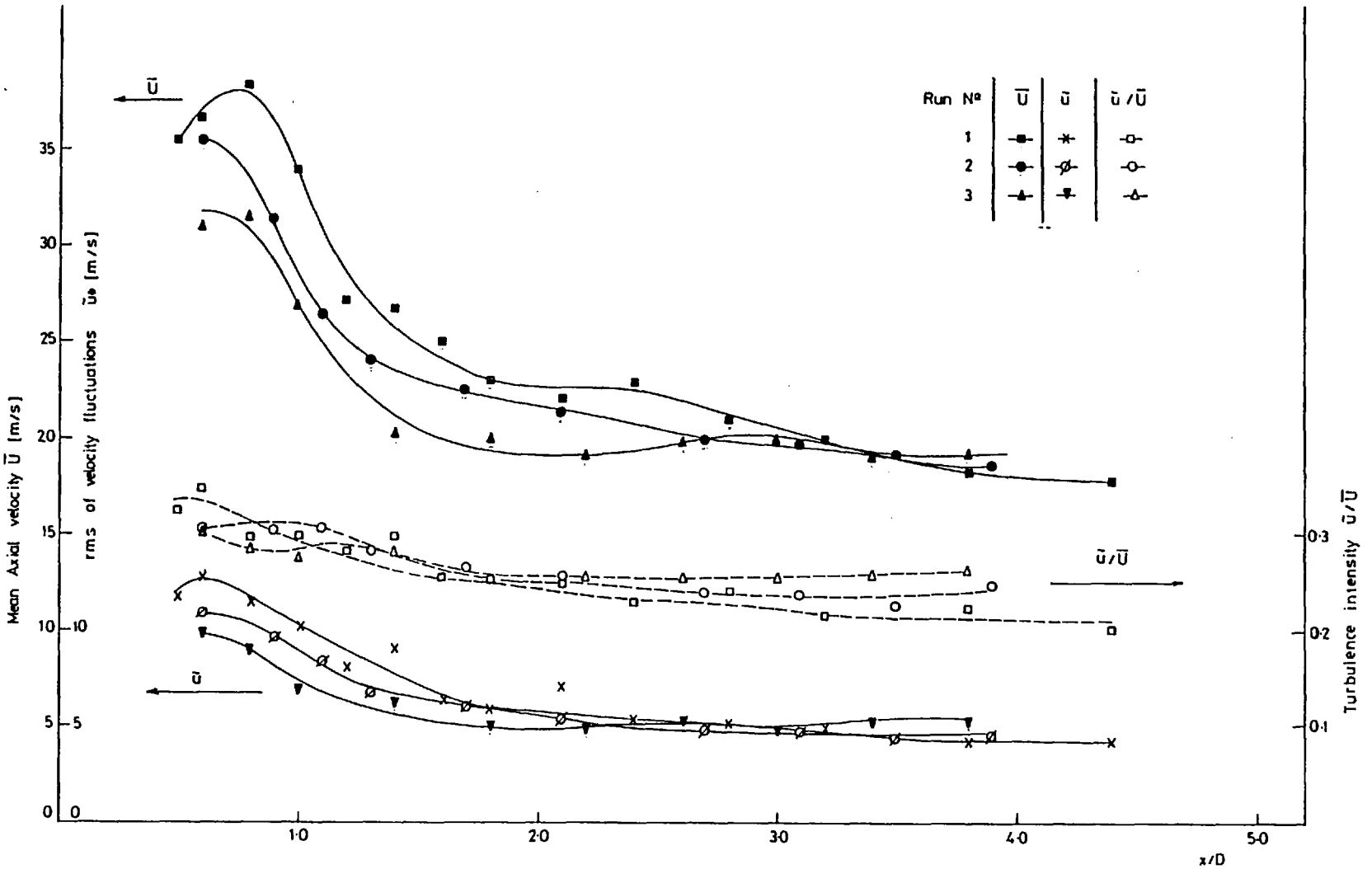

Fig. 2.15 Centreline distributions of mean axial velocity, rms of fluctuations and turbulence intensity - runs 1, 2 and 3

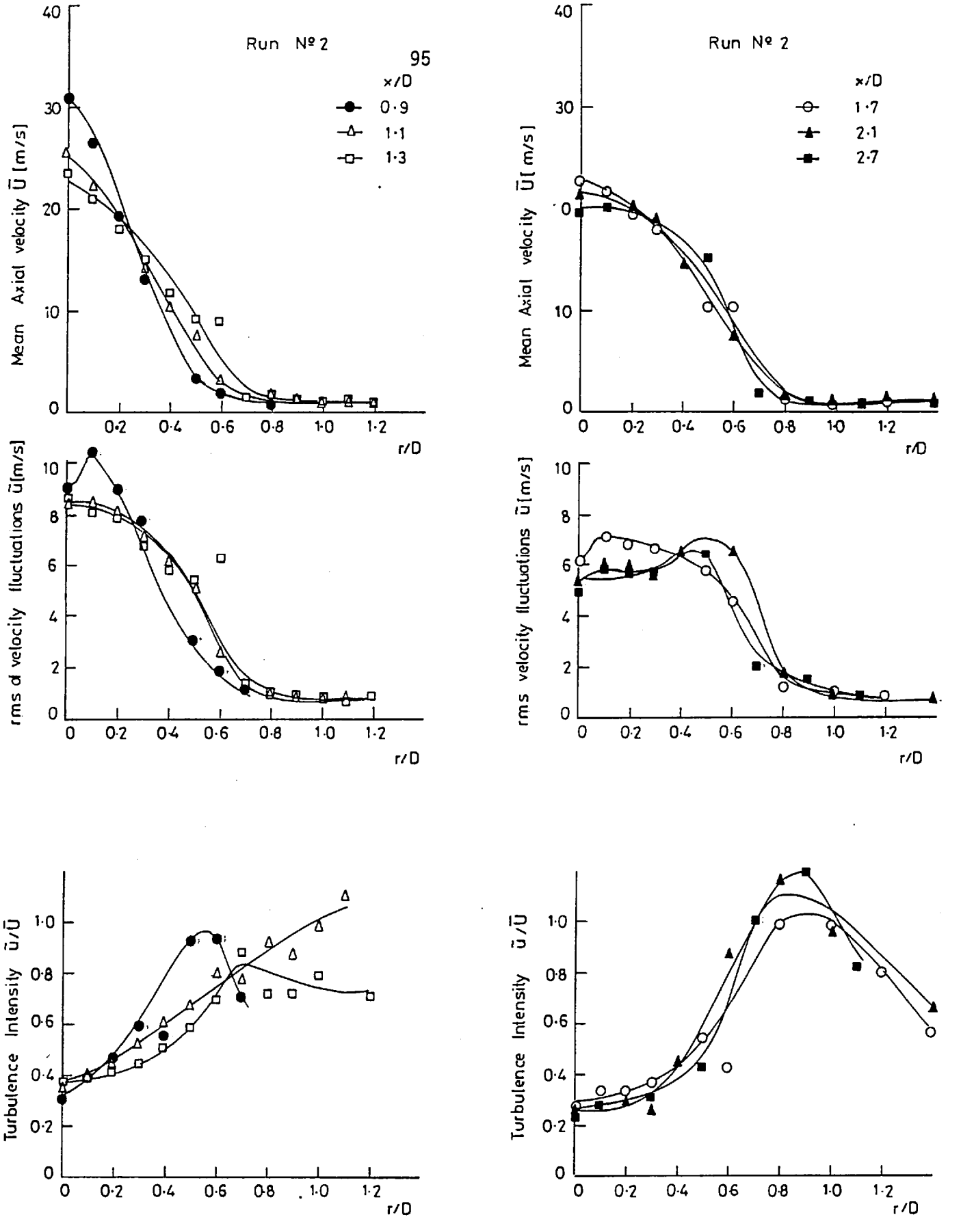

Fig. 2.16 Radial profiles of mean axial velocity, rms of fluctuations and turbulence intensity - run 2

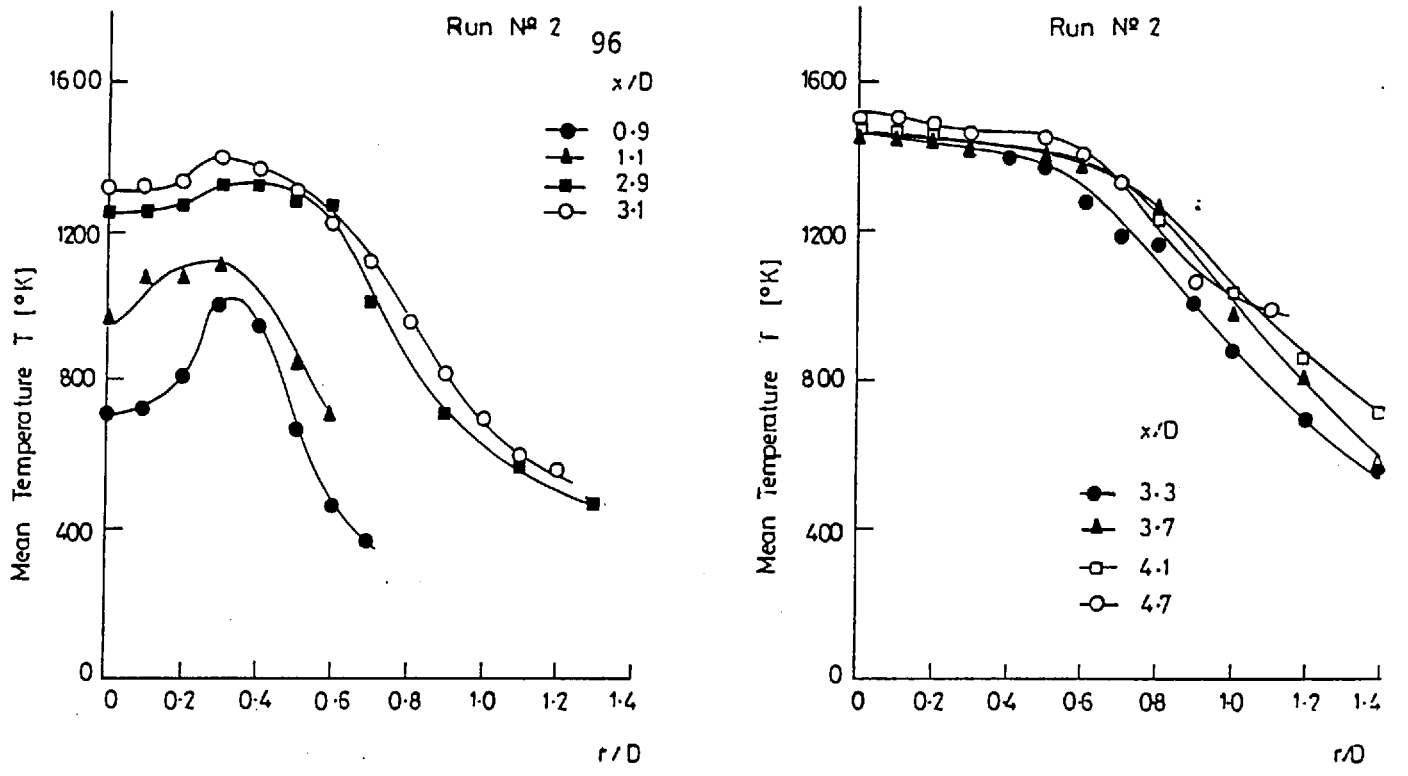

Fig. 2.18 Radial profiles of mean gas temperature - run 2

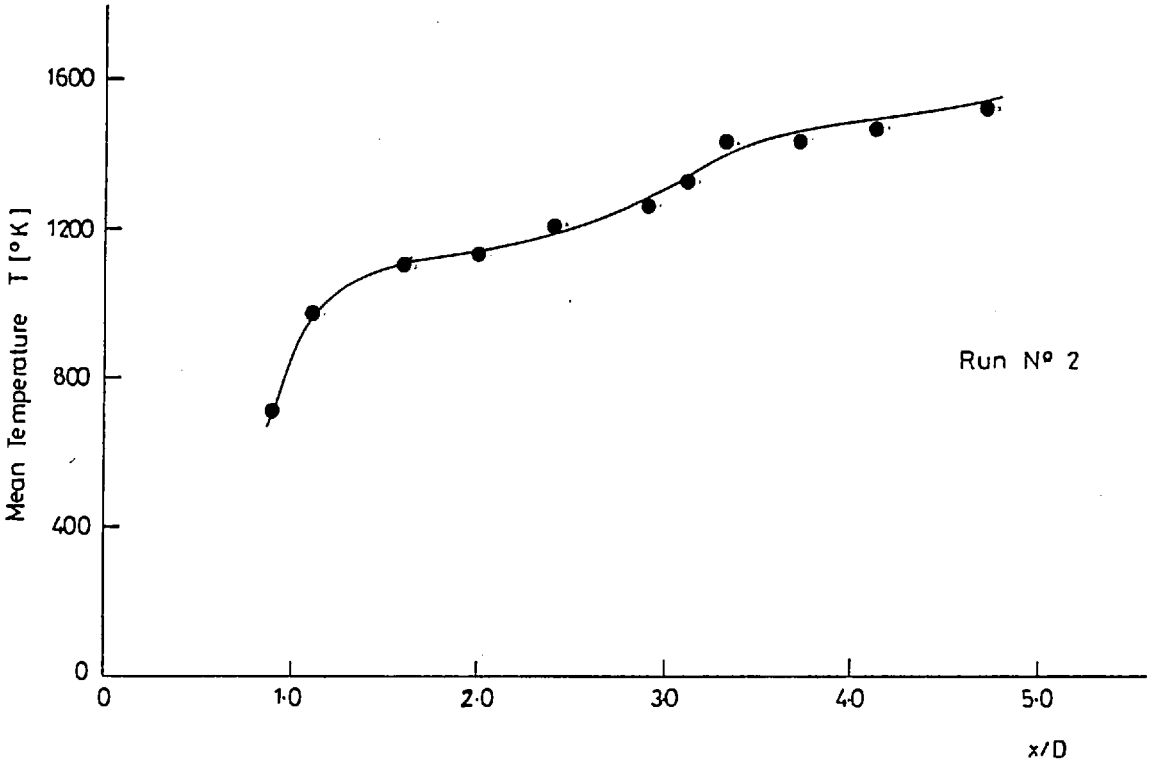

Fig. 2.17 Centreline mean gas temperature distribution - run 2

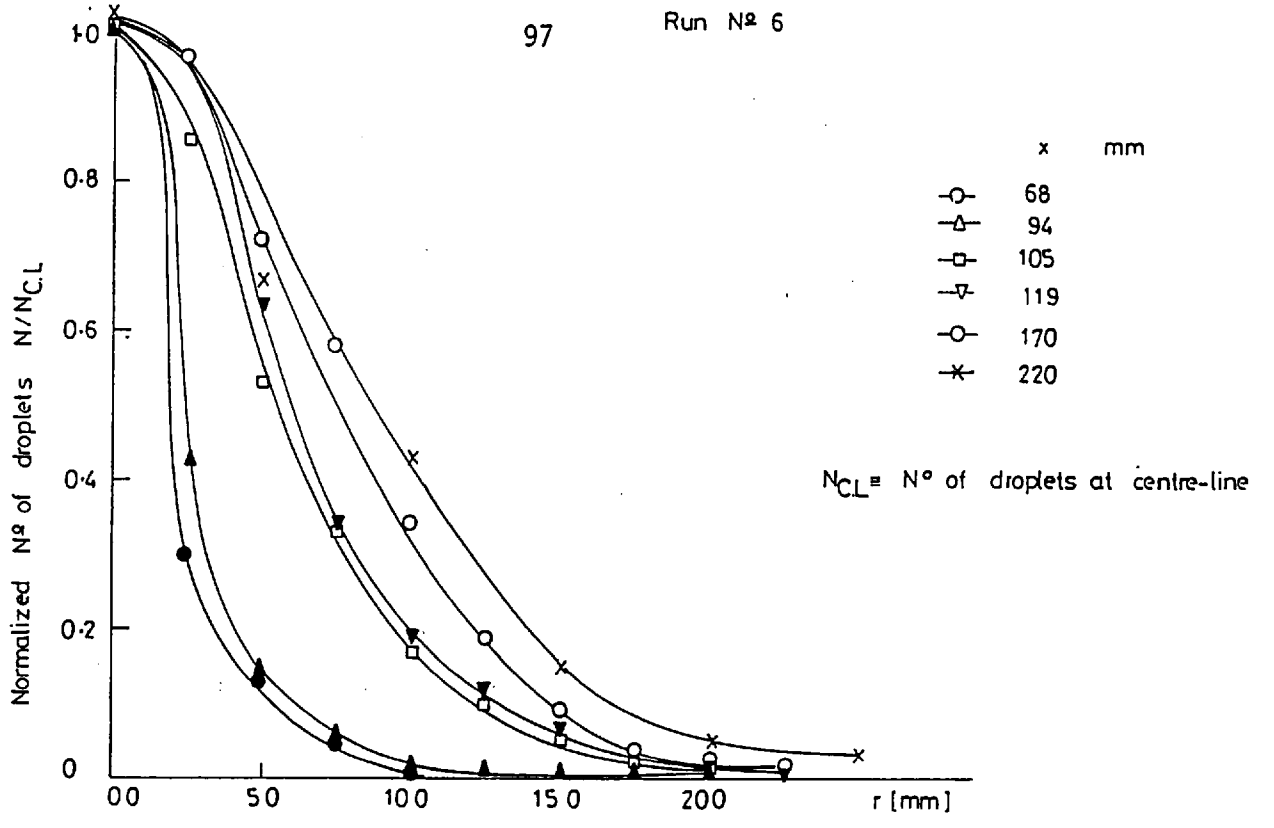

Fig. 2.20 Radial profiles of normalized number of droplets - run 6

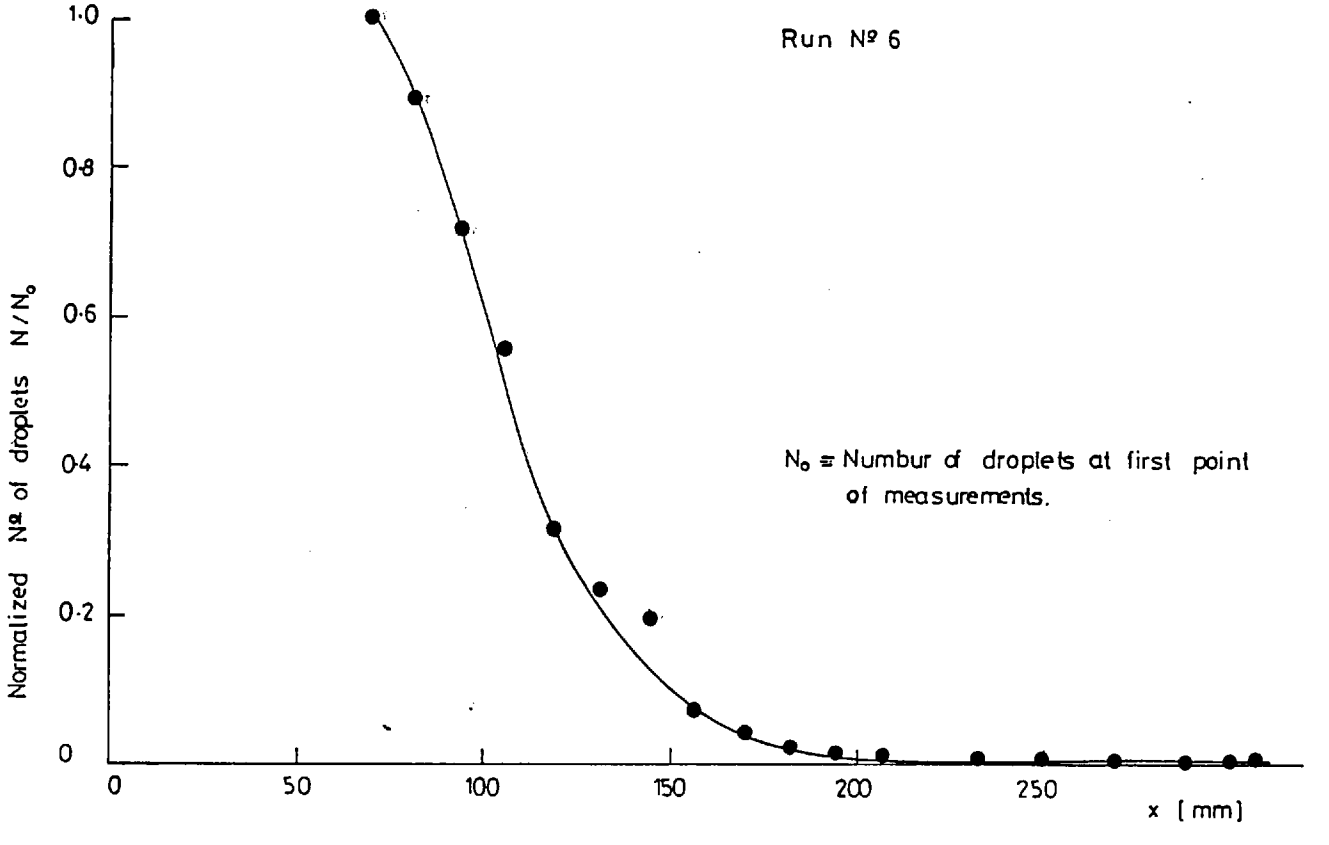

Fig. 2.19 Centreline distribution of the normalized number of droplets - run 6

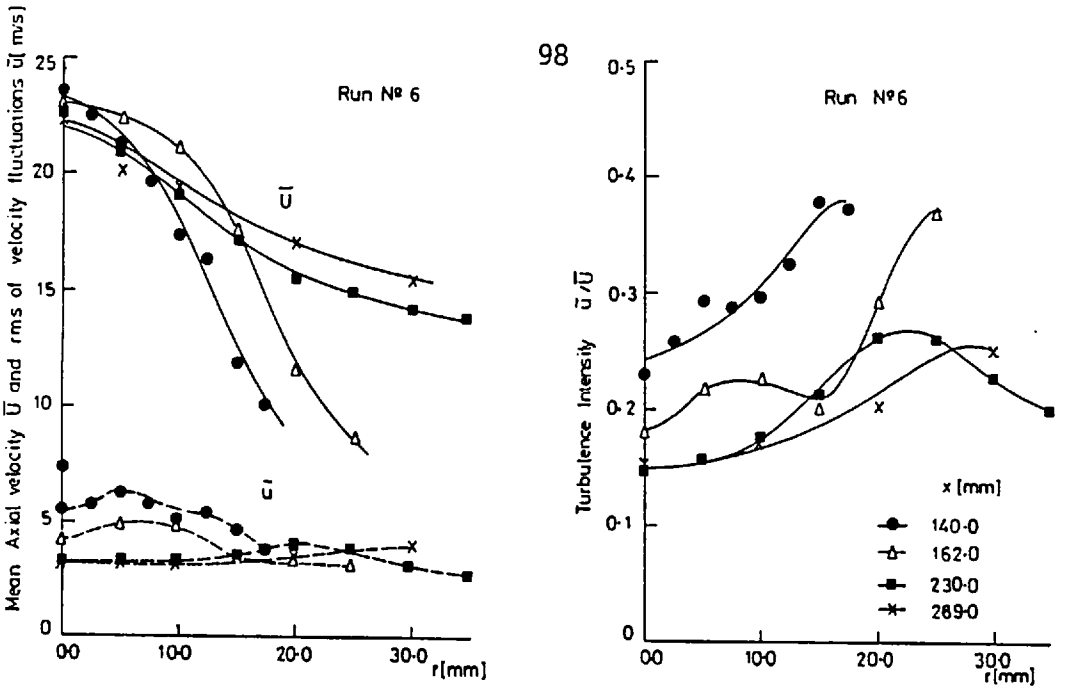

Fig. 2.22 Radial profiles of mean axial velocity, rms of fluctuations and turbulence intensity - run 6

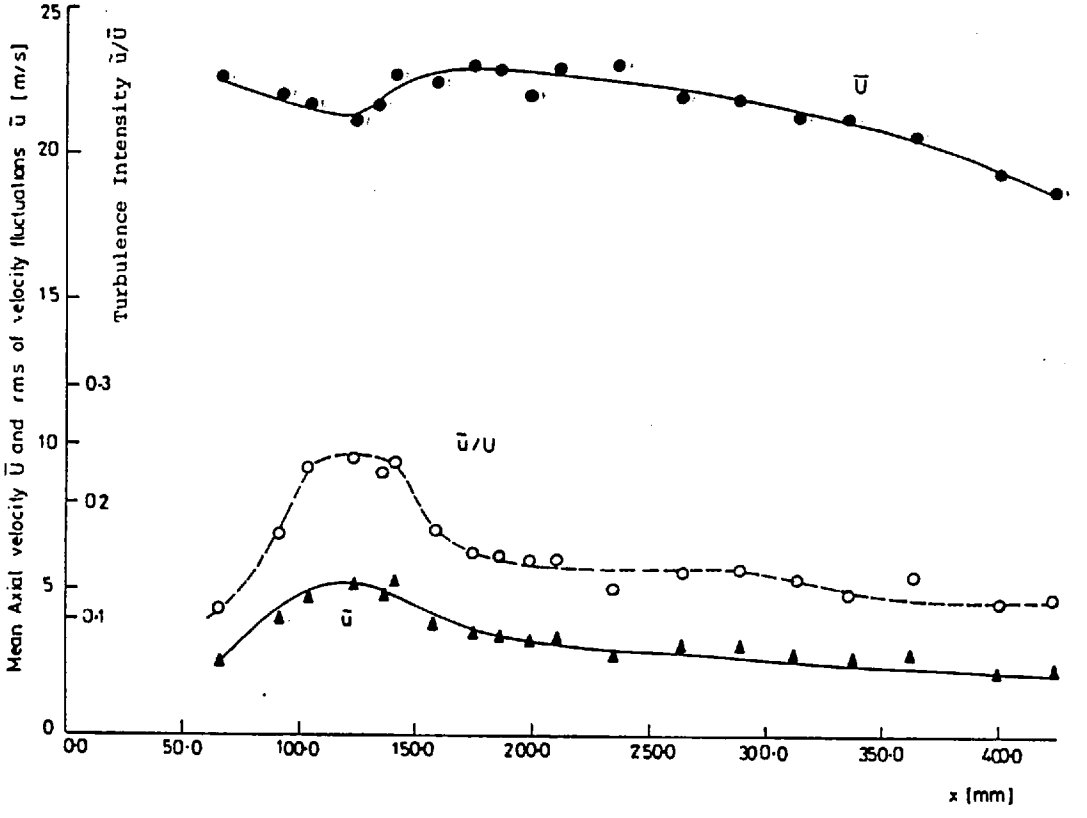

Fig. 2.21 Centreline distributions of mean axial velocity, rms of fluctuations and turbulence intensity - run 6

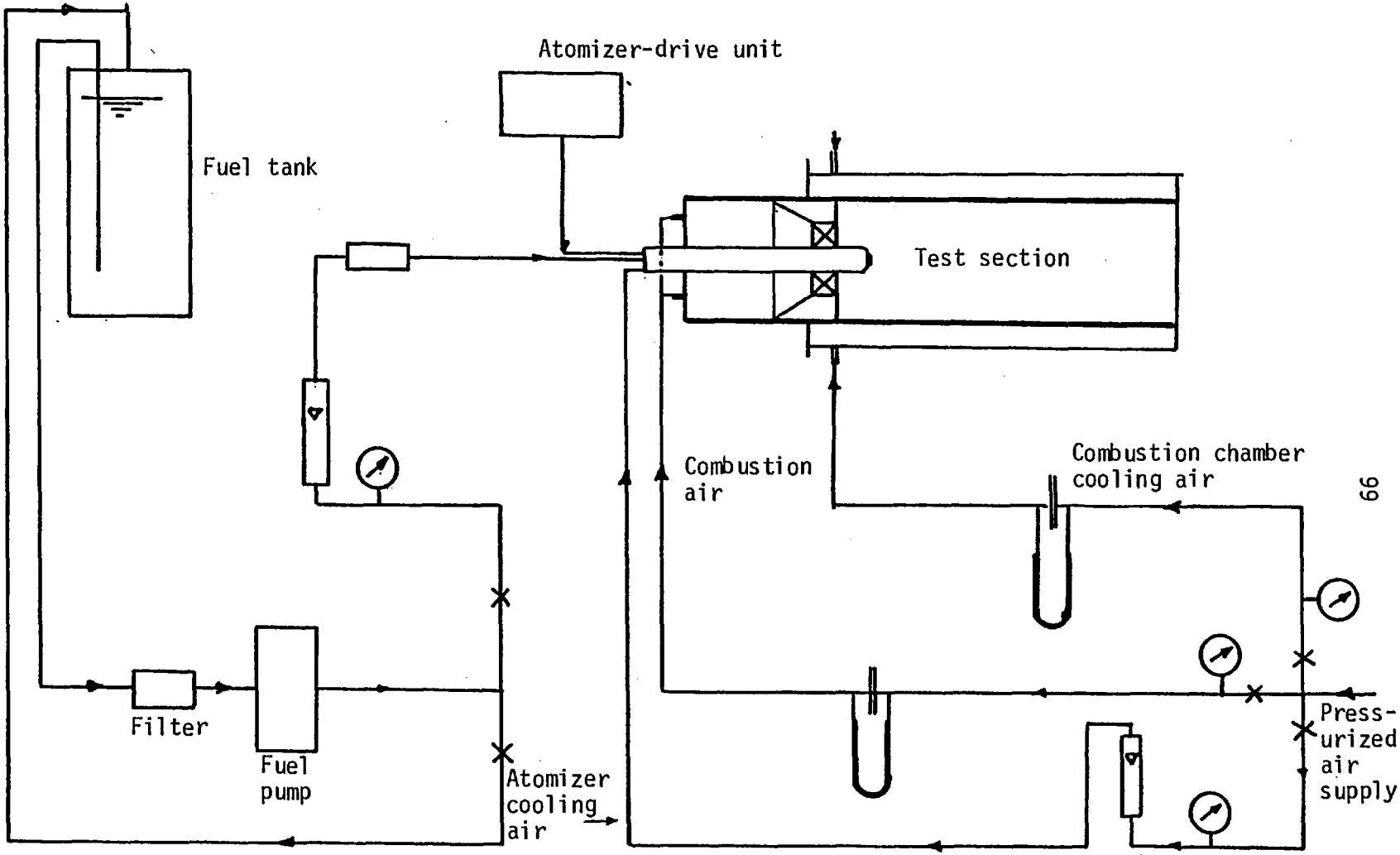

Fig. 2.23 Experimental set-up for confined flame experiments

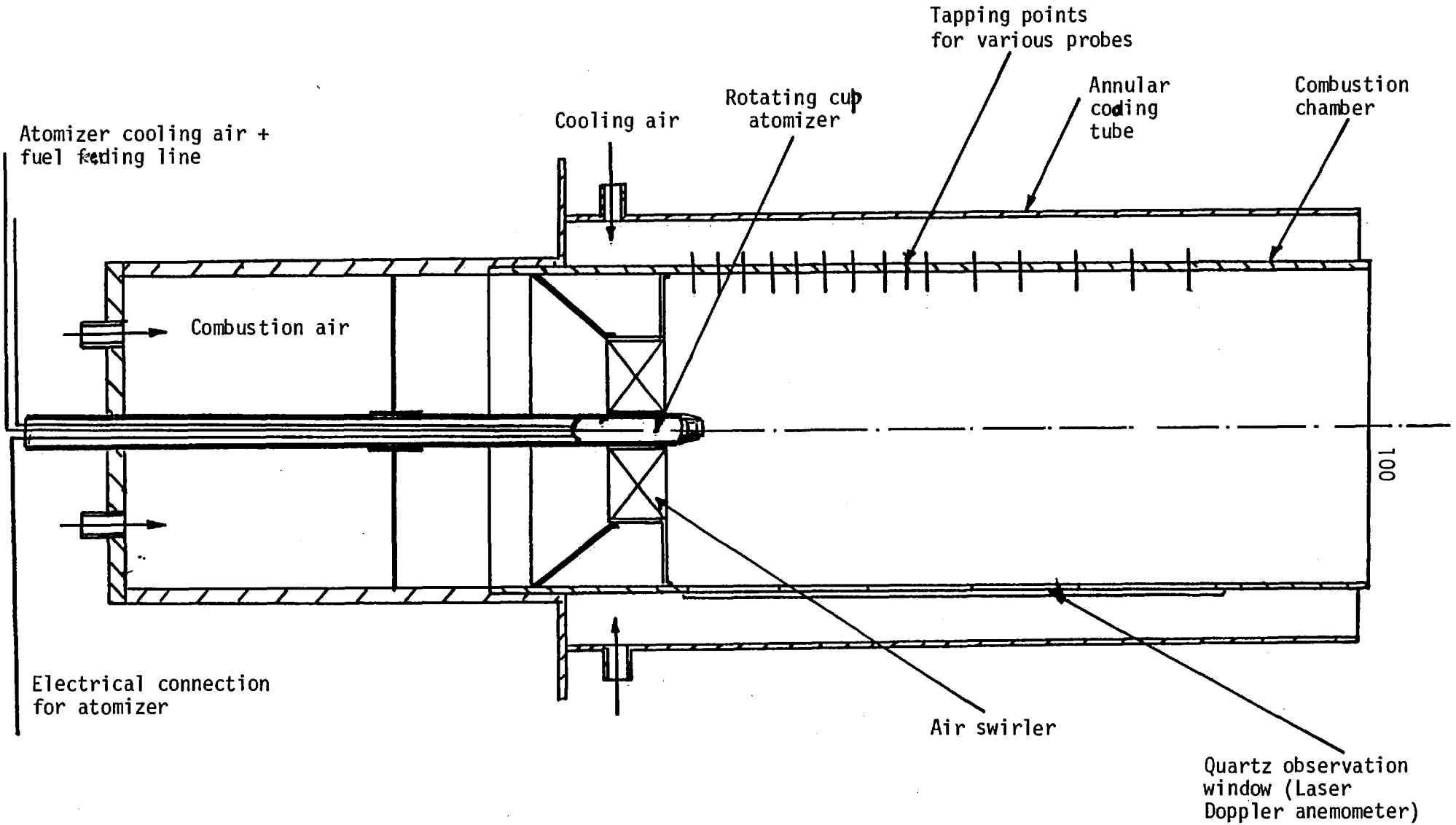

Fig. 2.24 Details of the test section, confined flames

Diameter of test section
D = 157 mm

Swirler outer diameter
D_s = 98 mm

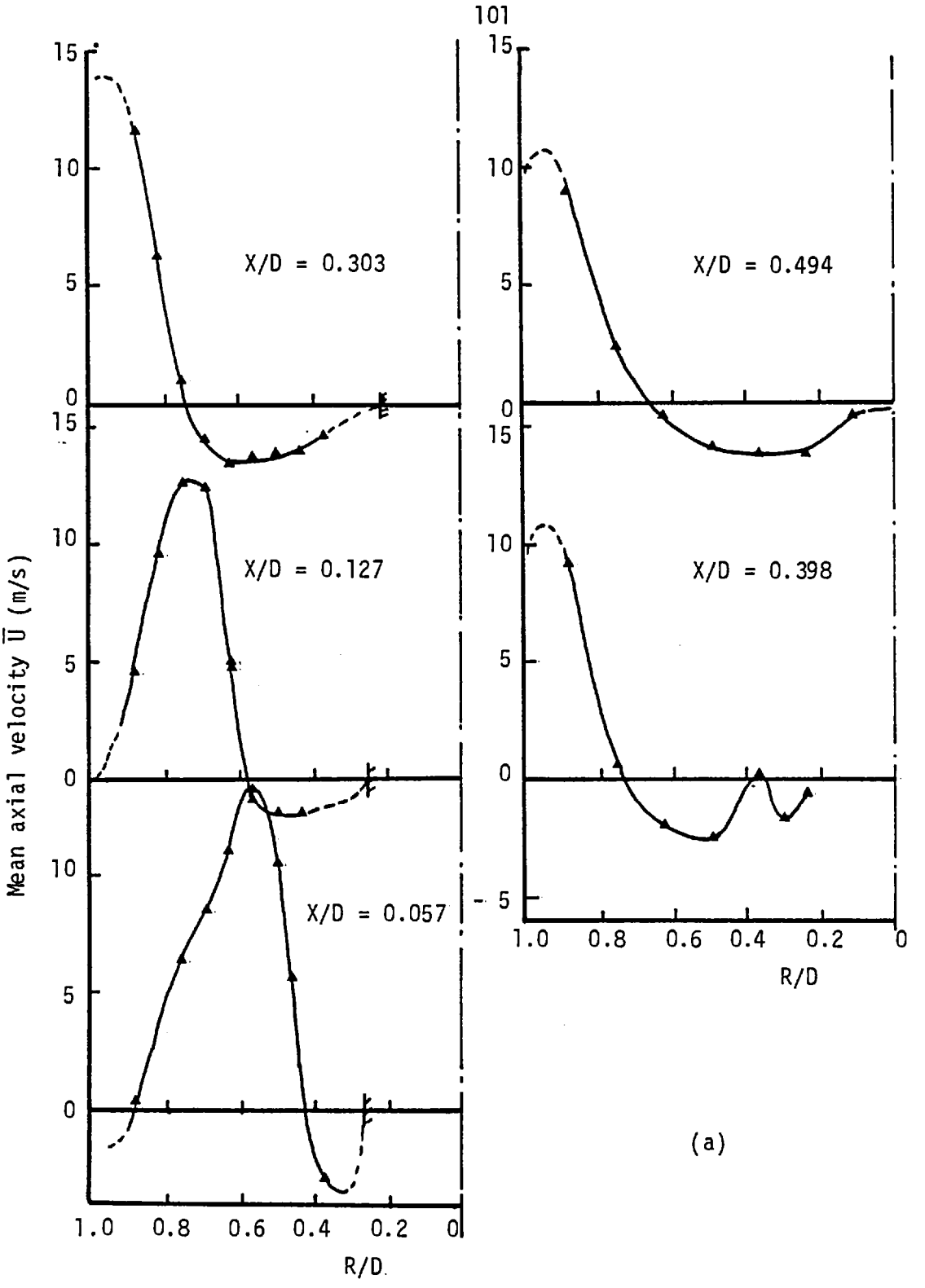

Fig. 2.25 Isothermal radial profiles of mean axial velocity

(a) Run 7

(b) Run 8

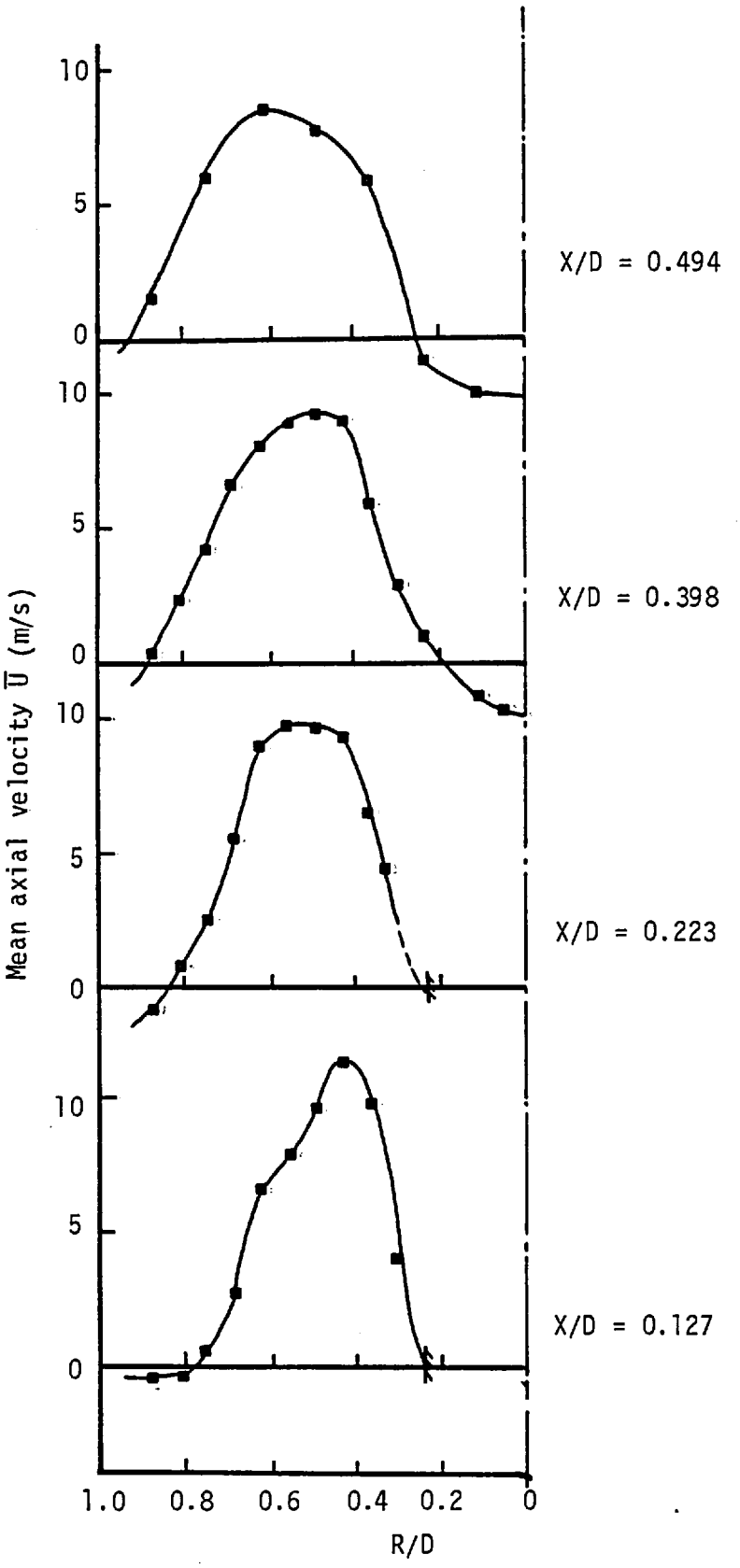

(b)

Fig. 2.25 (Contd.)

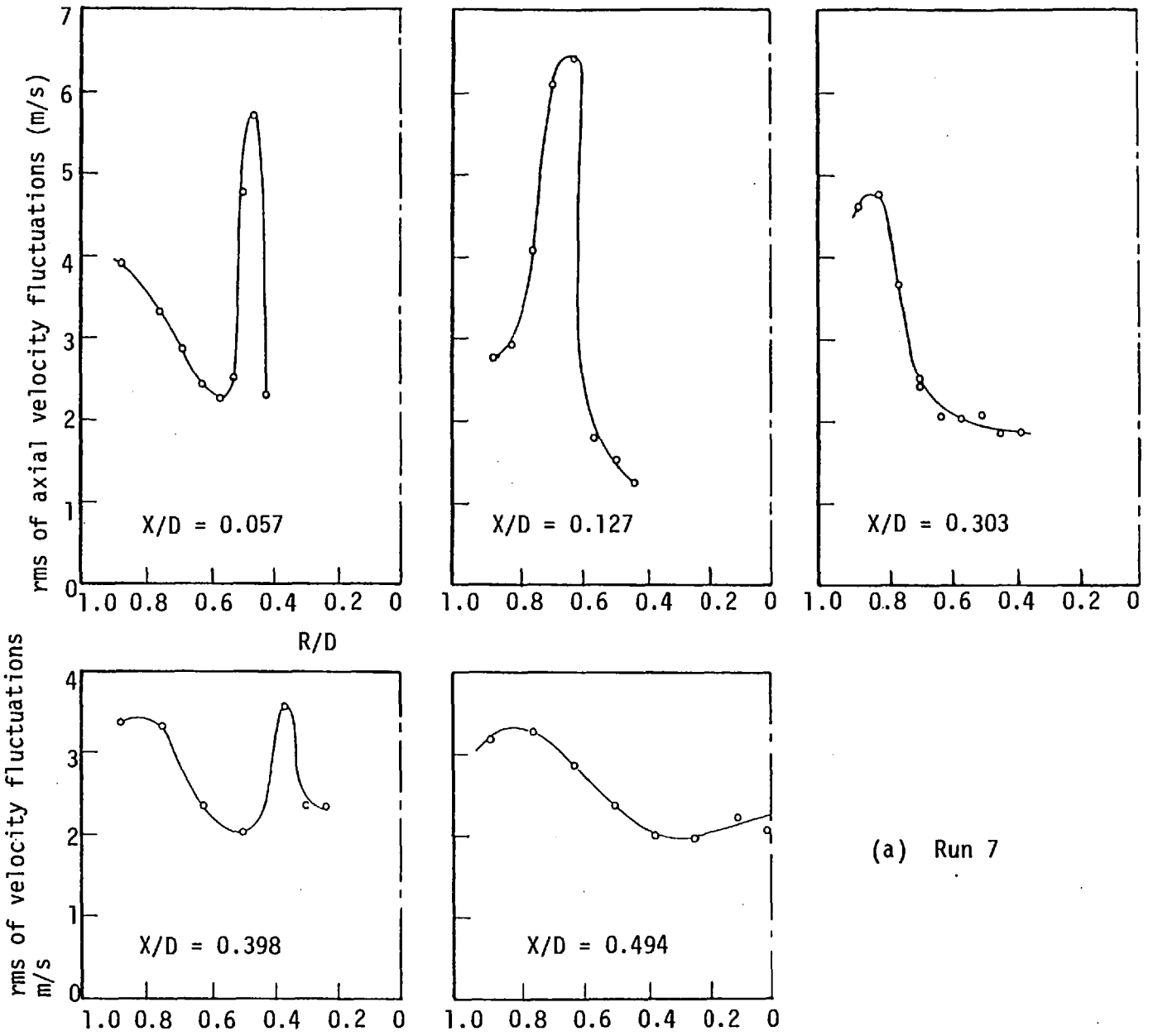

Fig. 2.26 Isothermal radial profiles of the rms of axial velocity fluctuations

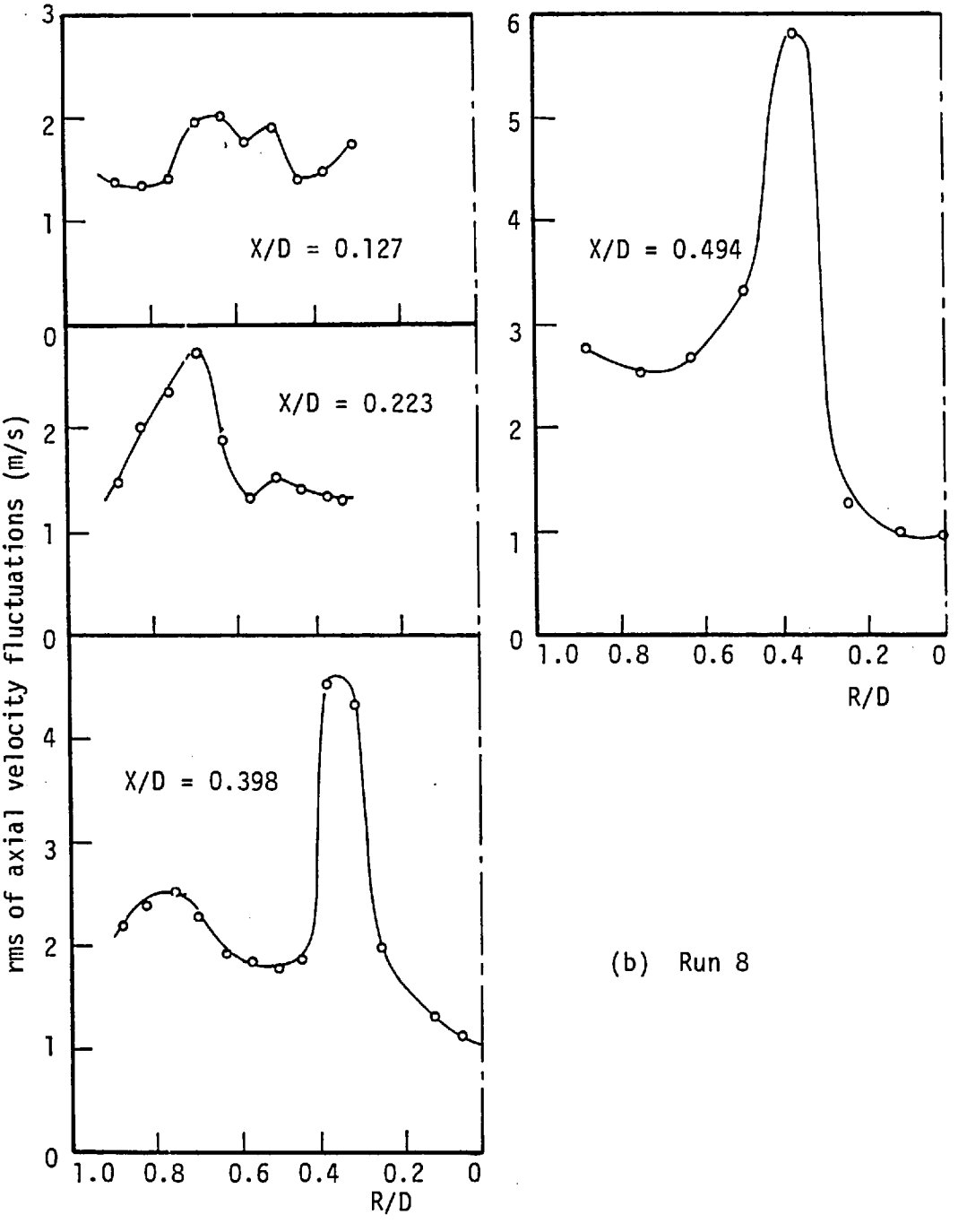

Fig. 2.26 (Continued)

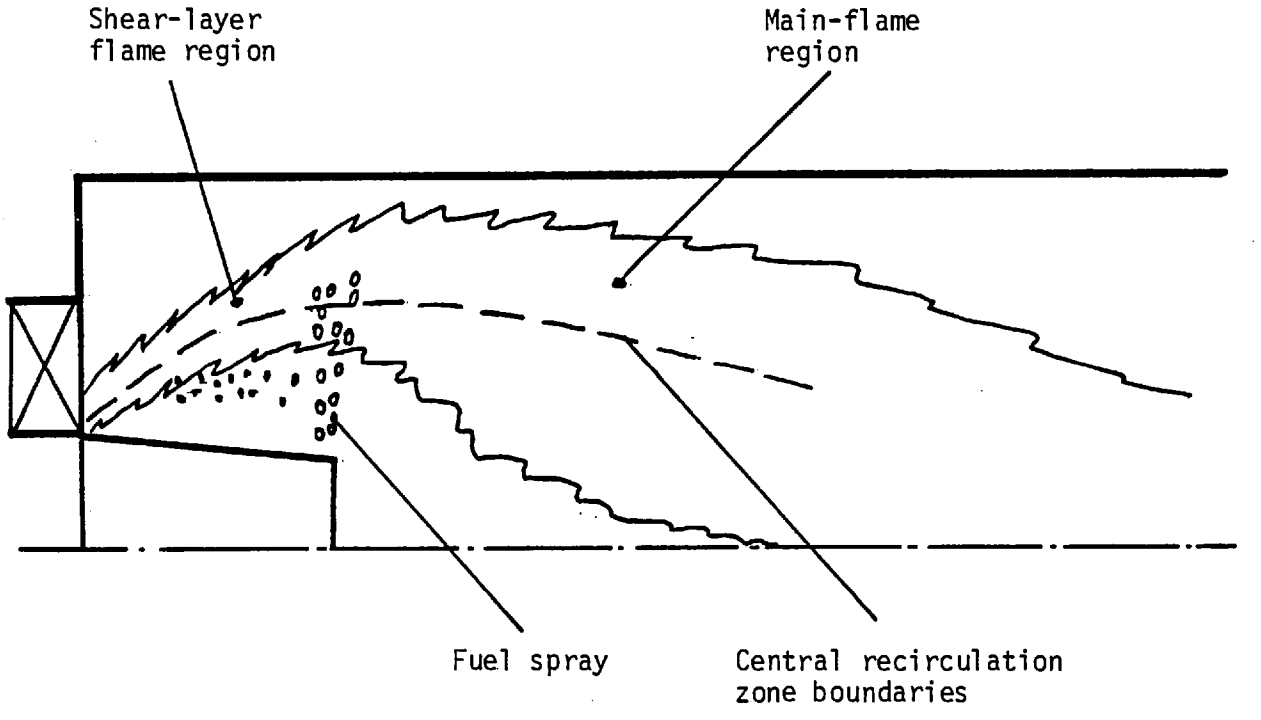

Fig. 2.27 Basic flame structure, runs 1, 2 and 3

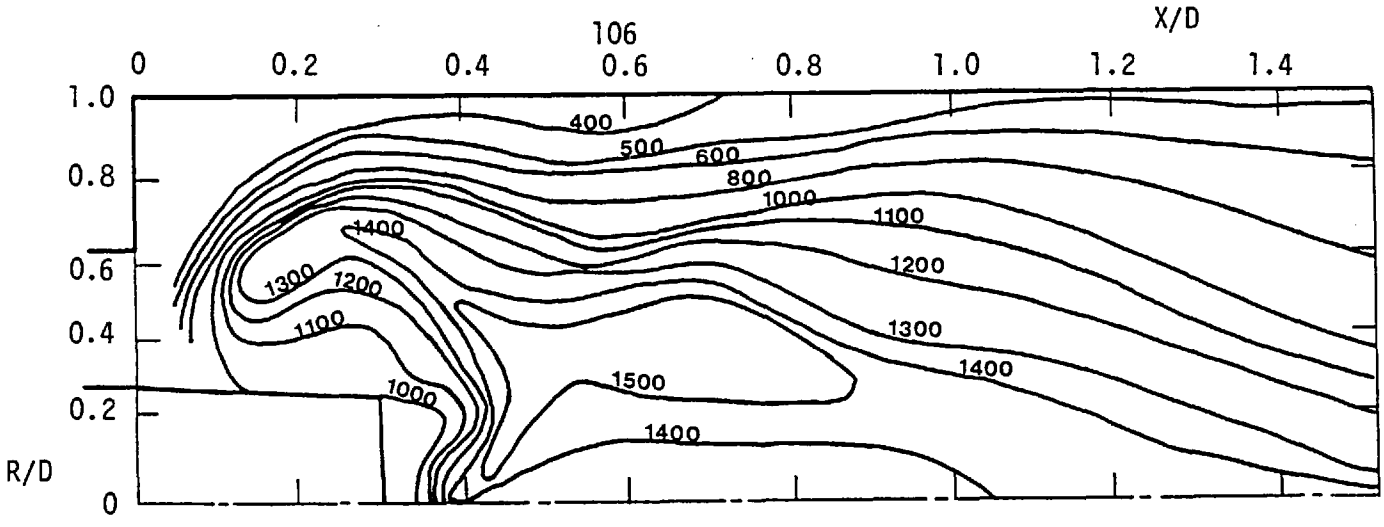

(a) Run 3

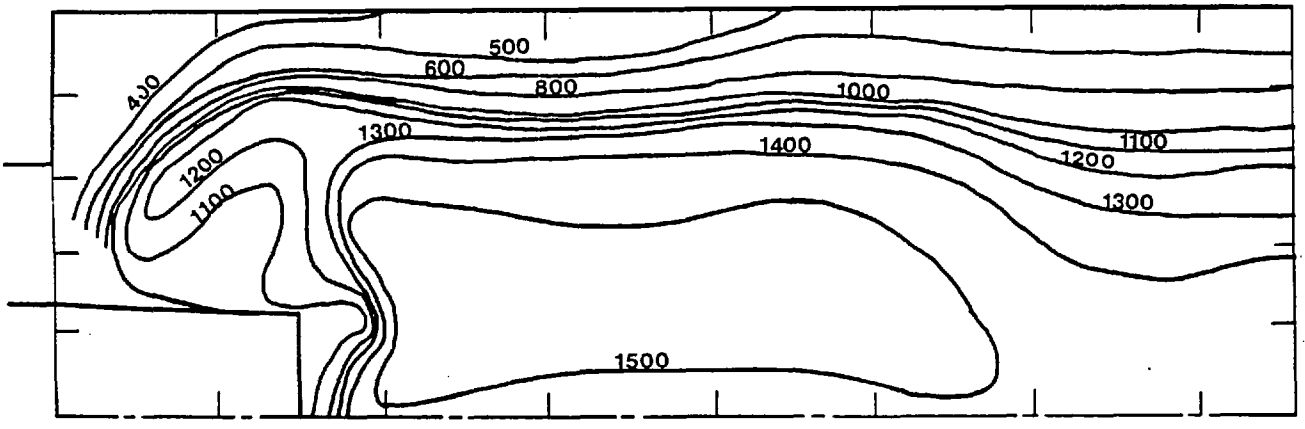

(b) Run 2

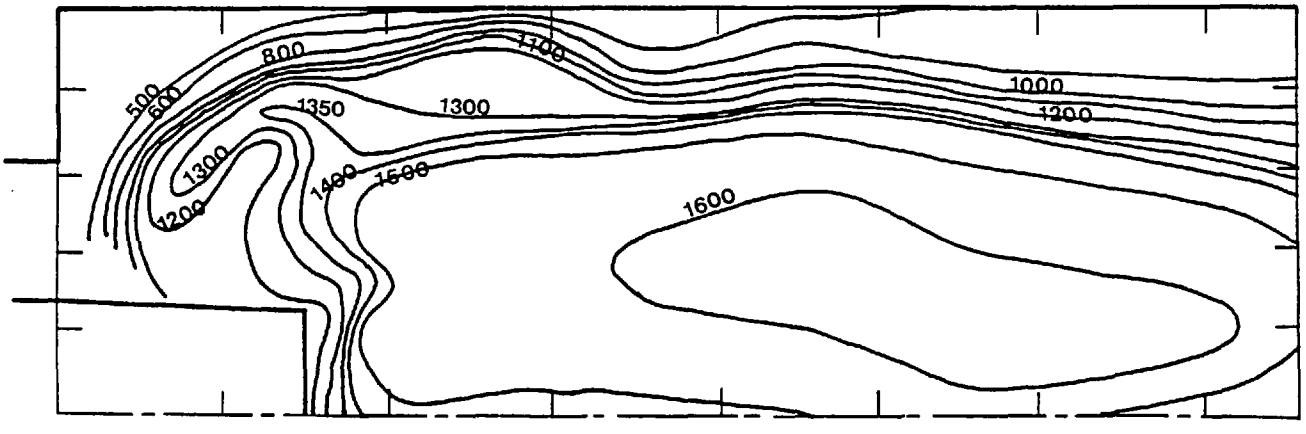

(c) Run 1

Fig. 2.28 Temperature contour maps, runs 1, 2 and 3 (temperature in ^{o}K)

X : Axial distance
R : Radial distance
D : Combustor diameter (157 mm)

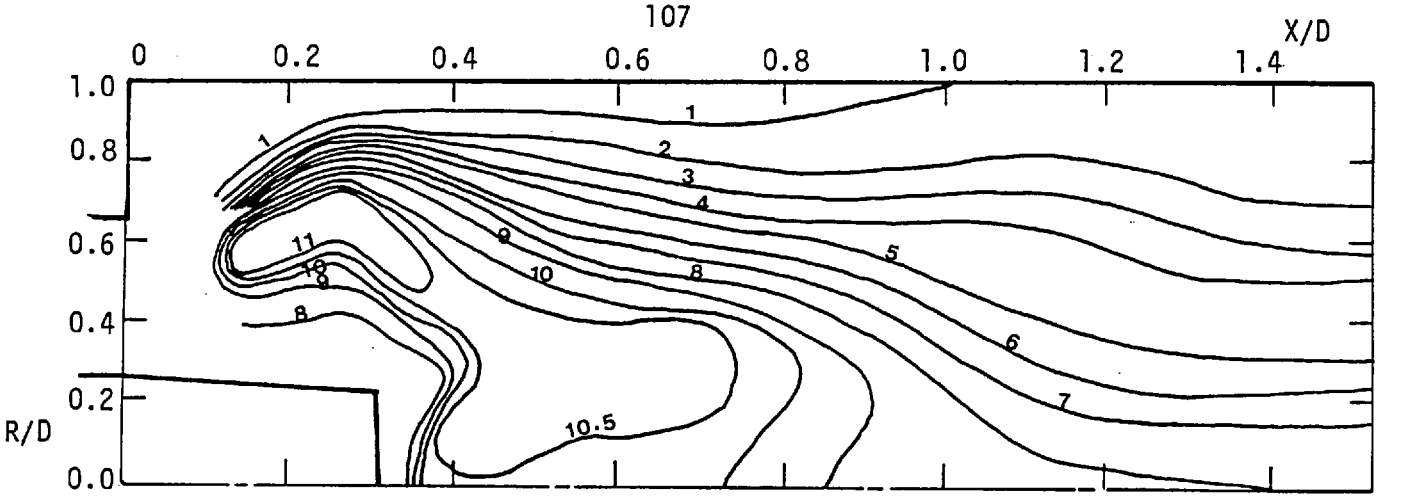

(a) Run 3

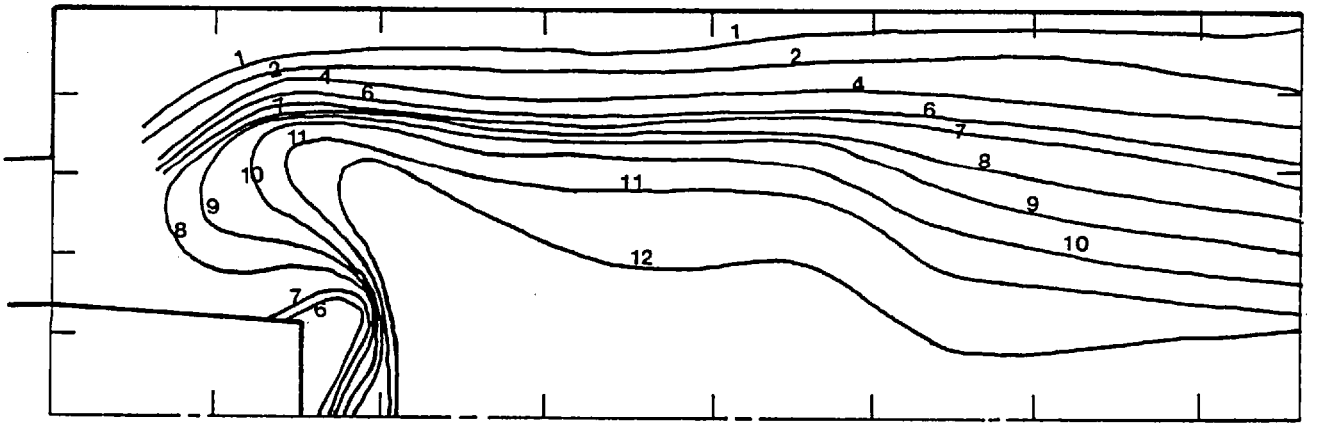

(b) Run 2

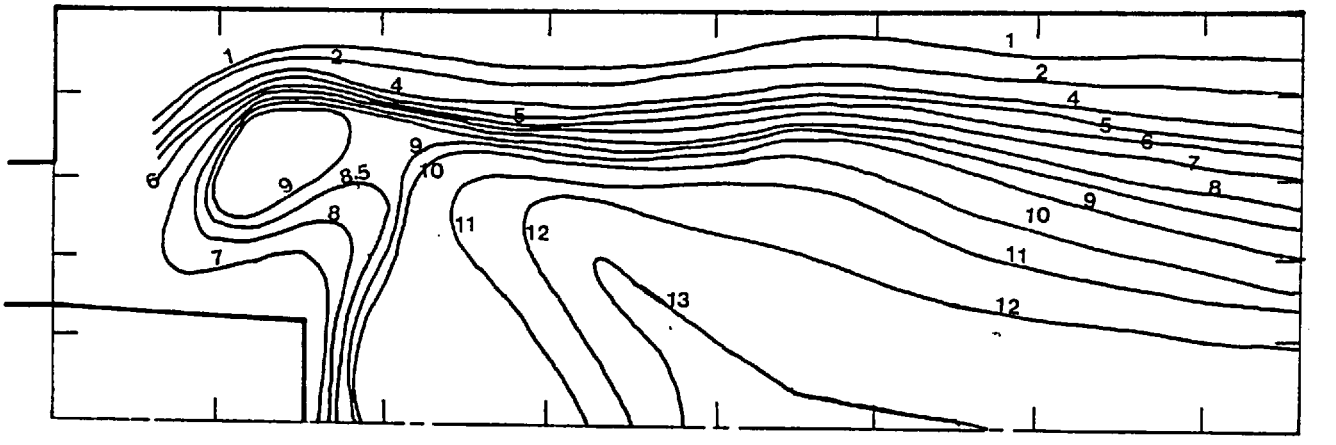

(c) Run 1

Fig. 2.29 Contour maps of the percentage CO_2 volume concentration - runs 1, 2 and 3

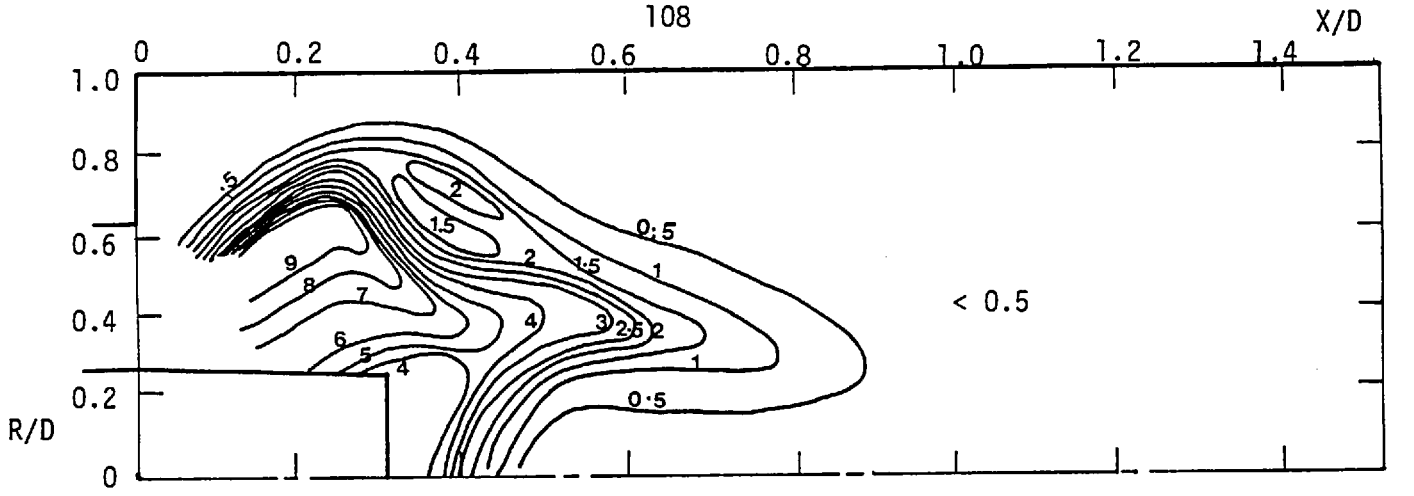

(a) Run 3

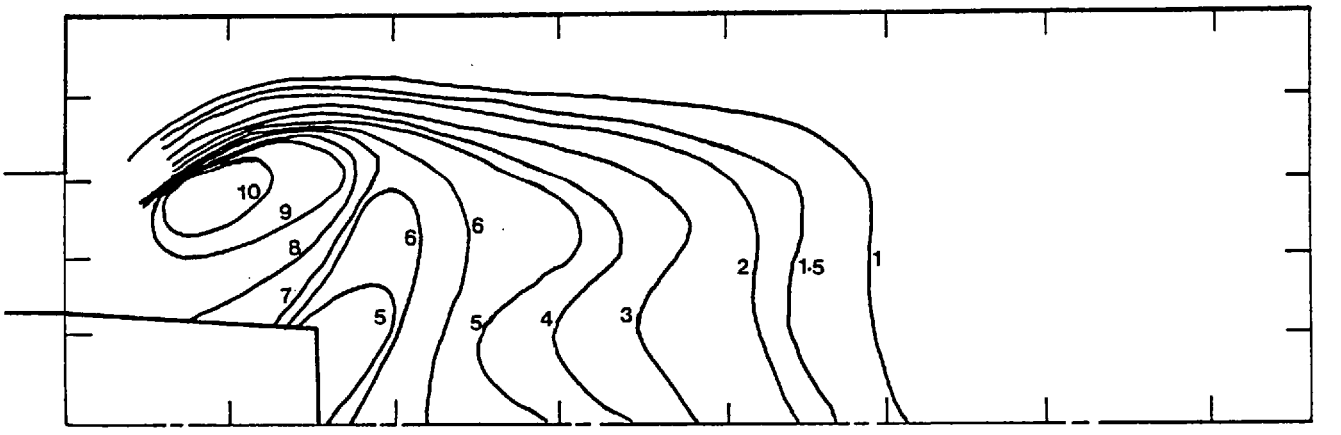

(b) Run 2

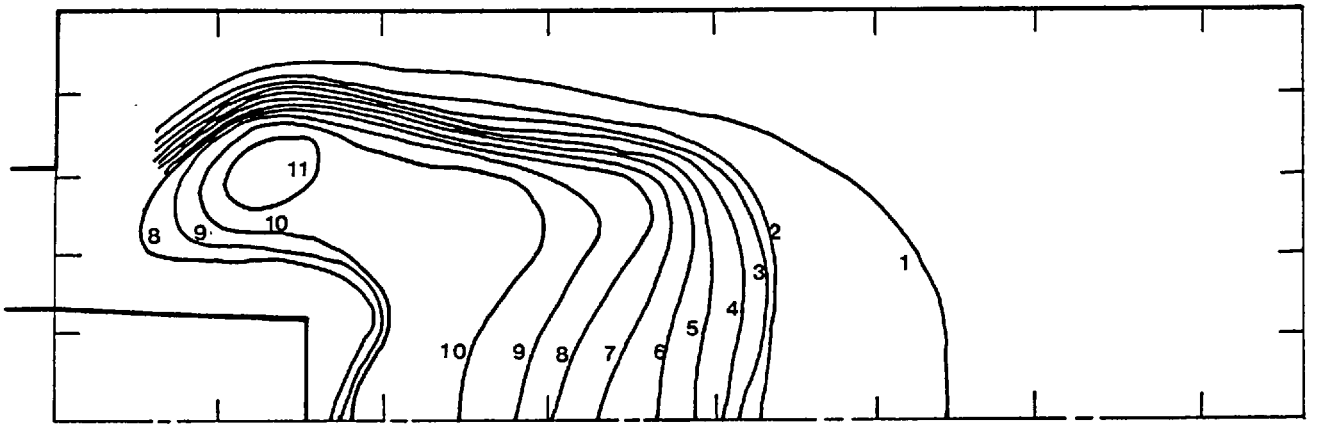

(c) Run 1

Fig. 2.30 Contour maps of the percentage CO volume concentration - runs 1, 2 and 3

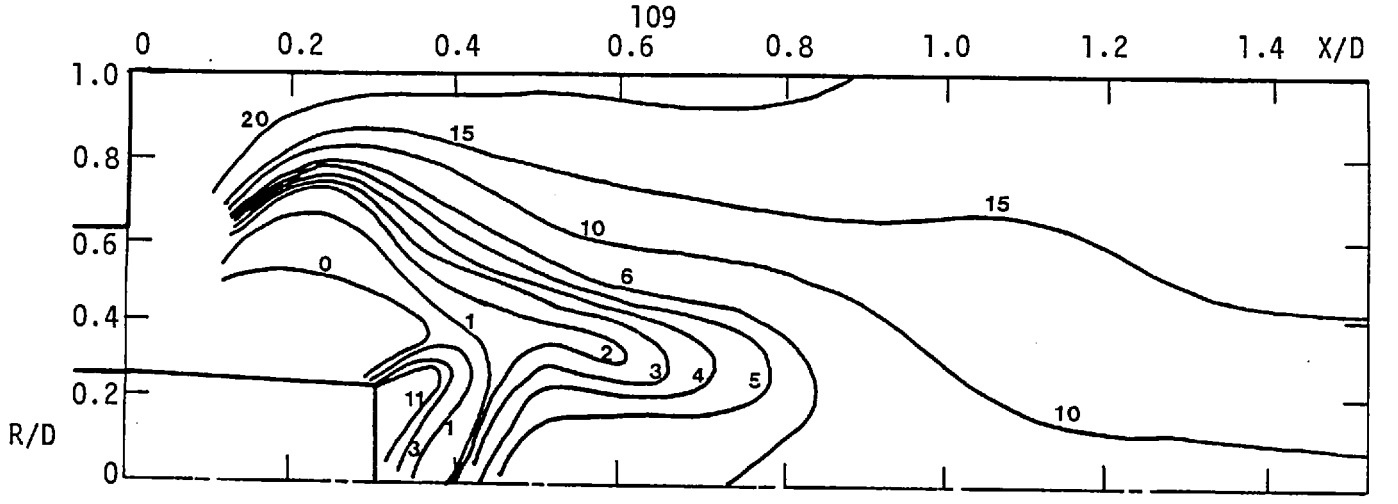

(a) Run 3

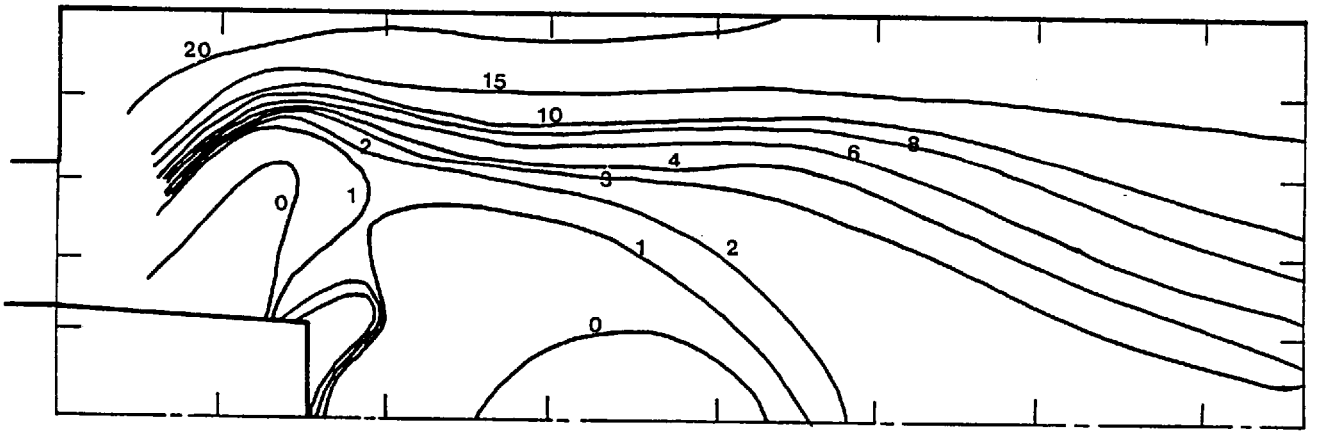

(b) Run 2

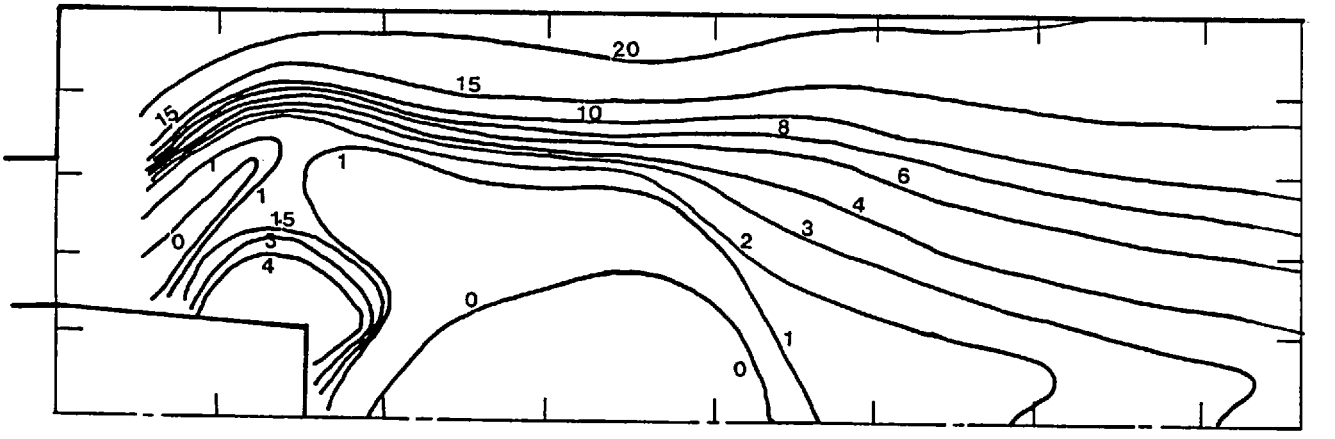

(c) Run 1

Fig. 2.31 Contour maps of the percentage O_2 volume concentration - runs 1, 2 and 3

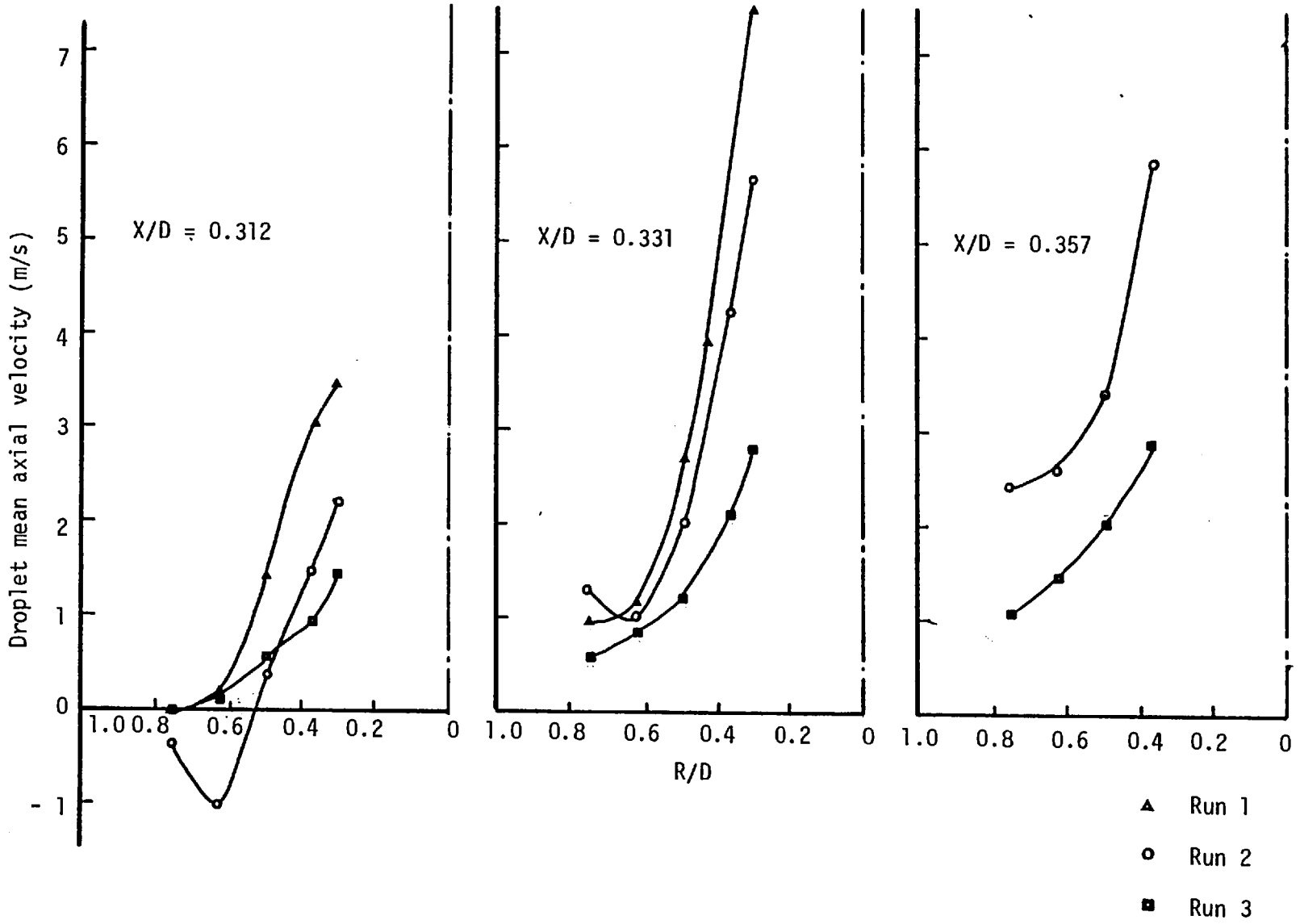

Fig. 2.32 (a) Radial profiles of droplet mean axial velocity - runs 1, 2 and 3

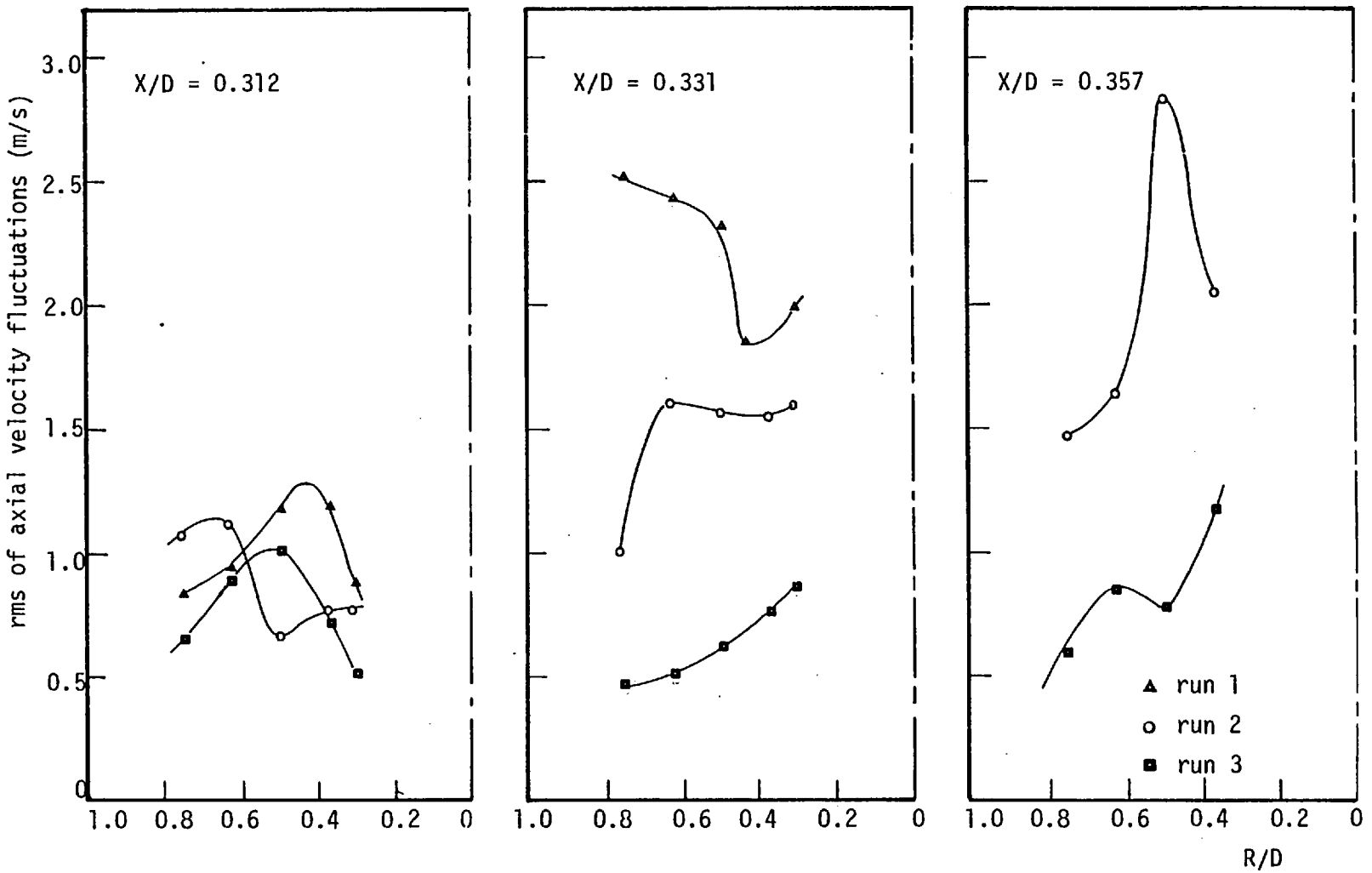

Fig. 2.32 (b) Radial profiles of the rms of droplet axial velocity - runs 1, 2 and 3

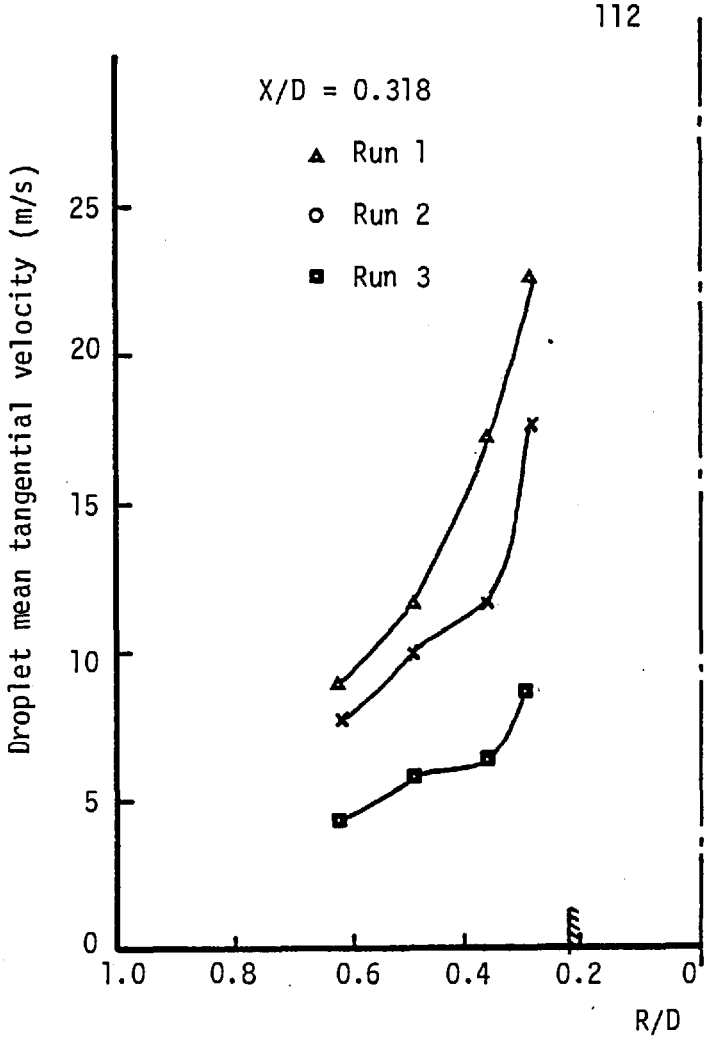

Fig. 2.33 Radial profiles of droplet mean tangential velocity - runs 1, 2 and 3

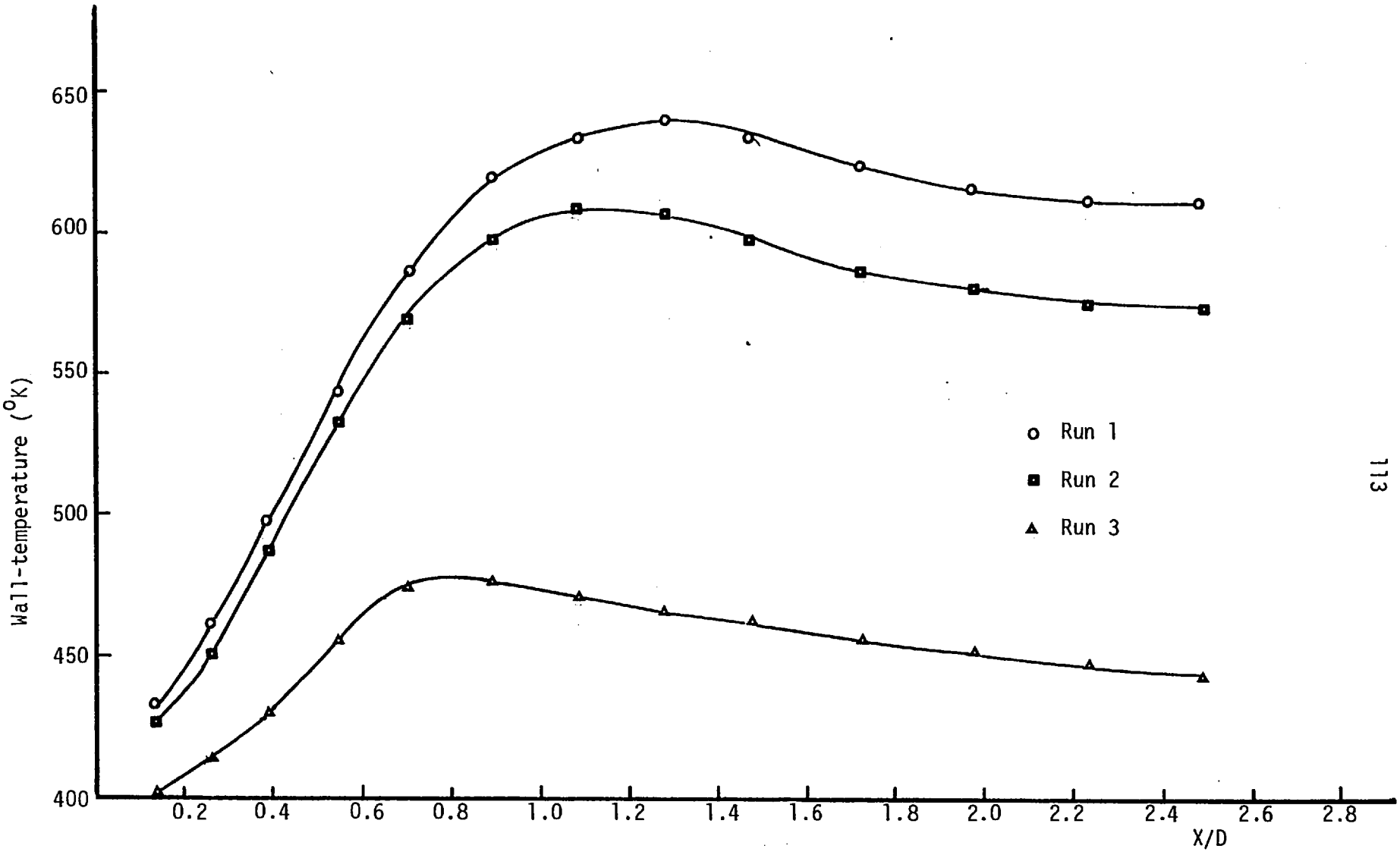

Fig. 2.34 Wall-temperature distributions - runs 1, 2 and 3

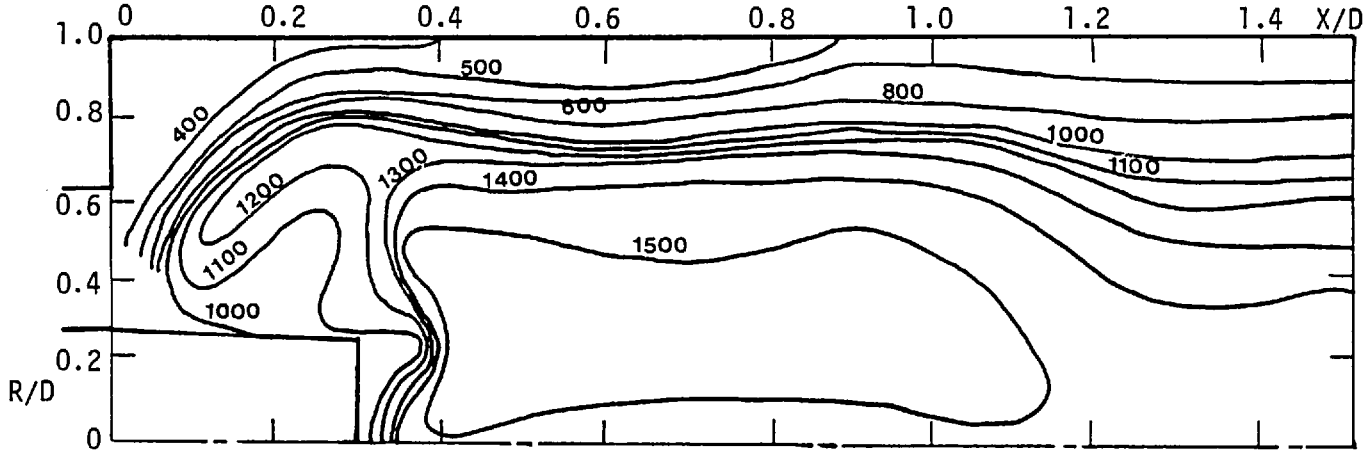

(a) Run 2

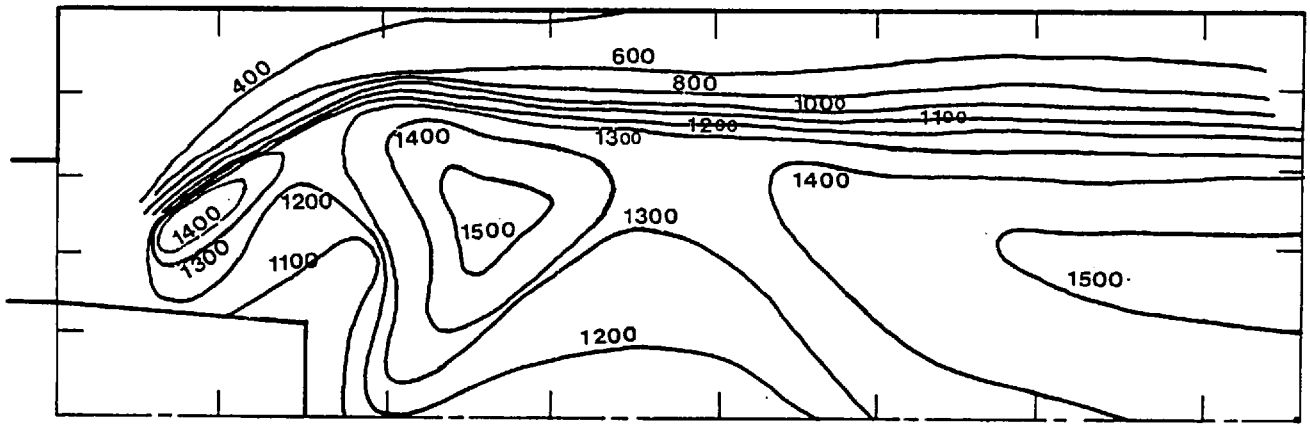

(b) Run 4

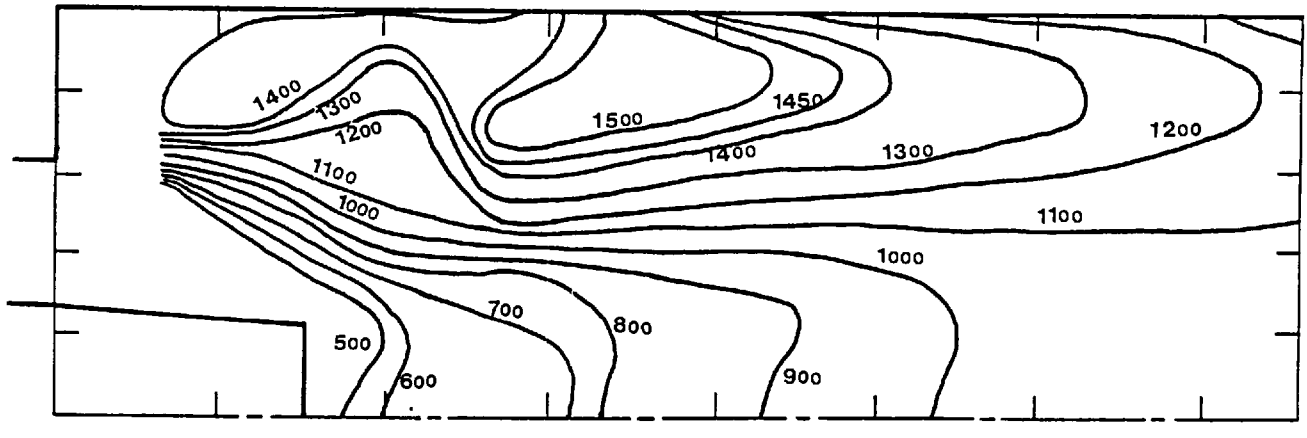

(c) Run 5

Fig. 2.35 Temperature contour maps - runs 2, 4 and 5 (temperature in ^{o}K)

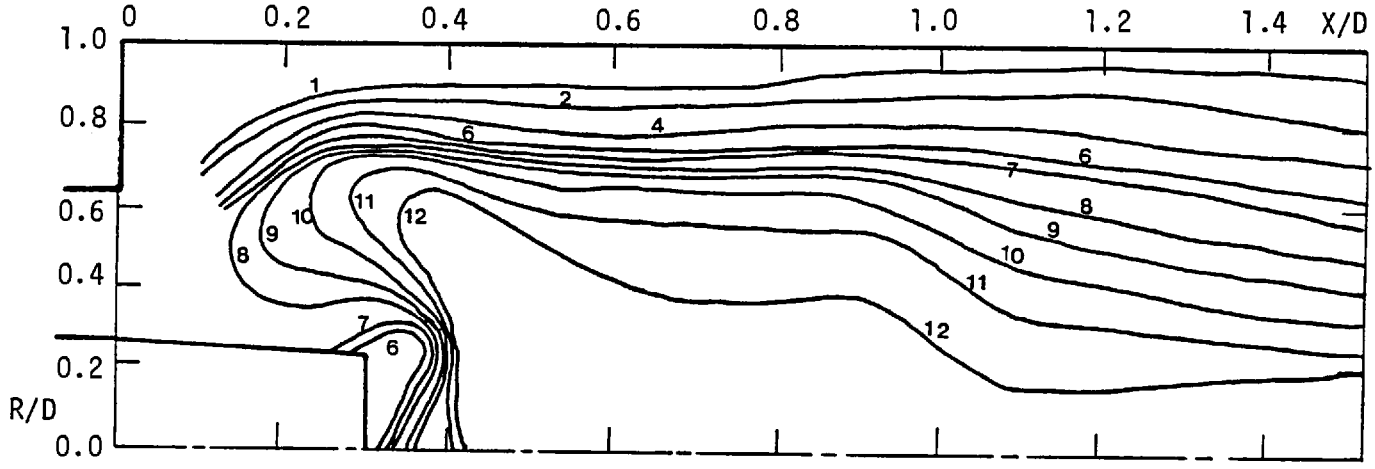

(a) Run 2

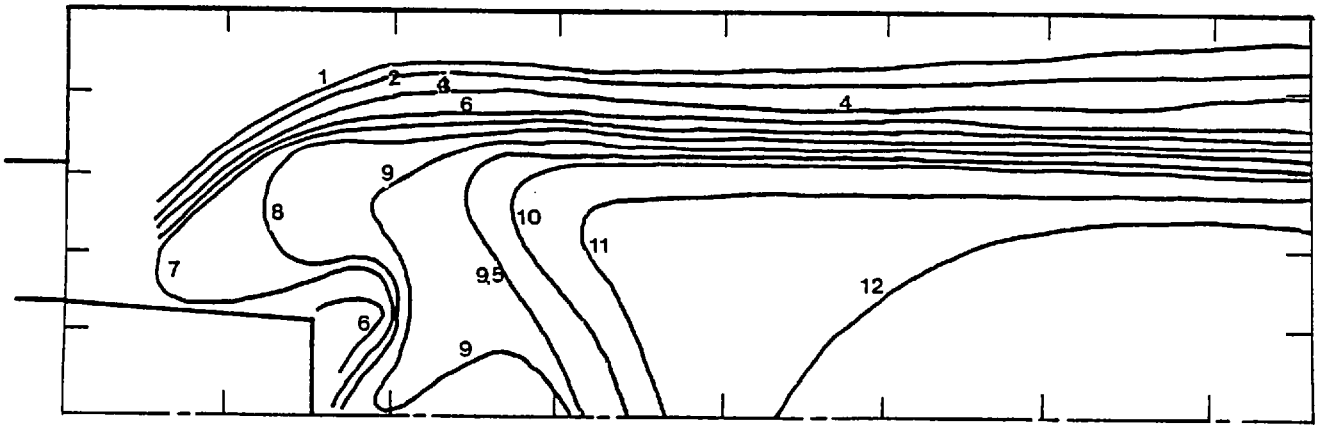

(b) Run 4

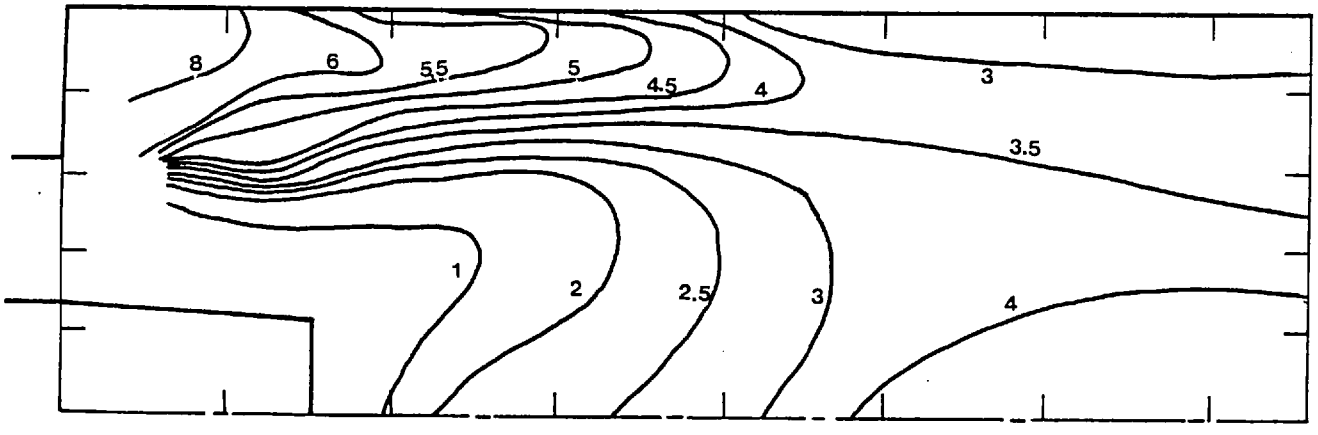

(c) Run 5

Fig. 2.36 Contour maps of the percentage CO_2 volume concentration - runs 2, 4 and 5

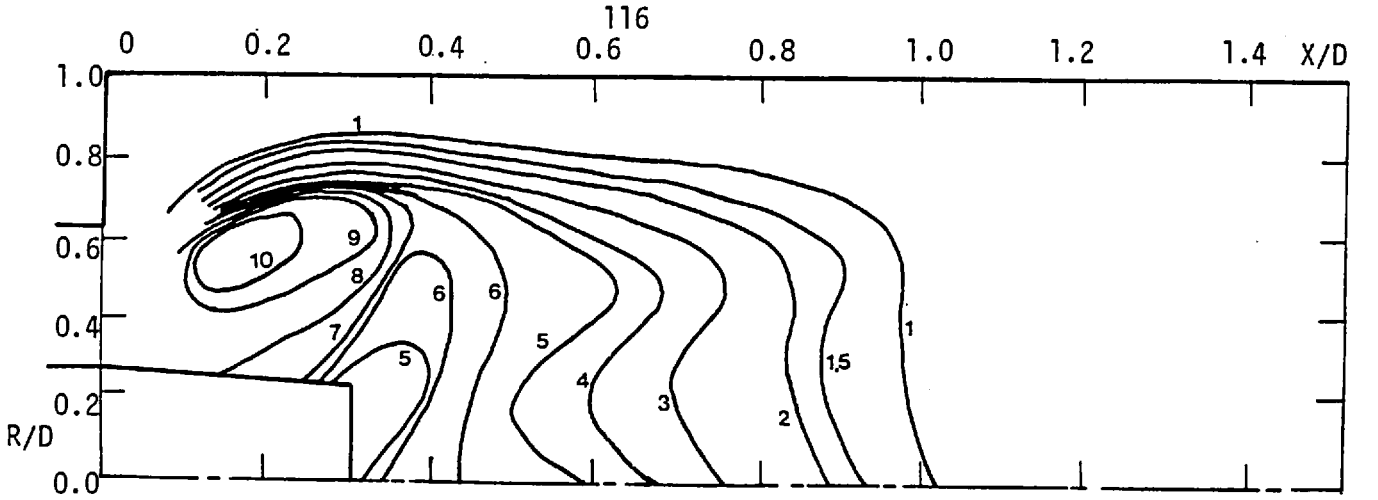

(a) Run 2

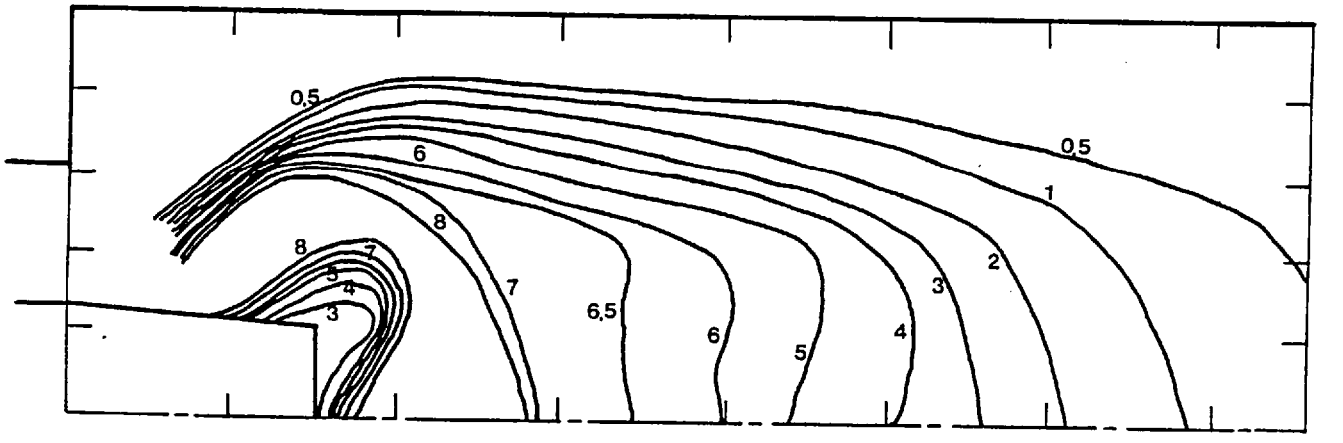

(b) Run 4

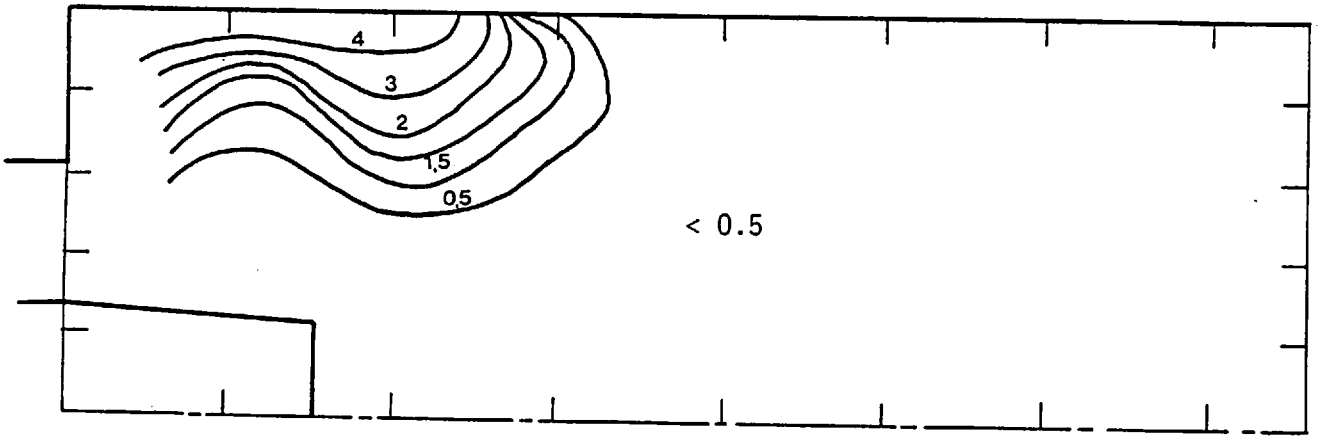

(c) Run 5

Fig. 2.37 Contour maps of the percentage CO volume concentration - runs 2, 4 and 5

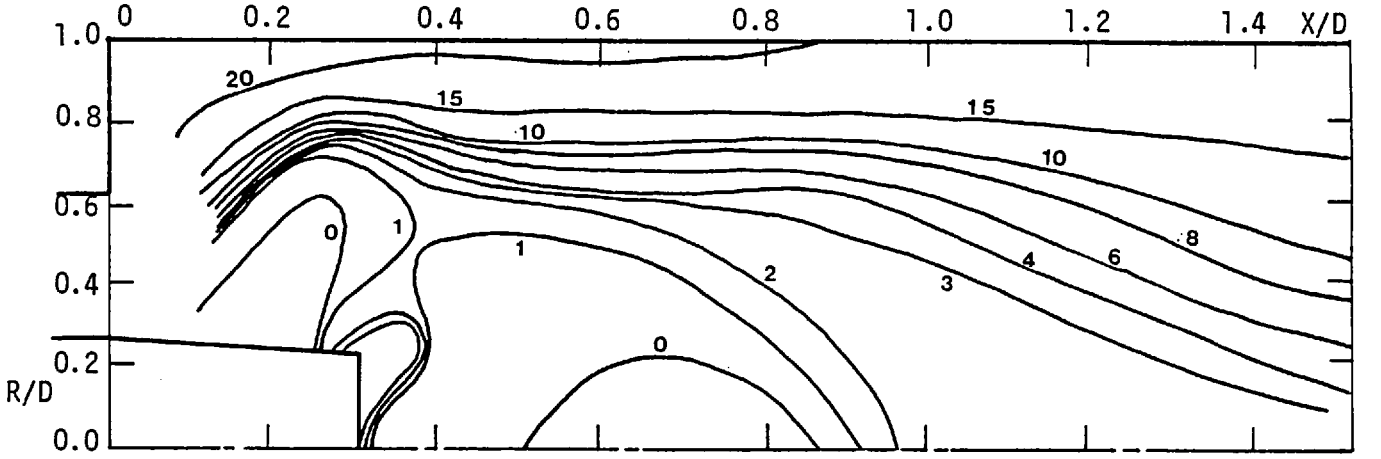

(a) Run 2

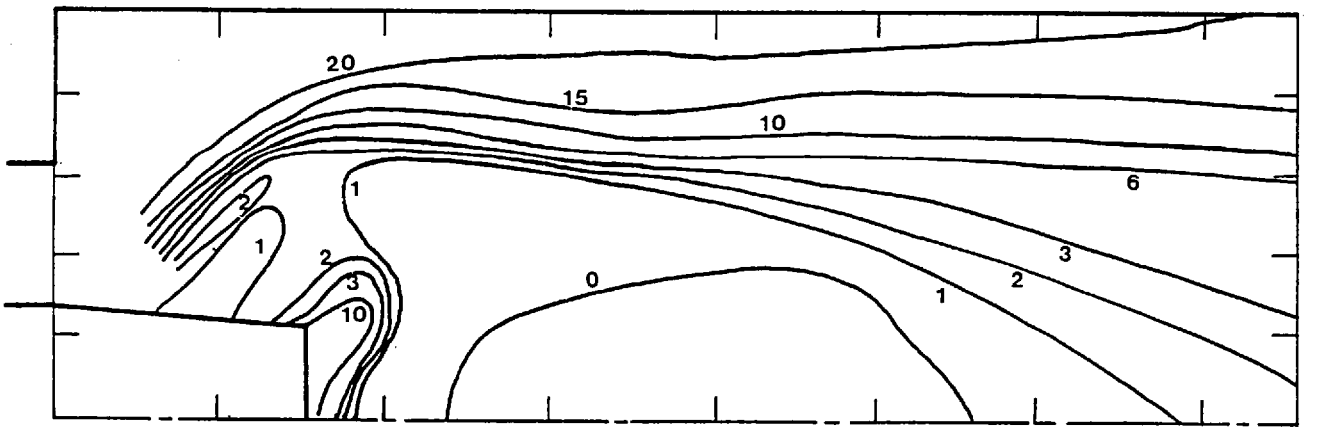

(b) Run 4

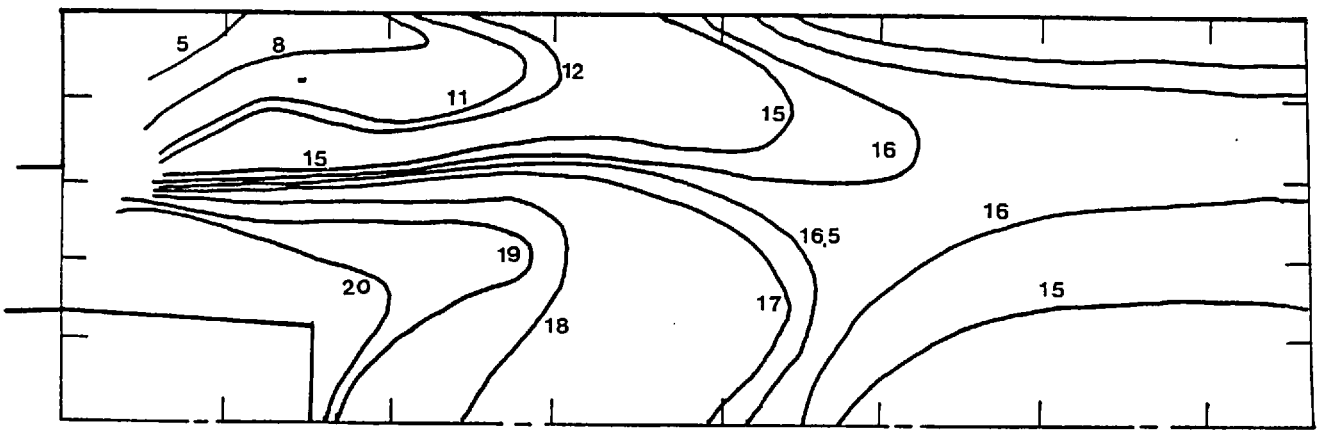

(c) Run 5

Fig. 2.38 Contour maps of the percentage O_2 volume concentration - runs 2, 4 and 5

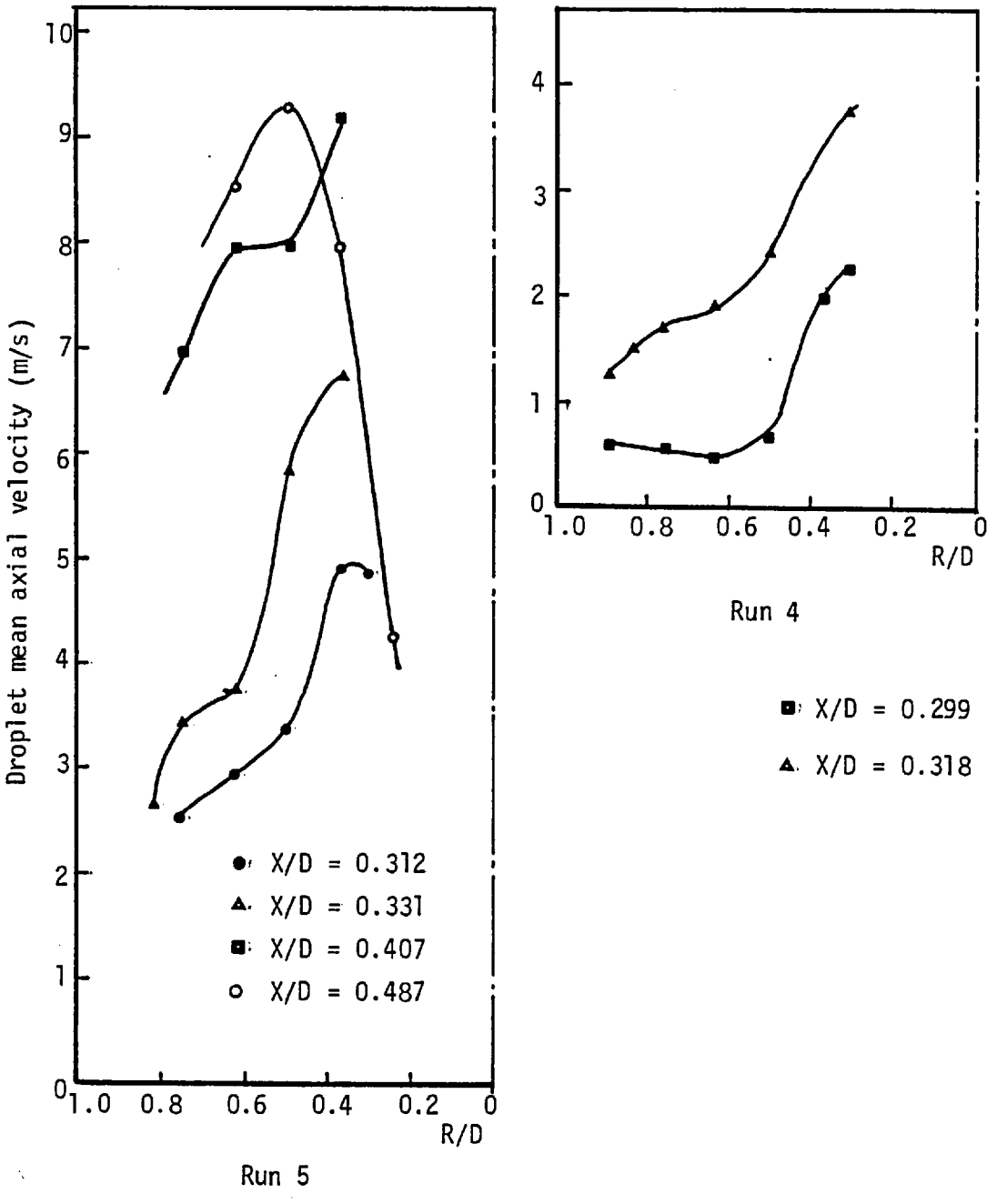

Fig. 2.39 Radial profiles of droplet mean axial velocity - runs 4 and 5 (run 2 - see Fig. 2.32)

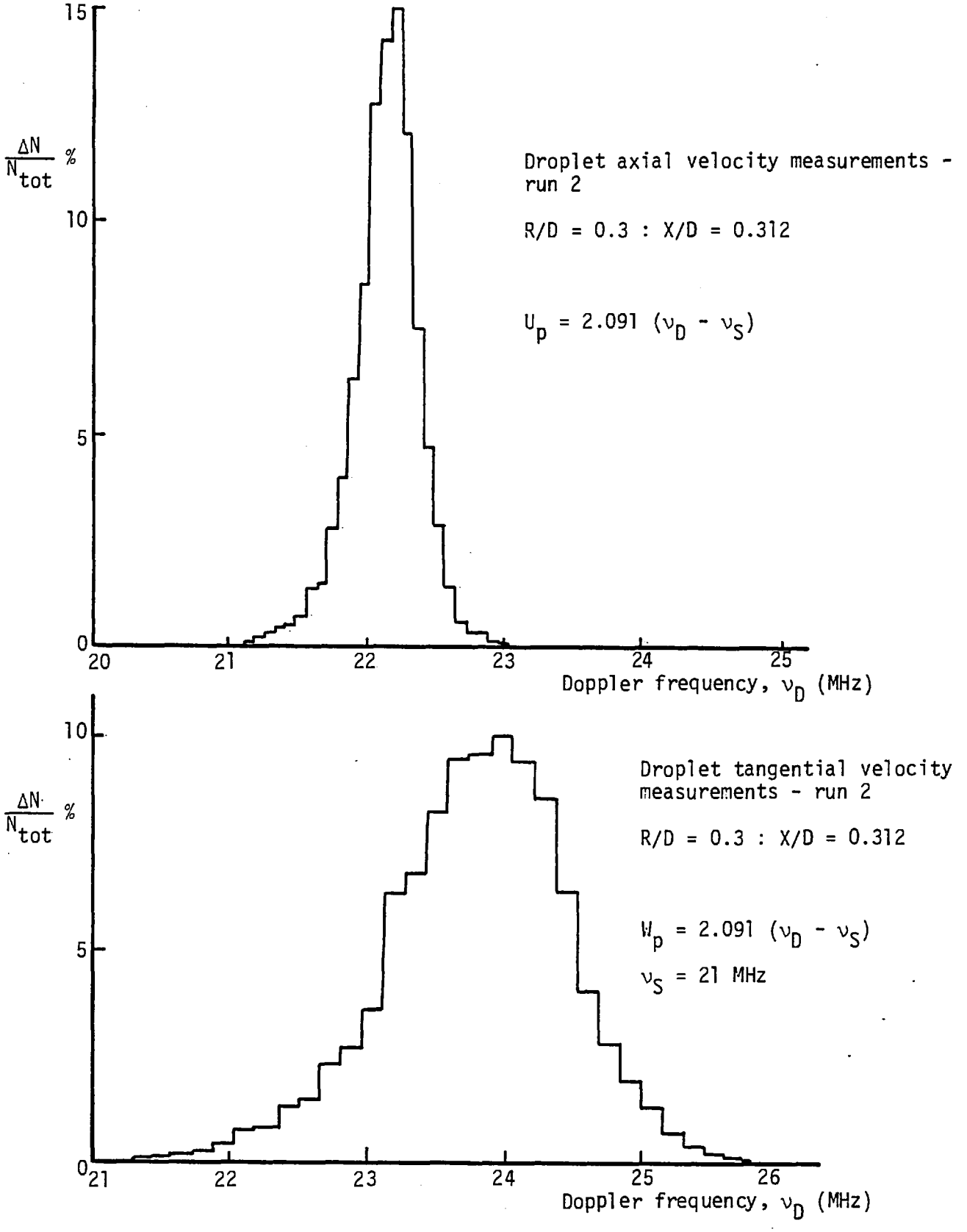

Fig. 2.40 Samples of velocity probability distributions

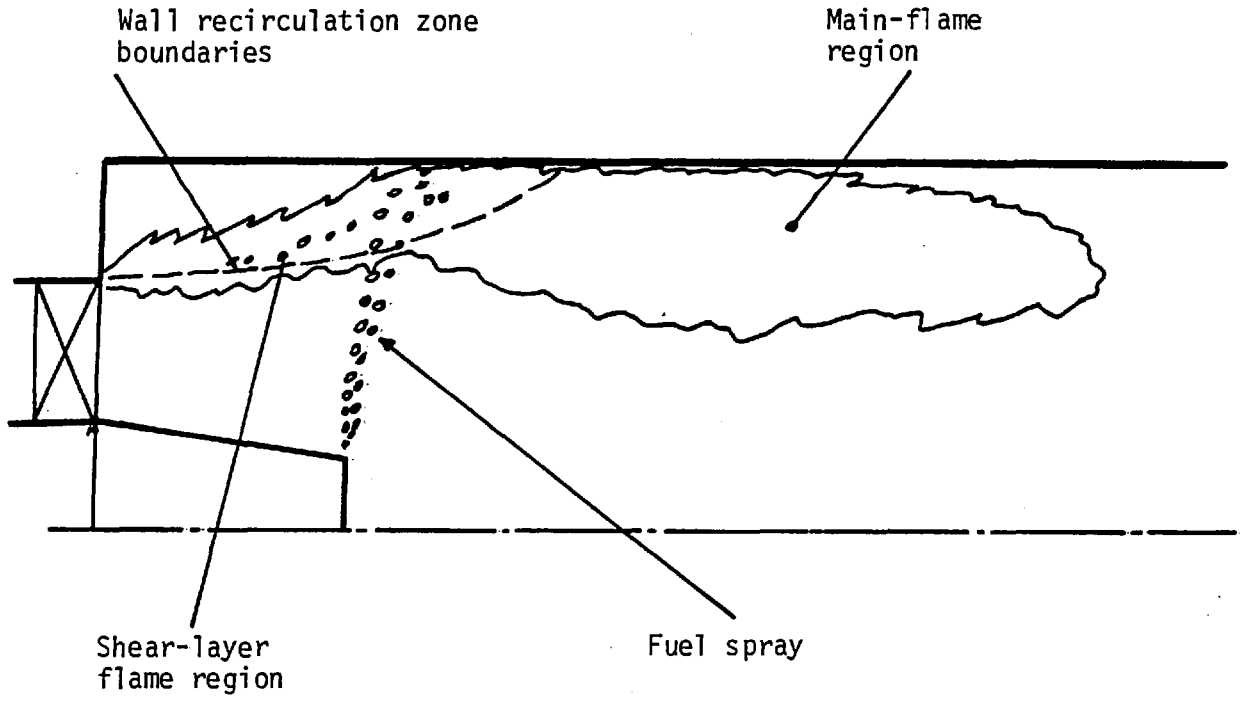

Fig. 2.41 Basic flame structure - run 5

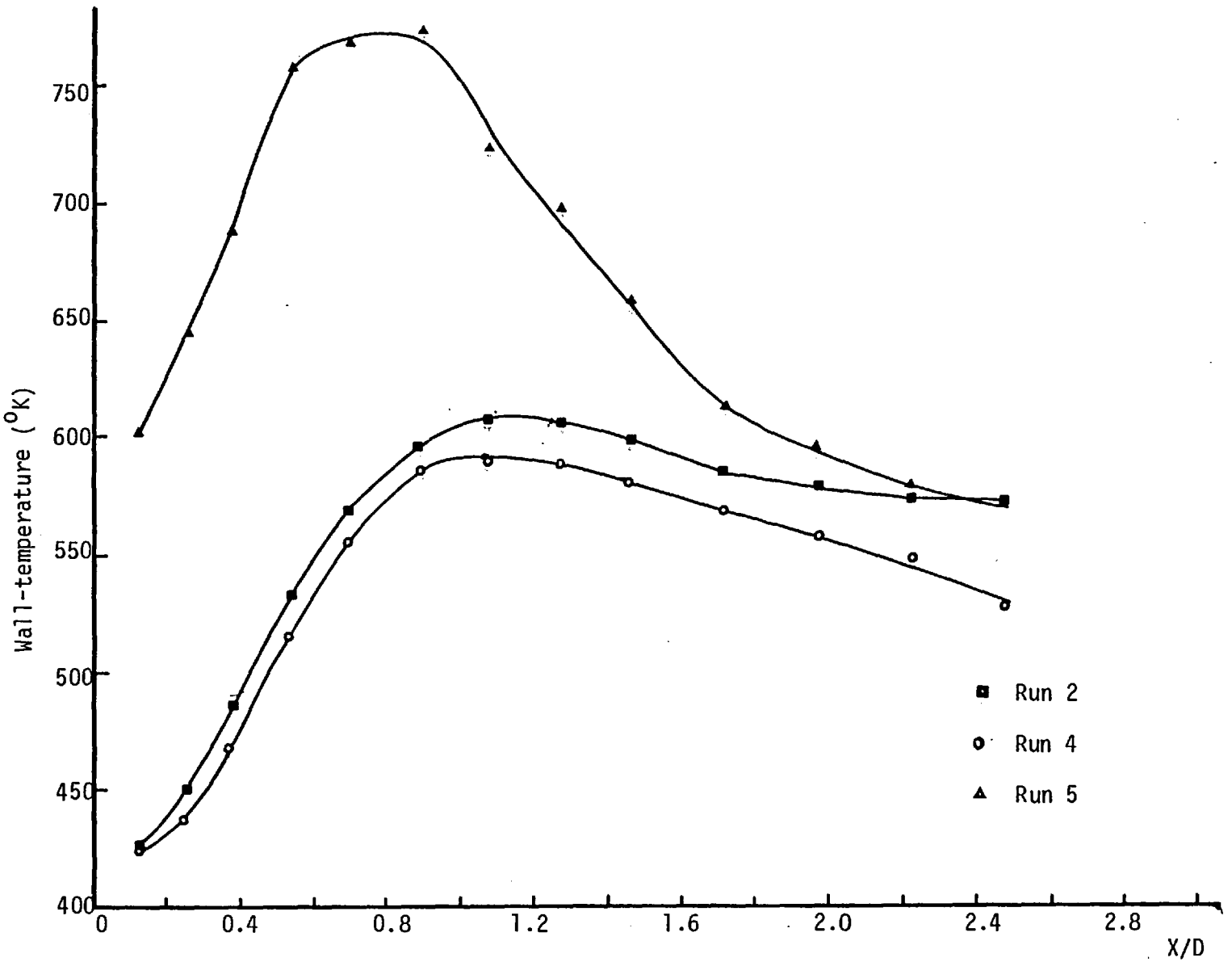

Fig. 2.42 Wall-temperature distributions - runs 2, 4 and 5

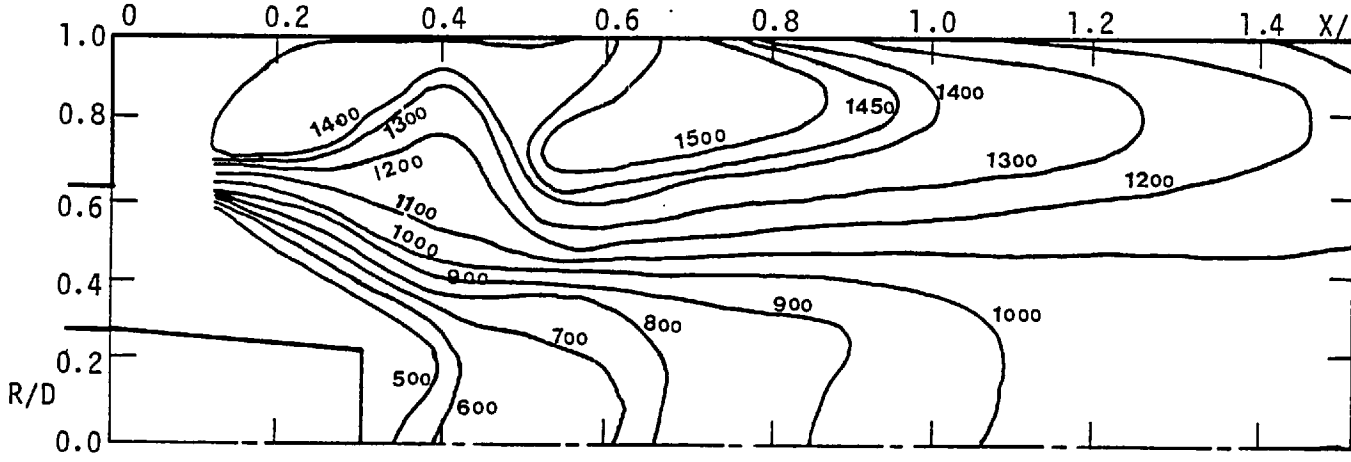

(a) Run 5

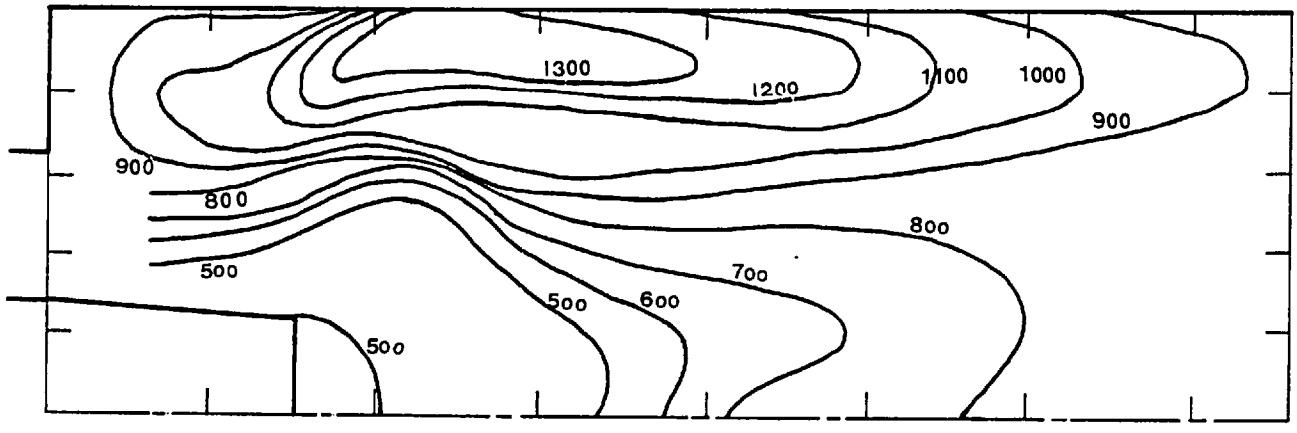

(b) Run 6

Fig. 2.43 Temperature contour maps - runs 5 and 6

CHAPTER 3

THEORETICAL CONTRIBUTION

3.1 Introductory Remarks

The prediction of the hydrodynamic and thermal characteristics of spray flames requires consideration of the two phases in the flow field which are coupled through exchange processes of mass, heat and momentum. The main mathematical burden is associated with the modelling of the discontinuous liquid-phase and the coupling between the two phases. Moreover, the modelling of the combustion process requires consideration of the spray characteristics, including evaporation rate, penetration, droplet size and velocity, which act as additional combustion-rate controlling parameters. The combustion process is dependent, therefore, on the relative importance of the mixing, chemical reaction rate and spray characteristics.

This chapter describes the method used for the calculation of the local flow properties of spray flames and reports results for a range of flame geometries. The mathematical formulation involves the application of Eulerian conservation equations to the gas-phase and Lagrangian equations of droplet motion and thermal balance to a finite number of size ranges representing the droplet-size distribution within the spray. The two sets of equations are explicitly coupled through droplet source terms, representing the various exchange processes, which are calculated from the solution of the droplet field equations and by utilizing a droplet-tracking technique. The spray combustion model assumes that the evaporating droplets act as distributed point injectors of fuel vapour within the flame and that the combustion process of the fuel vapour can be regarded as gaseous.

Sections 2 through 7 of the present chapter provide a

detailed description of the equations solved together with the various models employed, including those for turbulence, combustion, spray and radiation. The numerical scheme used to solve the coupled set of gas-droplet equations is summarized in Section 8. The results of the calculations performed for the four flame geometries of Khalil et al (1977), Styles et al (1977), Tuttle et al (1976), and the present confined flame geometry and the comparison with the corresponding experimental data are presented and discussed in the separate parts of Section 9. The chapter ends with brief concluding remarks.

3.2 Differential Equations

The equations representing conservation of mass, momentum, enthalpy and concentration of chemical species for a chemically reacting, turbulent, droplet-free gas phase, can be expressed as:-

Continuity

$$\frac{\partial \rho}{\partial t} + \frac{\partial \rho U_i}{\partial x_i} = 0 \qquad (3.2.1)$$

Momentum

$$\frac{\partial \rho U_j}{\partial t} + \frac{\partial \rho U_i U_j}{\partial x_i} = - \frac{\partial \tau_{ij}}{\partial x_i} - \frac{\partial p}{\partial x_j} \qquad (3.2.2)$$

ρU_j represents the momentum in the x_j-direction/per unit volume and the shear-stress tensor τ_{ij} represents the diffusive flux of x_j- direction momentum in the x_i-direction. The source of momentum is represented by (minus) the pressure gradient, $- \partial p / \partial_{xj}$.

Enthalpy

$$\frac{\partial \rho h}{\partial t} + \frac{\partial \rho U_i h}{\partial x_i} = - \frac{\partial \Lambda_i^h}{\partial x_i} + S_h \qquad (3.2.3)$$

Chemical Species

$$\frac{\partial \rho m_\alpha}{\partial t} + \frac{\partial \rho U_i m_\alpha}{\partial x_i} = - \frac{\partial \Lambda_i^\alpha}{\partial x_i} + S_\alpha \qquad (3.2.4)$$

m_α and h are the mass fraction of species α and enthalpy respectively. $(\rho U_i h)$ and $(\rho U_i m_\alpha)$ represent the convective flux in the i-direction while Λ_i^α and Λ_i^h are the analagous diffusive flux.

The gas density and temperature can also be expressed as:-

$$\rho = \rho\ (m\ ,\ h\ ,\ p)$$

$$T = T\ (m\ ,\ h\ ,\ p)$$

For low Mach number flow, the density and temperature dependence upon pressure can be removed and the above expressions read:-

$$\rho = \rho\ (m\ ,\ h) \qquad \text{and} \qquad T = T\ (m\ ,\ h)$$

The diffusive flux $\Lambda_i^{\alpha,h}$ and $\tau_{i,j}$ can be represented by simple gradient expressions, i.e.:-

$$\Lambda_i^\alpha = - \Gamma_\alpha \frac{\partial m_\alpha}{\partial x_i} \quad , \quad \Lambda_i^h = - \Gamma_h \frac{\partial h}{\partial x_i} \quad , \quad \tau_{i,j} = - \mu \left(\frac{\partial U_i}{\partial x_j} + \frac{\partial U_j}{\partial x_i} \right)$$

where Γ_α, Γ_h and μ are the laminar exchange coefficients.

Substitution in Equations (3.2.1) - (3.2.4) leads to:-

$$\frac{\partial \rho}{\partial t} + \frac{\partial \rho U_i}{\partial x_i} = 0 \tag{3.2.5}$$

$$\frac{\partial \rho U_j}{\partial t} + \frac{\partial \rho U_i U_j}{\partial x_i} = \frac{\partial}{\partial x_i} \mu \left[\frac{\partial U_i}{\partial x_j} + \frac{\partial U_j}{\partial x_i} \right] - \frac{\partial p}{\partial x_j} \tag{3.2.6}$$

$$\frac{\partial \rho \Phi}{\partial t} + \frac{\partial \rho U_i \Phi}{\partial x_i} = \frac{\partial}{\partial x_i} \Gamma_\Phi \frac{\partial \Phi}{\partial x_i} + S_\Phi \tag{3.2.7}$$

where $\Phi \equiv m_\alpha$ or h

Equations (3.2.5) through (3.2.7), together with the appropriate boundary conditions and auxiliary expressions for the calculation of density and for the form of the enthalpy-temperature dependence, represent a closed set of equations for the instantaneous dependent variables. In turbulent flows, however, the variations in the dependent variables cover a wide range of time and length scales and preclude the direct numerical solution of the governing equations. As a consequence, turbulent flows are represented with the decomposition of the dependent variables into mean and fluctuating components and by averaging the conservation equations. As a result of the non-linearity of the equations averaging results in a loss of information so that the equations are no longer closed and closure assumptions are necessary before solution is possible.

In the treatment of variable density flows, two types of decomposition can be used; either the unweighted form conventionally used for constant density flows or the density weighted decomposition

proposed by Favre (1969). The present formulation is based on the former type. However, as will be indicated later in this section, the omission of the density correlation terms appearing in the final equation set reduces it to a similar form of that obtained with density weighted decomposition, see Bilger (1976) and Jones (1979).

The unweighted decomposition and averaging are represented by:-

$$U_i = \overline{U}_i + u_i'' \qquad \text{and} \qquad \Phi = \overline{\Phi} + \Phi''$$

$$\overline{u}_i'' = 0 \qquad\qquad \overline{\Phi}'' = 0$$

where the overbars denote ensemble averages. The averaged form of Equations (3.2.5) - (3.2.7) for steady gas flow can be written as:-

$$\frac{\partial}{\partial x_i}\left[\overline{\rho} \cdot \overline{U}_i + \overline{\rho'' u_i''}\right] = 0 \tag{3.2.8}$$

$$\frac{\partial}{\partial x_i}\left[\overline{\rho} \cdot \overline{U}_i \cdot \overline{U}_j + \overline{\rho} \cdot \overline{u_i'' u_j''} + \overline{U}_j \cdot \overline{\rho'' u_i''} + \overline{U}_i \cdot \overline{\rho'' u_j''} + \overline{\rho'' u_i'' u_j''}\right] =$$

$$= \frac{\partial}{\partial x_i}\mu\left[\frac{\partial \overline{U}_i}{\partial x_j} + \frac{\partial \overline{U}_j}{\partial x_i}\right] - \frac{\partial \overline{p}}{\partial x_j} \tag{3.2.9}$$

$$\frac{\partial}{\partial x_i}\left[\overline{\rho} \cdot \overline{U}_i \cdot \overline{\Phi} + \overline{\rho} \cdot \overline{u_i'' \Phi''} + \overline{\Phi} \cdot \overline{\rho'' u_i''} + \overline{U}_i \cdot \overline{\rho'' \Phi''} + \overline{\rho'' u_i'' \Phi''}\right] =$$

$$= \frac{\partial}{\partial x_i}\Gamma_\Phi \frac{\partial \overline{\Phi}}{\partial x_i} + \overline{S}_\Phi \tag{3.2.10}$$

The gas density and temperature can also be represented by the

expressions:-

$$\overline{\rho} = \rho(\overline{\Phi}) \qquad \text{and} \qquad \overline{T} = T(\overline{\Phi}) \tag{3.2.11}$$

It is clear that additional information of the correlations $\overline{u_i' u_j'}$, $\overline{u_i' \Phi'}$ and those involving density, and of the mean formation rate of species α, $\overline{S}_\Phi$, is required to close the above set of equations. The problems associated with determining the correlation $\overline{u_i' u_j'}$ and $\overline{u_i' \Phi'}$ are common for both variable and constant density flows and are resolved by devising turbulence models which allow their calculation in terms of "known" quantities. The turbulence model adopted in the present work is described in the next Section 3.3; it involves an assumed, laminar-like, linear relationship between the Reynolds stress, $\overline{u_i' u_j'}$, and rate of strain, see for example Launder et al (1972) and Jones (1979):-

$$\overline{\rho} \cdot \overline{u_i' u_j'} = \frac{2}{3} \delta_{ij} \left[\overline{\rho} \cdot k + \mu_T \frac{\partial \overline{U}_\ell}{\partial x_\ell} \right] - \mu_T \left[\frac{\partial \overline{U}_i}{\partial x_j} + \frac{\partial \overline{U}_j}{\partial x_i} \right]$$

and the turbulent viscosity, μ_T, is expressed as:-

$$\mu_T = C_\mu \cdot \overline{\rho} \cdot \frac{k^2}{\varepsilon}$$

The values of the turbulent kinetic energy, k, and its rate of dissipation, ε, are obtained from the solution of their respective transport equations which are described in Section 3.3. The turbulent fluxes, $\overline{u_i' \Phi'}$, are also obtained via the gradient-type expression:-

$$\overline{\rho} \cdot \overline{u_i' \Phi'} = - \frac{\mu_T}{\sigma_T} \cdot \frac{\partial \overline{\Phi}}{\partial x_i}$$

The problems associated with the evaluation of the mean formation rate of the chemical species α, $\overline{S}_\alpha$, are the subject of the combustion model and, therefore, will be discussed in Section 3.4. It remains, however, to resolve the difficulties associated with the specification of the density-correlation terms in Equations (3.2.8) - (3.2.10). Here, it must be recognized that these terms do not appear in the final set of equations obtained with density-weighted decomposition and averaging. However, if the density correlation terms are negligible, the two types of decomposition yield identical equations. Transport equations for the density-correlation terms are available, see for example Khalil (1976) and Jones (1979) and can be solved simultaneously with the equation set (3.2.8) - (3.2.10). However, due to the uncertainties in the assumptions involved in their derivation and the additional computing storage and run time associated with their application, all density-correlation terms have been omitted in the final set of equations used in the present work. The implication is that the present differential equations can be regarded as written in density-weighted form. This also implies that the calculated results should be compared with density-weighted measurements and it is likely that concentration measurements, in particular, are close to density-weighted.

Finally, the form of Equations (3.2.8) - (3.2.10), after substitution of appropriate expressions for the Reynolds stresses and turbulent fluxes terms, suggests that they can all be written in the same general form which for two-dimensional turbulent, axi-symmetric, combusting and steady gas flow with recirculation is:-

$$\frac{\partial}{\partial x}(\rho \cdot U \cdot \Phi) + \frac{1}{r}\frac{\partial}{\partial r}(r \cdot \rho \cdot V \cdot \Phi) = \frac{\partial}{\partial x}\left[\Gamma_{eff}\frac{\partial \Phi}{\partial x}\right] +$$

$$+ \frac{1}{r} \frac{\partial}{\partial r} \left(r \, \Gamma_{eff} \frac{\partial \Phi}{\partial r} \right) + S + S_d \qquad (3.2.12)$$

The source term, S, represents the generation or destruction of the dependent variable, Φ, by processes concerned only with the gas-phase. Expressions for the source term, S, and the exchange coefficient, Γ_{eff}, corresponding to the different dependent variables used in the present work are assembled in Table 3.1. The additional source term, S_d, which is introduced into the final equation, represents the generation or destruction due to the fuel droplets and will be described later in Section 3.5.5. In the present work, it is assumed that the fuel droplets do not influence the turbulent structure other than through the release of thermal energy, i.e. the droplet concentration is small.

3.3 Turbulence Model

3.3.1 Classification of Models

Reynolds stress terms, $\overline{u_i' u_j'}$, and turbulent fluxes, $\overline{u_i' \Phi'}$, which were introduced in Section 3.2, represent unknowns in the conservation equations and additional equations are, therefore, required to enable these terms to be calculated. The necessary set of equations collectively constitute a "turbulence model". A classification scheme for turbulence models and examples of their applications are provided by Launder and Spalding (1972). In general, the turbulence models are of two main types: in one type, the Reynolds stresses are represented by way of a turbulent viscosity hypothesis and the turbulent fluxes, $\overline{u_i' \Phi'}$, by way of an effective turbulent Prandtl or Schmidt number. In the other type, transport equations for these correlations are derived and closure approximations

for the higher order correlations are used. The resulting equations can, therefore, be simultaneously solved with other conservation equations. In the former category, the Reynolds stresses are assumed to be related to the rate of strain via the expression:-

$$\rho \cdot \overline{u_i' u_j'} = \frac{2}{3} \delta_{ij} \left(\rho \cdot k + \mu_T \frac{\partial U_\ell}{\partial x_\ell} \right) - \mu_T \left(\frac{\partial U_i}{\partial x_j} + \frac{\partial U_j}{\partial x_i} \right) \qquad (3.3.1)$$

and the turbulent fluxes are represented by a simple gradient-type expression, i.e.:-

$$\rho \cdot \overline{u_i' \Phi'} = - \frac{\mu_T}{\sigma_T} \cdot \frac{\partial \Phi}{\partial x_i} \qquad (3.3.2)$$

Typically, the turbulent viscosity is taken to be proportional to the product of a velocity-scale and a length-scale characteristic of the local turbulent flow. For example, in one- and two-equation models, see Launder and Spalding (1972), the turbulent viscosity is related to the kinetic energy of turbulence, $k = \frac{1}{2} \overline{u_i'^2}$, and a length scale ℓ by the expression:-

$$\mu_T = C_\mu \cdot \rho \cdot k^{1/2} \cdot \ell$$

where C_μ is an empirical constant. One-equation models solve a differential transport equation for k but require an empirical specification of ℓ. Two-equation models, however, provide a more general approach by solving transport equations for both k and a quantity related to ℓ. The latter is usually taken to be the dissipation rate of the turbulent kinetic energy which is related to ℓ by the expression:-

$$\varepsilon = C_D \cdot k^{3/2}/\ell$$

and the constant C_D has a typical value of unity. Therefore, μ_T can be expressed by:-

$$\mu_T = C_\mu \cdot \rho \cdot \frac{k^2}{\varepsilon} \qquad (3.3.3)$$

In view of the uncertainties in the closure approximations, even in constant density flows, for higher order turbulence models which solve additional transport equations for the Reynolds stresses and turbulent fluxes and of the additional uncertainties introduced by the combustion model, their inclusion in calculation procedures for turbulent reacting flows cannot be justified at this time. Therefore, a two-equation turbulence model of the type represented by expressions (3.3.1) - (3.3.3) has been used in the present calculation.

However, it must be recognized that the closure assumptions of this turbulence model are based on the characteristics of constant density flows. Whether these assumptions are valid for variable density flows and whether explicit modifications of it is required are questions which remain to be answered. However, the model has been used extensively for the calculation of turbulent reacting flows, see for example Khalil (1976), Hutchinson et al (1978) and Magnussen et al (1976), and yielded satisfactory results.

3.3.2 Transport Equations for Turbulent Kinetic Energy and Dissipation Rate

The exact transport equation for turbulent kinetic energy, see for example Jones et al (1973), is obtained from the equation for the turbulent velocity fluctuations u_i' which can be

derived by subtracting the time-averaged momentum Equation (3.2.9) from the time-dependent momentum Equation (3.2.6). By multiplying the resulting equation by u_i', time averaging, and introducing the definition $k \equiv \frac{1}{2}\overline{u_i'^2}$, the turbulent kinetic energy equation is obtained and, for two-dimensional axi-symmetric flow in the absence of density fluctuations, takes the form:-

$$\rho \cdot U \frac{\partial}{\partial x} k + \frac{\rho V}{r} \frac{\partial}{\partial r} (rk) = \frac{\partial}{\partial x}\left[\frac{\mu_{eff}}{\sigma_k} \frac{\partial k}{\partial x}\right] + \frac{1}{r}\frac{\partial}{\partial r}\left[r \frac{\mu_{eff}}{\sigma_k} \frac{\partial k}{\partial r}\right] +$$

$$+ \mu_{eff}\left[2\left\{\left(\frac{\partial U}{\partial x}\right)^2 + \left(\frac{\partial V}{\partial r}\right)^2 + \left(\frac{V}{r}\right)^2\right\} + \left(\frac{\partial W}{\partial x}\right)^2 + \left\{r \frac{\partial}{\partial r}\left(\frac{W}{r}\right)\right\}^2 + \left(\frac{\partial U}{\partial r} + \frac{\partial V}{\partial x}\right)^2\right] - \rho\varepsilon \qquad (3.3.4)$$

The exact equation for ε can be derived by a similar procedure and the resulting equation takes the form:-

$$\rho \cdot U \frac{\partial \varepsilon}{\partial x} + \frac{\rho V}{r} \frac{\partial}{\partial r} (r\varepsilon) = \frac{\partial}{\partial x}\left[\frac{\mu_{eff}}{\sigma_\varepsilon} \frac{\partial \varepsilon}{\partial x}\right] + \frac{1}{r}\frac{\partial}{\partial r}\left[\frac{r\mu_{eff}}{\sigma_\varepsilon} \cdot \frac{\partial \varepsilon}{\partial r}\right] +$$

$$+ \mu_{eff} \cdot C_1 \cdot \frac{\varepsilon}{k}\left[2\left\{\left(\frac{\partial U}{\partial x}\right)^2 + \left(\frac{\partial V}{\partial r}\right)^2 + \left(\frac{V}{r}\right)^2\right\} + \left(\frac{\partial W}{\partial x}\right)^2 + \left\{r \frac{\partial}{\partial r}\left(\frac{W}{r}\right)\right\}^2 +\right.$$

$$\left. + \left(\frac{\partial U}{\partial r} + \frac{\partial V}{\partial x}\right)^2\right] - C_2 \cdot \rho \frac{\varepsilon^2}{k} \qquad (3.3.5)$$

The form of Equations (3.3.4) and (3.3.5) is similar to the more general form of Equation (3.2.12) which will be used in the finite difference formulation in Section 3.7. The values of the empirical constants introduced in Equations (3.3.3) and (3.3.5) and the turbulent Prandtl numbers used in the present work are summarized in

Table 3.3.2.

3.4 Combustion Model

A typical requirement of a calculation procedure for reacting turbulent flows is to provide local values of mixture composition, temperature and density. These can, in principle, be obtained from the solution of a set of equations of the type described in Section 3.2 and, in particular, Equations (3.2.10) and (3.2.11). They are rewritten, incorporating Equation (3.3.2), neglecting density correlation terms and including the additional source terms, S_d, due to the liquid fuel droplets:-

$$\frac{\partial}{\partial x_i}\left[\rho \cdot U \cdot \Phi\right] = \frac{\partial}{\partial x_i}\left(\frac{\mu_{eff}}{\sigma_{eff}}\frac{\partial \Phi}{\partial x_i}\right) + S_\Phi + S_d \qquad (3.4.1)$$

$$\rho = \rho(\Phi) \qquad \text{and} \qquad T = T(\Phi) \qquad (3.4.2)$$

where Φ stands for the mass fraction of species α or the stagnation enthalpy.

In the absence of thermal radiation, zero source term, the solution of Equation (3.4.1) with enthalpy as the dependent variable can be directly obtained and part of the requirements stated above is, therefore, partially resolved. It remains, however, to solve Equation (3.4.1) for the chemical species, α, involved in the chemical reaction. The combustion of most fuels encompasses a wide range of intermediate reactions involving many intermediate species and free radicals. Even if this can be tolerated from the point of view of the capabilities of the present computing facilities, a major problem still exists in that the evaluation of the mean formation/destruction rate, S_Φ, must be determined for each equation. The source of difficulty stems

from the highly non-linear dependence of this rate on temperature and species concentrations. For example, if a simplified global one-step reaction between fuel and oxidant is assumed and the instantaneous reaction rate $\hat{R}_\ell$ is represented by an Arrhenius type expression, i.e.:-

$$\hat{R}_\ell = \chi_\ell \cdot \exp(-E/R\hat{T}) \cdot \hat{m}_{fu} \cdot \hat{m}_{ox}$$

where χ_ℓ is the pre-exponential factor and E is the activation energy and ℓ stands for either the fuel or the oxidant, the application of the decomposition and averaging procedure described in Section 3.2, see for example Borghi (1975), results in a final form of the averaged reaction rate expression where additional new correlations exist (e.g. $\overline{m'_{fu} \cdot m'_{ox}}$, $\overline{m'^2_{fu}}$, $\overline{m'_{fu} \cdot T'}$, ... etc.). The complexities introduced by these terms render it difficult to obtain a practical solution of the transport equations. The idea of "combustion-modelling" starts here where a variety of reaction rate expressions are devised and closure assumptions introduced to relate them to calculable flow properties and where, as will be described later, the calculation of the reaction rate terms, for a certain type of flame, is completely eliminated.

Combustion models which are relevant to the present spray flame study, where fuel and air are introduced separately into the combustion-space, are briefly described in the next Subsection 3.4.1, and the two models adopted in the present procedure are introduced in Subsections 3.4.3 and 3.4.4.

3.4.1 Classification of Models

In one group of combustion models, which have been used extensively for the calculation of gaseous diffusion flames, see for example Khalil (1976), Lockwood et al (1975) and Spalding (1975),

the calculation of the mean-reaction rate is by-passed by assuming a global, one-step, infinitely fast chemical reaction between fuel and oxidant where both combine in stoichiometric proportion. Further, the effective exchange coefficient, $\Gamma_\Phi = (\mu/\sigma)_{eff}$, is assumed equal for all species. A consequence of these assumptions is that chemical equilibrium prevails everywhere in the flame and that the thermodynamic state of the mixture is related to a single strictly conserved scalar variable for which a transport equation of the type of Equation (3.4.1) (but with no source term) can be solved. The influence of the turbulence-induced fluctuations of this scalar variable on the calculation of the mean values of all variables dependent on it is considered by adopting a statistical approach in which a probability density function, pdf, is used to describe the temporal nature of these fluctuations. In most models the shape of the pdf is specified a priori, for example, a double-delta form was proposed by Spalding (1971), a clipped Gaussian distribution is proposed and used by Lockwood and Naguib (1975) and a Beta-function form used by Jones (1979). However, the pdf can, in principal, be calculated from a modelled version of an exact transport equation as indicated, for example, by Pope (1976).

A different approach which avoids, to some extent, the problem of modelling the probability density function is to use Equation (3.4.1) directly and model the mean reaction rate term. This approach was suggested by the "Eddy-break-up" model of Spalding (1976) in premixed flows. A closely related model has been also used by Magnussen et al (1976, 1978) for arbitrary-fuelled flames. In the latter, the rate of reaction is assumed to be determined by the rate of intermixing on a molecular scale of fuel and oxygen eddies or, effectively, by the rate of dissipation of the eddies. This was expressed in terms of the mean concentration of the reacting species instead of the concentration

fluctuations as used by Spalding (1976).

The two groups of combustion models mentioned above are not appropriate if it is desired to predict intermediate or pollutant species such as carbon monoxide, unburned hydrocarbons and nitric oxides. There are two main difficulties associated with the development of combustion models which can be used to predict such species. The first relates to the kinetics of the chemical reaction and the second to the modelling of the influence of turbulence on combustion. The prediction of these intermediate or pollutant species requires a detailed knowledge of the reaction mechanisms, see for example Caretto (1976), Bowman (1976) and Jones (1979). Although these are well-known for some reactions; for example, the formation of thermal nitric oxide and the conversion of CO to CO_2, their use in modelling calculations is limited by the difficulties involved in describing the kinetic schemes for the initial hydrocarbon oxidation. The typical approach in most of the models which take some account of these processes is to introduce drastic simplifying assumptions to the initial hydrocarbon oxidation mechanism and even to the detailed reaction mechanisms for the species under consideration. In most cases, the validity of these assumptions is questionable and even, they are restricted to certain specific conditions. The need to account for the turbulence effects on combustion adds greatly to above difficulties. For example, if the probability density function approach is utilized, the treatment in this case will involve specifying a multi-parameter joint probability density function.

In the initial part of the present study, a combustion model of the first group was used with a presumed double-delta probability density function. This form of the pdf is undoubtedly simplistic and as indicated by the results of the calculations performed by Jones

(1978) with different forms of the pdf; the uncertainties in the model, due to the presumed form, would be greatest at regions where the fluctuations in the scalar variable (mixture fraction) encompass stoichiometric conditions. However, this model is economic of computer storage and time and, in view of the additional uncertainties imposed by the present droplet model, probably of acceptable precision. The model has been also appraised in connection with the calculation of gaseous diffusion flames as indicated, for example, by Khalil (1976), Jones (1978), Syed (1977) and Salooja (1978).

The model of Magnussen et al (1978) which can accommodate diffusion, premixed and arbitrary fuelled flames was more relevant to the present spray flame geometries where the finite rate of droplet evaporation suggests that the fuel feed resembles the conditions of arbitrary fuelled flames. This model was used for most of the calculations reported in Section 3.9 and it is probably more simpler than the former model in that the reaction rate is related to the mean mass fractions of fuel and oxidant. The two models are described in detail in the next subsections.

3.4.2 Spray Combustion

The spray combustion model used in this study is based on the assumption that liquid droplets act as distributed sources of fuel vapour within the spray and eventually form a cloud of vapour. The implication is that chemical reaction in spray flames can be treated in a way similar to that used for turbulent gaseous flames. Experimental evidence for this assumption can be found in the reported results of Chigier et al (1973, 1974), Komiyama et al (1977), Onuma et al (1975, 1977), Tuttle et al (1976) and Styles et al (1977).

3.4.3 The Double-Delta-pdf Model

The model assumes a global, one-step chemical reaction between fuel and oxidant. The reaction is assumed to be instantaneous so that fuel and oxidant combine in stoichiometric proportion to produce one type of product, i.e.:-

1 kg fuel + i kg oxidant → (1 + i) kg products

The effective exchange coefficients for all species, Γ_Φ, assumed equal and consequently a passive scalar of the flow can be expressed as:-

$$\hat{\Phi} = \hat{m}_{fu} - \frac{\hat{m}_{ox}}{i} \qquad (3.4.3)$$

which, in a non-dimensional form, is typically defined by:-

$$\hat{f} = (\hat{\Phi} - \Phi_A) \; / \; (\Phi_F - \Phi_A) \qquad (3.4.4)$$

where $\hat{f}$ is the mixture fraction defined as the mass of fuel (burned and unburnt) at a point divided by the total mass at that point. $\hat{m}_{fu}$ and $\hat{m}_{ox}$ are the instantaneous fuel and oxidant mass fractions, i is the stoichiometric oxidant requirement and the subscripts A, F designate the oxidant and fuel-bearing streams. A consequence of the chemical equilibrium assumption (infinitely fast chemical reaction) is that the following expressions can be used to describe the relationship between the mass fractions of fuel and oxidant and the mixture fraction, f. For:-

$$0 \leq \hat{f} \leq f_{st} \qquad : \qquad \hat{m}_{fu} = 0$$

$$\hat{m}_{ox} = m_{ox,A} \, (f_{st} - \hat{f}) \, / \, f_{st}$$

and for:-

$$f_{st} \leq \hat{f} \leq 1 \qquad : \qquad \hat{m}_{fu} = m_{fu,F} \, (\hat{f} - f_{st}) \, / \, (1 - f_{st})$$

$$\hat{m}_{ox} = 0 \tag{3.4.5}$$

where f_{st} is the stoichiometric mixture fraction for which $\Phi = 0$. The mass fraction of the products can be obtained from the expression:-

$$\hat{m}_{pr} = 1 - \hat{m}_{fu} - \hat{m}_{ox}$$

It is clear from the two expressions (3.4.3) and (3.4.4) that by algebraic manipulation of the differential equations for $\overline{m}_{fu}$ and $\overline{m}_{ox}$ (Equation (3.4.1)), a differential equation for the time averaged mixture fraction, $\overline{f}$, which has no source term can be obtained. For two-dimensional axisymmetric turbulent flow in the presence of fuel droplets, this can be written as:-

$$\frac{\partial}{\partial x} (\rho \, . \, U \, . \, \overline{f}) + \frac{1}{r} \frac{\partial}{\partial r} (r \, . \, \rho \, . \, V \, . \, \overline{f}) = \frac{\partial}{\partial x} \left[\Gamma_{eff} \frac{\partial \overline{f}}{\partial x} \right] +$$

$$+ \frac{1}{r} \frac{\partial}{\partial r} \left[r \, \Gamma_{eff} \frac{\partial \overline{f}}{\partial r} \right] + S_d \tag{3.4.6}$$

The generation source term, S_d, in the equation accounts for the evolution of fuel vapour due to droplets evaporation. More details about the calculation of this term are given in Section 3.5.5.

The turbulence-induced fluctuations in the mixture fraction, f, and the non-linear relationship between f and the fuel and oxidant mass fractions (expression (3.4.5)) implies that the mean value of f, $\overline{f}$, is insufficient to determine the corresponding mean values of m_{fu} and m_{ox}. However, they can be obtained if the probability-density-function, which describe the temporal nature of the mixture fraction fluctuations, is known. In this case the mean values of any property, $\hat{\Phi}$, solely dependent on f can be expressed as:-

$$\overline{\Phi} = \int_0^1 \hat{\Phi}(f) \cdot P(\hat{f}) \cdot d\hat{f} \qquad (3.4.7)$$

There are two alternative routes which may be followed to determine the pdf. The first, used in this model, is to specify it empirically; the second is to calculate it from a modelled transport equation as suggested for example by Pope (1976). The approach adopted here involves specifying a two-parameter form of the pdf, in terms of the mean mixture fraction, $\overline{f}$, and its variance, $\overline{f'^2}$, which are determined from the solution of their respective conservation equations. Spalding (1971) proposed a modelled transport equation for the variance, $\overline{f'^2}$ (termed g), which has a form similar to the turbulent kinetic energy (Equation (3.3.4)). For steady, two-dimensional and axisymmetric flow it has the form:-

$$\frac{\partial}{\partial x}(\rho U g) + \frac{1}{r}\frac{\partial}{\partial r}(\rho V r g) = \frac{\partial}{\partial x}\left[\Gamma_{g,eff}\frac{\partial g}{\partial x}\right] + \frac{1}{r}\frac{\partial}{\partial r}\left[r\,\Gamma_{g,eff}\frac{\partial g}{\partial r}\right] +$$

$$+ C_{g_1}\,\mu_{eff}\left[\left(\frac{\partial f}{\partial x}\right)^2 + \left(\frac{\partial f}{\partial r}\right)^2\right] - C_{g_2}\cdot\ \rho\cdot\frac{\varepsilon}{k}\cdot g \qquad (3.4.8)$$

where C_{g_1} and C_{g_2} are constants with typical values of 2.8 and 2.0 respectively.

The probability density function must satisfy the following conditions:-

$$P(f) \geq 0 \qquad 0 \leq f \leq 1$$
$$P(f) = 0 \qquad f < 0 \quad , \quad f > 1$$

It remains, however, to presume the shape of the pdf and for stationary flows it is related to the variation of f with time. In the present model, the time variation of f is assumed to have the square-wave form suggested by Spalding (1971), which has been used, for example, by Khalil (1976), Serag-Eldin (1977), Salooja (1978) and Jones (1979), i.e.:-

$$f_+ = f + g^{1/2} \qquad \text{and} \qquad f_- = f - g^{1/2}$$

except where the value of f_+ exceeds unity and where the value of f_- is less than zero. The time averaged value of f is given as:-

$$\overline{f} = \alpha f_+ + (1 - \alpha) f_-$$

where the factor α is defined to satisfy the above-mentioned conditions on f_+ and f_-. This time-variation form of f corresponds to two Dirac delta functions located at f_+ and f_- with:-

$$P(f) = \alpha \, \delta(f - f_-) + (1 - \alpha) \, \delta(f - f_+)$$

The mass fractions of fuel and oxidant are correspondingly calculated from the following two expressions, (see expression (3.4.5)):-

$$m_{fu_{\pm}} = m_{fu,F} \cdot \frac{(f_{\pm} - f_{st})}{(1 - f_{st})}$$

$$m_{ox_{\pm}} = m_{ox,A} \cdot \frac{(f_{st} - f_{\pm})}{f_{st}} \qquad (3.4.9)$$

and the mean values are obtained from the expression:-

$$\overline{m} = \alpha\, m_{+} + (1 - \alpha)\, m_{-} \qquad (3.4.10)$$

where $\overline{m}$ stands for either the fuel or oxidant concentration.

3.4.4 The Eddy-Dissipation Model

This model, see Magnussen et al (1978), stems from the fact that chemical reaction takes place when the reactants are mixed at a molecular scale and at sufficiently high temperature. In turbulent flows the molecular mixing is associated with the smallest eddies in the turbulence structure and the process of molecular mixing can be assumed as similar to the dissipation of turbulence kinetic energy. It is further assumed that the dissipation is not homogeneously distributed in the turbulent fluid, but rather takes place in concentrated, highly strained regions that occupy only fractions of the total volume. These regions are occupied by fine structures within which it can be assumed that the reactants are mixed at a molecular scale. On the basis of similarity considerations of the transfer of energy from the macroscales to the fine structures, the mass transfer between them is represented by, see Magnussen et al (1978):-

$$\dot{m} = 23.6 \left(\frac{\nu \cdot \varepsilon}{k^2}\right)^{1/4} \cdot \frac{\varepsilon}{k} \qquad (3.4.11)$$

If the rate of reaction between fuel and oxygen is considered infinitely fast, the combustion rate will be limited by the mass transfer represented by Equation (3.4.11). The rate of combustion, if it is assumed that reaction takes place in all the fine structures, would be expressed by:-

$$\overline{S}_{fu} = 23.6 \left[\frac{\nu \cdot \varepsilon}{k^2}\right]^{1/4} \cdot \frac{\varepsilon}{k} \cdot \overline{m}_{min} \cdot \rho \qquad (3.4.12)$$

where $\overline{m}_{min}$ is the smaller of m_{fu} and m_{ox}/i. However, not all the fine structures will be sufficiently heated to react. The fraction of the fine structures which reacts can be assumed to be proportional to the ratio between the local concentration of reacted fuel and the total fuel concentration. Thus:-

$$\chi = \frac{(1 - m_{fu} - m_{ox}) / (1 + i)}{(1 - m_{fu} - m_{ox}) / (1 + i) + m_{fu}}$$

and the general expression for the rate of combustion at infinite reaction rate between fuel and oxygen can be written as:-

$$\overline{S}_{fu} = 23.6 \left[\frac{\nu \cdot \varepsilon}{k^2}\right]^{1/4} \cdot \frac{\varepsilon}{k} \cdot \rho \cdot \chi \cdot \overline{m}_{min} \qquad (3.4.13)$$

The solution of Equation (3.4.1) with the reaction rate expression (3.4.13) provides the local values of time averaged mass fraction of fuel. The mass fraction of other species can be obtained from the solution of the mixture fraction Equation (3.4.6). The mass fraction of oxygen is calculated from the definition of f:-

$$f = \frac{(m_{fu} - m_{ox}) - \Phi_A}{\Phi_F - \Phi_A}$$

and the mass fraction of products from the expression:-

$$m_{pr} = 1 - m_{ox} - m_{fu}$$

3.5 The Spray Model

The spray model is used to represent, both physically and mathematically, the fuel spray and the way by which the different exchange processes (of mass, heat and momentum) between the fuel droplets and the surrounding gas field are accounted for. Both are generally described in the next Subsections 3.5.1 and 3.5.2. The equations used to describe the behaviour of the fuel droplets are represented in Subsection 3.5.3. The droplet-tracking technique adopted in the present model and the droplet source terms which provide the means for coupling the gas and droplet fields are presented in Subsections 3.5.4 and 3.5.5 respectively.

3.5.1 Treatment of the Fuel Spray

The present model assumes that fuel is injected into the combustion space as a fully atomized spray which consists of spherical droplets. This assumption is reasonable especially for cases where good atomization is achieved and where the droplet deformation is negligible, i.e. the droplet Weber's number is small ($We < 20$), see Williams (1962). The Weber number is defined as:-

$$We = \frac{D_p \cdot \rho \cdot U_r}{S}$$

where D_p is the droplet diameter, ρ is the gas density, U_r is the droplet relative velocity and S is the surface tension. The droplet-size-distribution within the spray can be represented, for example,

by a correlation of the following form, see Abu-Elleil (1974):-

$$\frac{dn}{n} = A \left(\frac{D_p}{D_{32}}\right)^{\alpha} \cdot \exp\left[-B \left(\frac{D_p}{D_{32}}\right)^{\beta}\right] \cdot \frac{dD_p}{D_{32}}$$

where:-

dn, n = Number of droplets in the size range $D_p - D_p + dD_p$ and total number of droplets respectively.

D_{32} = Sauter mean diameter.

α, β = Constants to be determined experimentally.

A, B = Constants depending on α, β.

Fig. 3.1 shows a typical droplet size distribution for D_{32} = 188 μm, α = 3.5 and β = 0.4. In the present model the size distribution within the spray is assumed to be represented by a finite number of size ranges, for example as shown in Fig. 3.1. It is clear that the number of size ranges to be selected will be limited by the computing time and storage requirements and by the required level of accuracy. For each size range droplet trajectories, velocities, size and temperature history within the flame can be obtained by solving the respective balance equations for the droplet representing this size range. It must be recognised that fuel sprays emerging from most practical atomizers encompass a wide range of droplets size, velocity and probably shape and although the approach adopted in the present model assumes the representation of the spray by the size of droplets contained within it only, the spread in the droplets injection velocity is, however, implicitly considered. This can be done through assigning different initial velocities for the droplet representing a certain size range.

3.5.2 The Coupling Between Droplet and Gas Fields

The solution of the governing equations for the gas field incorporates a finite difference procedure where a staggered-grid is used to divide the flow field into computational cells (control volumes) for the application of the conservation principles, see Section 3.8 and Fig. 3.2. The knowledge of the droplet properties (size, velocity, number, etc.) at the cell boundaries, see Fig. 3.2, allows the calculation of the loss or gain of the droplet mass, heat and momentum within each cell which appears as source or sink terms in the corresponding finite difference equations for the gas phase. These source terms represent the link between the droplet and gas fields. Droplet properties at cell boundaries are obtained from the solution of the droplet equations coupled with a droplet tracking technique, see Section 3.5.4.

The coupling between the solution of the two fields requires: solution of the droplet-free gas-field to provide local gas properties which are used in the solution of the droplet equations. The droplet-source terms are then calculated and the corrected gas-field solution obtained with the interaction between droplets and surrounding gas considered. This process is repeated iteratively until all equations are satisfied as will be indicated in Section 3.8.4.

The present model is limited to dilute sprays and this implies the neglect of any effect of droplets on the turbulent behaviour and properties of the gas-phase and the cancellation of terms, representing direct and indirect interactions between droplets in the droplet equation of motion. For most practical sprays this assumption is reasonable except for short regions in the vicinity of the atomizer.

The calculation of the droplet source terms requires knowledge of the rate of number of droplets entering and leaving each

calculation cell; it is assumed that the number of droplets associated with each size range is constant along its trajectory and this implies that turbulent diffusion of droplets and the effects of droplet collision and break-up are neglected. Hotchkiss et al (1972) considered droplet diffusion and modelled an extra term, which include a random function, in the droplet-equation of motion and used a considerably large number of size ranges. However, in cases where the velocity-slip between the droplet and surrounding gas is of appreciable magnitude, the neglect of diffusion has only a small effect on the calculations. In most practical burners, this condition prevails especially at near-atomizer locations.

3.5.3 Mathematical Analysis of the Droplet-Field

The coupling between the droplet and gas phases, through the droplet source terms, necessitates the determination of the droplet location, size, temperature and velocity within the combustion domain. This could be done by tracking different droplets throughout their movement inside the calculation domain. Consequently, a Lagrangian framework is used to describe the droplet behaviour.

Momentum Balance Equations

For each droplet representing a size range and moving in the i-direction in the gas field, the momentum balance equation, see for example Hinze (1971), is written as:-

$$m_p \frac{d}{dt} (U_{p,i}) = F_i \qquad (3.5.1)$$

where m_p is the droplet mass and $U_{p,i}$ is the droplet velocity in the i-direction. The force, F_i, acting on the droplet has many contributions

which have to be approximated. They include:-

(a) The flow resistance due to the rectilinear motion of the droplet relative to the fluid, i.e. the drag force which, for a spherical droplet, is equal to:-

$$F_D = f(Re_\ell) \cdot D_p \cdot \mu \cdot U_{r,i}$$

Re_ℓ is the droplet Reynolds number based on its diameter, D_p, and its relative velocity to the gas-field, $U_{r,i}$. For a laminar, Stoke's, resistance:-

$$f(Re_\ell) = \text{Constant}$$

and for the case of a quadratic resistance law:-

$$f(Re_\ell) = \text{Constant} \cdot Re_\ell$$

(b) Forces due to gravity ($m_p \cdot g$), pressure gradient in the surrounding fluid in the direction of motion, $\left(-\frac{m_p}{\rho_p} \cdot \frac{\partial P}{\partial x}\right)_i$, and inertial forces due to the rotation of a droplet relative to a fixed axis.

(c) Forces due to direct and indirect interactions with all other neighbouring droplets.

In the present model the drag, inertial and pressure forces are taken to be the only contributions to the total force function F_i. The droplet momentum balance Equation (3.5.1), after substitution of

the appropriate force expressions, can be rewritten in the three cylindrical coordinate directions x, r, θ as follows:-

$$\frac{dU_p}{dt} = -\frac{1}{\rho_p} \cdot \left(\frac{\partial P}{\partial x}\right) + \frac{6\mu}{\pi\rho_p \cdot D_p^2} \cdot (U - U_p) \cdot f\,(Re_\ell) \qquad (3.5.2)$$

$$\frac{dV_p}{dt} - \frac{W_p^2}{r_p} = -\frac{1}{\rho_p}\left(\frac{\partial P}{\partial r}\right) + \frac{6\mu}{\pi\rho_p \cdot D_p^2} (V - V_p) \cdot f\,(Re_\ell) \qquad (3.5.3)$$

$$\frac{dW_p}{dt} + \frac{V_p \cdot W_p}{r_p} = \frac{6\mu}{\pi\rho_p \cdot D_p^2} (W - W_p) \cdot f\,(Re_\ell) \qquad (3.5.4)$$

The function $f\,(Re_\ell)$, appearing in the drag force, was calculated from a quadratic resistance law, i.e.:-

$$f\,(Re_\ell) = \frac{\pi}{8} \cdot C_D \cdot Re_\ell$$

Several correlations for the drag coefficient, C_D, can be found in the literature, see for example, Williams (1965), Ingebo (1962) and Ioannides (1978). A correlation which has been used by several investigators and found to be reasonably accurate is used in the present study, see Williams (1973), i.e.:-

$$C_D = 27.0\ Re_\ell^{-0.84} \qquad 0 < Re_\ell < 80$$

$$= 0.271\ Re_\ell^{0.217} \qquad 80 < Re_\ell < 10^4$$

$$= 2.0 \qquad Re_\ell > 10^4$$

The effects of evaporation and droplet distortion on C_D are included implicitly in the above correlation.

Droplet-Size-Change Expression

The size of a droplet changes during its movement within the flame as a result of evaporation which is influenced by the heat supplied by the surrounding gases. Most of the work reported in the literature concerning droplet evaporation, see for example, Williams (1965), Ohta (1975) and Spalding (1953), relates to single, isolated droplet in a stagnant or moving gas stream. However, the interaction between adjacent droplets in burning sprays influences the evaporation characteristics of individual droplets, see Williams (1973) and Ioannides (1978). Although some attempts have been made to obtain data concerning evaporation of droplet-arrays and groups, see Samson et al (1978a, 1978b) and Chiu et al (1977), the treatment of evaporating droplets within a spray is extremely difficult and very rare in the literature.

In the present spray model an expression based on single droplets has been used for reasons of simplicity, see Spalding (1953), with the implication of insignificant influence of the interaction. However, it should be emphasised that, with better understanding of droplets evaporation within sprays, more advanced expressions can be embodied in the present solution procedure. The mass transfer rate from the liquid to the gas phase is given by:-

$$\dot{m}_p = 2\pi D_p \cdot \frac{k}{c_p} \cdot \ln (1 + B) \qquad (3.5.5)$$

where the transfer number B is:-

$$B = c_{p_v} (T - T_{sat.}) / L$$

This expression for the transfer number, B, has been derived for evaporating droplets in the absence of chemical reaction around the droplet. The influence of the excess heat of reaction, associated with the occurrence of chemical reaction, on the evaporation rate of a droplet has been considered by previous investigators, see for example, Ohta (1975) and Spalding (1953), but, again, for single, isolated droplets with the assumption of enveloping flame surrounding the droplet. The transfer number in this case, see Spalding (1953), is:-

$$B = c_{p_v} (T - T_{sat.}) / L + \left[\frac{m_{ox}}{i} \cdot H_{fu} \right] / L$$

The present spray model assumes cloud-burning of droplets rather than burning with individual enveloping flames and, therefore, the first expression of B has been used throughout the present study.

$\dot{m}_p$ can also be expressed as:-

$$\dot{m}_p = - \frac{\pi}{2} \cdot \rho_p \cdot D_p^2 \cdot \frac{dD_p}{dt} \qquad (3.5.6)$$

from Equations (3.5.5) and (3.5.6). The rate of change of droplet diameter with time, dD_p/dt, can be expressed as:-

$$\frac{dD_p}{dt} = - \frac{4 \cdot k}{\rho_p \cdot c_p} \cdot \frac{1}{D_p} \cdot \ln (1 + B) = \frac{- 32}{D_p} \cdot k_e$$

where k_e is the evaporation rate constant for stagnant conditions. For moving droplets k_e is corrected by the following expression, see Ingebo (1962):-

$$k_{ef} = 0.5 (2.0 + 0.56 \, Re_{\ell}^{0.5}) \cdot k_e$$

Then:-

$$\frac{dD_p}{dt} = \left[- \frac{2 \cdot k}{\rho_p \cdot c_p} (2.0 + 0.56\ Re_\ell^{0.5}) \cdot \ln (1 + B) \right] \cdot \frac{1}{D_p} \qquad (3.5.7)$$

Thermal Balance Equation

The droplet temperature during the preheating period, prior to the start of evaporation, is determined by solving the thermal balance equation for a droplet moving in a gas stream. By assuming that the prevailing mode of heat transfer is forced convection, no evaporation takes place during the preheating period and the temperature is uniform across the droplet radius; the resulting thermal balance differential equation is:-

$$\frac{dT_p}{dt} = \frac{6}{D_p \cdot \rho_p \cdot c_{p_p}} \cdot h\ (T - T_p) \qquad (3.5.8)$$

where h is the heat transfer coefficient, Ingebo (1962), i.e.:-

$$h = Nu \cdot \frac{k}{D_p} = \frac{k}{D_p} (2.0 + 0.56 \cdot Re_\ell^{0.5})$$

where Nu is the Nusselt number. Equation (3.5.8) can be rewritten as:-

$$\frac{dT_p}{dt} = \frac{6.0}{D_p \cdot \rho_p \cdot c_{p_p}} \cdot \frac{k}{D_p} (2.0 + 0.56 \cdot Re_\ell^{0.5}) \cdot (T - T_p) \qquad (3.5.9)$$

Equations (3.5.2) - (3.5.4), (3.5.7) and (3.5.9) represent a closed set of equations which, with appropriate initial conditions and knowledge of gas properties, provide the variation of the droplet

velocity, size and temperature in the time domain. The corresponding droplet properties in the space domain are obtained by using a droplet-tracking technique, for example, that described in the next subsection.

3.5.4 Droplet-Tracking

The simultaneous differential Equations (3.5.2) - (3.5.4), (3.5.7) and (3.5.9), are solved numerically using a Runge-Kutta-4 method. The coefficients of the droplet equations are updated each time step of the calculation according to the position of the droplet in the flow field. The numerical procedure provides the axial, radial and tangential droplet velocity components at the start and end of each time step. These velocity components are used through a tracking method to determine the position of the droplet relative to the gas field where the following relations are used, see Fig. 3.2,:-

$$X_{end} = X_{start} + 0.5\ (U_{start} + U_{end})\ .\ \Delta t \qquad (3.5.10)$$

$$Y_{end} = Y_{start} + 0.5\ (V_{start} + V_{end})\ .\ \Delta t \qquad (3.5.11)$$

Droplet properties at the end of the time step are stored at X_{end}, Y_{end}. In cases where a swirling fuel spray is used axisymmetry is assumed and, although the droplets are moving in a spiral-like motion, their position is identified only by the two coordinates X and Y.

The treatment of droplets impinging on the combustion chamber walls is one of the important difficulties in modelling spray flames. In the present method, the calculations proceed by assigning a negative value for the radial velocity component and reducing the three velocity components by a factor accounting for the loss of

momentum upon impingement if droplets are found to cross the wall.

3.5.5 Interaction Source Terms

Droplet-tracking allows the recording of the size, velocity and position of the droplet in the calculation domain which is divided into computational cells, see Section 3.8 and Fig. 3.2. Droplet source terms are obtained by calculating the loss or gain of the droplet mass, enthalpy and momentum within each cell. Summing the respective source terms for droplets representing different size ranges gives the total droplet-source terms.

The mass exchange rate between the droplet and gases in a cell is given by the expression, Crowe (1974):-

$$S_{dM} = \sum_{L=1}^{N} (\dot{m}_{d_i} - \dot{m}_{d_o})_L \qquad (3.5.12)$$

where $\dot{m}_{d_i}$ and $\dot{m}_{d_o}$ are the mass flux of the droplet at entry and exit to the cell respectively, and N is the total number of size ranges representing the spray. Also:-

$$\dot{m}_{d_L} = \frac{\pi}{6} \cdot \rho_p \cdot D_{pL}^3 \cdot \dot{n}_L$$

where $\dot{n}_L$ is the number of droplets issuing from the spray nozzle per second and having diameters correspond to the size range, L.

The momentum exchange rates are given as, for the axial momentum:-

$$S_{dU} = \sum_{L=1}^{N} (\dot{MU}_{do} - \dot{MU}_{di})_L \qquad (3.5.13)$$

where $\dot{MU}_{do}$ and $\dot{MU}_{di}$ are the axial momentum fluxes of the droplet at exit and entry to the cell respectively, and:-

$$\dot{MU}_{dL} = \frac{\pi}{6} \rho_p D^3_{p_L} \cdot U_{p_L} \cdot \dot{n_L}$$

Similarly:-

$$S_{dV} = \sum_{L=1}^{N} (\dot{MV}_{do} - \dot{MV}_{di})_L \qquad (3.5.14)$$

and:-

$$S_{dW} = \sum_{L=1}^{N} (\dot{MW}_{do} - \dot{MW}_{di})_L \qquad (3.5.15)$$

The total enthalpy exchange rate is given by:-

$$S_{dH} = \sum_{L=1}^{N} (\dot{m_{d_i}} - \dot{m_{d_o}}) \cdot (H_{fu} - L) \qquad (3.5.16)$$

3.6 Radiation Model

The radiant energy transfer within an emitting-absorbing-scattering medium is represented by the following balance equation, see for example, Viscanta (1966), Bartelds (1976) and Truelove et al (1976), for the monochromatic radiant intensity in a specified direction:-

$$(\underset{\sim}{\Omega} \cdot \underset{\sim}{\nabla}) I_\lambda (\underset{\sim}{r}, \underset{\sim}{\Omega}) = - \left[k_{\lambda a}(\underset{\sim}{r}) + k_{\lambda s}(\underset{\sim}{r})\right] I_\lambda (\underset{\sim}{r}, \underset{\sim}{\Omega}) +$$

$$+ k_{\lambda a}(\underset{\sim}{r}) I_b (\underset{\sim}{r}) + k_{\lambda s}(\underset{\sim}{r}) \int_{4\pi} I_\lambda (\underset{\sim}{r}, \underset{\sim}{\Omega}) \, d\underset{\sim}{\Omega}$$

For most practical combustion systems, the equation could be reasonably simplified by assuming a gray, non-scattering medium. Therefore:-

$$(\underset{\sim}{\Omega} \cdot \underset{\sim}{\nabla})\ I\ (\underset{\sim}{r}, \underset{\sim}{\Omega}) = -\ k_a(\underset{\sim}{r})\ .\ I\ (\underset{\sim}{r}, \underset{\sim}{\Omega}) + k_a(\underset{\sim}{r})\ .\ I_b\ (\underset{\sim}{r}) \qquad (3.6.1)$$

where $I\ (\underset{\sim}{r}, \underset{\sim}{\Omega})$ is the total radiant intensity at position $\underset{\sim}{r}$ in direction $\underset{\sim}{\Omega}$, $k_a(\underset{\sim}{r})$ is the absorption coefficient of the medium, and $I_b\ (\underset{\sim}{r})$ $\left[\equiv \sigma T^4(\underset{\sim}{r})/\pi\right]$ is the total intensity of black body radiation at the temperature of the medium. The expression on the left is the gradient of the intensity in the direction $\underset{\sim}{\Omega}$; the two terms on the right represent the changes in intensity due to absorption and emission respectively.

As the radiation energy is distributed in all directions, integration of Equation (3.6.1) over the solid angle of 4π yields the complete radiation field, i.e.:-

$$\int_{\underset{\sim}{\Omega}=0}^{4\pi} (\underset{\sim}{\Omega} \cdot \underset{\sim}{\nabla})\ .\ I\ (\underset{\sim}{r}, \underset{\sim}{\Omega})\ .\ d\underset{\sim}{\Omega} = -\int_{\underset{\sim}{\Omega}=0}^{4\pi} k_a(\underset{\sim}{r})\ .\ I\ (\underset{\sim}{r}, \underset{\sim}{\Omega})\ .\ d\underset{\sim}{\Omega} +$$

$$\int_{\underset{\sim}{\Omega}=0}^{4\pi} k_a(\underset{\sim}{r})\ .\ I_b\ (\underset{\sim}{r})\ .\ d\underset{\sim}{\Omega} \qquad (3.6.2)$$

Equations (3.6.1) and (3.6.2) are completely equivalent descriptions of radiative transfer and each with appropriate boundary conditions can be readily solved.

The difficulty of solving the multi-dimensional radiative transfer Equations (3.6.1) and (3.6.2) has led to the development

of a number of approximate methods of solution. Of these, the zone method; see Hottel et al (1967), which represents a numerically exact treatment of the integro-differential equation, has been applied extensively and successfully to the prediction of radiant heat transfer in furnaces, for example, see Johnson et al (1974). The method is based on the integral form of the radiation transport equation and for this reason does not couple easily to the differential equations for flow and chemical reaction. The Monte-Carlo method, see Howell (1968), is well suited to the calculation of radiant heat transfer within complex enclosure geometries. However, it can be subject to significant statistical error unless a large number of events are sampled and as a consequence, the computing time and storage requirements of the method is considerably large. Flux methods, of which the method adopted in the present work, are based on the use of some simplifying assumptions for the angular variation of the radiant intensity. This allows the exact integro-differential radiant transport equation to be reduced to a system of approximate differential equations in the space variables only which are compatible with numerical technique used for the fluid flow.

The radiation model of the present study is based on the flux model proposed by de Marco and Lockwood (1975) where the directional dependence of the radiant intensity is approximated by a truncated Taylor series expansion as:-

$$I\ (\underset{\sim}{r},\ \underset{\sim}{\Omega}) = A_1\ \mu + A_2\ \eta + A_3\ \xi + B_1\ \mu^2 + B_2\ \eta^2 + B_3\ \xi^2 \qquad (3.6.3)$$

where A_1, A_2, A_3, B_1, B_2 and B_3 are functions of the space variable $\underset{\sim}{r}$ only, and (μ, η, ξ) are the direction cosines of the unit vector $\underset{\sim}{\Omega}$. A set of flux equations is obtained by substituting $I\ (\underset{\sim}{r}, \underset{\sim}{\Omega})$ from

Equation (3.6.3) into the transport Equation (3.6.1) and integrating over six selected solid angles. Further details of this procedure are described by Lockwood et al (1976). For axisymmetric geometries and with the assumption of an absorbing-emitting non-scattering gray gas in local thermodynamic equilibrium, the flux equations can be written as, see Khalil (1976):-

$$\frac{\partial}{\partial x}\frac{1}{k}\frac{\partial R_x}{\partial x} = \frac{4}{3}\,k\,(2R_x - R_r - \sigma\,\bar{T}^4) \qquad (3.6.4)$$

$$\frac{1}{r}\frac{\partial}{\partial r}\frac{r}{k}\frac{\partial R_r}{\partial r} = \frac{4}{3}\,k\,(2R_r - R_x - \sigma\,\bar{T}^4) \qquad (3.6.5)$$

where R_x and R_r are respectively the total axial and radial radiation fluxes defined in terms of the B's as $R_x = \frac{\pi}{4}(B_1 + B_2 + 2B_3)$ and $R_r = \frac{\pi}{4}(2B_1 + B_2 + B_3)$. k is the absorption coefficient. It should be noted that Equations (3.6.4) and (3.6.5) have the same form as the general Equation (3.2.12) which describes the conservation principles for the gas field. The radiant energy contribution to the source term in the enthalpy equation is expressed as:-

$$S_H = \frac{16}{9}\,.\,k\,(R_x + R_r - 2\sigma\,\bar{T}^4) \qquad (3.6.6)$$

The boundary conditions for the flux Equations (3.6.4) and (3.6.5) may take the form of a prescribed wall temperature or a prescribed wall radiant heat flux. The former was used in the present study and the appropriate expressions are described by Khalil (1976).

The radiative characteristics of the gas medium are represented here by a single gray gas with an absorption coefficient, k, obtained by matching a single gray gas representation to the multi-

gray gas representation at a path length equal to the mean beam length for the enclosure and a temperature equal to the mean radiating temperature of gases, see Truelove (1976) for details of the calculations. The effect of droplet and luminous radiation was not included in the present study. With these assumptions, the value of k was found to be around 0.3 m^{-1}. The effective wall emissivity was assumed as 0.8.

3.7 Summary of the Mathematical Formulation

The mathematical formulation described in the preceding sections can be summarized as follows, see Table 3.1. The three velocity components U, V and W and pressure P are obtained from the corresponding momentum and continuity (pressure correction equation described in the next section) equations as indicated in Table 3.1. The effective viscosity appearing in these equations is calculated from:-

$$\mu_{eff.} = \mu_{lam.} + \mu_T = \mu_{lam.} + C_\mu \cdot \rho \cdot \frac{k^2}{\varepsilon}$$

The kinetic energy of turbulence, k, and its rate of dissipation, ε, (turbulence model) are calculated from Equations (3.3.4) and (3.3.5), see Table 3.1. The local gas density, ρ, also appearing in the above equations is determined from the equation of state for a perfect gas:-

$$\rho = P \; / \; (\bar{R} \; . \; T/M_{mix})$$

where $\bar{R}$ is the universal gas constant and M_{mix} is the mixture molecular weight defined as:-

$$1/M_{mix} = \sum_{\text{all } i} m_i/M_i$$

with m_i the mass fraction of species i calculated through the "combustion model". In the case of the double-delta pdf model, this involves the solution of the mixture fraction Equation (3.4.6) and the transport equation for its variance, g, Equation (3.4.8) and utilizing Equation (3.4.9). Where the eddy-dissipation combustion model is used, the mass fraction of species i, m_i, is obtained from the solution of the mixture fraction Equation (3.4.6) and the conservation Equation (3.4.1) for the mean fuel concentration, see Table 3.1. The gas mean temperature, T, in the density expression is obtained from the enthalpy Equation (3.4.1) given in Table 3.1. The mixture enthalpy in the present study is defined as:-

$$h \equiv \sum_{\text{all } i} m_i \int_{T_{ref}}^{T} c_{p_i}(T) \cdot dT + m_{fu} \cdot H_{fu}$$

The reference temperature, T_{ref}, is taken in this study as 300 ^{o}K. The constant pressure specific heat of the species i, c_{p_i}, is determined from third order polynomials in temperature given by Tribus (1961). In cases where radiation is neglected the enthalpy equation is solved with a zero source term. If radiation is important the enthalpy equation is solved with the source term given by expression (3.6.6). The axial and radial total radiation fluxes in that expression are calculated from Equations (3.6.4) and (3.6.5).

The droplet source terms appearing in all the above equations are obtained from the solution of the droplet Equations (3.5.2) - (3.5.4), (3.5.7) and (3.5.9) and by using expressions (3.5.12) to (3.5.16).

The elliptic nature of the differential equations described above requires that each dependent variable, or its gradient, be

specified on all sides of the solution domain. In the present study, wall and symmetry-line values were easily prescribed and zero-axial gradients were prescribed at downstream locations where this assumption did not influence the upstream calculated results. Specific comments on the treatment of boundary conditions are given in Section 3.8.5.

Upstream flow boundary conditions are based on experimental information, where available, and on sensible guesses where not. The use of a sensible guess implies that its influence should be tested. In general, the flow boundary conditions for turbulence quantities are of secondary importance and are estimated on the basis of a mixing-length hypothesis. The values of the mean-velocity components are more important and specific comments will be made when the results are presented.

3.8 Numerical Solution Procedure

3.8.1 Preliminary Remarks

The mathematical formulation outlined in Section 3.7 calls for the solution of a coupled set of partial differential equations describing both the main conservation principles of mass, heat and momentum and the various physical models employed, including the turbulence, combustion and radiation models. In addition, it requires the solution of a different set of first order differential equations which describe the behaviour of the fuel spray and provide the droplet-gas interaction source terms required in the former set of equations. Solution methods for first order differential equations similar to those representing the fuel spray are well documented in the literature, see Korn et al (1961). The method used in the present work was briefly stated in Subsection 3.5.4. The present section concentrates on the solution procedure adopted for the gas-phase equations.

The coupled set of elliptic partial differential equations to be solved can be cast in a general form, as indicated previously in Section 3.2, i.e.:-

$$\frac{\partial}{\partial x}(\rho U\Phi) + \frac{1}{r}\frac{\partial}{\partial r}(r\rho V\Phi) = \frac{\partial}{\partial x}\left(\Gamma \frac{\partial \Phi}{\partial x}\right) + \frac{1}{r}\frac{\partial}{\partial r}\left(r\Gamma \frac{\partial \Phi}{\partial r}\right) + S + S_d \qquad (3.8.1)$$

Table 3.1 gives the details of the Φ's, Γ's, S and S_d.

A finite-difference procedure has been used to solve the equation set (3.8.1) where the flow domain is sub-divided into a number of finite volumes or "cells". The finite-difference counterpart of the axially-symmetric Equation (3.8.1) is derived by integration over the cell surrounding the variable under consideration and then approximation of the resulting flux and source integrals. The final set of "algebraic" finite-difference equations were solved by an iterative procedure through the TEACH-Code computer program of Gosman et al (1973).

3.8.2 The Finite-Difference Grid

In order to derive the finite-difference analogue of the differential equations, a rectangular, two-dimensional grid was formed by the coordinate lines of an x-r cylindrical frame as shown in Fig. 3.3.. A typical node, P, and its neighbours labelled E, W, N and S, represent the locations at which all variables except the velocity components, U and V, were calculated. The control volumes for the axial and radial velocity components are shown in Fig. 3.3. The U and V velocities were stored and calculated at points which lie mid-way between the grid nodes and are denoted by the arrows in Fig. 3.3. The points mid-way between P and its neighbours are labelled e, w, n and s.

3.8.3 The Finite-Difference Equations

Integration of the differential Equation (3.8.1) over the control volume appropriate to each dependent variable yields:-

$$\sum_{\text{all b}} \left[\int_{A_b} \left(\rho U_j \Phi - \Gamma_{\Phi,j} \cdot \frac{\partial \Phi}{\partial x_j} \right) \right] dA_b + \int_{V_p} S_\Phi \cdot dV = 0 \qquad (3.8.2)$$

where the summation is over all the four boundaries of the cell, A_b is the area of the cell boundary and U_j and x_j are the velocity and coordinate normal to that boundary. V_p is the cell volume. The four integrals of the first term can now be approximated by way of a combined flux, J, due to convection and diffusion at the four faces of the cell. For example, the flux J_w at the w-face of a cell containing the variable Φ can be expressed as:-

$$J_w = (\rho UA)_w \cdot \left(f_w \Phi_w + (1 - f_w) \cdot \Phi_p \right) \qquad (3.8.3)$$

where f is a weighting factor defined so as to give central differencing, i.e.:-

$$f_w \equiv \frac{1}{2} (1 + Re_w^{-1})$$

where Re is the cell Reynolds number which for the w-face of the cell is:-

$$Re_w \equiv (\rho U)_w \cdot \delta x / \mu_{eff}$$

where δx is a characteristic dimension of the cell in the velocity direction.

The integral of the second term of Equation (3.8.2) is expressed in linearised form as:-

$$\int_{V_p} S_\Phi \cdot dV = S_P \cdot \Phi + S_u \qquad (3.8.4)$$

This linearisation of the source term S_Φ was found to promote stability especially when S_Φ is itself a function of Φ, see Gosman et al (1973).

The resultant finite-difference equation with allowance for droplet-gas coupling can be expressed as:-

$$J_E - J_W + J_N - J_S = S_P \cdot \Phi + S_u + S_d \qquad (3.8.5)$$

where S_d stands for the droplet-source terms. The finite-difference equation for mass conservation is:-

$$G_E - G_W + G_N - G_S = S_{d_M} \qquad (3.8.6)$$

where S_{d_M} is the droplet mass source term and G is the mass flow rate through the cell boundaries.

Substituting the total flux expressions (3.8.3) into Equation (3.8.5) and utilizing Equation (3.8.6) yields:-

$$A_P \cdot \Phi_P = \sum_j A_j \cdot \Phi_j + (S_P - S_{d_M}) \cdot \Phi_P + S_u + S_d \qquad (3.8.7)$$

where:-

$$A_P = A_W + A_E + A_S + A_N$$

and:-

$$A_W = G_W \cdot f_w \quad , \quad \text{similarly } A_S$$

$$A_E = G_E \, (f_E - 1) \quad , \quad \text{similarly } A_N$$

The summation $\sum_j$ is carried for all cell faces.

Equation (3.8.7) is the general finite-difference equation which is used to solve for the dependent variables U, V, W, $\tilde{h}$, f, R_x, R_y, g, m_{fu}, k and ε together with the pressure correction referred to in Section 3.8.4.

3.8.4 The Solution of the Finite-Difference Equations

The finite-difference Equation (3.8.7) was solved for all the dependent variables by an iterative method known as "SIMPLE" (for Semi Implicit Pressure Linked Equations), see Caretto et al (1973). It is a semi-implicit procedure that starts from guessed initial fields for all the dependent variables, and iterates progressively towards the final solution.

3.8.4.1 Solution Algorithm for Velocities and Pressure

The local pressure values appearing in the S_u term of the differential Equation (3.8.1), written for the axial and radial velocity components, are required to be accurately calculated so that the solution yields velocities which satisfy the continuity equation. The pressure, however, does not possess a differential equation in which it is dominant. This problem was treated in the present procedure by applying the pressure-correction method described by Caretto et al (1973). The method can be described as follows. The

momentum equations are solved for a guessed pressure field, denoted by P*, and the solution yields preliminary velocities, U*, V* and W*, which in general, will not satisfy the continuity equation because the initially assumed pressure field is incorrect. These velocities are linked to corrections P′ to the pressure field to satisfy the continuity equation. These pressure corrections are derived from both the continuity and momentum equations as described in the following part.

The velocities U* and V* should satisfy the finite-difference momentum equations, i.e.:-

$$U_p^* = \beta_u + D_u (P_W^* - P_P^*) \tag{3.8.8a}$$

$$V_p^* = \beta_v + D_v (P_S^* - P_P^*) \tag{3.8.8b}$$

where β_u and β_v include all the terms in Equation (3.8.7), written for U and V, that do not appear in the right-hand sides of Equation (3.8.8). D_u and D_v are constants appearing in the pressure term of S_u in Equation (3.8.7), written for U and V respectively. The subscripts at the base of the pressures denote their relative positions with respect to the velocity node, P, as indicated in Fig. 3.3. Equation (3.8.8) expresses linear relations between the velocity components, and the local pressures. Consequently, a change in the local pressure of P′ results in new velocities linked to the old ones through:-

$$U_p = U_P^* + D_u (P_W' - P_P') \tag{3.8.9a}$$

$$V_p = V_P^* + D_v (P_S' - P_P') \tag{3.8.9b}$$

The pressure corrections P' are then required to be calculated such that the velocities obtained from Equation (3.8.9) satisfy the finite-difference form of the continuity equation, i.e.:-

$$G_E - G_W + G_N - G_S = S_{d_M} \tag{3.8.10}$$

where G is the mass flow across the surfaces of the control volume. For example:-

$$G_E = \rho A \cdot U\Big)_E$$

Substituting the right-hand side of Equation (3.8.9) for the velocities in Equation (3.8.10) results in the following equation for P' at each main grid node:-

$$A_p \cdot P'_P = \sum_J A_J \cdot P'_J + S_o \tag{3.8.11}$$

where:-

$$A_J = \rho A \, D_{\frac{U}{V}}\Big]_J$$

and:-

$$A_p = \sum_J A_J$$

$$S_o = - \sum_J G^*_J + S_{d_M}$$

The summation $\sum_j$ is carried for all cell faces.

Equation (3.8.11) is the required pressure correction equation whose solution leads to the desired pressure corrections which are used to adjust the guessed pressure values according to the relation:-

$$P_P = P_P^* + P_P' \qquad (3.8.12)$$

and the velocity values according to Equation (3.8.9).

3.8.4.2 The Calculation Sequence

The solution procedure for all the dependent variables proceeds by the iterative repetation of the following steps:-

1. First, U*, V* and W* are calculated from the corresponding finite-difference equations using P*'s, which may be initial guesses or values from a previous iteration.

2. The pressure correction Equation (3.8.11) is solved, and then the pressure and velocity fields are corrected using Equations (3.8.12) and (3.8.9).

3. The general finite-difference Equation (3.8.7) is then solved successively for the remaining dependent variables and the auxiliary quantities such as viscosity and temperature are calculated.

4. The resulting field of variables is now used as the starting point for the next iteration and this process is repeated,

with updating of the coefficients of the difference equations, until the latter are adequately satisfied by the prevailing solution.

The solution is considered as satisfied when the summation, over all the calculation cells, of the residuals of Equation (3.8.7) normalized by a representative value at the inlet (e.g. mass flow rate for the mass residual) is smaller than a pre-specified value, i.e.:-

$$R_{res.}/R_{ref.} \leq 0.20\%$$

where $R_{res.}$ is defined as:-

$$R_{res.} \equiv \sum_{N} \left[\sum_{J} A_J \cdot \_J + (S_p - S_{d_M}) \Phi_P + S_u + S_d - A_P \cdot \Phi_P \right]$$

and N is the total number of the computational cells. $R_{ref.}$ is a reference value at inlet. The value of the normalized residual gives a measure for the accuracy of the solutions obtained with the present method.

The droplet-gas coupling is incorporated in the above procedure as follows. Isothermal, droplet-free solution of the gas-field is first obtained then droplet trajectories, size and temperature history are calculated through the droplet-field equations, with known gas properties. The droplet-source terms are then calculated for each cell in the calculation domain and fed to the finite-difference Equation (3.8.7) to obtain adjusted values for the dependent variables. These are used again in the solution of the

droplet equations. This process of solving the gas-field equations followed by the droplet equations is repeated until all the equations are satisfied.

3.8.5 Treatment of Boundary Conditions

The practices employed in the present study for the treatment of boundary conditions are outlined in this subsection.

(a) Inlet Plane

At the inflow boundary, a specified distribution of the variable Φ was supplied at all grid nodes in the entry plane of the solution domain.

(b) Walls

At solid boundaries the computational grid is modified as shown in Fig. 3.3, such that the boundary passes through the Φ nodes. Boundary conditions of the specified value type can be applied by assigning the required values of Φ at the boundary node. In the case of a given boundary flux or gradient, the appropriate values are introduced into the finite-difference equation of the near boundary grid node as an additional source term, and the coefficient linking the boundary grid node to the near boundary node is set to zero. Details of the further special practices required for turbulent flows will be given in Section 3.8.6.

(c) Symmetry Plane

At a symmetry plane, the convection and diffusion fluxes are both zero. The condition for convection is imposed by setting the velocity component normal to the boundary to zero. Diffusion can be made zero by way of the flux coefficient at the boundary.

(d) Outlet Plane

Provided that the downstream boundary is located where the velocity normal to the boundary is directed everywhere outwards, the parabolic or boundary layer nature of the flow there ensures that downstream conditions have no influence on the upstream flow; hence, knowledge of these conditions is not required in the calculations. An exception to this rule is the normal velocity, which has to be monitored to ensure overall conservation of mass, heat and fuel mass flow rate. The practice adopted for this quantity ensures that mass conservation is satisfied for the whole solution domain. The velocity imposed at the grid nodes in the outflow plane is deduced by adding to the adjacent upstream velocity an incremental value calculated from:-

$$U_{inc.} = \frac{\dot{m}_{in} - \int_A \rho \cdot U_u \cdot dA}{\int_A \rho \, dA}$$

where $\dot{m}_{in}$ is the net mass inflow across the entry plane of the solution domain. The integral $\int_A \rho \cdot U_u \cdot dA$ represents the calculated net mass outflow at the outlet plane. As the solution proceeds to convergence $U_{inc.}$ tends to zero as overall continuity for the solution domain is achieved. A similar procedure is also applied to ensure overall conservation of heat and mass of fuel.

3.8.6 The Wall Functions

The turbulence model adopted in the present study is appropriate only to flows where the local turbulence Reynolds number ($Re_T \equiv k^{1/2} \cdot \ell/\nu$) is high ($\gtrsim 5000$). However, close to solid walls

viscous effects are dominant (small Re_T) and the assumptions of the turbulence model will be invalid. In addition, both the dependent variables and the exchange coefficients vary steeply in the near-wall region. To overcome these problems, without the need to modify the turbulence model or to use excessively large computer storage and time, Patankar et al (1970) proposed the use of wall-functions in which the dependent variables at the wall are linked to those at the first grid node from the wall by an algebraic relation.

Near a wall, at point P shown in Fig. 3.4, the flow is predominantly parallel to the wall and the shear stress is assumed constant, see for example, Patankar et al (1970). It follows that the wall shear stress can be expressed as a function of the velocity parallel to the wall, i.e.:-

$$\tau_w = U_p \cdot Y_+ / Y_1 \cdot u_+$$

From the logarithmic law of the wall:-

$$u_+ = \frac{1}{\kappa} \ln E\, Y_+$$

and:-

$$Y_+ = Y_1 \cdot \rho \cdot k_p^{1/2} \cdot c_\mu^{1/4} / \mu$$

Therefore:-

$$\frac{U_p}{(\tau_w/\rho)} \cdot c_\mu^{1/4} \cdot k_p^{1/2} = \frac{1}{\kappa} \ln (E \cdot Y_+) \qquad (3.8.8)$$

The suffices w and P refer to the conditions at the wall and the near wall grid node respectively. U is the averaged component of velocity parallel to the wall. Y_1 is the distance from the wall to point P. The constants of the logarithmic law of the wall κ and E, depend on the wall roughness and have values of 0.4175 and 8.8 respectively. The value of the kinetic energy of turbulence at point P, k_p, is calculated from the transport equation of k with the diffusion of energy to the solid wall set to zero. The corresponding value of the dissipation rate of k, ε, is assumed, see Gosman et al (1973), to be calculated from:-

$$\varepsilon \cdot Y_1 = c_\mu^{3/4} \cdot \frac{k_P^{3/2}}{K}$$

The wall function expressed by Equation (3.8.8) represents the dependence of the flux of momentum to the wall on the turbulence characteristics at a point P remote from it. The heat flux to the wall can be represented in a similar manner, i.e.:-

$$\frac{c_p (T_p - T_w)}{(q_w''/\rho)} \cdot c_\mu^{1/4} \cdot k_P^{1/2} = \frac{\sigma_{h,t}}{K} \left(E \cdot c_\mu^{1/4} \cdot k_P^{1/2} \cdot Y_1 \cdot \frac{\rho}{\mu} \right) + P_J$$

where T_w is the wall temperature and q_w'' is wall heat flux per unit area. The value of P_J is obtained from the expression:-

$$P_J = \sigma_{h,t} \frac{\pi/4}{\sin \frac{\pi}{4}} \cdot \left(\frac{A}{K}\right)^{1/2} \cdot \left[\frac{\sigma_h}{\sigma_{h,t}} - 1 \right] \left[\frac{\sigma_{h,t}}{\sigma_h} \right]^{1/4}$$

where A is the Van Driest's constant (= 26 for smooth walls), $\sigma_{h,t}$ is the effective Prandtl number for fully turbulent flows and σ_h is the laminar Prandtl number.

3.8.7 Numerical Stability and Accuracy

The representation of the continuous distributions of the dependent variable, Φ, in terms of values at the discrete grid nodes of the finite difference mesh, and applying interpolation formulae between them, can give rise to numerical errors which lead to instabilities in the solution. These errors are related to the differencing scheme used to derive the finite-difference equations. Spalding (1972), Gosman et al (1973) and Tatchel (1975) considered a simplified problem of steady-state transfer of heat in a one-dimensional moving medium to assess the accuracy of two differencing schemes (central and upwind) by comparison with exact solution. Central differencing scheme was found to be stable and second-order accurate for small values of the cell Reynolds number, $< |2|$, whereas for large values, the accuracy was reduced with consequent instability in the solution. However, for the latter range, upwind differencing was found to be unconditionally stable. As indicated in Section 3.8.3, the formulation of the present finite-difference equations has been based on central differencing. However, to retain the stability features of upwind differencing, it has been used in the present calculations when the cell Reynolds number exceeds $|2|$. Therefore, the weighting factor, f, in Equation (3.8.3) was defined in these cases as:-

$$f \equiv \left.\begin{array}{ll} 1 & \text{for } (\rho U) > 0 \\ 0 & \text{for } (\rho U) < 0 \end{array}\right\} \qquad Re > |2|$$

It is clear in this definition of f that the diffusive contribution to the total flux of Equation (3.8.3) has been neglected to achieve better accuracy as suggested by Spalding (1972) and Gosman et al (1973). It has been, however, shown by Roache (1976), Castro (1978) and

McGuirk et al (1978) that the first-order up-wind differencing approximation of the convection terms have the effect of introducing numerical, or false, diffusion into the equations. The magnitude of the associated errors was found, see for example Taylor (1979), to be dependent on the local flow characteristics and the grid distribution in both the axial and radial directions. For example, it can be large in highly strained regions and where the streamlines do not othogonally cross the finite-difference mesh. These errors can, however, be reduced to an acceptable level by making the grid non-uniform so as to concentrate nodes in regions of high gradients and by performing tests in which the grid dimension is systematically increased until solutions with successive grids are the same. A sample of these tests is presented in Section 3.9.6.

The accuracy of the solution method is also dependent on the extent to which the numerical solution satisfies the finite-difference equations. This can be assessed by ensuring that the residual sources, see Section 3.8.4, for each variable have been reduced to a negligible value. In the present calculations, iterations were continued until the residual mass and momentum sources were both less than 0.2%.

Because of the non-linearities of the partial differential equations and the strong inter-linkages between them, numerical instability may develop leading to divergence of the solution during the computations. The typical practices of employing under-relaxation, appropriate specification of initial fields and the use of sufficient number of iterations in the solution of the algebraic finite-difference equations were adopted in the present work, see for example, Gosman et al (1973). However, the present calculations had practical convergence problems associated with the highly swirling motion of most of the flows considered, large density variations and the explicit way by which the solution of the gas and droplet fields are coupled.

Large values of swirl velocities generate strong centrifugal fields that require steep radial pressure gradients to balance them. Since the pressures are calculated from successive pressure corrections to the initial pressure field, which in this case, is bound to be very different from the true one, large values of pressure corrections are required. These in turn imply large velocity corrections. If these corrections are too large per iteration, the non-linearity of the equations may cause the solution to diverge. The practice employed in the present study to procure stability involves gradual introduction of swirl by increasing the values of the inlet swirl velocity gradually with iteration to the specified value. Convergence problems associated with density variations were treated by heavily under-relaxing the calculation of the local mixture density. A typical under-relaxation factor of 0.2 was used in the present study.

Due to the strong two-way interaction between the fuel spray and surrounding gases and the explicit way of coupling the solution of their respective equations, updating of the droplet source terms every iteration was found to introduce large imbalances

to the finite-difference equations and, therefore, causes numerical instability. Thus, it was found necessary to maintain numerical stability by:-

1. Proceeding with the solution of the droplet-free isothermal gas-field equations until the residual of each equation is less than 2%.

2. Introducing gradually the calculated droplet-source terms to the gas-phase equations and, at the same time, allow 15 iterations of the solution before updating the source terms.

3.9 Validation of the Procedure

3.9.1 Preliminary Remarks

The main object of this section is to assess the ability of the calculation procedure presented in the previous Sections 3.1 - 3.7, to predict the local flow properties of spray flames. The procedure is evaluated against four sets of experimental data obtained for both confined and unconfined flames, different types of fuel atomizers, and with preheating of the combustion air in one case. The experimental data employed stem from the measurements of Chapter 2 and from those reported by Khalil et al (1977), Tuttle et al (1976) and Styles et al (1977). Details of the flame geometries, inlet conditions and measured quantities for the four test cases are summarized in Table 3.3 and Fig. 3.5.

The computational details of the four test cases are presented in Subsection 3.9.2. These include the equations solved, grid distribution, computational time, and boundary conditions. The four test cases are described and the results presented and discussed

in Subsections 3.9.3 through 3.9.10.

3.9.2 Details of the Predictions

Equations Solved

The mathematical model employed in the calculations of the present four cases comprises continuity and the elliptic partial differential equations for U, V, W, k, ε, $\tilde{h}$, f and m_{fu} presented in Section 3.7, see also Table 3.1. As indicated previously, Section 3.4, the combustion model of the first test case was that of Section 3.4.3 and, therefore, the m_{fu} equation was replaced by that for g. The non-swirling flow of the third and fourth test cases results in the elimination of the swirl-velocity, W, equation. The differential equations together with the appropriate boundary conditions are solved by the finite-difference procedure described previously in Section 3.8 through the TEACH-Code computer program of Gosman et al (1973).

Computational Grid

The above equations are solved on a computational grid formed by the coordinate lines of an x-r cylindrical frame. Figs. 3.6 - 3.9 show the grid node distributions used in the present calculations for each of the four test cases.

Boundary Conditions

The values assigned to the dependent variables at the combustion air exit boundary are summarized in Table 3.4 and Fig. 3.10 for all the test cases. Due to the unconfined flame geometry of test case 4, special treatment at the flame boundaries was necessary and specific comments will be made when the results of this case are presented. The boundary conditions and the special treatment at a

wall are the same as those described previously in Section 3.8 and will not be repeated here. For the second test case, the wall-temperature values were taken from Fig. 2.34, see Section 2.4.3. However, for the first and third test cases, experimental information of the wall-temperature distribution were not provided and a constant temperature of 500 ^{o}K and 600 ^{o}K respectively was assigned at the wall-boundary. As the boundary conditions of the fuel spray form an important part of the present calculations they will be described in detail when the different test cases are presented.

Under-Relaxation Factors and Computing Time

The under-relaxation factors employed in the present calculations are given in Table 3.5. The computing time for the present calculations varied according to the number of size ranges considered and the flow features of each test case. Table 3.6 shows samples of the computing time for the different test cases. As indicated, it varies between 6 and 14 minutes of CDC 6600 time.

3.9.3 The First Test Case

Details of the Experiment

The experimental data of this test case were reported by Khalil, K. H. et al (1977) and comprised, as indicated in Table 3.3, detailed measurements of temperature, axial and tangential velocity components within the cylindrical combustor shown in Fig. 3.5. The combustion air entered the chamber through a vaned-swirler having a 45^{o} angle to the direction of the flow. The fuel nozzle, which was placed coaxially with the air swirler, was of the swirl atomization type. As a consequence, the fuel spray produced has a hollow-cone shape. The velocity measurements were obtained by a water-cooled

3-hole pitot probe and a water-cooled suction pyrometer was used for the temperature measurements. The main experimental parameters for this test case are summarized in Table 3.3. A kerosene fuel was used and Table 3.7 provides the details of the physical properties used in the calculations, see Abu El-leil(1974).

Program of Calculations

The characteristics of the fuel spray including the droplet-size distribution and injection velocities at exit from the atomizer, are obtained either through direct measurements or from empirical correlations. In both cases they are subject to large uncertainties as a result of the abilities of available measuring techniques, see for example, Fraser et al (1957), Jones (1976) and Yule et al (1977). Since the spray characteristics and the presumed number of size ranges, see Section 3.5, are required as an inlet condition to the calculation method, a greater part of the calculations performed for this test case was mainly concerned with determining the sensitivity of the calculations to these parameters.

The calculations were performed for six cases, corresponding to the spray inlet conditions summarized in Table 3.8, and allowed the study of the influence of the droplet-size-distribution, injection velocity and the number of size ranges on the predicted results. Also, the influence of combustion on increasing the evaporation rate of individual droplets has been considered.

The Boundary Conditions of the Fuel Spray

The droplet-size-distribution within the fuel spray corresponding to the operating conditions of the present case is shown in Fig. 3.1. It was obtained from the results of Abu El-leil (1974) where measurements of the size-distribution under different

conditions were reported for a fuel atomizer similar to the one used in this case. The following correlation which describes the size-distribution was also reported, i.e.:-

$$\frac{dn}{n} = A \left(\frac{D}{D_{32}}\right)^{\alpha} \cdot \exp\left[- B \left(\frac{D}{D_{32}}\right)^{\beta}\right] \cdot \frac{dD}{D_{32}}$$

The constants α, β and the sauter mean diameter, D_{32}, are related to the operating conditions of the fuel nozzle and are determined experimentally. The experimental results for the present fuel atomizer suggest that α, β and D_{32} can be expressed as:-

$$\alpha = 3.5\ (\Delta P)^{0.24}\ (1.54\ P_a^{-\ 0.18} - 0.54)\left[1.54\left(\frac{T_a}{T_o}\right)^{-\ 0.38} - 0.54\right]$$

$$\beta = 0.4\ (\Delta P)^{0.36}\ (P_a^{-\ 0.125})\left[\left(\frac{T_a}{T_o}\right)^{0.23}\right]$$

$$D_{32} = 188 \Big/ \left[(\Delta P)^{0.35} \cdot P_a^{0.26} \cdot \left(\frac{T_a}{T_o}\right)^{0.56}\right]$$

where ΔP is the pressure drop across the fuel atomizer (atm.), P_a is the combustor pressure (atm.), T_a is the air temperature at the operating condition and T_o is a reference air temperature (T_o = 300 ^{o}K).

The coefficients A and B are functions of α and β, i.e.:-

$$A = \left[\left(\frac{\Gamma\ \{(\alpha + 4)\ /\beta\}}{\Gamma\ \{(\alpha + 3)\ /\beta\}}\right)^{\alpha+1} \cdot \frac{\beta}{\Gamma\left(\frac{\alpha + 1}{\beta}\right)}\right]$$

$$B = \left[\frac{\Gamma\left(\frac{\alpha + 4}{\beta}\right)}{\Gamma\left(\frac{\alpha + 3}{\beta}\right)}\right]^{\beta}$$

where $\Gamma(\alpha, \beta)$ is the Gamma function.

The values of α, β, D_{32}, A and B corresponding to the present case are:-

$\alpha = 3.5$ $\beta = 0.4$ $D_{32} = 188.0\ \mu m$

$A = 4.21 \times 10^6$ $B = 16.98$

The calculations are also performed for a spray with a size-distribution characterised by:-

$\alpha = 2.252$ $\beta = 0.469$ $D_{32} = 127.0\ \mu m$

$A = 0.0203 \times 10^6$ $B = 11.723$

The average total number of droplets in the spray, n^*, is calculated from the expression:-

$$\dot{m}_{fu} = n^* \cdot \frac{\pi}{6} \cdot D_{30}^3 \cdot \rho_d$$

where the mass-median diameter, D_{30}, is given by:-

$$D_{30} = \frac{\Sigma\ D_p^3 \cdot \left(\frac{dn}{n}\right)}{\Sigma\ \frac{dn}{n}}$$

where Σ indicates summation over all size ranges and dn is the number

of droplets in the size range D_p to $D_p + dD_p$.

The droplets axial and tangential velocity components at the fuel nozzle are calculated from the following two expressions reported by Abu El-leil (1974):-

$$u_x = \frac{\dot{m}_{fu}}{\rho_p \cdot \pi \cdot c_c \cdot R_J^2}$$

and:-

$$u_t = c_t \frac{\dot{m}_{fu} \cdot R_i}{\rho_p \cdot \pi \cdot R_p^2 \cdot n_1 \cdot R_J}$$

To account for the spread of the fuel spray downstream of the fuel nozzle, the droplets are assigned a radial velocity component which is calculated from the spray angle, around 65^o in the present case. Droplets representing different size ranges are assumed to have injection angles slightly different from the mean spray angles and consequently, each size range is injected with a different velocity. Details of the droplet velocity are shown in Table 3.8.

3.9.4 Presentation and Discussion of the Results, Test Case 1

The presentation of the results is arranged to allow general comments regarding the comparison between the experimental and predicted results, case 1.A, see Table 3.8, and separate consideration of the influence of the droplet-size-distribution, injection velocity and the evaporation rate expression.

The experimental and predicted results, for the axial velocity, temperature and tangential velocity profiles, at different axial distances from the burner, are shown in Figs. 3.11 and 3.12

respectively and correspond to case 1.A, see Table 3.8. The results of Fig. 3.11 show clearly that the predicted temperature values at regions close to the burner and at small radii of the combustion chamber, $r/r_o < 0.5$, are well below the values obtained experimentally. On the other hand, close to the combustion chamber wall the predicted temperature values are comparatively high. Related discrepancies, due to density effects, are observed in the corresponding axial and tangential velocity profiles, Figs. 3.11 and 3.12. The axial velocity profiles also indicate a comparatively large under-prediction of the size and strength of the central recirculation zone.

The under-prediction of the temperature is probably related to errors in the calculated evaporation and spreading rates of the fuel spray and to the under-prediction of the size and strength of the recirculation zone. The former is likely to stem from uncertainties in the presumed droplet-size-distribution, the calculated droplet velocities and trajectories, and the expression used to calculate the evaporation rate of different droplets. The implication of these will be discussed in the following parts of this subsection. The latter reduces the amount of hot combustion products recirculated from downstream regions of the flame which, otherwise, would cause an increase in temperature at near-burner locations. The experimental results seem to confirm this as the initial high-temperature region is shown to be associated with strong reverse-velocities.

The droplet-trajectories of the 10 size ranges, representing the spray, are shown in Fig. 3.13. It is clear that there is no significant differences between the trajectories of different size ranges and this confirms the expected hollow-cone shape of the spray associated with the present swirl atomizer. Even with a hollow-cone spray and due to the interaction between the spray and the swirling combustion air stream, it was expected that some of the droplet-

trajectories, especially those for small-diameter droplets, would pass through the near-centreline region of the flame. However, the calculated trajectories do not show this tendency which may be a result of inaccurate representation of the droplets injection velocity and of the neglect of the influence of the turbulent gas motion, droplets breaking-up and collision on the droplet motion. This deficiency in the calculated trajectories may explain the observed under-prediction of temperature at regions near to the flame centre-line as insufficient fuel vapour will, therefore, reach this region. It also may explain the predicted high temperature values close to the wall and at small axial distances, $X < 0.17$.

The distribution of the mass fraction of the evaporated fuel along the combustion chamber, is shown in Fig. 3.14 and the corresponding radial distributions are shown in Fig. 3.15. The results of Fig. 3.15 indicate that fuel evaporation starts at around $X = 0.04$ with a low rate which increases with downstream distance and that evaporation takes place up to $X \simeq 0.4$. It is also shown in Fig. 3.14 that 80% of the fuel has evaporated by around $X = 0.6$. The predicted temperature profiles, Fig. 3.11, show comparatively high values at downstream sections, for example at $X = 1.7$, which indicates that combustion continues up to this region. This implies an under-estimation of the calculated spray evaporation rate which is likely to be due to inconsistent spray inlet conditions and/or uncertainties associated with the expression used to calculate droplet evaporation. As droplet evaporation is a function of its diameter, inaccuracy in representing the spray droplet-size-distribution has a large effect on the calculated evaporation rate. The droplet heating-up period prior to evaporation, and its evaporation rate, depends on its relative Reynolds number and consequently droplet injection velocity also contributes largely to the overall evaporation rate of the spray.

The influence of the spray inlet conditions on the predicted results is considered in the following parts of this section.

The under-prediction of the reverse-velocity zone observed in Fig. 3.11, which, as previously mentioned, influences the temperature profiles at small axial distances is associated with uncertainties in the two-equation turbulence model (for kinetic energy and its dissipation rate) employed in the present procedure. Previous numerical calculations employing the same turbulence model, see for example, Khalil (1976), indicated the same trend. It is also likely that inaccuracy in the swirl number quoted in connection with the experimental data (not measured) and, therefore, used in the present calculations may contribute to this under-prediction of the central-recirculation zone.

In the present calculations, consideration has not been given to modelling the process of radiative heat transfer within the flame and to the combustion chamber walls, see for example, Lockwood et al (1976) and Bartelds (1976), mainly for reasons of simplicity. This implies that the predicted profiles are possibly in error especially at regions of high temperature and high concentrations of absorbing and radiating species (e.g. CO_2 and H_2O) and at regions where hot soot particles, produced by thermal decomposition of fuel, exist. The contribution of the neglection of radiative heat transfer to the observed differences between the experimental and predicted results is, however, expected to be insignificant compared to the other influences of the spray inlet conditions mentioned previously. For example, in high temperature regions, the expected uncertainty in the temperature values will be in the order of 150 ^{o}K.

The observed discrepancies between the experimental and predicted results should be considered together with estimates of the uncertainties in the measured temperature and velocity profiles. The

temperature was measured by a suction pyrometer with around 10% average error, see Khalil et al (1977), which may increase to 15% at regions within the spray boundaries due to droplets impingement on the thermocouple element. The velocity was measured by a 3-hole pitot-tube probe and the maximum error was about 15%, Khalil et al (1977).

Droplet-Size-Distribution

The influence of the droplet-size-distribution on the predicted results has been considered in the present work; the calculations were carried out (case 1.B and 1.D), see Table 3.8. with the two size-distributions shown in Fig. 3.1. The size-distribution used in connection with case 1.B represents a spray with a comparatively large number of small-diameter droplets.

Radial profiles of axial velocity, and temperature, are shown for the two cases in Fig. 3.16. The results of Fig. 3.16 are very significant in showing the influence of shifting the size distribution towards smaller droplet-diameters on the predicted temperature profiles. The results indicate a large increase in the temperature values at near-burner locations and around the flame centreline associated with a decrease in temperature at the near-wall region of the downstream sections, for example at X = 0.52. Consequent changes in the axial velocity profiles are observed in Fig. 3.16. The central recirculation zone has completely vanished, due partly to the excessive increase in temperature, and indicates an over-estimation of the evaporation rate as the high temperature in this region would result, as previously mentioned, from hot combustion products circulated from downstream regions. The increase in the evaporation rate is also evident from the results of Fig. 3.17 which shows the distribution of the percentage evaporated mass along the

combustion chamber. The heating-up period of a droplet and the rate of change of its diameter with time are both proportional to its diameter and consequently small-diameter droplets start evaporation very shortly downstream of the atomizer with a high evaporation rate. Therefore, high evaporation rate, especially at upstream regions, would be expected if the spray contains a comparatively large number of small-diameter droplets. The increase in evaporation is also enhanced by the resulting high temperature region close to the burner.

Droplets Injection Velocity

In the present procedure, droplet injection velocity is calculated from the expressions given in Section 3.5.3 with the implication of equal injection velocity for all droplets. To demonstrate the extent to which changes in the calculated injection velocity affects the predicted profiles, the results of case 1.A have been compared with those of case 1.C which has a lower injection velocity, see Table 3.8.

The radial profiles of axial velocity and temperature are shown in Fig. 3.18 for the two cases. The temperature profiles of case 1.C show an increase in the centreline temperature values associated with a shifting of the location of the radial temperature maxima towards the centreline. This implies an increase in the evaporation rate at small axial distances and a decrease in the spray spreading rate which is confirmed by the results of Figs. 3.14 and 3.19. The increase in evaporation is due to the increase in the droplets relative velocity which consequently increase the heat and mass transfer to and from the droplet respectively.

Number of Size Ranges

To demonstrate the influence of the number of size ranges,

used to represent the spray, on the predicted results, the calculations were performed for 5 and 20 size ranges (case 1.D and 1.E, see Table 3.8) and compared with case 1.A (10 size ranges). The predicted results of the axial velocity and temperature profiles are shown in Fig. 3.20 for the three cases. Comparison between the three cases indicates that an increase in the number of size ranges tends to decrease the differences between the experimental and predicted results but the magnitude of the change is small. It is likely that, in sprays of the present hollow-cone type, where the droplets are confined to a small spatial volume, the use of a small finite number of size ranges is sufficient to represent the spray provided that the overall evaporation rate calculated from these size ranges is correct.

Droplet trajectories for cases 1.A and 1.E are shown in Figs. 3.13 and 3.21 and also indicate that, even with an increase in the number of size ranges from 10 to 20, the trajectories are almost confined to the same small spatial volume. The distribution of the percentage evaporated mass along the flame is shown in Fig. 3.14 for the two cases and indicates insignificant changes in the calculated spray evaporation rate with the number of size ranges.

The Evaporation Rate Expression

The evaporation rate from individual droplets has been calculated in the present work from the expression given in Section 3.5.3, see Equation (3.5.5). As previously mentioned, the transfer number, B, in this expression is derived for droplet evaporation in the absence of chemical reaction surrounding the droplet. The cloud-burning assumption of the present droplet-model does not, however, exclude the occurrence of reaction at some distance from the droplet which is expected to influence the droplet-evaporation rate. Evaporation rate expressions which take account of this influence are

not available in the literature and, therefore, a crude representation of it would be through the use of the transfer number expression, Section 3.5.3, for droplet evaporation with envelope-flame. The results of case 1.F, see Table 3.8, were obtained using this expression.

The predicted results of the axial velocity and temperature radial profiles at different distances from the burner are shown in Fig. 3.22 for the two cases 1.D and 1.F. Although the predicted temperature profiles, case 1.F, at upstream sections, $X < 0.24$, are apparently in agreement with the experimental results, the axial velocity profiles show a large under-prediction of the size of the central-recirculation zone. This implies that the increase in temperature at the near-burner region is mainly due to combustion of the fuel vapour and that the contribution of the recirculated hot combustion is insignificant. This again indicates an over-estimation of the droplets evaporation at this region, see Fig. 3.17. However, both the temperature and velocity profiles at downstream sections are shown to be in agreement with the experimental results.

It is evident, therefore, that a more realistic expression for the evaporation rate of individual droplets within the spray is needed for further validation work of the present procedure. It is likely that a combination of the above-mentioned two expressions, for example, in a way similar to that used by Spalding (1955) for droplet evaporation associated with wake-flame, would, to a first approximation, be sufficient for this purpose.

3.9.5 The Second Test Case

The experimental data of this test case correspond to the measurements of Chapter 2 and those used here comprised the isothermal

velocity measurements obtained with the 60^{o} swirler vane angle, see run 7 - Table 2.4, and the measurements obtained for the two flames which have 47 μm and 96 μm spray mean droplet diameters, see runs 2 and 3 - Table 2.4. The isothermal velocity measurements were selected to allow an assessment of the accuracy of the present numerical procedure in the absence of the complications and uncertainties associated with combustion and spray models. As indicated in Chapter 2, the spray mean droplet diameter and droplet injection velocity for the above two flames are known and reported in Section 2.4.3. Accurate representation of the spray inlet conditions was, therefore, possible and reduced the uncertainties in the spray model to those relating to the expression used to calculate the droplet evaporation rate.

The Boundary Conditions of the Fuel Spray

The fuel spray emerging from the present rotating cup atomizer, see Appendix A.I, comprises two types of droplets; the main and the satellite droplets. Each has a diameter which is a function of the rotational speed of the atomizer and that for the satellite droplet depends also on the fuel mass flow rate. For the operating conditions corresponding to the two flames used here, see Table 2.4, the diameter of the main and the satellite droplet is obtained from the data reported by Macfarlane et al (1969), i.e.:-

The First Flame (case 2.A)

D_m = 47 μm and D_s = 24 μm

The Second Flame (case 2.B)

D_m = 96 μm and D_s = 48 μm

The percentage mass of fuel contained in the main and satellite droplets is also obtained as:-

% mass main = 70%

% mass satellite = 30%

This simplification of the droplet-size-distribution within the spray allowed the calculations of the present test to be performed with only two size ranges as indicated in Table 3.9, which summarizes the spray inlet conditions.

The droplet axial and tangential injection velocity components are obtained from the measurements reported in Chapter 2, see Section 2.4.3. The radial velocity component was not measured and was, therefore, obtained from the following expression given by Fraser et al (1957), i.e.:-

$$V_R = 0.0131 \left[\frac{\rho_p \cdot N^2 \cdot Q^2}{\mu \cdot D}\right]^{1/3} \qquad \text{(m/s)}$$

where:-

ρ = Density in lb/cu. ft.

Q = Volume flow rate cu. ft./min

μ = Viscosity in centipoise

N = rpm of atomizer

D = Diameter of atomizer cup in ft.

Fig. 2.40 shows a sample of the measured droplet velocity probability distributions at the immediate vicinity of the atomizer, X/D = 0.31 and R/D = 0.3. The results indicate a comparatively large

spread in velocity, for example, the axial velocity varies between 0.2 and 4 m/s around the mean value of 2.5 m/s. It is evident that the accuracy of representing the spray will improve if this variation in the droplet injection velocity is taken into consideration. However, it should be recognized that accurate account of this variation would require two, or probably more, parameters joint probability distribution involving both the droplet diameter and the velocity components. In view of the lack of such information, a simple approach has been adopted in the present case in which the droplet velocity components are allowed to vary, around the mean value, by small increments so that the injection velocity always lies within the limits of the probability distribution. For example, in the first flame considered here, case 2.A, see Table 3.9, each of both the main and satellite droplet, 47 μm and 24 μm respectively, was assigned three different injection velocities. For the main droplet, the axial velocity component was 5.42, 8.03 and 2.8 m/s, the radial velocity 2.34, 8.0 and 2.34 m/s and the tangential velocity 18.4, 11.69 and 25.13 m/s respectively. It is clear that by allowing this variation in injection velocity, the actual number of droplets used to represent the spray was increased to 6.

The average number of droplets associated with the main and satellite droplet diameters is calculated from the expression:-

$$\dot{n}_m = \frac{\dot{m}_{fu} \cdot \alpha_m}{\frac{\pi}{6} \cdot D_m^3 \cdot \rho_p}$$

and:-

$$\dot{n}_s = \frac{\dot{m}_{fu} \cdot \alpha_s}{\frac{\pi}{6} \cdot D_s^3 \cdot \rho_p}$$

where α_m and α_s are the percentage of mass associated with the main and satellite droplets respectively.

3.9.6 Presentation and Discussion of the Results, Test Case 2

In this subsection the results of the calculations performed for the isothermal velocity measurements of run 7, see Table 2.4, and those for the two flames of runs 2 and 3, Table 2.4, which differ in the spray mean droplet diameter, are presented and discussed.

I. Isothermal Velocity Calculations

Fig. 3.23 shows the experimental and predicted radial profiles of mean axial and tangential velocity components corresponding to run 7, Table 2.4. The calculations were obtained, as indicated, with three different grid arrangements comprising 20 x 20, 25 x 25 and 30 x 30 grid nodes. The increase in the number of grid nodes was concentrated in the initial region of the calculation domain where the gradients of the dependent variables are more likely to be large. The reduction in the grid spacing reduces the cell Reynolds number and, therefore, the possibility of numerical errors, in particular those associated with the use of up-wind differencing scheme when the Reynolds number is high, see Section 3.8.7. For example, with the 25 x 25 grid, the maximum values of the cell Reynolds number in this region range between 10 and 25 while those for the 30 x 30 grid range between 5 and 20.

Fig. 3.23 shows that the agreement between the experimental and predicted results in the initial region of the test section, $X/D < 0.127$, is better than that obtained further downstream. It is likely that the predicted results in this region are influenced by the upstream boundary conditions which were specified from the

experimental data. The results obtained at the downstream sections, X/D > 0.127, indicate that the predicted profiles for the three grid arrangements are, in general, shifted radially inward with a corresponding underprediction of the size of the central recirculation zone by around 15 - 20%. However, it is clear that the extent of the under-prediction decreases with the increase in the grid dimension. It is also shown that the largest discrepancies between the experimental and predicted results (2 - 4 m/s) and between the predicted results with different grid arrangement (1 - 2 m/s) are concentrated in the near-wall region of the test section, around R = 70 mm. The predicted axial velocity component in this region decays at a higher rate than the experimental results and the decay rate is shown to decrease with the finer grids. The above observations and in particular the trend of the influences of grid refinement suggest that the momentum transport by diffusion is over-estimated in both the axial and radial directions. It is probable that this is influenced by the numerical errors associated with the upwind differencing scheme, see Section 3.8.7, which have the effect of introducing false diffusion into the solution. The cell Reynolds number in this region was comparatively high, around 10 - 20. It is also likely that the observed differences between the experimental and predicted results are influenced by the uncertainties of the turbulence model associated with the isotropic viscosity assumption in the calculation of highly swirling flows, see for example, Habib et al (1979).

The 25 x 25 grid arrangement was adopted in the combusting flow calculations to be described in the following part of this sub-section. This grid was selected for reasons of economy in computer time, see Section 3.9.2, and storage. The storage requirements of the 25 x 25 grid for the isothermal calculations were around 32 K of

CDC 6600 storage and those for the 30 x 30 were 43 K and both increase to 42 K and 57 K respectively for the combusting flow calculations. It is also shown, Fig. 3.23, that the increase in the grid dimension from 25 x 25 to 30 x 30 has a small influence on the predicted profiles (a difference of around 1 m/s) which, in view of the additional uncertainties introduced by the spray and combustion models, suggests that the calculations with the 25 x 25 grid would be of sufficient accuracy for the combusting flow calculations.

II The 47 μm Spray Mean Droplet Diameter Flame - Case 2.A

The experimental data of the flame of this case, 2.A, corresponds to the operating conditions of run 2 in Table 2.4, see also Table 3.9. Fig. 3.24 shows the calculated and measured radial profiles of temperature, mass fractions of carbon dioxide (CO_2) and oxygen (O_2) at different axial distances along the combustion chamber. Also shown, for reference purposes, are the corresponding measured profiles of carbon monoxide (CO) concentrations. The results show that the general features of the temperature and species concentrations are correctly predicted. However, discrepancies in the extent of chemical reaction and the corresponding temperature values are clearly indicated. At locations close to the combustion chamber wall, the O_2 concentrations are under-predicted, by approximately 5%, with a consequent over-prediction of the temperature values, where discrepancies of around 100 ^{o}K can be observed. The accelerated consumption of oxygen, in this region, may be attributed to deficiencies in the coupled turbulence/chemistry models and, to a less extent, the boundary condition specifications. In the initial flame region, X/D < 0.3, and at radii corresponding to the maximum gradients in the measured temperature and species concentrations, around R/D ≃ 60 mm, the predicted profiles of O_2 and CO_2 are seen to be shifted towards

smaller radii which indicates an under-estimation of the chemical reaction rates. With the presumed dependence of the reaction rate on the turbulent kinetic energy and its dissipation rate, this result is consistent with the under-prediction of the central recirculation zone at this region which is evident in Fig. 3.23. The large discrepancies in the temperature values, around 400 ^{o}K, which can be seen in the radial profiles at X/D = 0.127 and 0.255 and at R < 50 mm may be attributed to uncertainties in the present combustion model and in particular to the assumption of single step chemical reaction and the neglect of intermediate species such as soot and carbon monoxide. It is clear that, although the O_2 concentrations are, in their general behaviour, correctly predicted, the CO_2 concentrations are over-estimated by around 30% and can be explained by referring to the high CO values (10%) measured in this zone. In effect, and due to the comparatively high calorific value of CO, the calculated heat release rates are much higher than the actual values. At the far downstream regions of the flame, for example at X/D = 1.45, the differences between the calculated and measured temperature values decreases to around 100 ^{o}K and are again probably due to deficiencies in the coupled turbulence/chemistry models.

Fig. 3.25 shows a plot of the trajectories for the droplets representing the fuel spray. Also shown in the figure are the calculated droplet axial and tangential velocity components along the path of each droplet. The measured radial profiles of droplet velocity are also plotted for reference purposes. The arrows indicate the positions where the droplet diameter reaches a specified value. The droplet trajectories for the satellite droplets are very short due to their much smaller diameters which correspond to a relatively high evaporation rate. As indicated previously in Section 2.4.3, the droplet velocity measurements for this case were obtained in the

narrow region of the spray which covers the axial locations between X/D ≃ 0.312 and X/D ≃ 0.357. Close inspection of the results indicates that the calculated droplet trajectories are, however, concentrated in the region between X/D ≅ 0.31 and X/D = 0.5 which implies that the calculated spray angle is slightly under-estimated. It is, however, unlikely that this small change in angle contributes to the above-mentioned discrepancies between the experimental and predicted results. The calculated droplet velocities shown in Fig. 3.25 cannot be directly compared with the measured values along the combustor radius but do suggest the trend of velocity distribution within the spray. The variations in the droplets evaporation rate, which can be extracted from the position of the arrows in Fig. 3.25, are associated with change in velocity and show the influence of the droplets injection velocity on the overall characteristics of the spray.

III The 96 μm Spray Mean Droplet Diameter Flame - Case 2.B

The calculated and measured radial profiles of temperature, mass fractions of CO_2, CO and O_2 for this flame are shown in Fig. 3.26. As indicated previously, the operating conditions for this flame are the same as those for the flame described in the previous case, 2.A, except that the spray mean droplet diameter has increased to 96 μm. Again, the predicted results are shown to be in a qualitative agreement with measurements. However, the calculations at the near-wall region show an over-estimation of the chemical reaction rate where the O_2 concentrations are lower than the measurements by around 2% O_2 and the temperature and CO_2 values are higher by 100 - 200 ^oK and 2% CO_2 respectively. In the vicinity of the centreline and in the upstream region, X/D < 0.3, the temperature values are over-predicted at some points by more than 400 ^oK with a corresponding over-estimation of the CO_2 mass fractions. At the downstream sections, on the other

hand, the calculated temperature values are lower than the measurements (100 - 150 ^{o}K difference) and related discrepancies in the mass fractions of O_2 (2 - 3% O_2) and CO_2 (2% CO_2) can be easily detected.

The over-prediction of temperature in the upstream region and at small radii, can be attributed mainly to the neglect of CO formation in the present procedure as indicated in the previous case (flame 2.A). In confirmation, the measured CO mass fractions in this region are shown in Fig. 3.26 to be relatively high. The deficiencies observed at the downstream section of the combustion chamber can be related to the uncertainties associated with the expression used to calculate the droplet evaporation. Fig. 3.27 shows the trajectories for the droplets used to represent the spray and, again, the arrows shown in the figure indicate the positions where the droplet diameter reaches a specified value. It is evident that, for the 96 μm droplets, the rate of change of droplet diameter is small in the initial part of the trajectory and that the droplet evaporation continues at the downstream parts of the chamber, up to X ≃ 200 mm, and close to the wall. The initial slow evaporation of the droplets is likely to be the reason for the under-prediction of temperature and CO_2 and the over-prediction of O_2 concentrations close to the centreline as indicated in Fig. 3.26 at X/D = 0.7 and X/D = 1.45. As a consequence of the former, smaller amounts of fuel are transported to the central part of the flame which led to an under-estimation of the chemical reaction rate. On the other hand, most of the fuel is evaporated near the wall and gives rise to a higher chemical reaction rate compared to the experiments. It is unlikely that the results for the flame of case 2.A were influenced by the same deficiencies in the calculation of the droplets due to the much smaller droplet diameters involved in that flame. The small diameter droplets evaporate with a high rate and it is anticipated that any uncertainties in the

calculation of the evaporation rate would have a relatively small influence on the overall spray evaporation.

3.9.7 The Third Test Case

The experimental data of this test case correspond to those reported by Tuttle et al (1976) and the geometry of the cylindrical combustion chamber is shown in Fig. 3.5. Heated, 500 ^{o}K, vitiated air entered the chamber through the annulus surrounding the stabilizer disc and commercial purity liquid propane was injected from a simplex pressure atomizer placed at the centre of the disc. The dimensions of the disc and the combustion chamber corresponded to a blockage ratio of 61%. The operating conditions for the flame of this test case are given in Table 3.3. Detailed measurements of temperature, carbon monoxide, unburned hydrocarbons and nitric oxides were obtained within the combustion chamber. A water cooled stainless steel sampling probe was used for the concentration measurements and a platinum/10 per cent platinum rhodium bare wire thermocouple, mounted to the side of the sampling probe, provided estimates of local gas temperature. The readings of the latter were not corrected for any radiation or conduction losses which implies that the reported values are likely to be less by up to 200 ^{o}K in regions of high temperatures. The accuracy of the concentration measurements is anticipated to be of the order of ± 15%.

3.9.7.1 Fuel Spray

The details of the present fuel atomizer and its operating conditions were described by Tuttle et al (1976) and the characteristics of the fuel spray (size-distribution and injection velocity) are assumed to be calculated from expressions similar to those used in the first test case, see Subsection 3.9.3. The flow number of the

atomizer nozzle, F_N, can be defined as:-

$$\dot{m} = F_N \sqrt{\Delta P}$$

where $\dot{m}$ is the mass flow rate and ΔP is the pressure difference across the atomizer. As indicated by Tuttle et al (1976), the fuel atomizer delivered 35 gallons/hr of water at a differential pressure of 125 p.s.i.g. Therefore, the flow number, based on water properties, is calculated as $F_N = 1.262 \times 10^{-2}$. The corresponding value for liquid propane (specific gravity $\simeq 0.508$) is $F_N = 0.901 \times 10^{-2}$. For the fuel flow rate of the present case, see Table 3.3, the pressure difference across the atomizer was calculated as $\Delta P \cong 0.5$ atm. From the correlations presented in Section 3.9.3 the droplet-size-distribution for the present case can be expressed as:-

$$\frac{dn}{n} = 4.21 \times 10^6 \left(\frac{D}{188}\right)^{3.5} \cdot \exp\left[-16.98 \left(\frac{D}{188}\right)^{0.4}\right] \cdot \frac{dD}{188}$$

The average total number of droplets in the spray, n, is calculated from the expressions given previously in Section 3.9.3. The axial velocity component of the droplets was calculated from the expression:-

$$u_x = \frac{\dot{m}_{fu} \cdot 4.0}{\rho_p \cdot \pi \cdot c_c \cdot d_J^2}$$

The atomizer nozzle diameter, d_J, is obtained from the flow number, F_N, and has a value of $\simeq 1.07$ mm. The area contraction factor, c_c, was calculated as 0.6. The radial and tangential velocity components are assigned the values given in Table 3.9.

The liquid propane fuel, C_3H_8, used in the experiment of the

present case presented some difficulties in specifying its physical properties. The data available in the literature, see for example, Rose et al (1977)are incomplete. Table 3.6 gives the values of the physical properties used in the present study. The latent heat of vaporization was calculated from the expression:-

$$L = (251.3 - 0.377 \cdot t) / \rho_p \qquad K_J/Kg$$

where t is the liquid temperature in ^oC and ρ_p is the density in Kg/m^3. The specified heat of the liquid and vapour fuel are given as:-

$$c_{p_p} = (1.6848 + 0.00399 \cdot t) / \sqrt{\rho_p}$$

and:-

$$c_{p_v} = c_{p_p} - 0.377/\rho_p$$

Table 3.9 summarizes the spray inlet conditions used in this test case.

3.9.8 Presentation and Discussion of the Results, Test Case 3

The calculations for this test case were performed, as indicated in Table 3.9, for 5 and 10 droplet size ranges; the calculated and measured radial profiles of temperature and unburned hydrocarbon (UHC) concentrations are shown in Fig. 3.28. The calculated profiles in the upstream part of the flame, X/DISC $\leq$ 0.437, indicate a large over-prediction of the temperature values, by around 400 ^oK, and are qualitatively in error especially in the region surrounding the

intense-combustion zone, which is indicated by the high temperature values at R/DUCT around 0.4. The present flow geometry, see Fig. 3.5, suggests that this region coincides with the shear layer separating the recirculation zone behind the disc and the surrounding air stream. It is likely that the large over-prediction of the chemical reaction rate at this region, which is evidenced by the calculated radial profiles of UHC, is mainly due to inaccurate calculation of the mean flow and the turbulence characteristics within the shear layer and to uncertainties in the calculation of the evaporation and spreading of the fuel spray. Fig. 3.29 shows the axial distribution of the spray evaporation rate and it is clear that although 80% of the fuel has evaporated at X = 60 mm, the droplets continue to evaporate up to around X = 150 mm. In view of the preheating of the combustion air, 500 ^{o}K, see Table 3.3, and the comparatively short preheating time of the propane droplets prior to evaporation, the results of Fig. 3.29 suggest an under-estimation of the spray evaporation rate. The predicted high temperature values in the initial flame region are also influenced by the uncertainties in the assumption of single step reaction as the measurements indicate comparatively high CO concentrations. The predicted and measured temperature profiles, in the downstream part of the flame, X/DISC > 0.6, are shown to be qualitatively in agreement although the temperature values are generally under-estimated by around 100 - 200 ^{o}K. It can also be observed that the predicted UHC concentrations are well below the measured values. Apart from the related influence of the over-prediction of the chemical reaction rate in the initial flame region, these discrepancies are due mainly to inaccuracies in representing the turbulent transport and spreading of the air stream surrounding the stabilizer disc which had a consequent dilution and cooling effect on the downstream part of the flame.

The calculated results of Fig. 3.28, which were obtained with 5 and 10 droplet-size ranges, indicate clearly that the increase in the number of size ranges has a very small influence on the predicted profiles. This small difference is related to both the spray type and the aerodynamic features of the present geometry. The hollow-cone type of the spray for this test case implies that most of the droplet trajectories are confined to a small spatial volume and it is likely that changes in the discretization level used in representing the spray would have insignificant influence on its overall characteristics, including both the evaporation and spreading rates. It is also likely that the high turbulent mixing rates in the near-spray region of the present flow geometry tend to diminish the influences of any small differences in the details of the spray evaporation and spreading processes associated with the change in the number of size ranges.

3.9.9 The Fourth Test Case

The calculations were performed in this test case to predict the local flow properties in the spray flame geometry reported by Styles et al (1977). The experimental burner geometry is shown in Fig. 3.5. Kerosene fuel is injected from a twin-fluid atomizer into a CO-flowing air stream and both react in an unconfined situation. The operating conditions for the flame are given in Table 3.9. The measurements comprised radial and centreline distributions of mean temperature and species concentrations of CO_2, CO, O_2, CH_4 and H_2. A laser Doppler anemometer was also used to measure droplet-size-distribution within the non-reacting spray. The gas temperature was measured by a 75 μm diameter wire silica coated thermocouple and a 1 mm bore quartz microprobe was used for the concentration measurements. Although assessment of the uncertainties associated with each

technique is difficult, it is likely that the errors in temperature measurements will be around ± 40 - 80 ^{o}K, see Attya (1979). The accuracy of concentration measurements can be estimated, see Bilger (1977), as ± 15%. As indicated by Jones (1976) the technique of droplet-size-distribution measurements can detect changes of 0.1 in the Rosin-Rammler exponent N, described in the following part, and a variation of about 2% in the characteristic diameter $\overline{D}$.

The Boundary Conditions of the Fuel Spray

Measurements of droplet size within a non-reacting spray were reported by Styles et al (1977) for operating conditions corresponding to the present case. The droplet-size-distribution within the spray was correlated by a Rosin-Rammler expression which has the form:-

$$w = \exp (- D_p/\overline{D})^N$$

where:-

w = Weight fraction of droplets larger than size D_p.

$\overline{D}$ = Characteristic mean size such that 63.2% of the droplets are less than $\overline{D}$.

N = Exponent gives a measure of the spread of the distribution.

The values of N and $\overline{D}$ corresponding to the present case are:-

$N = 1.2 \qquad \overline{d} = 110\ \mu m$

Fig. 3.30 shows a plot of (1 - w) against the diameter ratio $(D_p/\overline{D})$. It is clear that the size distribution covers a wide range of droplet

diameters and to reduce the computing time of the present case, it was found necessary to truncate the size distribution as indicated in Fig. 3.30. The reported calculations for this test case were performed with 10 and 20 size ranges as shown in Fig. 3.30 and Table 3.9.

The mean axial injection velocity component assigned to the different size ranges was obtained from the reported measurements and a relatively small radial velocity was assumed at the point of injection as indicated in Table 3.9. The number of droplets associated with each size range is calculated from the corresponding values of w and D_p and the mass flow rate of the fuel.

The Conditions at the Free-Stream Boundary

The unconfined geometry of the present case required special treatment in specifying the conditions at the free stream boundaries. As shown in Fig. 3.5 the combustion air was supplied through a secondary air duct of 316 mm diameter. The spreading angle of the air jet was taken as that for a free jet, with the assumption that the presence of the stabilizer disc has a negligible influence. The value of the angle was $\theta = 7 - 8^{o}$. The half radius of the jet is related to θ, the duct diameter, $2\ r_o$, and the axial distance along the jet, X, through the expression:-

$$r_{1/2} = r_o + \tan\theta \cdot X$$

The calculation domain was extended to an axial distance of 700 mm (estimated from the experimental data) and to a radial distance of 240 mm corresponding to double the half radius. The axial and radial velocity components along the free-stream boundary in the jet direction were assumed zero and the gradients of other quantities

were set to zero. The pressure there was also assumed atmospheric. The radial velocity and pressure along the free-stream boundary normal to the jet direction were assumed zero and atmospheric respectively and zero gradients were taken for other quantities. Small axial velocity values (0.1 m/s) were assigned at that boundary. The influence of the calculation domain dimensions and the upstream axial velocity values was studied and the results showed insignificant influences in the more important region where the combustion process takes place (i.e. up to radial positions corresponding to the disc diameter). In the latter region, a fine grid distribution was used, see Fig. 3.8, as the experimental results showed large velocity and concentration gradients.

3.9.10 Presentation and Discussion of the Results, Test Case 4

The calculations for this test case were performed using 10 and 20 droplet size ranges as indicated in Table 3.9. The calculated and measured centreline distributions of temperature, mass fractions of O_2, CO (measured) and CO_2 are shown in Fig. 3.31 and the corresponding radial profiles, at axial distances of 80 mm and 250 mm in Fig. 3.32. It is evident from Fig. 3.31 that the calculated oxygen concentrations along the flame centreline and for the two cases with 10 and 20 size ranges are generally under-estimated. For example, the calculated values at some points drop to below half the measured concentrations. Related discrepancies in the temperature and CO_2 mass fraction can also be easily detected in Fig. 3.31. This over-prediction of the chemical reaction rate is due, in part, to inaccuracies in representing the spray evaporation rate and to uncertainties in the present combustion model. The former is clearly demonstrated by the comparatively better agreement between the

predicted and measured values obtained with the higher number of droplet size ranges. The latter may stem from the dependence of the reaction rate term on the turbulence characteristics of the flow which, in turn, are sensitive to the presumed upstream boundary conditions. It is also likely that, in the initial flame region, the combustion model may be deficient in its lack of direct consideration of the influence of the presence of high concentrations of fuel droplets on the calculation of the reaction rate.

It is clear from the radial profiles of Fig. 3.32 that the increase in the number of droplet size ranges had led to a better representation of the flame spreading rate and to a decrease in the discrepancies between the calculation and measurements. For example, the locations of the temperature maxima are shifted radially outward to coincide, approximately, with the measured locations. This is mainly due to the increased accuracy in calculating the evaporation and spreading rates of the fuel spray as a result of the reduced degree of discretization associated with the higher number of size ranges. The larger influence of the number of size ranges observed in this case is related to the spray type and the comparatively low turbulent mixing rates of the present flow geometry where an increase in the relative importance of the fuel spray characteristics in controlling the combustion process is anticipated.

3.10 Concluding Remarks

The calculation procedure described in the preceding sections of this chapter has been applied to the prediction of the flow properties of four different spray flame geometries and the results compared with the corresponding experimental data; comparisons indicate that the general features of the flow fields are correctly predicted. The extent of the agreement between the experimental and

predicted results and the relative importance of the sources of uncertainties in the modelling assumptions were found to vary according to the flame geometry considered. For example, in the results of the first test case discrepancies in temperature of more than 400 ^{o}K were observed, mainly at the near-burner locations and around the combustion chamber centreline. Consideration of the factors influencing the solution of the droplet field equations emphasized that these discrepancies were mainly related to uncertainties in the calculated spray evaporation and spreading rates. Inspection of the predicted velocity and temperature profiles also indicated that the observed deficiencies are related to uncertainties in the two-equation turbulence model adopted in the present work. The uncertainties in the droplet model were also found to contribute significantly to the observed discrepancies of test case 4. However, the results of test case 2 showed discrepancies in the temperature and oxygen concentrations of around 100 - 400 ^{o}K and 1 - 5 O_2 % respectively which were mainly influenced by the deficiencies in the coupled turbulence/combustion models. The calculations were performed for the first test case with the neglect of heat transfer by radiation while those for test cases 2, 3 and 4 were obtained with a simple radiation model. The results of the latter cases suggested that thermal radiation has a comparatively small influence in the calculations of the type of flames considered here. This is probably due to the small size of these flames or to the neglect of droplet and soot radiation in the present radiation model.

The first, third and fourth test cases of the previous section corresponded to significantly different spray and flow geometries and, therefore, allowed the influence of the number of size ranges assumed within the spray model to be examined over a wide range of spray flames. The calculated results of test case 1 showed that

increasing the number of size ranges from 5 to 20 caused an average reduction of 5% in the observed errors between the experimental and predicted results. However, the extent to which the results are improved does not justify the increase in computing time associated with the large number of size ranges. Moreover, droplet trajectories associated with the 5, 10 and 20 size ranges considered were almost confined to the same spatial volume which suggests that increasing the number of size ranges without taking into consideration the influences of the turbulent gas flow, droplets collision and break-up and the change of injection velocity with diameter on droplet motion is not sufficient for accurate representation of the spray. In agreement with the above observations, the results of test case 3 indicated relatively small influence of the number of size ranges. On the other hand, the results of test case 4 demonstrated clearly the importance of this number. Examination of both the spray characteristics and the aerodynamic flow features of the three cases suggests that the influence will be small for sprays where the majority of droplets are confined to a small spatial volume (for example, hollow-cone sprays) and for flow conditions where a high degree of turbulent mixing exists in the near-spray region.

Apart from the uncertainty in the evaporation rate expression, which was examined in the first test case, the results showed that the spray inlet conditions, including the droplet-size-distribution and droplets injection velocity, have a significant influence on the calculated spray evaporation and spreading rates and consequently on the predicted profiles. This presents a special difficulty in the assessment of the procedure by comparison with existing experimental data as accurate measurements of the size distribution and injection velocity is difficult to obtain with the available measuring techniques. However, this difficulty can be

overcome, to some extent, through the use of simplified empirical expressions.

TABLE 3.1

EXPRESSIONS APPEARING IN THE GENERAL PARTIAL DIFFERENTIAL EQUATION

Variable ϕ	Γ	S	S_d ***
U	μ_{eff}	$\frac{\partial}{\partial x}\left(\mu_{eff}\frac{\partial U}{\partial x}\right) + \frac{1}{r}\frac{\partial}{\partial r}\left(\mu_{eff}\, r\frac{\partial V}{\partial x}\right) - \frac{\partial p}{\partial x}$	$-\sum_{L=1}^{N}(M\dot{}U_{d_o} - M\dot{}U_{d_i})_L$
V	μ_{eff}	$\frac{\partial}{\partial x}\left(\mu_{eff}\frac{\partial U}{\partial r}\right) + \frac{1}{r}\frac{\partial}{\partial r}\left(\mu_{eff}\, r\frac{\partial V}{\partial r}\right) -$ $-\frac{2\mu V}{r^2} + \frac{8W^2}{r} - \partial P/\partial r$	$-\sum_{L=1}^{N}(M\dot{}V_{d_o} - M\dot{}V_{d_i})_L$
W	μ_{eff}	$-\left(\frac{\mu_{eff}}{r^2} + \frac{\rho V}{r} + \frac{1}{r}\frac{\partial \mu_{eff}}{\partial r}\right) W$	$-\sum_{L=1}^{N}(M\dot{}W_{d_o} - M\dot{}W_{d_i})_L$
k	$\frac{\mu_{eff}}{\sigma_k}$	$G_{k_1} - \rho\varepsilon$ *	0
ε	$\frac{\mu_{eff}}{\sigma_\varepsilon}$	$\frac{\varepsilon}{k}(C_1 G_{k_1} - C_2\rho\varepsilon)$	0

* $G_{k_1} = \mu_{eff}\left|2\left[\left(\frac{\partial U}{\partial x}\right)^2 + \left(\frac{\partial V}{\partial r}\right)^2 + \left(\frac{V}{r}\right)^2 + \left(\frac{\partial W}{\partial x}\right)^2 + \left[r\frac{\partial}{\partial r}\left(\frac{W}{r}\right)\right]^2 + \left(\frac{\partial U}{\partial r} + \frac{\partial V}{\partial x}\right)^2\right]\right|$

*** S_d values are added to Source term S in its finite difference form.

NB All constants are shown in Table 3.2

.... Contd.

TABLE 3.1 (CONTD.)

Variable ϕ	Γ	S	S_d ***
f	$\frac{\mu_{eff}}{\sigma_f}$	0	$+ \sum_{L=1}^{N} (\dot{m}_{d_i} - \dot{m}_{d_o})_L$
$\tilde{h}$	$\frac{\mu_{eff}}{\sigma_h}$	$\begin{cases} 0 \longrightarrow \text{No radiation} \\ \left(\frac{16}{9} \cdot k\ (R_x + R_r - 2\sigma\ \overline{T})^4\right. \end{cases}$	$+ \sum_{L=1}^{N} (\dot{m}_{d_i} - \dot{m}_{d_o})_L \cdot (H_{fu} - L)$
g	$\frac{\mu_{eff}}{\sigma_g}$	$C_{g_1} \cdot G_{g_1} - C_{g_2}\ \rho \frac{\varepsilon}{k} \cdot g$ **	0
m_{fu}	$\frac{\mu_{eff}}{\sigma_f}$	$23.6 \left(\frac{\nu \cdot \varepsilon}{k^2}\right)^{1/4} \cdot \frac{\varepsilon}{k} \cdot \rho \cdot \chi \cdot \overline{m}_{min.}$	$+ \sum_{L=1}^{N} (\dot{m}_{d_i} - \dot{m}_{d_o})_L$

** $G_{g_1} = \mu_{eff} \left| \left(\frac{\partial f}{\partial x}\right)^2 + \left(\frac{\partial f}{\partial r}\right)^2 \right|$

*** S_d values are added to Source term S in its finite difference form

NB All constants are shown in Table 3.2

TABLE 3.2

CONSTANTS OF THE TURBULENCE AND COMBUSTION MODELS AND EFFECTIVE TURBULENT PRANDTL NUMBERS

Constant	Value	Remarks
C_μ	0.090	Turbulence model
C_1	1.440	
C_2	1.920	
C_{G_1}	2.800	Constants of the concentration fluctuations equation
C_{G_2}	2.000	
σ_k	1.000	
σ_ε	$\kappa^2/(C_2 - C_1) \cdot C_\mu^{1/2}$	
σ_f	0.900	
$\sigma_{m_{fu}}$	0.900	Effective turbulent Prandtl numbers
σ_g	0.900	
σ_h	0.900	
κ	0.419	Logarithmic law of the wall constants
E	9.793	

TABLE 3.3

OPERATING CONDITIONS FOR THE FOUR TEST CASES

Test Case Number	1	2	3	4
Flame geometry	Fig. 3.5a	Fig. 3.5b	Fig. 3.5c	Fig. 3.5d
Fuel	Kerosene	Kerosene	Liquid propane	Kerosene
Fuel atomizer	Swirl atomizer	Rotating cup atomizer	Simplex pressure atomizer	Twin-fluid atomizer
Swirler angle	45^{o}	60^{o}	-	-
Combustor pressure	1 atm	1 atm	5 atm	Unconfined, 1 atm
Preheat temperature	310 ^{o}K	300 ^{o}K	500 ^{o}K	300 ^{o}K
Combustion air flow rate	355 Kg/hr	200 Kg/hr	3600 Kg/hr	-
Fuel flow rate	17 Kg/hr	4.75 Kg/hr	22.6 Kg/hr	2.3 Kg/hr
Experimental data	Radial profiles of T, U and W	Radial profiles T, CO, CO_2, O_2, droplet velocity - Isothermal axial velocity	Radial profiles T, CO, UHC, NO_X	Radial and centre-line profiles - T, CO, CO_2, H_2 and CH_4 - droplet size, droplet velocity

TABLE 3.4

MAIN DEPENDENT VARIABLES AT ENTRY TO THE DIFFERENT FLOW GEOMETRIES CONSIDERED

Boundary Condition for the Variable	Test Case 1	Test Case 2	Test Case 3	Test Case 4
U	Fig. 3.10a	Fig. 3.10b	Fig. 3.10c	Fig. 3.10d
V	0.0	0.0	Fig. 3.10c	0.0
W	Fig. 3.10a	Fig. 3.10b	-	-
k	$0.01\chi U^2_{av.}$			
ε	$C_\mu \cdot k^{3/2}/\ell$			
m_{ox}	0.232	0.232	0.232	0.232
m_{fu}	0.0	0.0	0.0	0.0
$\tilde{h}$	$C_p (T_a - T_{ref})$			
f	0.0	0.0	0.0	0.0
g	0.0	0.0	0.0	0.0
T_a ^oK	310	300	500	300

$U_{av.}$: average inlet mean axial velocity component

ℓ : characteristic length scale

TABLE 3.5

UNDER RELAXATION FACTORS

U	V	W	k	ε	P	$\tilde{h}$	m_{fn}	f	g	ρ	μ
0.5	0.35	0.3	0.6	0.5	0.7	0.9	0.9	0.9	0.9	0.2	0.6
0.4	0.30	0.3				0.5	0.5	0.5	0.5		

TABLE 3.6

SAMPLES OF COMPUTING TIME FOR THE FOUR TEST CASES

Test Case		Average computing time per iteration per grid node (sec)	Total computing time, CDC 6600 (sec)
1.A	see Table 3.8	3.479×10^{-3}	835
1.B		2.995×10^{-3}	719
1.D		3.060×10^{-3}	735
2.A	see Table 3.9	1.854×10^{-3}	927
2.B		1.954×10^{-3}	977
3 (5 size ranges)		1.886×10^{-3}	943
4 (10 size ranges)		1.860×10^{-3}	350

TABLE 3.7

PROPERTIES OF KEROSENE AND LIQUID PROPANE

Property	Kerosene	Liquid Propane
Chemical formula	$C_{12}H_{26}$ approximate	C_3H_8
Heat of reaction, H_{fu}	4.34×10^7 J/Kg	4.653×10^7 J/Kg
Latent heat of vaporization	2.73×10^5 J/Kg	3.8×10^5 J/Kg
Saturation temperature	450 ^oK	280 ^oK
Density, Kg/m^3	793	508
Oxidant/fuel stoichiometric ratio	3.41	3.635
Constant pressure specific heat	2520.0 J/Kg ^oK	2364.0 J/Kg ^oK
Vapour specific heat	444.5 + 3.685 T_{sat}	2000.0 J/Kg ^oK

TABLE 3.8

SPRAY INLET CONDITIONS FOR
THE FIRST TEST CASE

Case No.	Number of Size Ranges	Size * Distribution	Injection ** Velocity
A	10	I	a
B	5	II	a
C	10	I	b
D	5	I	a
E	20	I	a
F	5	I	a ***

* Size distribution of droplets:

$$\text{I} \quad \frac{dn}{n} = 4.21 \times 10^6 \left(\frac{D_p}{188}\right)^{3.5} \cdot \exp\left[-16.98 \left(\frac{D_p}{188}\right)^{0.4}\right] \cdot \frac{dD}{188}$$

$$\text{II} \quad \frac{dn}{n} = 0.0203 \times 10^6 \left(\frac{D_p}{127}\right)^{2.252} \cdot \exp\left[-11.723 \left(\frac{D_p}{127}\right)^{0.469}\right] \cdot \frac{dD}{127}$$

** Injection velocity of droplets:

a $U_p = 11.0$, $W_p = 6.1$, V_p varies from 0.5 to 2.5, the small value corresponds to smallest droplet diameter

b $U_p = 10.0$, $W_p = 2.0$, V_p varies from 0.5 to 2.5, the small value corresponds to smallest droplet diameter

*** Evaporation rate expression

TABLE 3.9

FUEL SPRAY UPSTREAM BOUNDARY CONDITIONS FOR TEST CASES 2, 3 AND 4

Test Case No.	2	3	4
Droplet size distribution	Near - monosized (measured) D_{mean} = 47 μm (70% mass), $D_{satellite}$ = 24 μm (30% mass) } Flame A D_{mean} = 96 μm (70% mass), $D_{satellite}$ = 48 μm (30% mass) } Flame B	$\frac{dn}{n} = 4.21 \times 10^6 \left(\frac{D_p}{188}\right)^{3.5} \exp.\left(-16.98\left(\frac{D_p}{188}\right)^{0.4}\right) \cdot \frac{dD_p}{188}$	$w = \exp.\left(\frac{D_p}{110}\right)^{0.68}$
No. of size ranges	2	5 - 10	10 - 20
Droplets injection velocity m/s	(measured) Flame A: U_p = 0.9 - 8, V_p = 1.0 - 2.34, W_p = 11.69 - 25.3 Flame B: U_p = 0.8 - 5, V_p = 1.31, W_p = 8 - 15	(calculated) U_p = 20, V_p = 2, W_p = 11.5	(measured) U_p = 20 - 25, V_p = 0.03 - 2

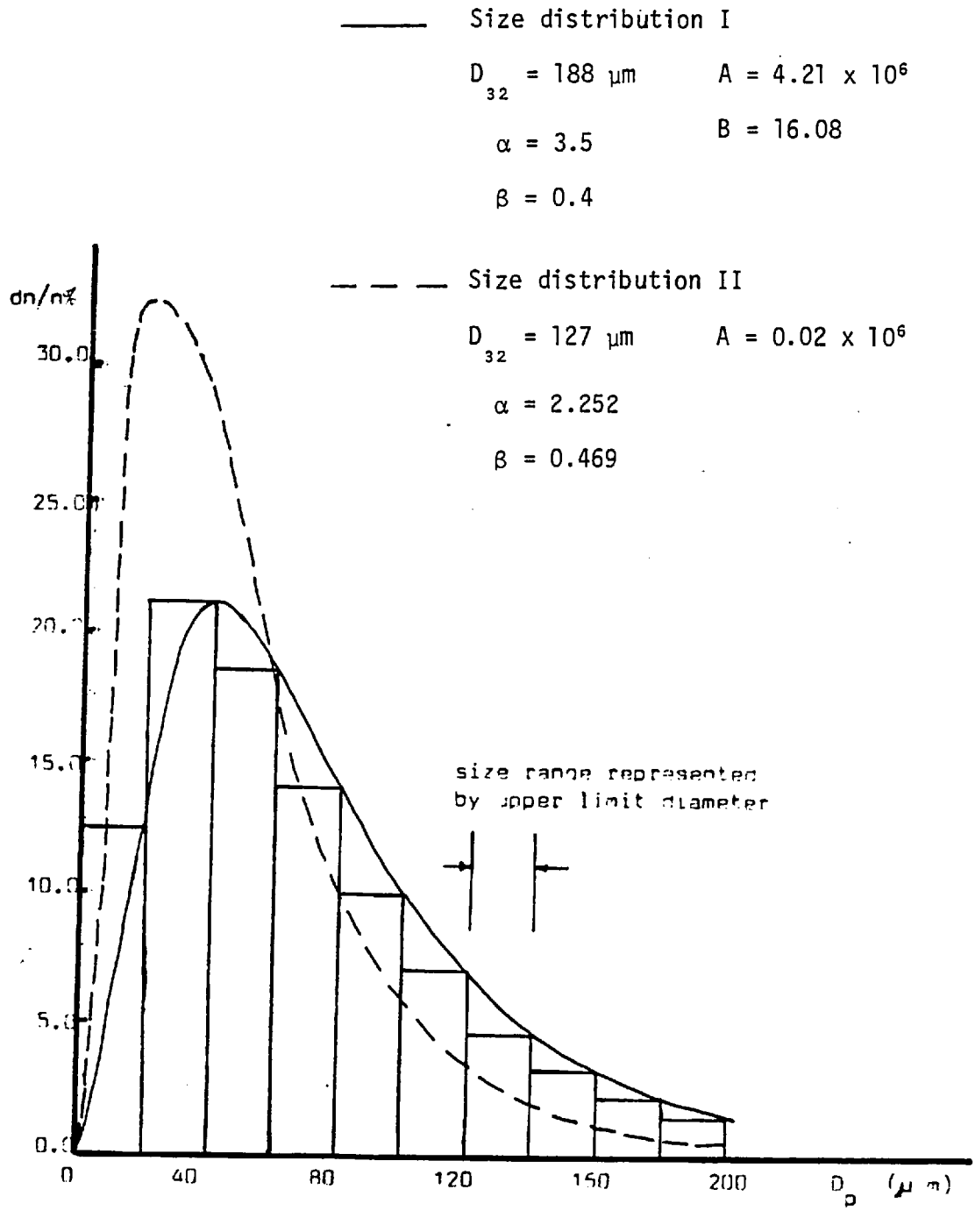

Fig. 3.1 Typical example of droplet size distribution

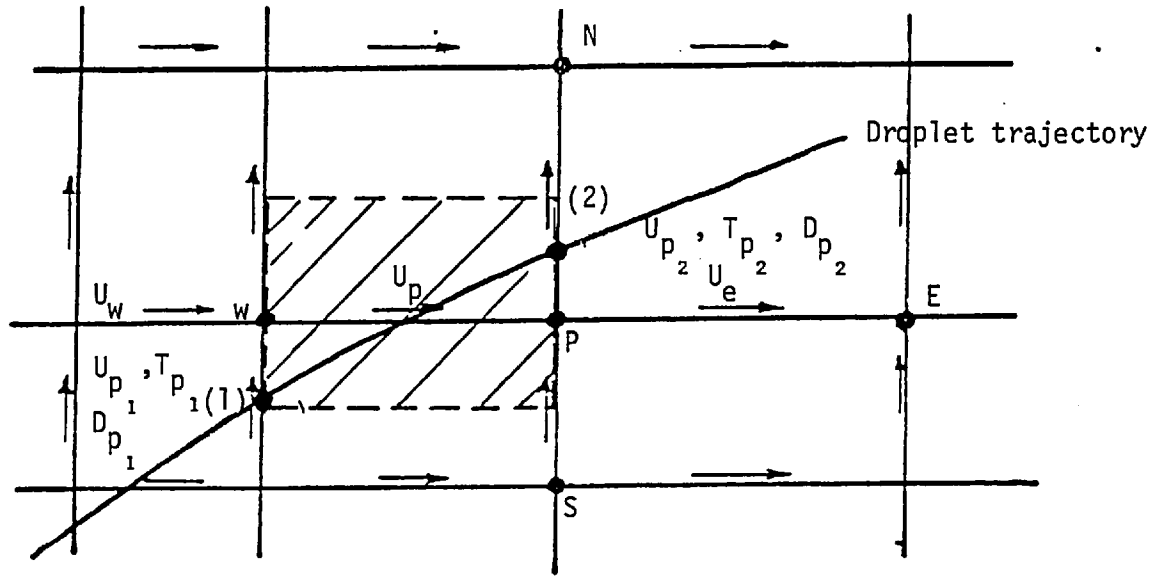

$$X_i = X_{i-1} + 0.5\,(U_i + U_{i-1}) \cdot \Delta t$$

$$Y_i = Y_{i-1} + 0.5\,(V_i + V_{i-1}) \cdot \Delta t$$

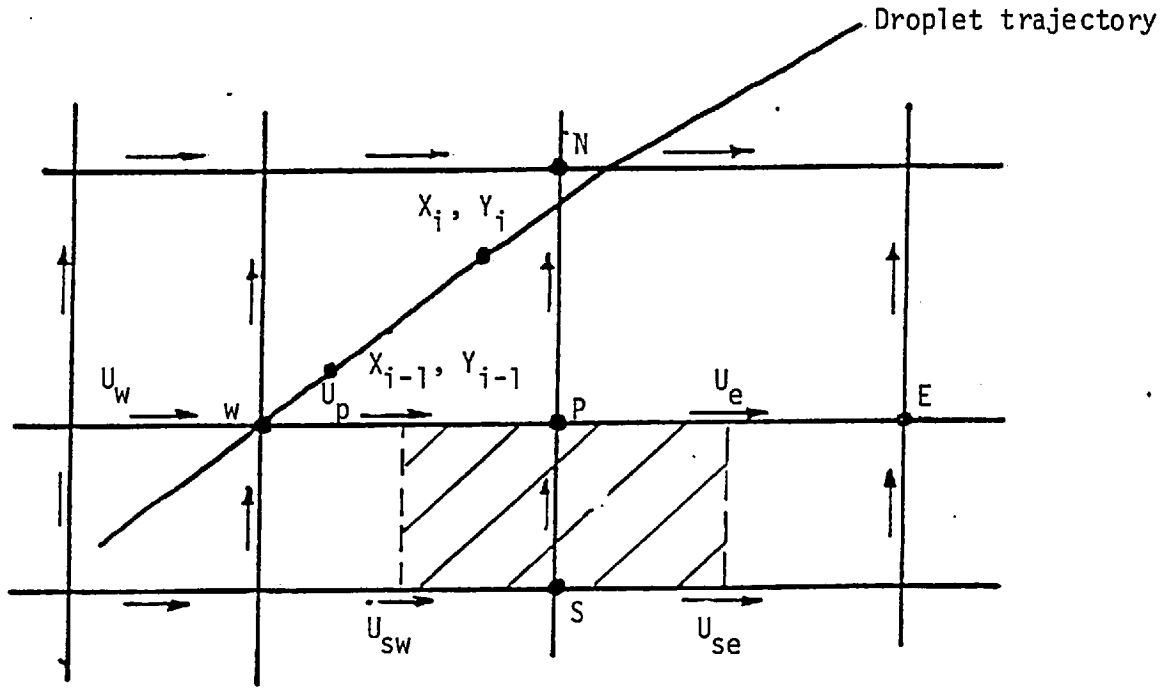

Fig. 3.2 Computational cells and droplet trajectory

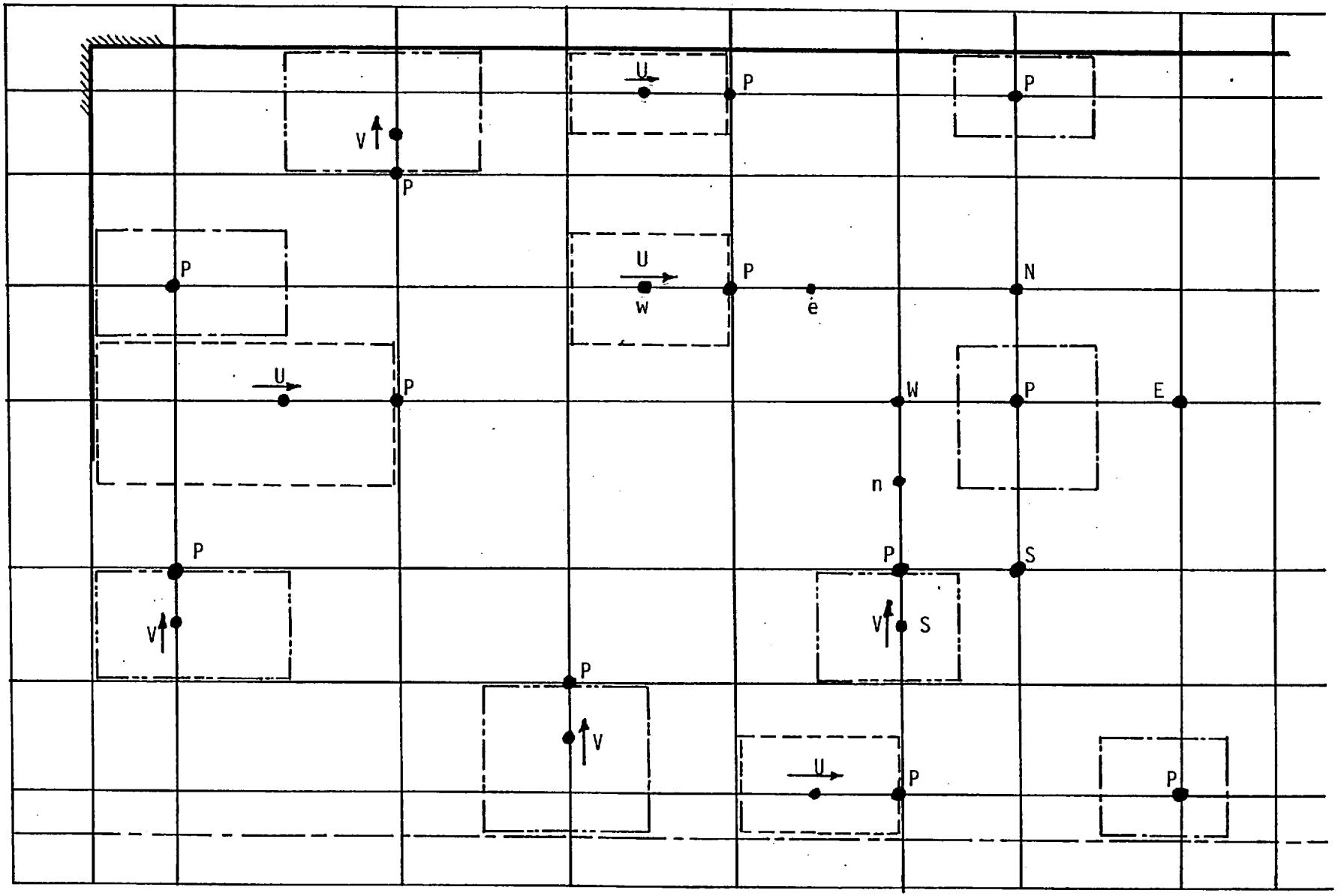

Fig. 3.3 Computational grid

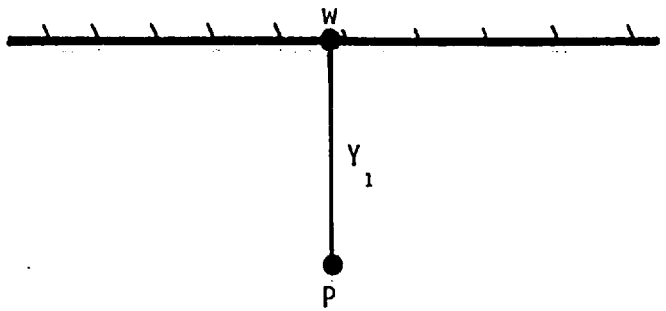

U_p, k_p

T_p, h_p

Fig. 3.4 Wall function

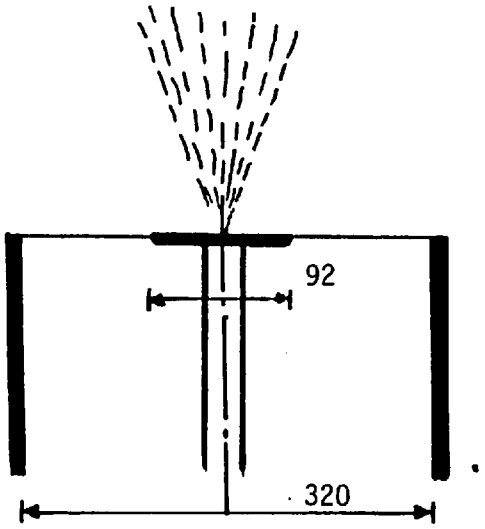

(D) TEST CASE 4

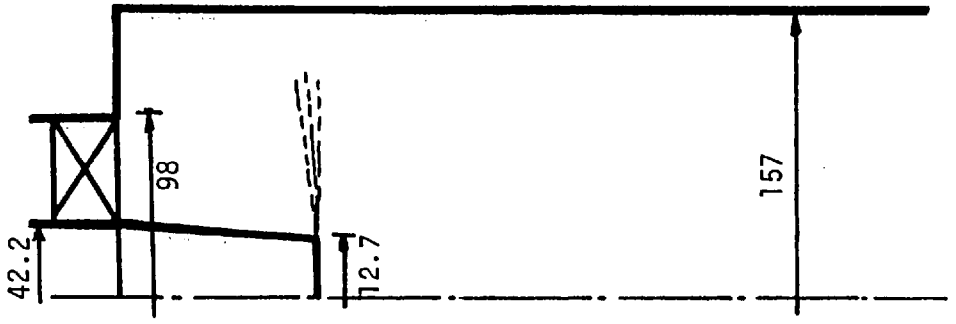

(B) TEST CASE 2

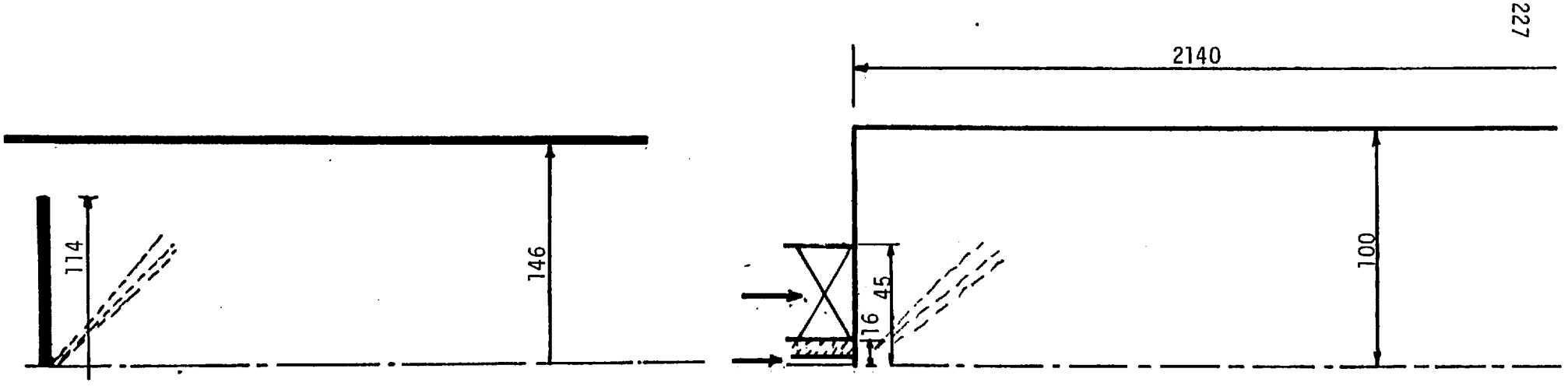

(C) TEST CASE 3

(A) TEST CASE 1

Fig. 3.5 Flame geometries for the four test cases (dimensions in mm)

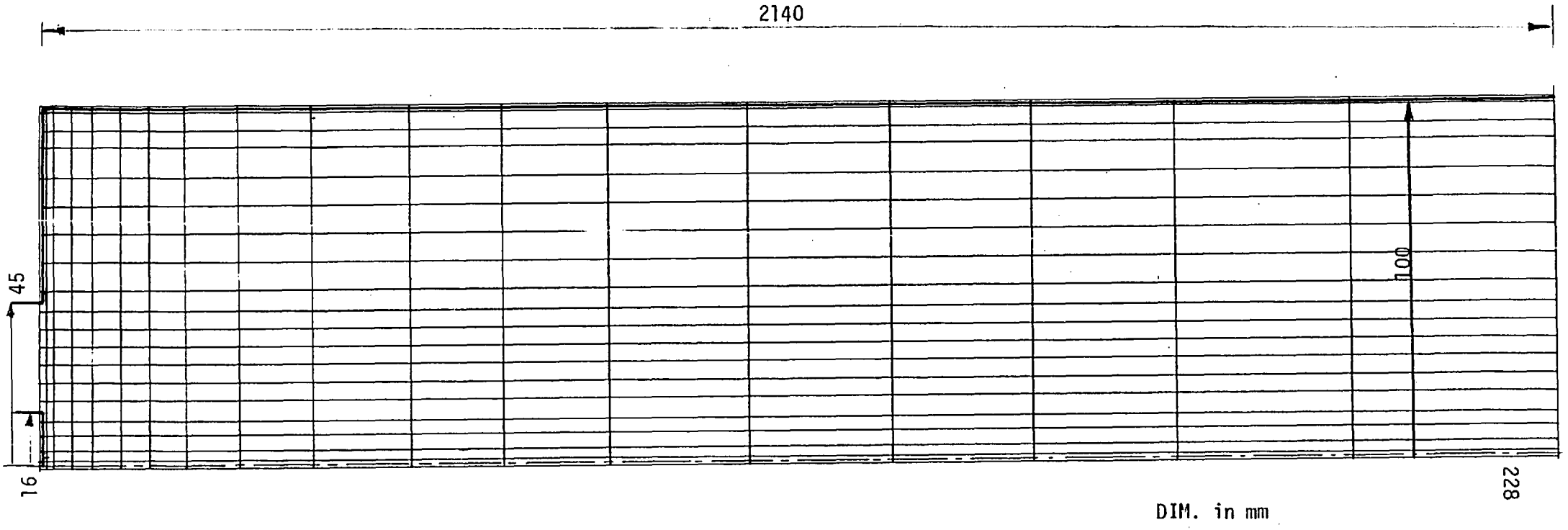

Fig. 3.6 Grid distribution - Test case 1

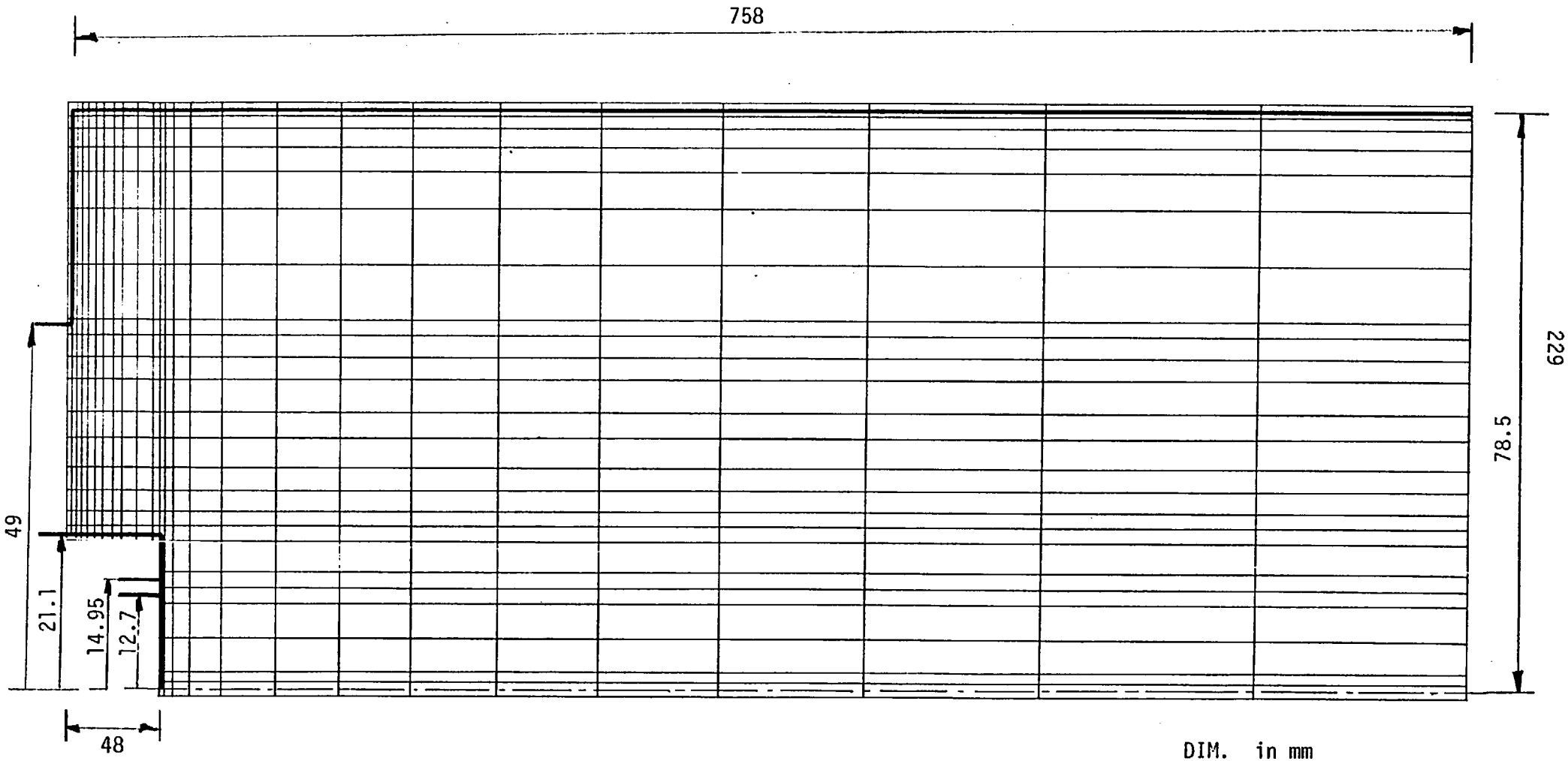

Fig. 3.7 Grid-distribution - Test case 2

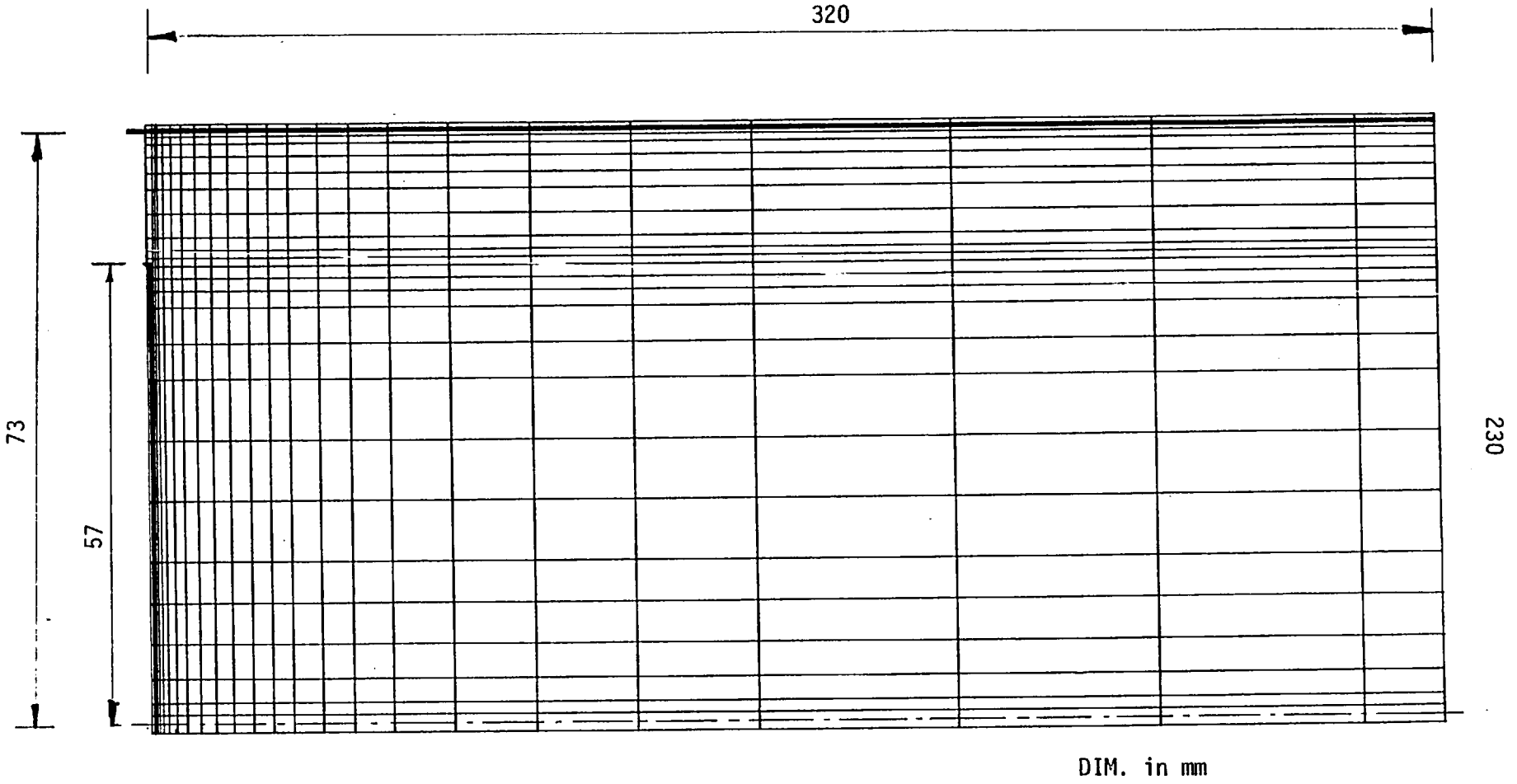

Fig. 3.8 Grid-distribution - Test case 3

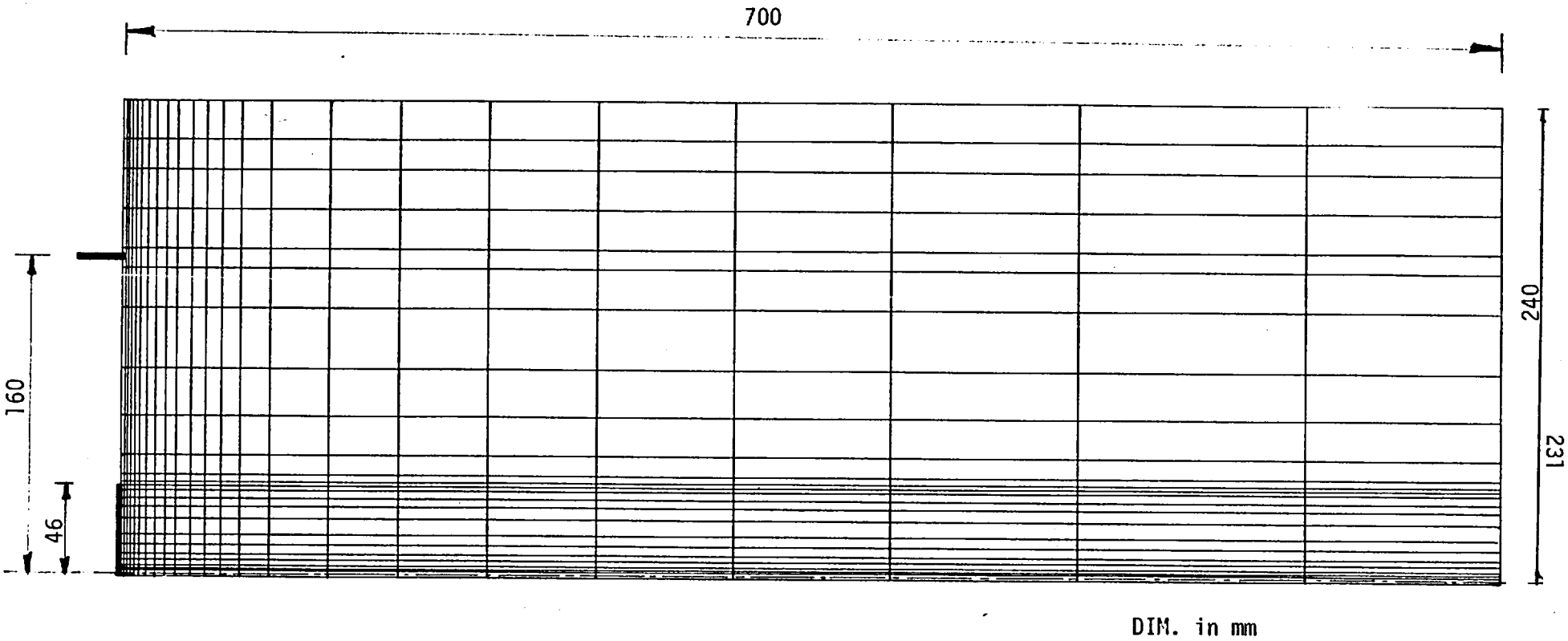

Fig. 3.9 Grid-distribution - Test case 4

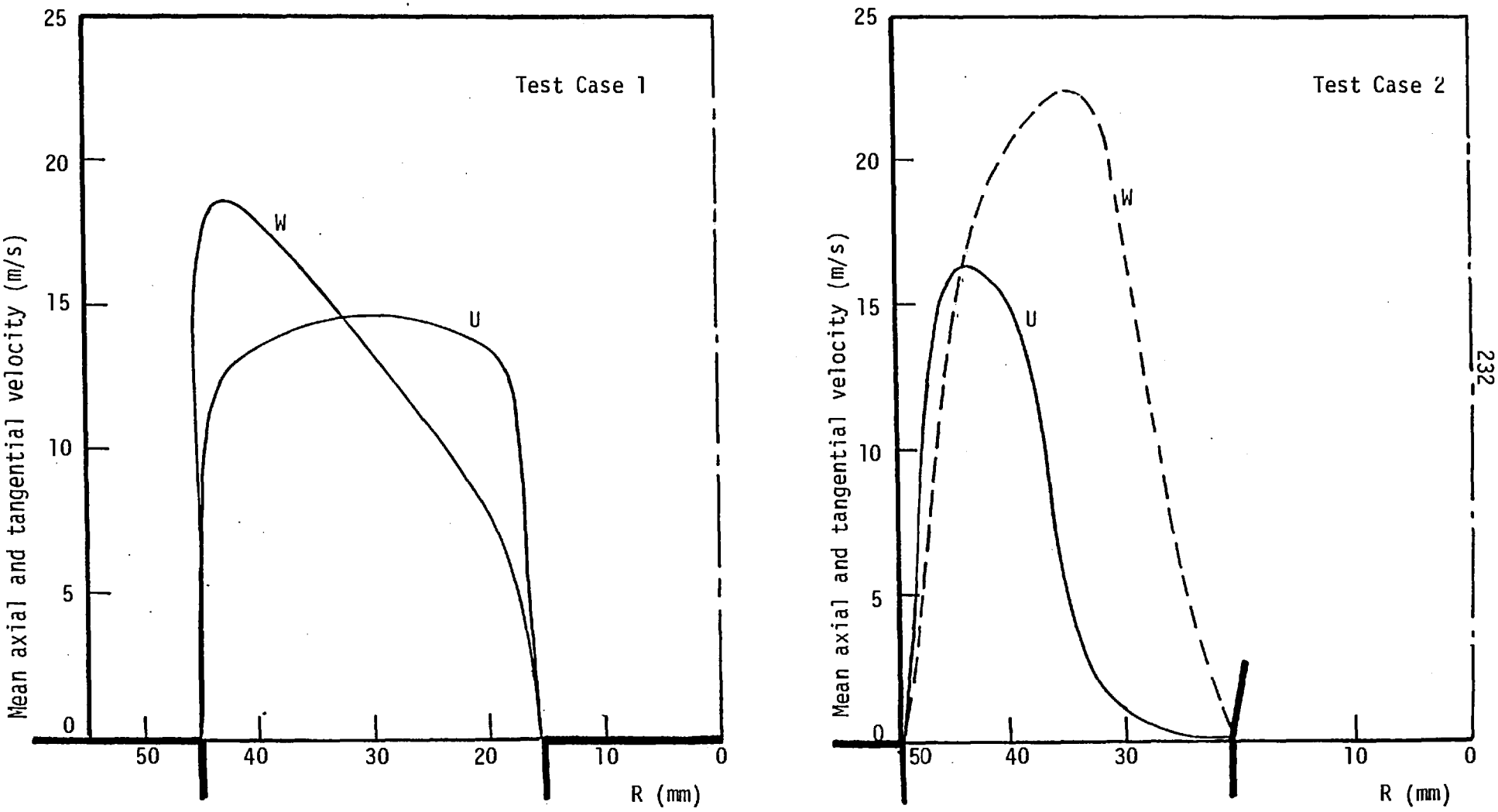

Fig. 3.10 Upstream boundary conditions for velocity components - Test cases 1, 2, 3 and 4

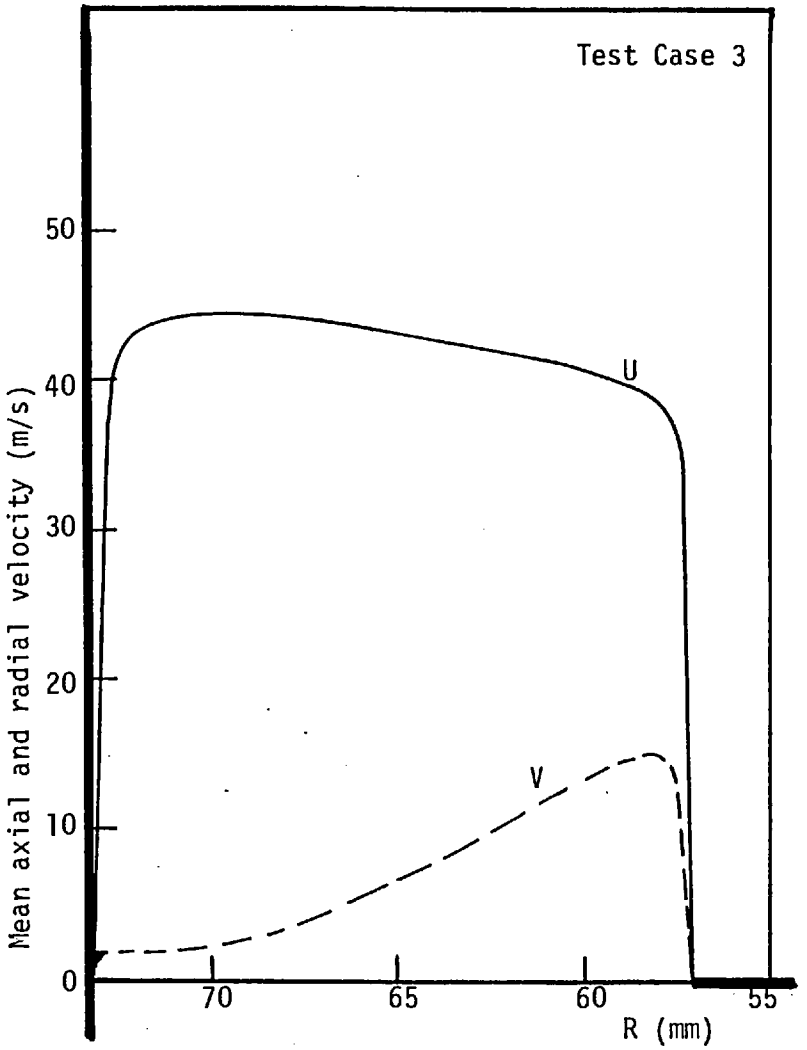

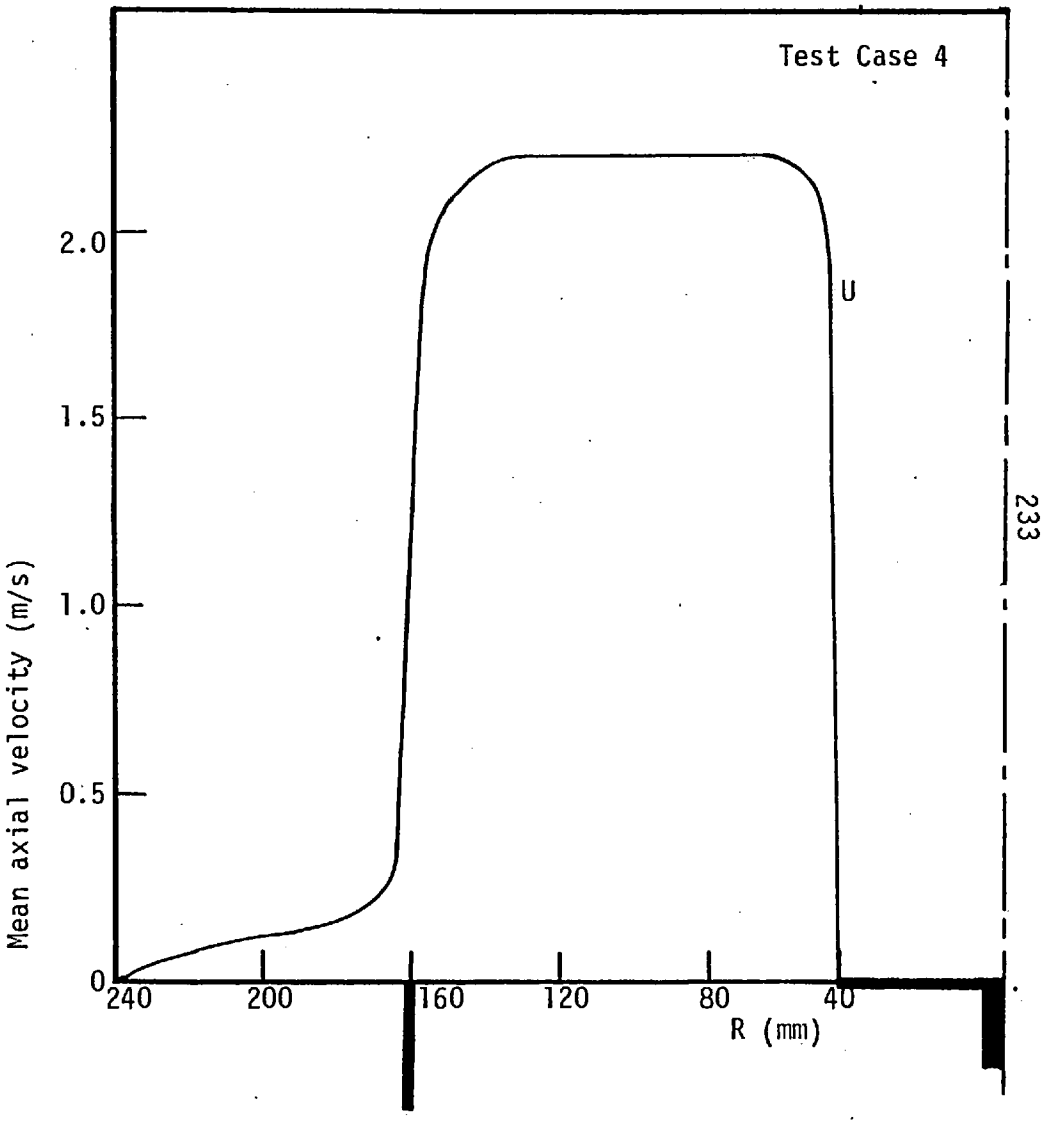

Fig. 3.10 Continued

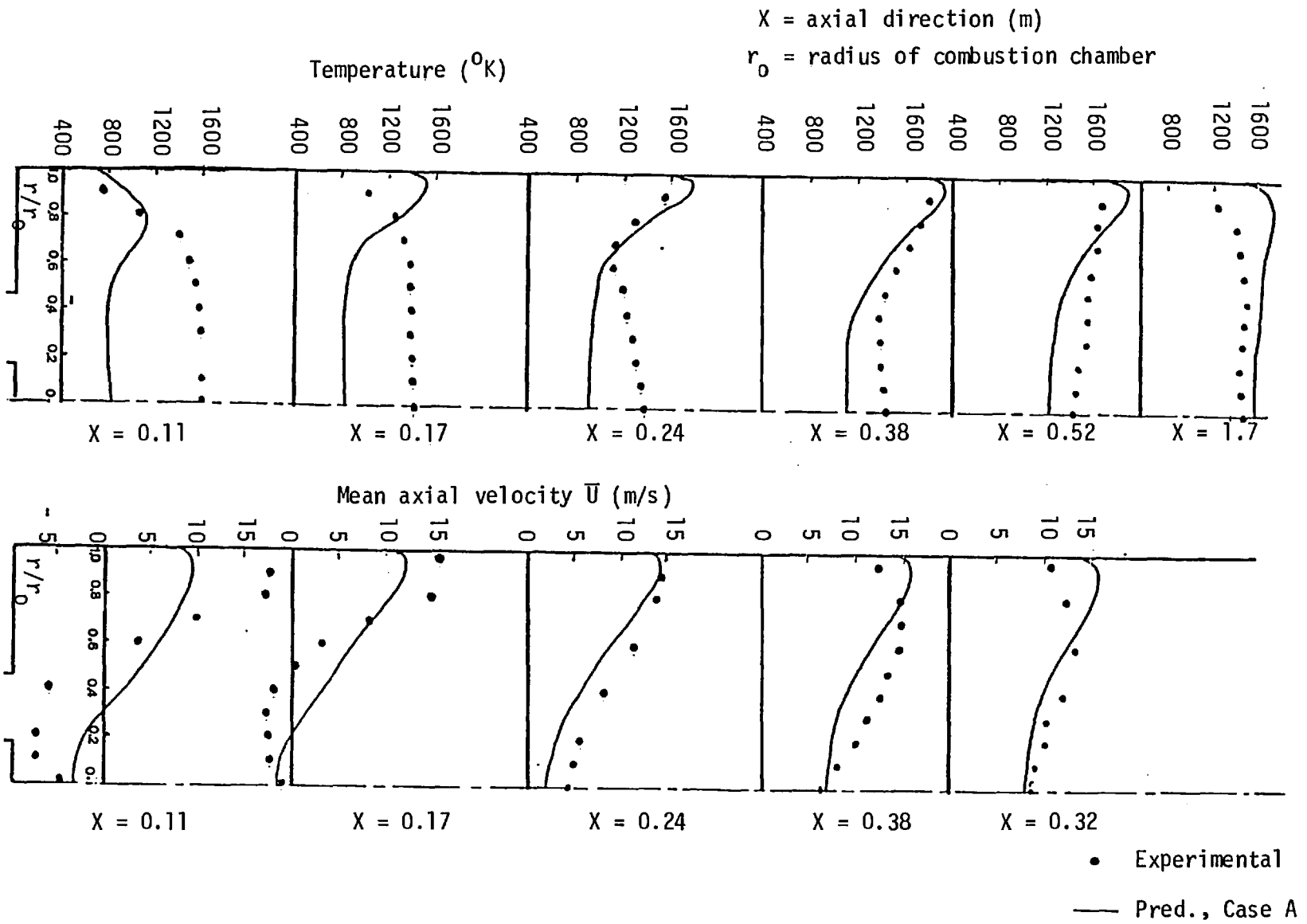

Fig. 3.11 Radial profiles of temperature and axial velocity for Case A and experimental data

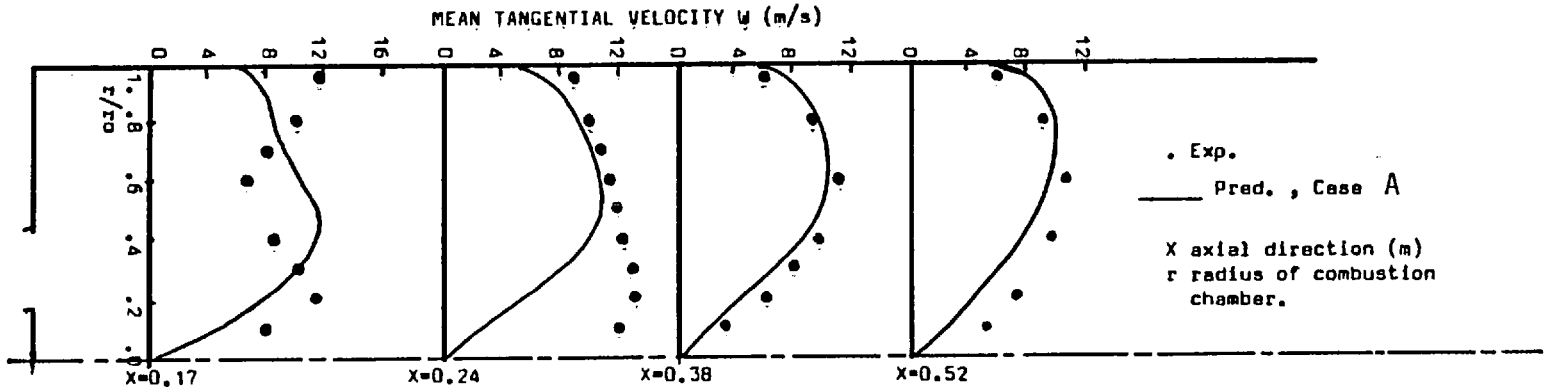

Fig. 3.12 Radial profiles of tangential velocity for Case A and experimental data

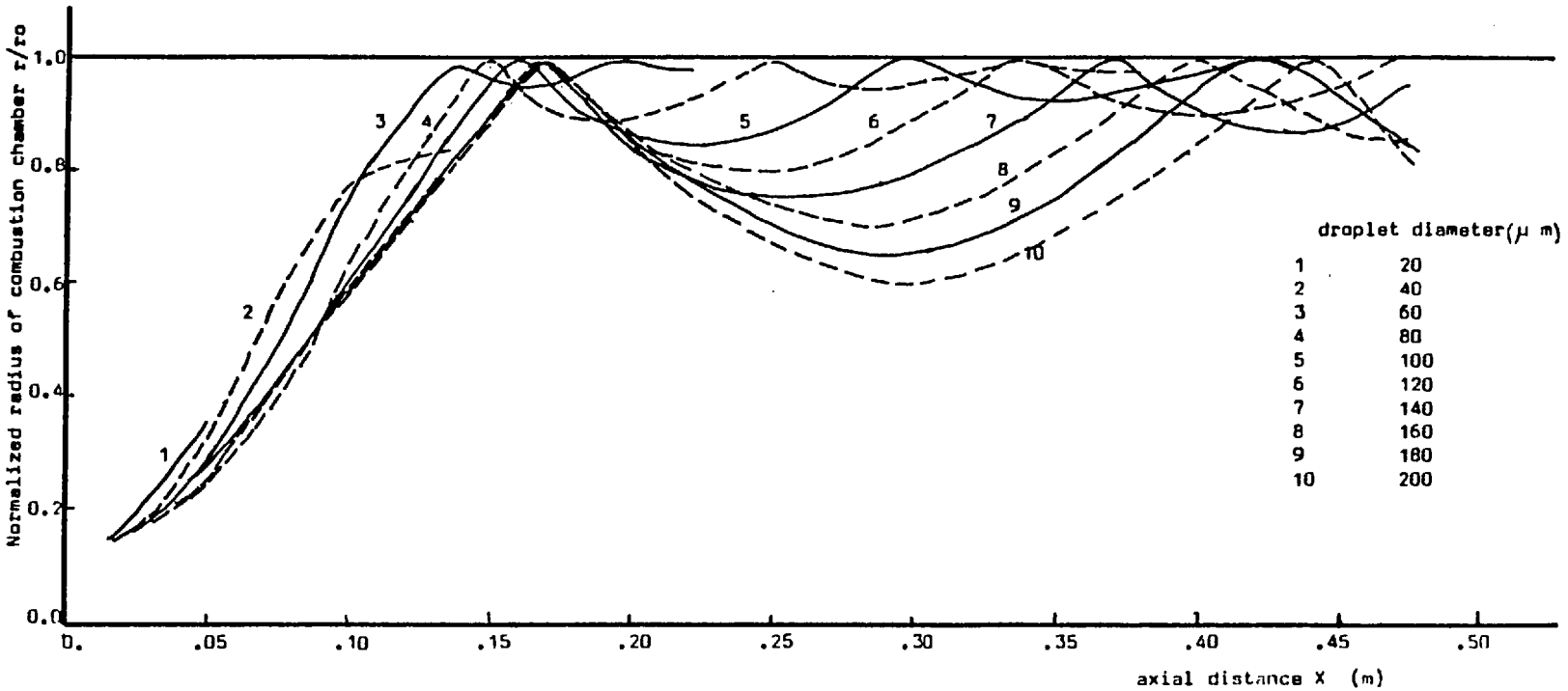

Fig. 3.13 Droplet trajectories, Case A

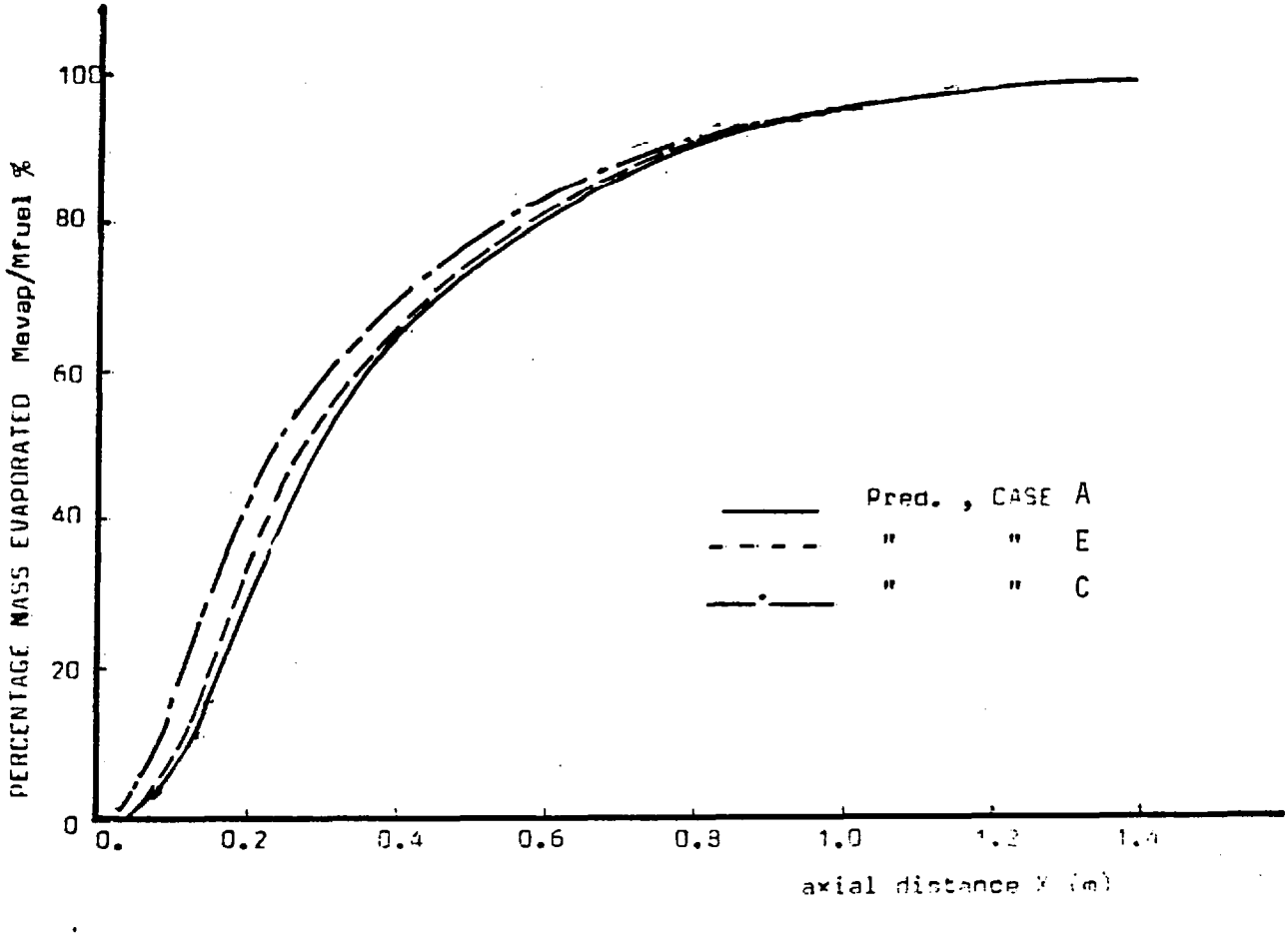

Fig. 3.14 Spray evaporation rate - Cases A, C and E

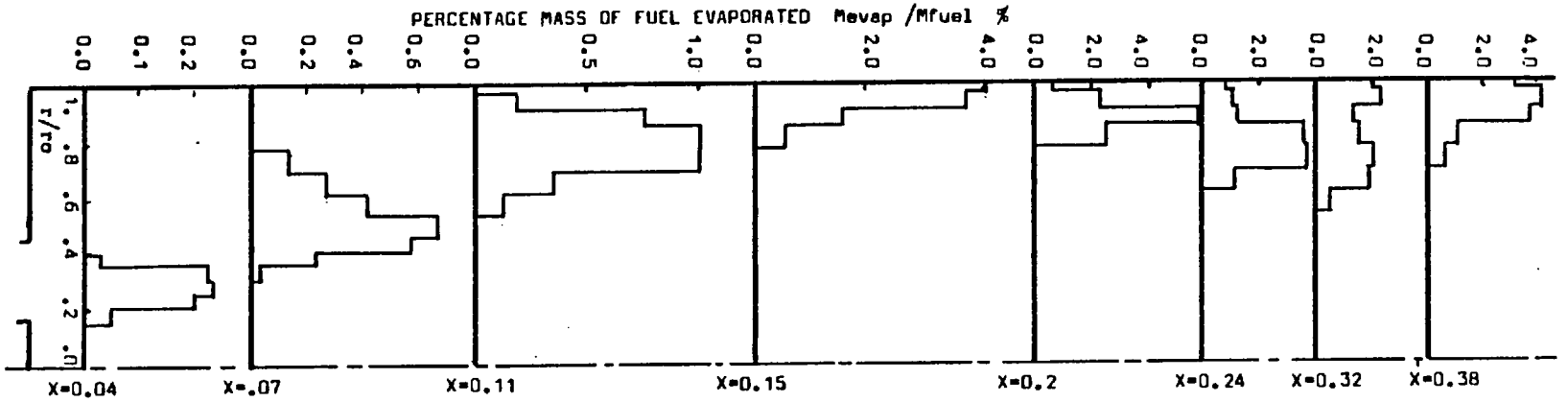

Fig. 3.15 Radial distributions of the percentage mass of fuel evaporated, Case A

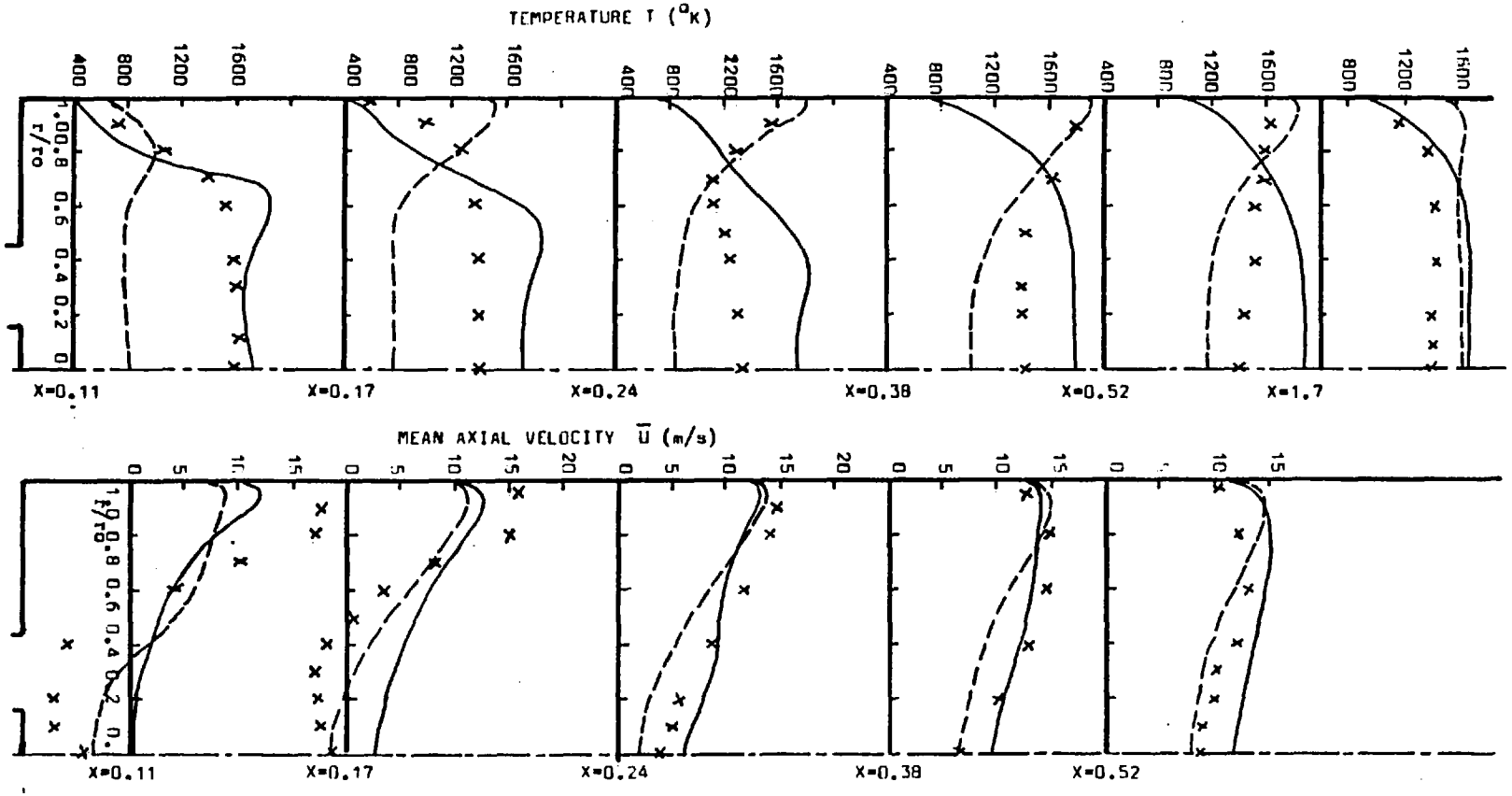

Fig. 3.16 Radial distributions of temperature and axial velocity for two droplet size distributions

—— Case B

— — — Case D

× Experimental data

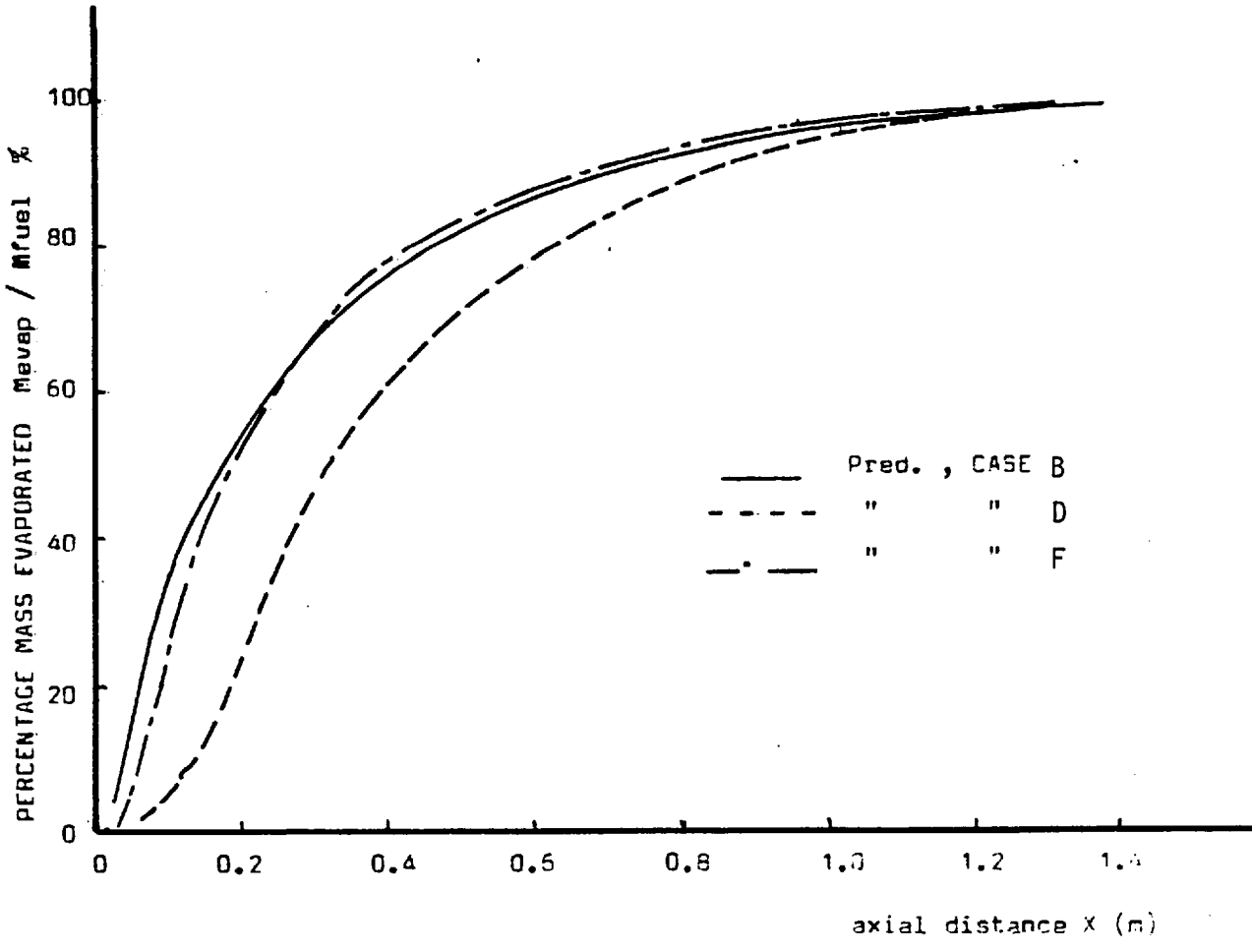

Fig. 3.17 Spray evaporation rate - Cases B, D and F

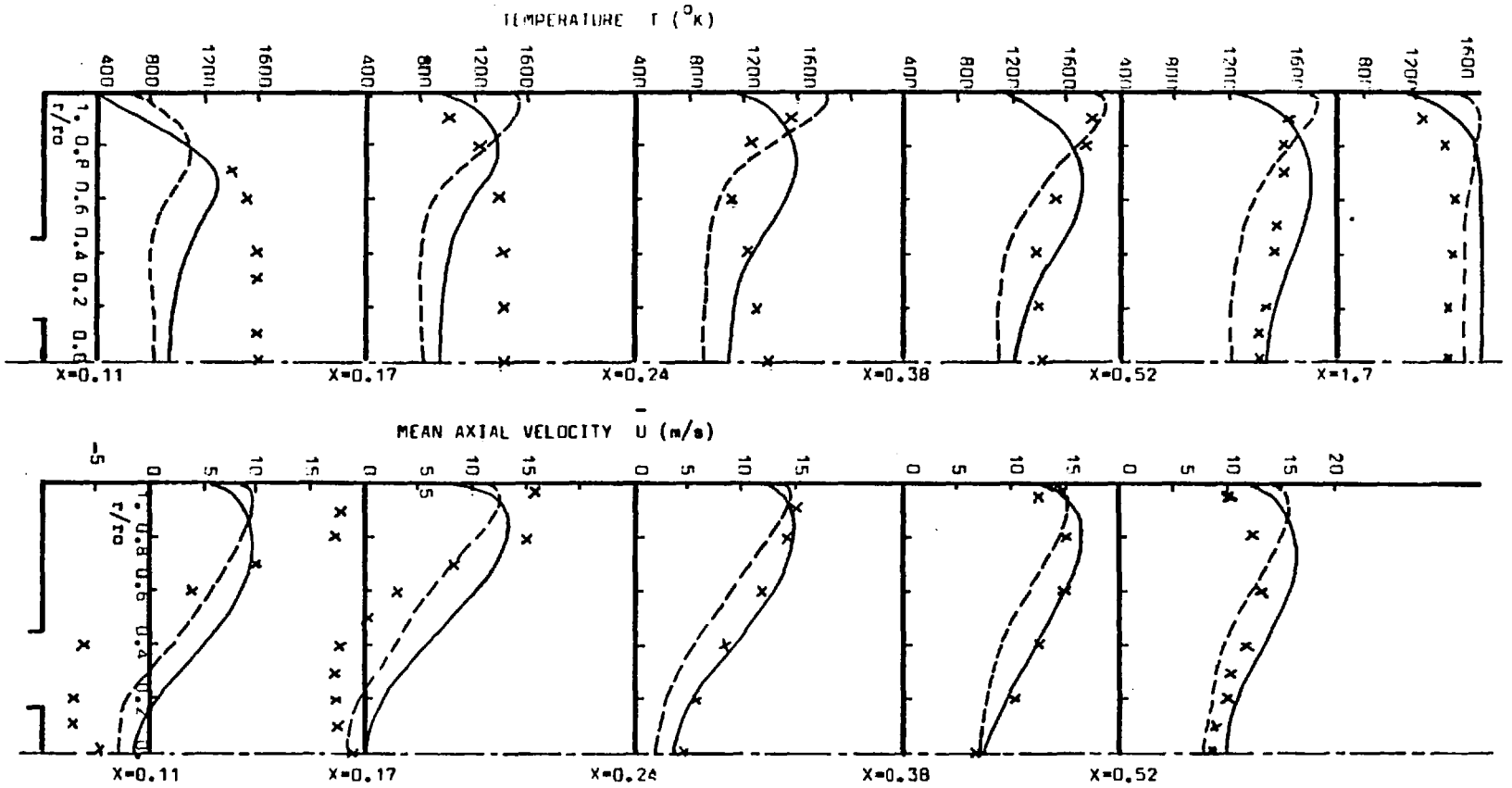

Fig. 3.18 Radial distributions of temperature and axial velocity for two droplet-injection velocities

——— Case C

— — — Case A

× Experimental data

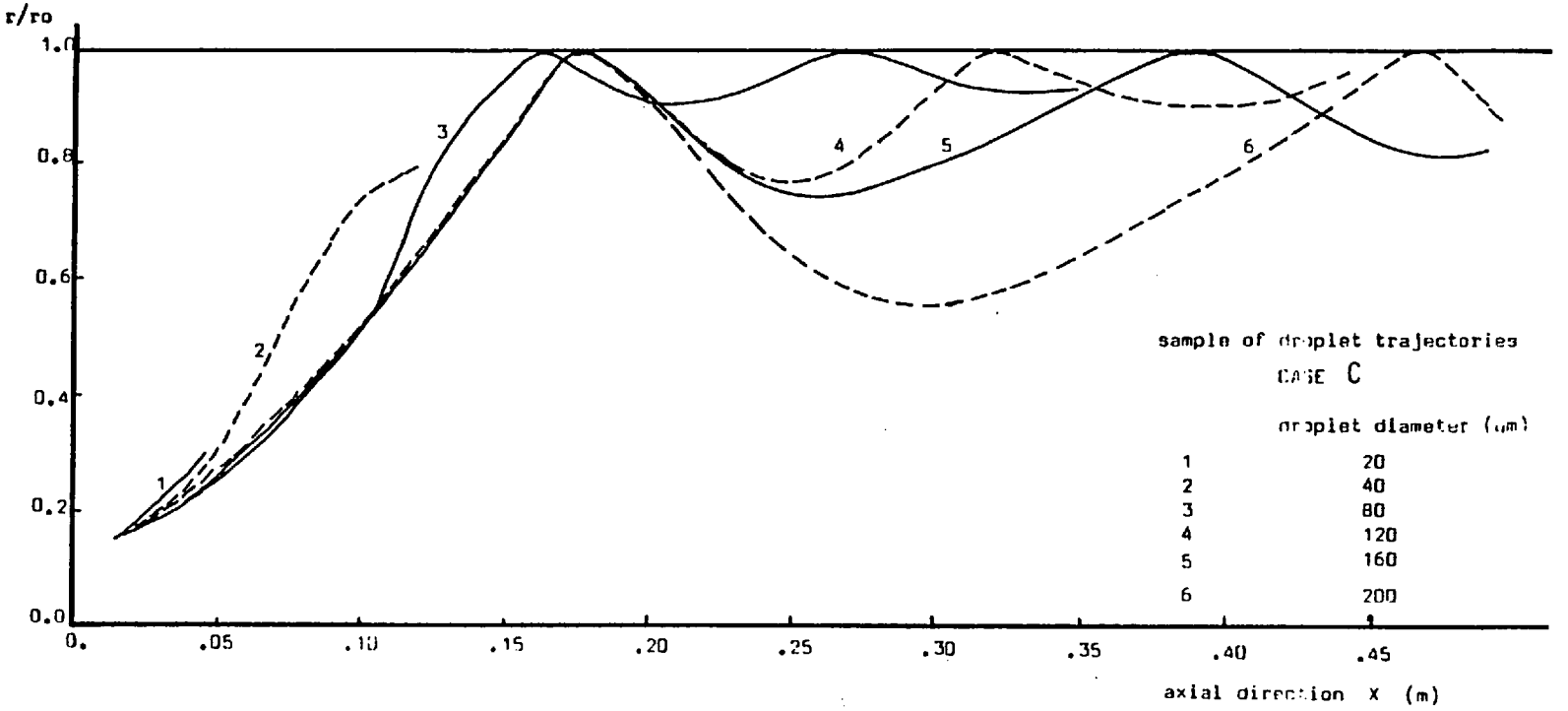

Fig. 3.19 Sample of droplet trajectories - Case C

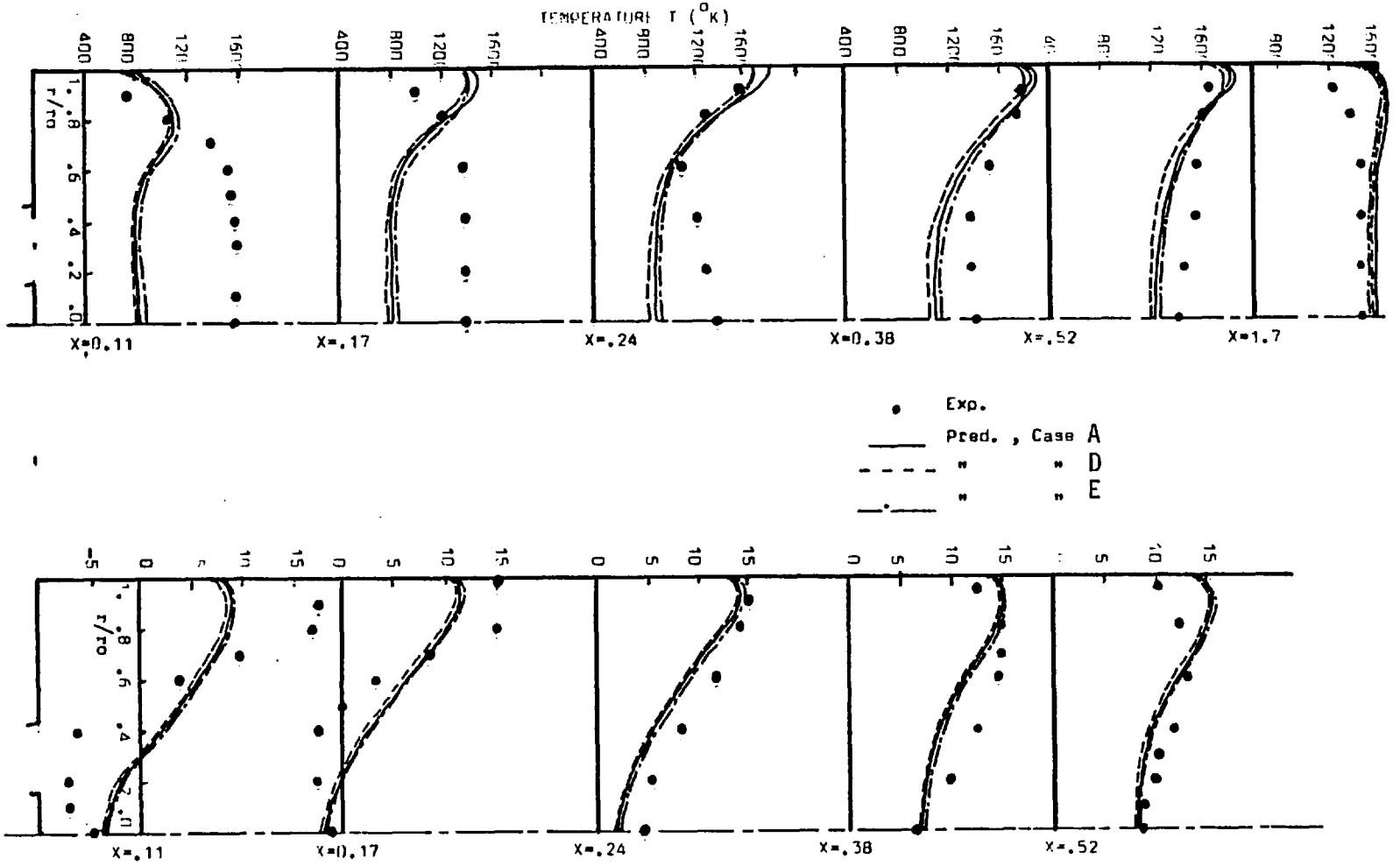

Fig. 3.20 The influence of the number of size ranges on the radial profiles of temperature and axial velocity

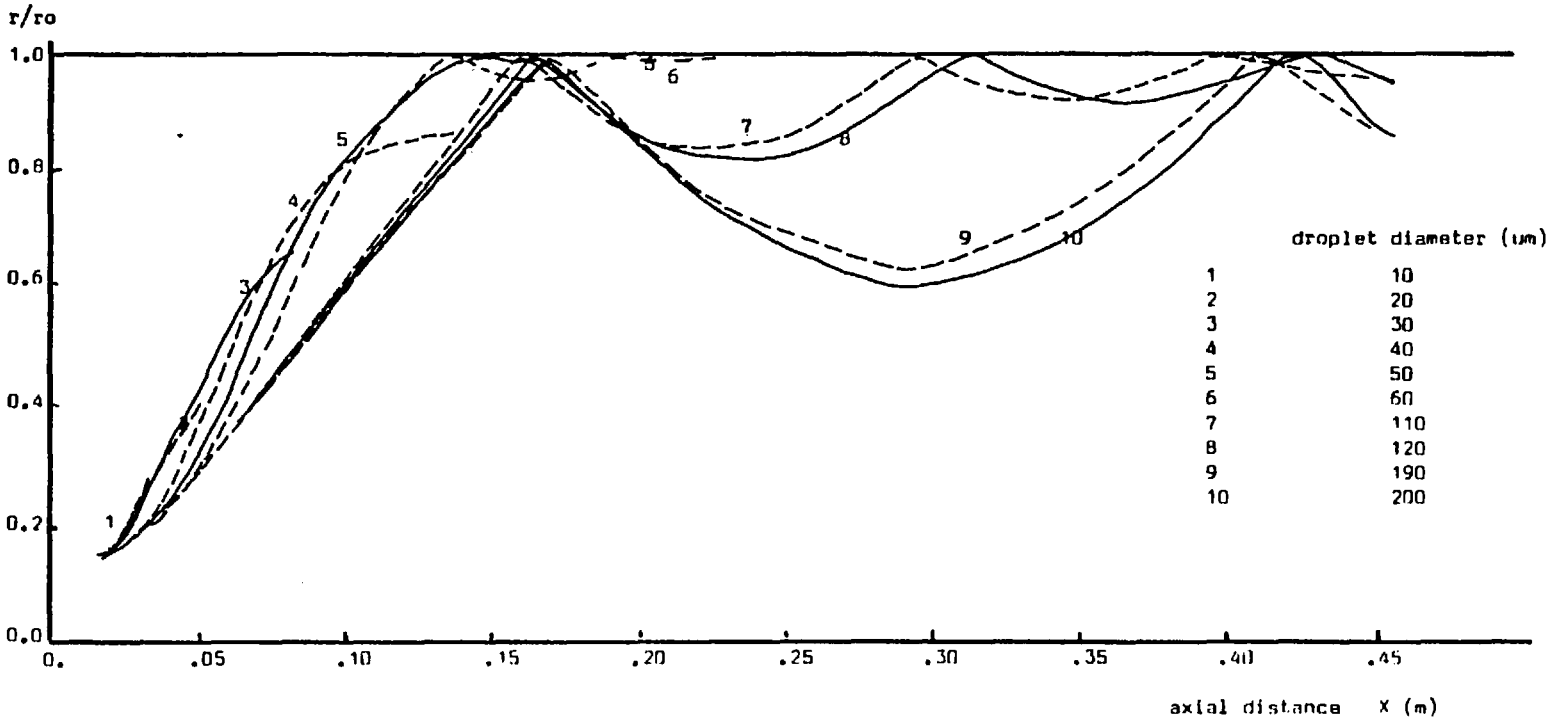

Fig. 3.21 Sample of droplet trajectories - Case E

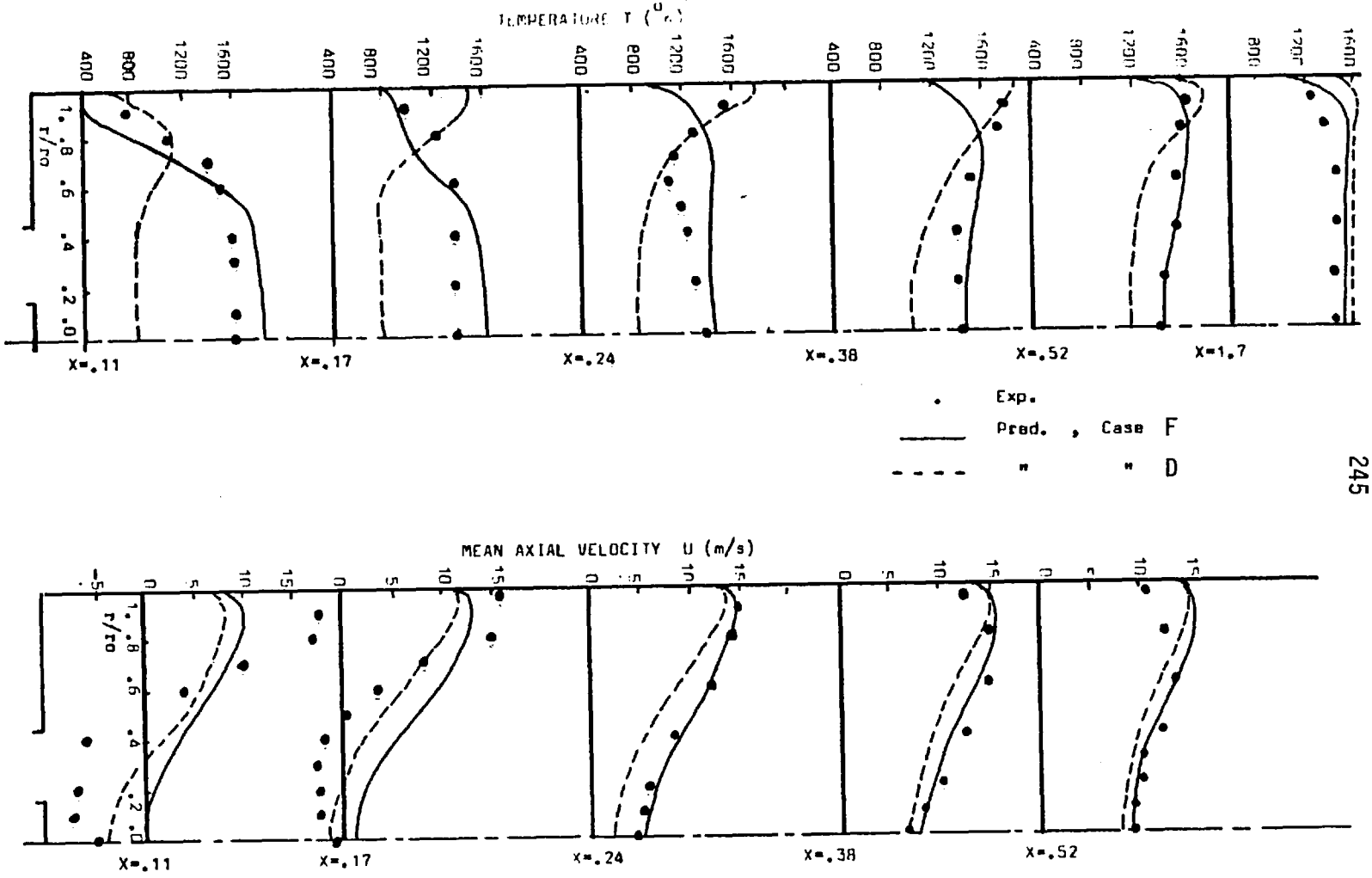

Fig. 3.22 The influence of evaporation rate expression on the radial profiles of temperature and axial velocity

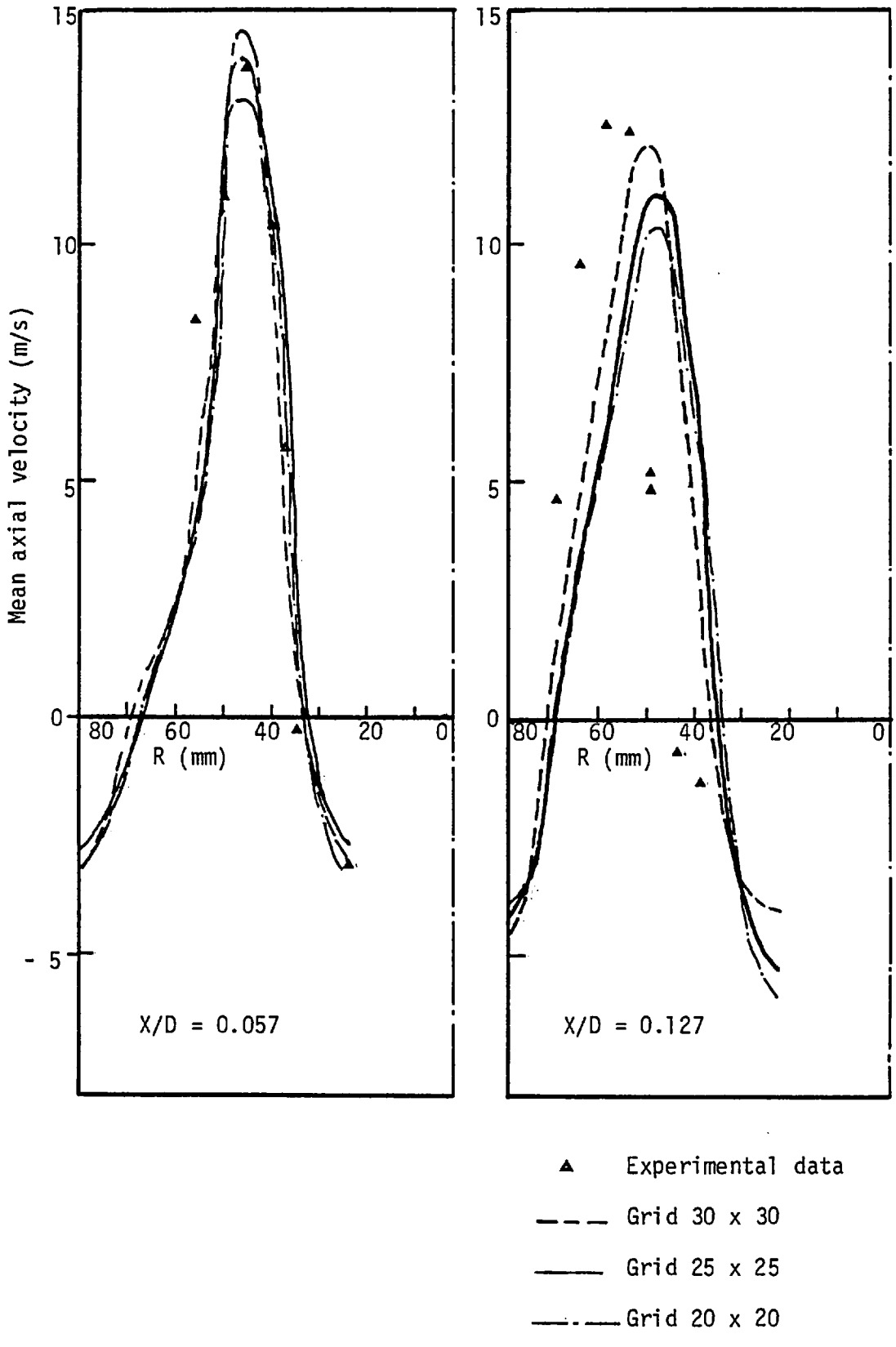

Fig. 3.23 (a) Measured and calculated radial profiles of mean axial velocity (isothermal)

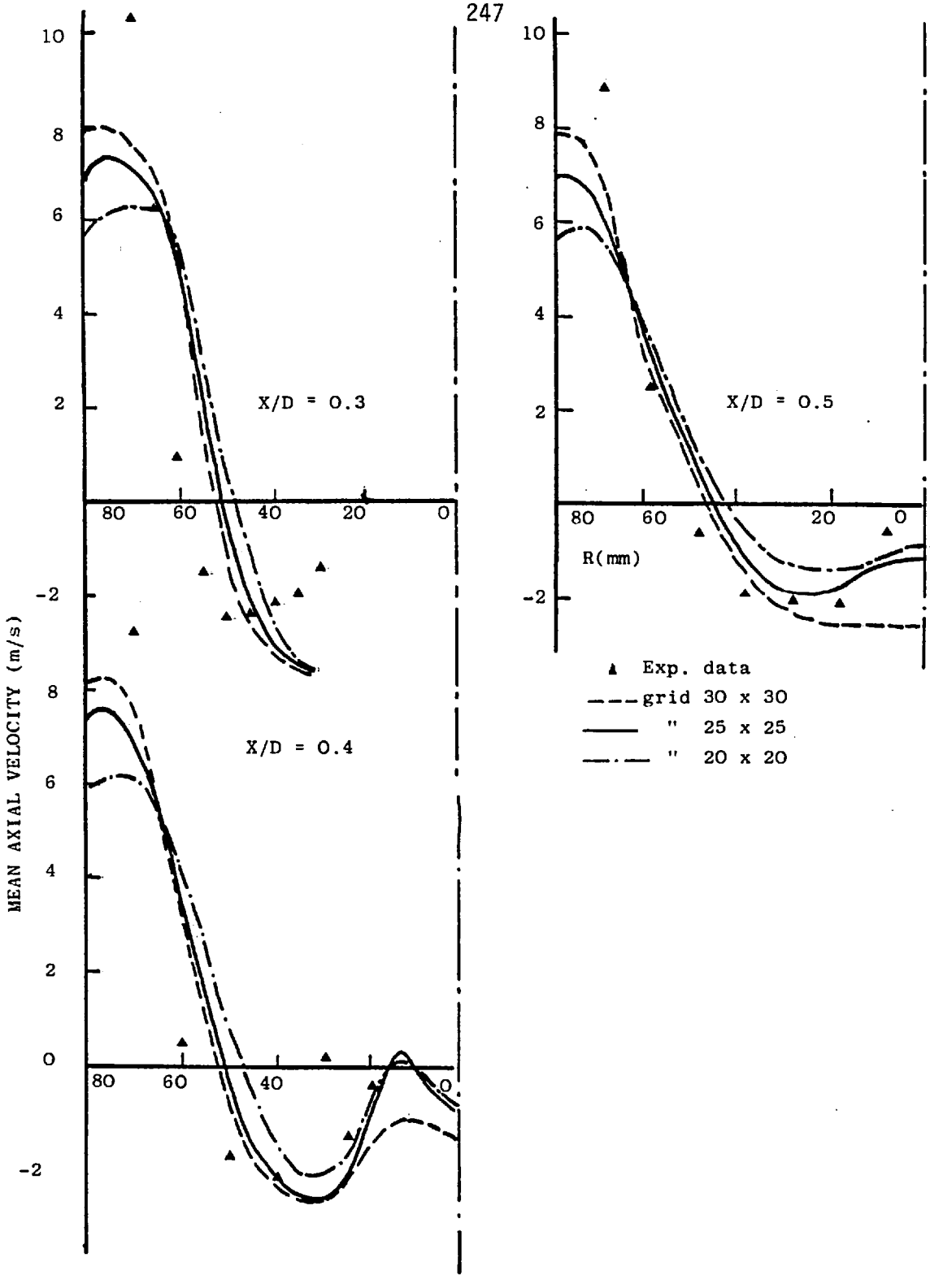

Fig. 3.23 (a) (Contd.)

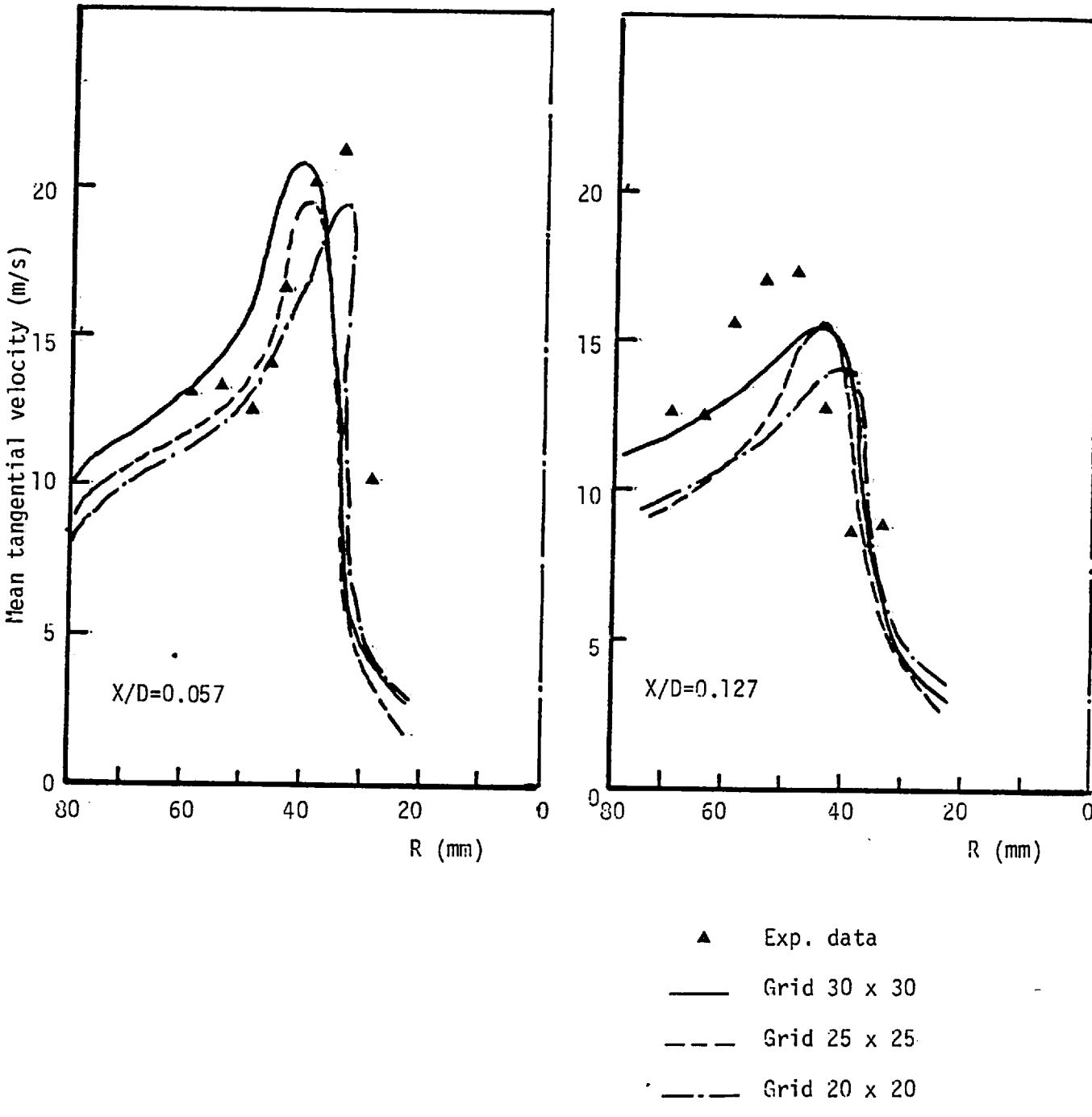

Fig. 3.23 (b) Measured and calculated radial profiles of tangential velocity (isothermal)

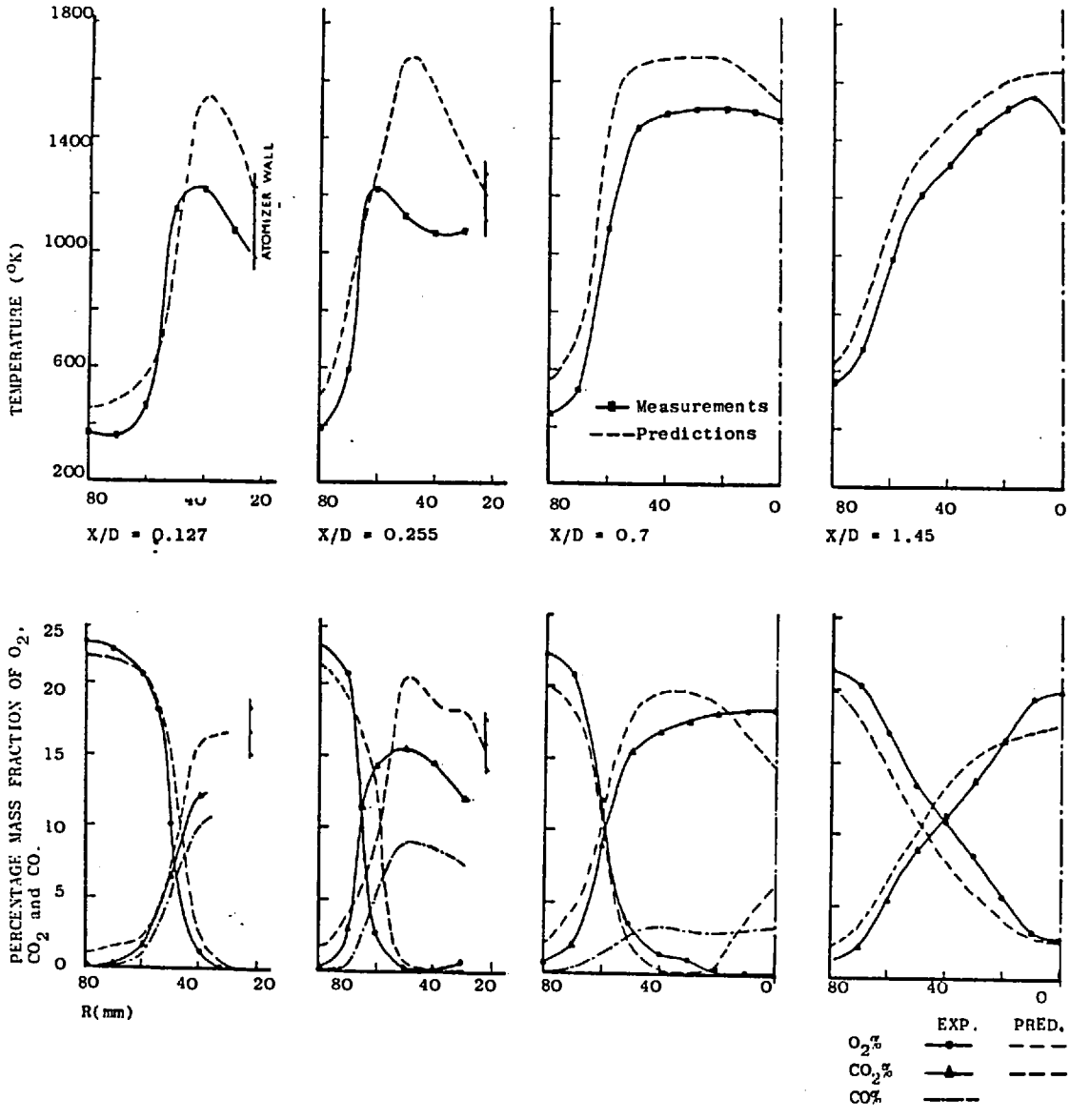

Fig. 3.24 Experimental and predicted radial profiles of temperature and mass fractions of O_2, CO_2 and CO. Test case 2A.

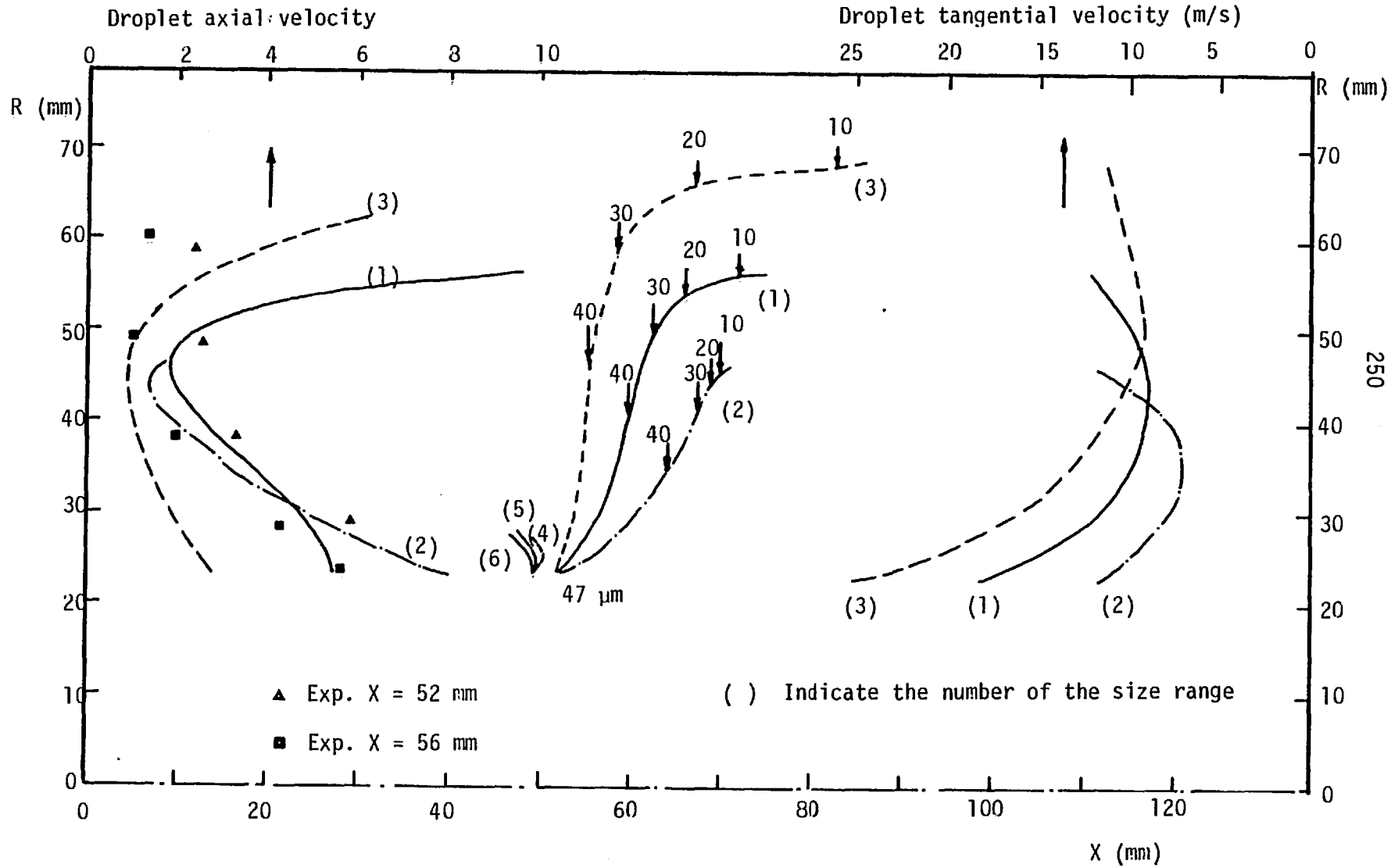

Fig. 3.25 Droplet trajectories, axial and tangential velocity

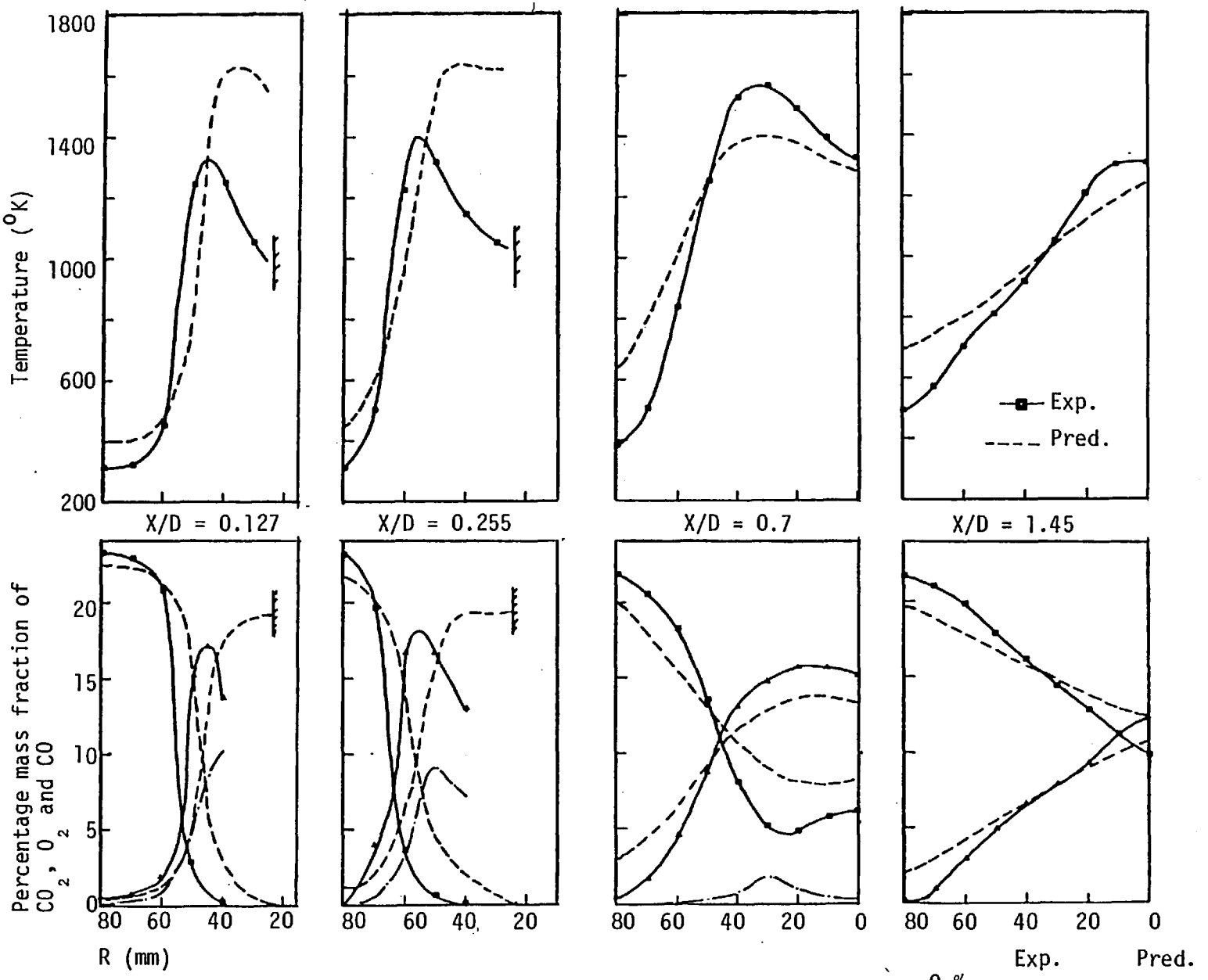

Fig. 3.26 Experimental and predicted radial profiles of temperature and mass fractions of O_2, CO_2 and CO. Test case 2B

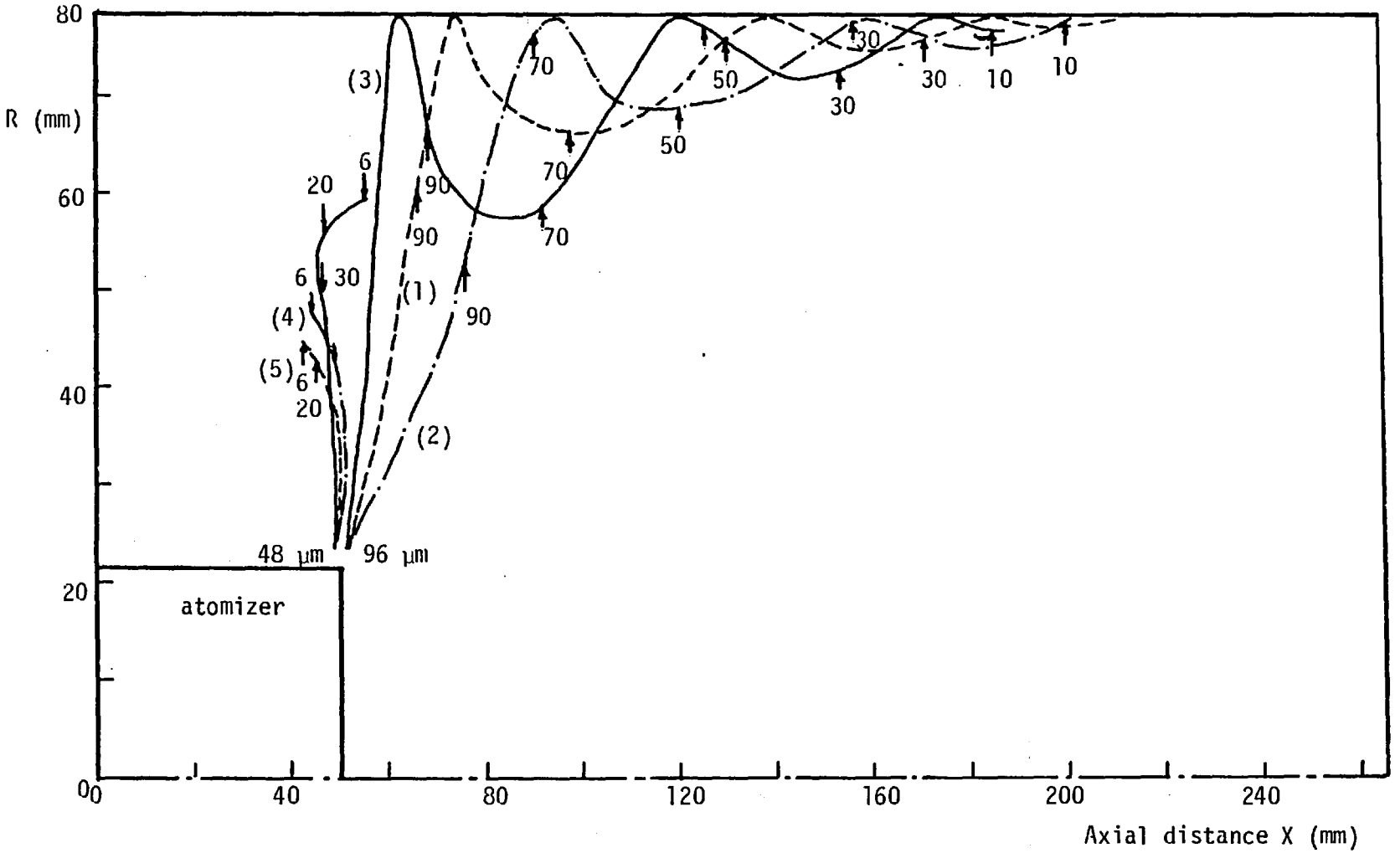

Fig. 3.27 Droplet trajectories, test case 2.B

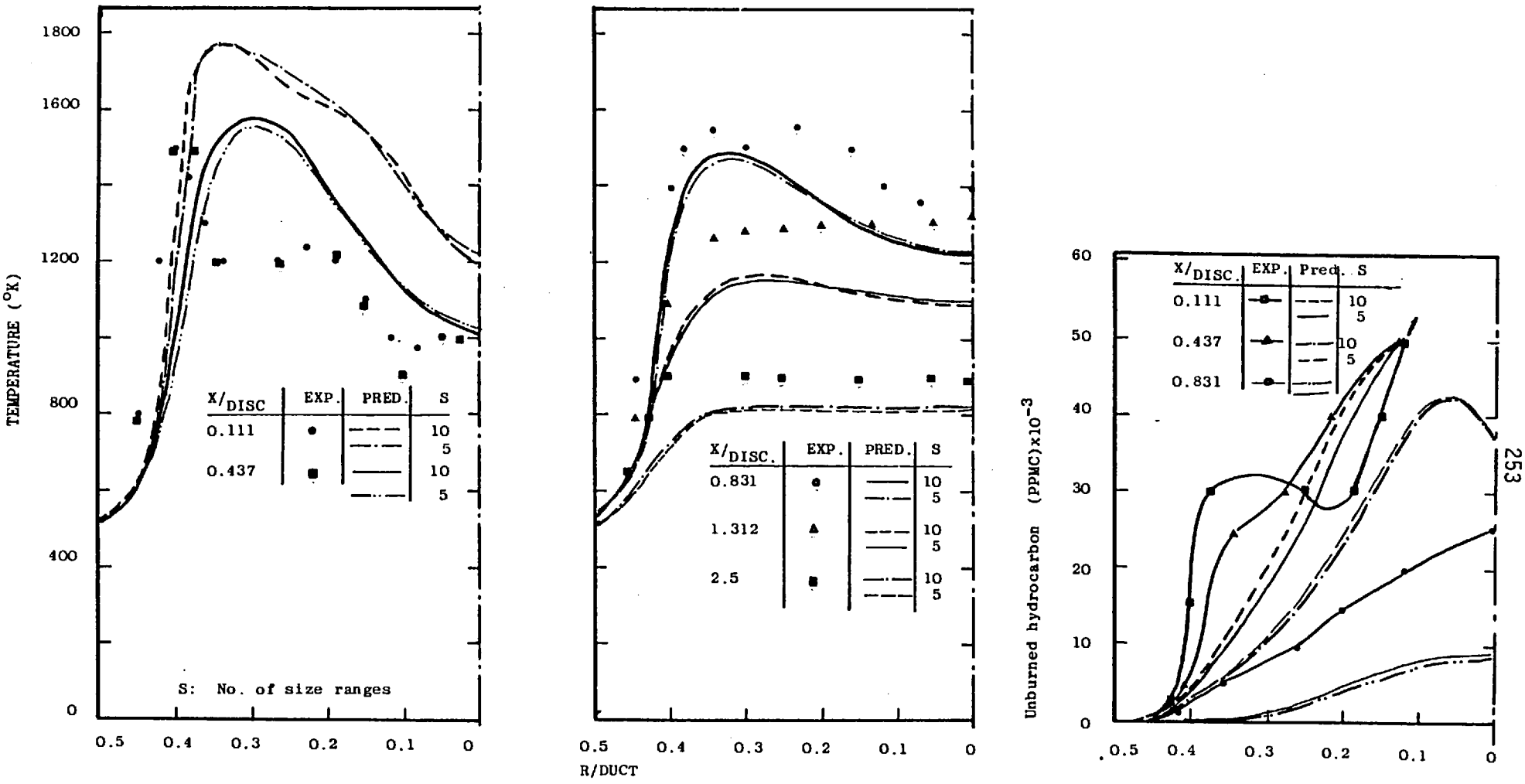

Fig. 3.28 Experimental and predicted radial profiles of temperature and unburned hydrocarbon concentration. Test case 3.

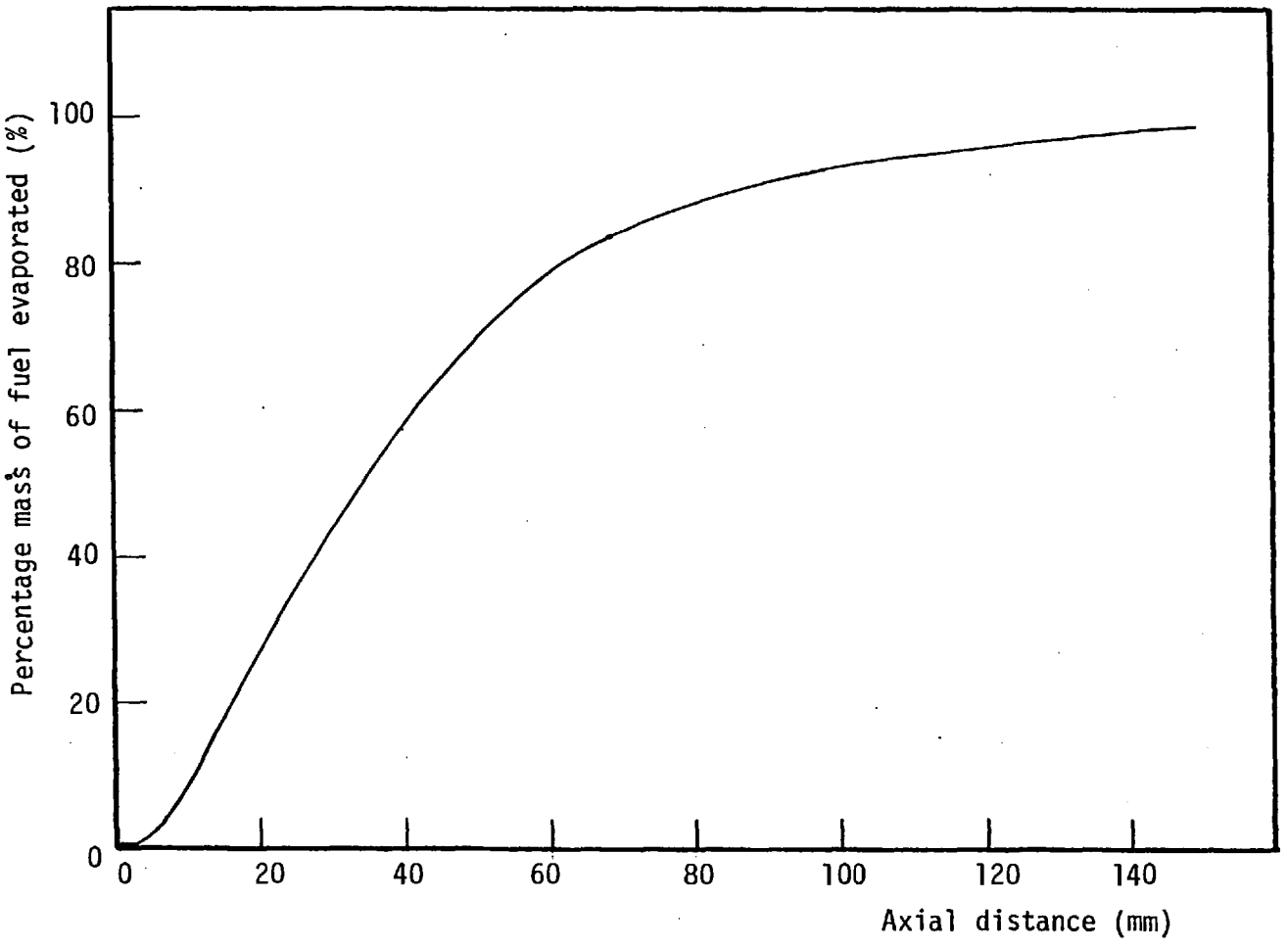

Fig. 3.29 Axial distance of the percentage mass evaporated, test case 3 (10 size ranges)

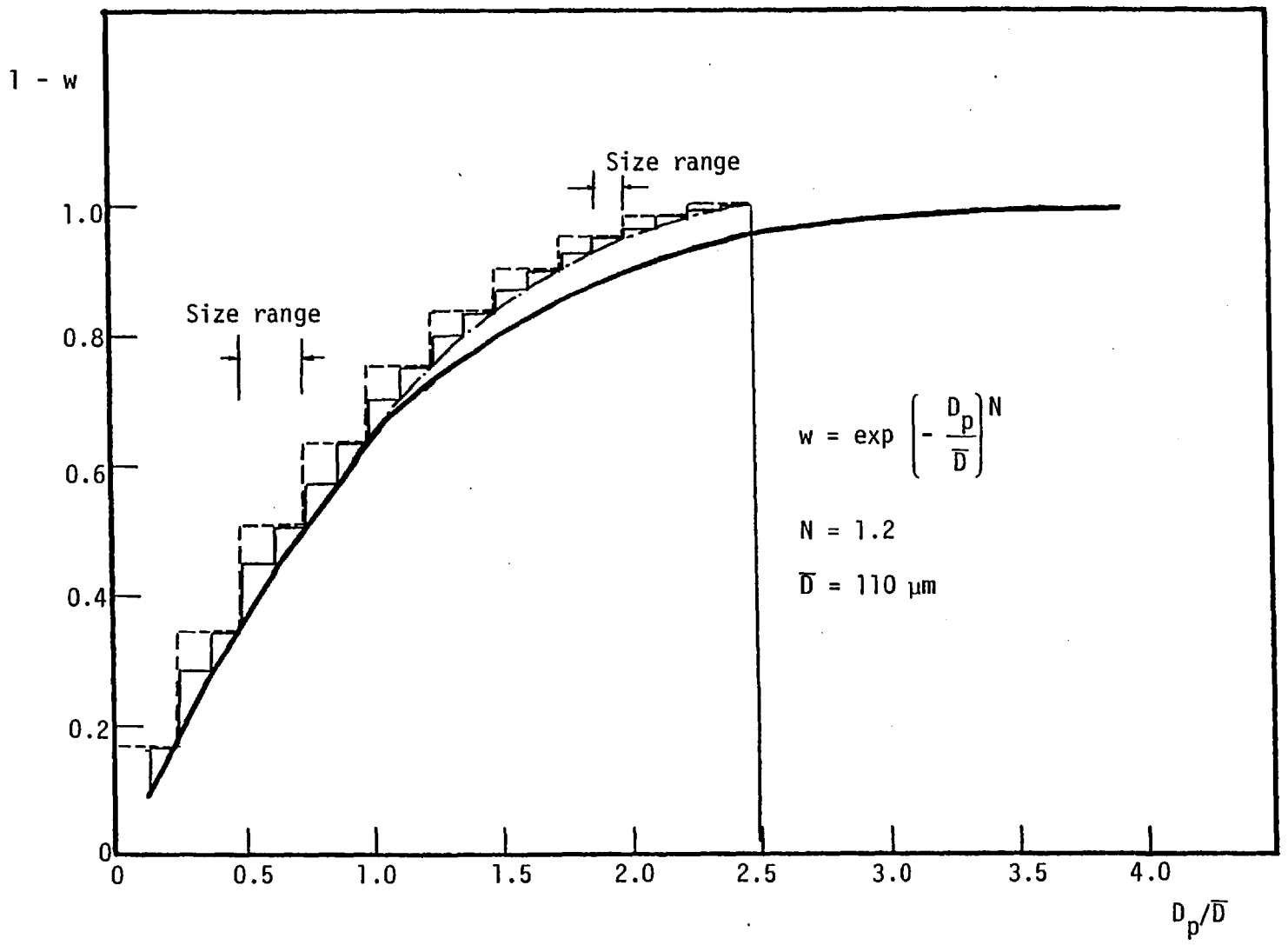

Fig. 3.30 Droplet-size-distribution - Test cast 4

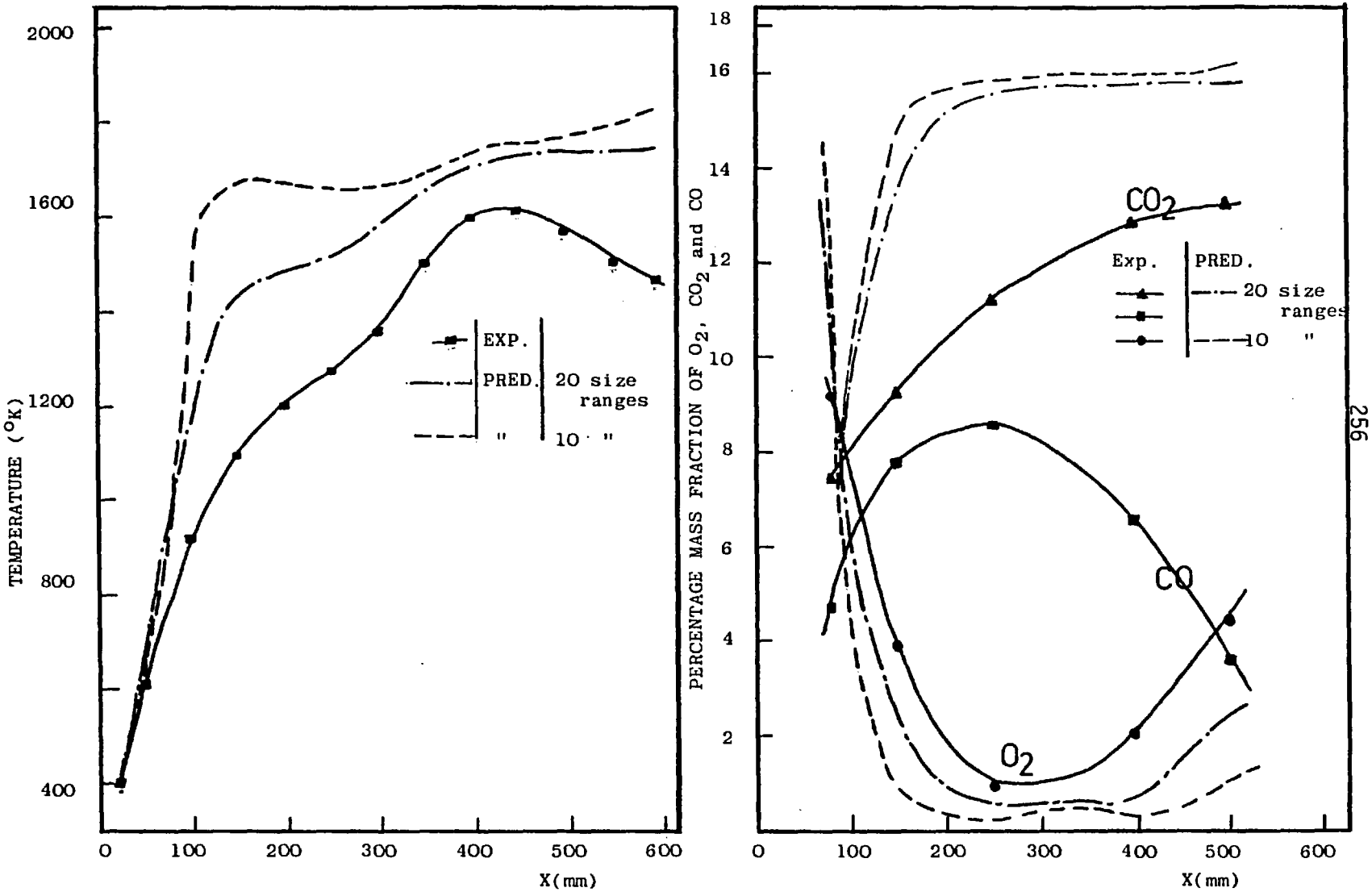

Fig. 3.31 Experimental and predicted centreline distributions of temperature and mass fraction of O_2, CO_2 and CO. Test case 4.

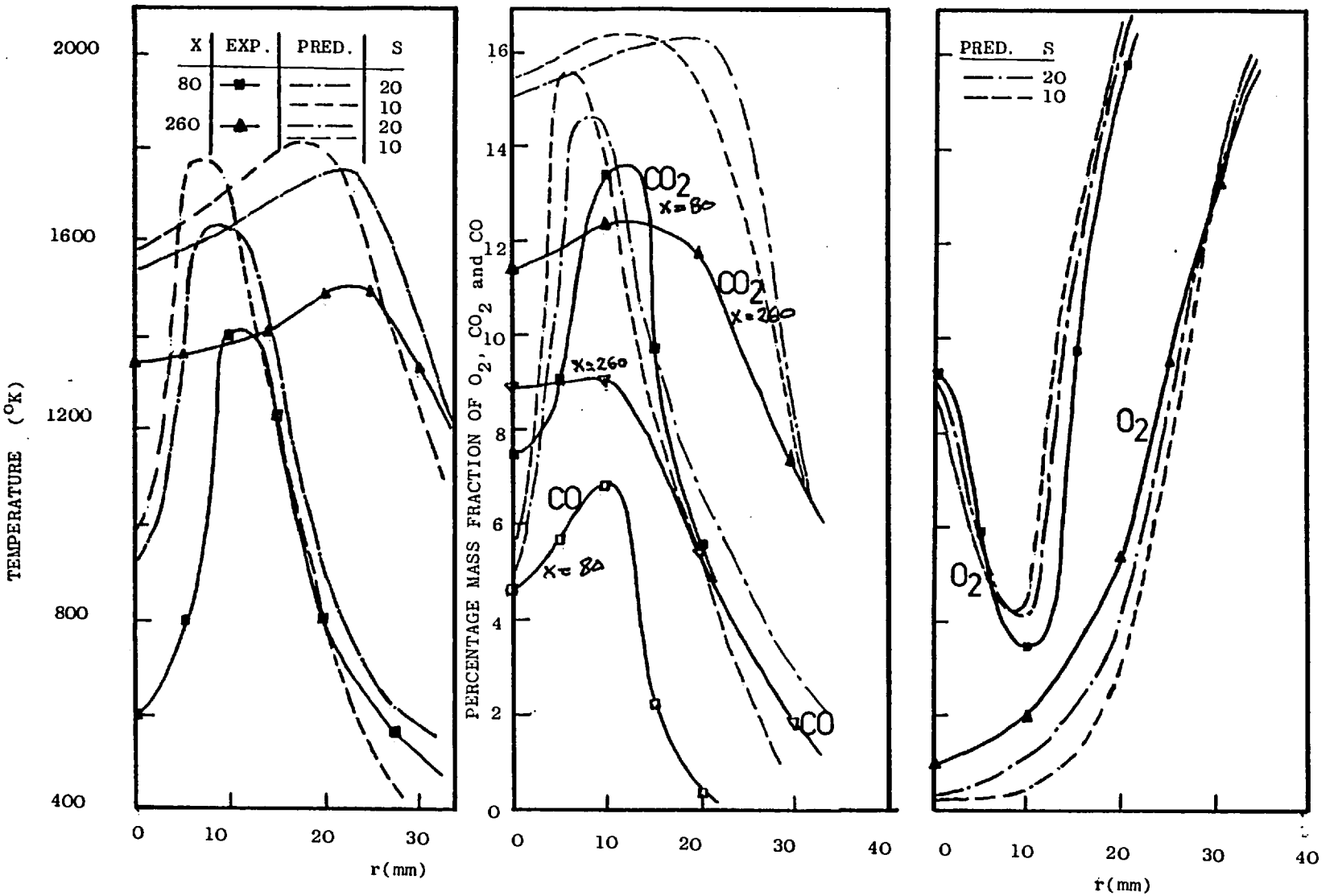

Fig. 3.32 Experimental and predicted radial profiles of temperature and mass fractions of O_2, CO_2 and CO. Test case 4.

CHAPTER 4

SUMMARY OF CONCLUSIONS AND RECOMMENDATIONS

A summary of the main conclusions of the present investigation is given in the first section of this chapter. Recommendations for future work, both experimental and theoretical, are discussed in the second section.

4.1 Summary of Conclusions

The main achievements of the present study and the conclusions thereof may be summarized as follows:-

1. Measurements of droplet mean axial velocity and the rms of the corresponding fluctuations, mean temperature and droplet number density have been obtained in a range of unconfined swirling and non-swirling kerosene spray flames. Interpretation of the measured profiles indicated that the combustion intensity at near-nozzle regions depends largely on the operating conditions of the combustion air swirl and fuel mass flow rate and this was related to the influence of the operating conditions on the spray characteristics. An increase in the degree of swirl of the co-flowing air caused an increase in turbulent mixing with consequently higher evaporation rate and increased combustion intensity. A reduction in the fuel mass flow rate results in an increase in the combustion intensity, particularly in the near-nozzle region, which is influenced by increased evaporation rate, due to the reduction in the mean droplet diameter, and by the overall fuel-air ratio which is closer to stoichiometric value.

2. Detailed measurements of temperature, species concentrations,

droplet velocities and wall-temperature have been obtained for kerosene spray flames in a cylindrical combustion chamber. The kerosene fuel was delivered to the combustion chamber through a rotating-cup-atomizer which produced sprays with mono-dispersed controlled droplet size. The influence of the spray mean droplet diameter on the combustion characteristics has been examined with two values of the combustion air swirl. For the high swirl cases, the increase in the mean diameter caused a reduction in the combustion intensity at the region downstream of the spray plane and, in particular, at large radii of the combustion chamber. Although the flame structure for the low swirl cases was different, the results showed the same trend of the reduction in the combustion intensity with the mean diameter.

3. The results obtained for two flames with 45^{o} and 60^{o} swirler angle indicated that the reduction in swirl resulted in reduced chemical reaction rates within the initial part of the flame and close to the centreline. However, chemical reactions continued, for the low swirl flame, at the far downstream region of the combustion chamber. The results obtained for the flame with 30^{o} swirl showed the main reaction zones to be concentrated in the near-wall region where flame stabilization was achieved. Chemical reaction was insignificant throughout the central part of the flame. The simultaneous reduction in droplet evaporation and the entrainment of a large number of droplets by the air stream surrounding the atomizer were associated with a reduction in the amount of fuel burnt out in the near-wall region and throughout the combustion chamber.

4. A method for the calculation of the local properties of spray flames has been developed and its capabilities and limitations

appraised by comparing calculated results with measurements. The method solves elliptic differential equations representing the conservation of mass, momentum, enthalpy and species concentrations in finite difference form. In addition, Lagrangian equations for the droplet motion and thermal balance are solved for finite ranges of droplet size. A two-equation turbulence model, a combustion model based on mean mass-fraction equations for fuel and oxidant and a four-flux radiation model are used. The spray model assumes that the evaporating droplets act as distributed point sources of fuel vapour.

5. The comparison between the experimental and predicted results for the four spray flame geometries considered in the present work indicated good qualitative agreement albeit with finite discrepancies. The magnitude of the discrepancies and the relative importance of the sources of uncertainties in the modelling assumptions were found to be dependent on the flow features of each case. In general, the main deficiencies in the calculation method were related to the assumptions of the turbulence, combustion and spray models. The uncertainties in the turbulence model were significant in the prediction of highly swirling flames and this stems from the crudeness of the effective viscosity assumption for such flows. The assumption of infinitely fast, single-step chemical reaction with the neglect of intermediate species (e.g. CO and unburned hydrocarbons) was found to be the main deficiency in the combustion model. The uncertainties in the spray model originated from two sources. The first is associated with the specification of the spray inlet conditions (droplet-size-distribution and droplet injection velocity) and the calculated results showed that the uncertainties in these had a large effect on the predicted profiles. The second stems from the modelling assumptions concerning the expression used to calculate droplet

evaporation, the neglect of the interaction between droplets and the number of size ranges used to represent the spray. The latter was examined over a wide range of flame geometries and it was concluded that its influence will be small for sprays where the majority of droplets are confined to a small spatial volume (e.g. hollow-cone sprays) and for flows with a high turbulent mixing levels in the near-spray region.

4.2 Recommendations for Future Work

The present investigation disclosed some areas where further research is required to aid the understanding of the various processes occuring in spray flames. The recommendations for further study cover three areas:-

(a) Measurement techniques.

(b) Extension of the present experimental program.

(c) Extension and modifications to the calculation method.

These topics are individually discussed.

(a) Measurement Techniques

The discussion of the measurement techniques and their accuracy presented in Chapter 2 indicated a number of deficiencies associated with probe measurements in turbulent reacting flows. These are mainly related to the probe-gas interference effects and the type of averaging produced by the probe. A preliminary analysis of the latter was presented in Chapter 2 and it is suggested that further

work, involving measurements of some correlations (e.g. density species mass fraction correlation) is required before a concrete relationship between the various types of averaging is established. Although the problem of probe gas interference effects has been recognized for a long time very few attempts have been made to determine and quantify the related influences on the measured quantities especially for turbulent flows. Simplified experiments, probably of enlarged scale and involving different probe/enclosure dimensions, probe orientation angles, suction rates, velocity and temperature gradients, and turbulence intensities, etc., are recommended. The experiments can be either with reacting or non-reacting flows and the probe-gas interaction effects can be determined and quantified by local measurements in the vicinity of the probe. Specific measuring techniques, which produce the least amount of disturbance to the flow (laser Doppler anemometer, fine-wire thermocouples, quartz sampling micro probes) can be used in this case. However, it must be recognized that these recommendations do not remove the necessity of developing alternative non-destructive techniques.

Although some attempts have been made to measure droplet-size-distributions in spray flames, see for example, Styles et al (1977), the available techniques are still under-developed and further work is required to allow accurate measurements of droplet size especially under combustion conditions. The application of laser Doppler anemometry can also be extended to allow simultaneous measurements of droplet and gas velocity and the velocity measurements of droplets with a certain size range. This type of measurement is extremely useful for the understanding of the various processes occurring in spray flames and, indirectly, for the development of calculation methods for such flames.

(b) Extension of the Experimental Study

Inspection of the previous work reviewed in Chapter 1 and the experimental study performed in the present work suggests that the available information of the detailed characteristics of spray flames is still inadequate. Taking the present study as reference, it is suggested that an extension of the experiments can be arranged to cover the points stated below:-

(i) The operating conditions of the present study covered a limited range of combustion air swirl, droplet diameters and fuel and air mass flow rates and these represent an obvious extension.

(ii) The measured quantities can also be extended to provide information of the radiation characteristics and soot formation in spray flames, the concentrations of various chemical species and, in particular, the pollutant species, size, velocity and number density of fuel droplets, turbulence characteristics, temperature and species concentration fluctuations and the probability distribution of scalar quantities.

(iii) Measurements should also be performed under conditions more typical of practical combustors where different levels of air-preheat and pressurized combustor operation are usually involved.

(iv) Experiments under different fuel-air entry arrange-

ments, combustor geometry, and fuel and atomizer types are recommended to cover the various applications of spray flames.

(c) Extension and Modifications to the Calculation Method

The calculation method and the validation study reported in Chapter 3 should be recognized as a preliminary step towards the prediction of the detailed flow properties of practical spray flames. This is so because of the many simplifying assumptions involved in the various physical models employed. However, the comparisons with experimental data may be regarded as encouraging and suggest that further refinement of the method can lead to more realistic predictions. The main areas where further work is needed are discussed in the following paragraphs.

(i) The fuel spray in the present model is represented by a finite number of droplet size ranges and this should be replaced by a representation where a droplet size and velocity are considered to take into account the variation in the injection velocity of droplets. However, this point requires further measurements of the joint probability distribution of droplet velocity and size.

(ii) The droplet evaporation rate in the present model is calculated from an expression based on single, isolated evaporating droplet in the absence of chemical reaction. More realistic expressions which consider the influences of the interaction

between adjacent droplets and chemical reaction on the evaporation characteristics can be easily embodied in the procedure. However, insufficient information is available and it is suggested that further theoretical studies, probably of the type described by Samson et al (1978a, 1978b) and Chiu et al (1977), and simplified experiments, see Twardus et al (1978), should be carried out.

(iii) The assumption of the constant number of droplets within each size range throughout its trajectory is deficient as it neglects the influences of droplets collision and break-up, and the turbulent interaction with the surrounding gas. Further work is, therefore, required in this point and as in all cases should be assisted with simplified experiments where detailed measurements of droplet characteristics are provided.

(iv) Finally, it must be mentioned that these improvements to the model should be associated with an optimization of the numerical solution method for the droplet equations in order to allow more economical computations.

(v) The results of the calculations and the comparison with the experimental data reported in Chapter 3 indicated that the deficiencies in the present combustion model, relating to the neglect of intermediate reaction species and the influence of

chemical kinetics on the rate of reaction, contribute largely to the uncertainties in the results. Attempts to predict intermediate species, such as carbon monoxide, were reported by Jones (1979) using the probability density function approach and by Ganesan et al (1979) using the eddy-breakup model. Large discrepancies were, however, indicated and it is, therefore, recommended that further work should be carried out to modify these models and to develop new models which account for the above-mentioned deficiencies.

(vi) The calculated results also indicated deficiencies in the turbulence model, due to the isotropic and effective viscosity assumptions, for cases where a highly swirling flow is considered. Although these are probably less important than those of the combustion model, a possible improvement to the present method would be achieved by employing a turbulence model which overcomes these deficiencies, see for example Launder et al (1972).

(vii) The assumption of non-scattering and gray gas employed in the present radiation model for the calculation of the radiation properties is simplistic and probably explains the observed small influences of the radiation heat transfer. The model can be improved by including the effects of multi-gas components, soot and

particulate radiation. However, the influence of these will be more significant for the calculation of comparatively large and industrial flames.

REFERENCES

ABU EL-LEIL, M. M. (1974)
"Theoretical and experimental investigation of the pre-combustion period events of fuel droplets in gas-turbine combustion chambers".
Ph.D. Thesis, Cairo University, Egypt.

ATTYA, A. E. (1979)
Private Communication.
Mech. Eng. Dept., Imperial College, London.

BAGHDADI, A. (1979)
Private Communication.
Mech. Eng. Dept., Imperial College, London.

BALLANTYNE, A. and MOSS, J. B. (1977)
"Fine wire thermocouple measurements of fluctuating temperature".
Comb. Sci. and Tech., 17, 63 - 77.

BARTELDS, H. (1976)
"Validity of radiation models".
International Flame Research Foundation, Ijmuiden, Holland, Doc. Nr. K20/a/91.

BEER, J. M. (1962)
"Some results of the first trials on pressure jet oil flames in the IJmuiden furnace".
J. Inst. Fuel, 15, 3 - 15.

BILGER, R. W. (1977)
"Probe measurements in turbulent combustion".
AIAA Progress in Astronautics and Aeronautics : Experimental Diagnostics in Gas Phase Combustion Systems, 53, Eds. Zinn, B. T., Bowman, C. T., Hartley, D., Price E. W. and Skifstad, J. F., 49 - 69.

BILGER, R. W. (1976)
"Turbulent jet diffusion flames".
Prog. Energy Combust. Sci., 1, 87 - 109.

BOWMAN, C. T. (1975)
"Kinetics of pollutant formation and destruction in combustion".
Prog. Energy Combust. Sci., 1, 33.

BOWMAN, C. T. (1977)
"Probe measurements in turbulent combustion".
AIAA Progress in Astronautics and Aeronautics : Experimental Diagnostics in Gas Phase Combustion Systems, 53, Eds. Zinn, B. T., Bowman, C. T., Hartley, D., Price E. W. and Skifstad, J. F., 3 - 24.

BORGHI, R. (1975)
Turbulent Mixing in Non-Reactive and Reactive Flows
Ed. Murthy, S. N. B., Plenum Press, 163.

BRADLEY, D. and MATTHEWS, K. J. (1968)
"Measurement of high gas temperature with fine wire thermocouples".
J. Mech. Eng. Sci., 10, 299 - 305.

CARETTO, L. S., GOSMAN, A. D., PATANKAR, S. V. and SPALDING, D. B. (1973)
Proc. 3rd Int. Conf. on Num. Methods in Fluid Mechanics, 2, 60, Springer-Verlag, Berlin.

CARETTO, L. S. (1976)
"Mathematical modelling of pollutant formation".
Prog. Energy Combust. Sci., 1, 47 - 71.

CASTRO, I. P. (1978)
"Numerical difficulties in the calculation of complex turbulent flows".
Proc. of Penn. State Conference on Turbulent Shear Flows, Academic Press.

CHIGIER, N. A. and McCREATH, C. G. (1974)
"Combustion of droplets in sprays".
Acta Astronautica, 1, 687 - 710.

CHIGIER, N. A. and YULE, A. J. (1977)
"Vaporization of droplets in high temperature gas streams, physical chemistry and hydrodynamics".
LEVICH Birthday Conference, Oxford.

CHIGIER, N. A., McCREATH, C. G. and ROETT, M. F. (1973)
"The structure of sprays in liquid fuel flames".
Dept. of Chem. Eng. and Fuel Tech., University of Sheffield.

CHIU, H. H. and LIU, T. M. (1977)
"Group combustion of liquid droplets".
Comb. Sci. and Tech., 17, 127 - 142.

CHEDAILLE, J. and BRANAD, Y. (1972)
Industrial Flames, Vol. 1, Measurements in Flames.
Arnold, London.

CLARE, H., DURÃO, D. F. G., MELLING, A. and WHITELAW, J. H. (1976)
"Investigation of a V-gutter stabilized flame by laser anemometry and schlieren photography".
AGARD, C.P. 193, Applications of Non-Intrusive Instrumentation in Fluid Flow Research.

CROWE, C. T., SHARMA, M. P. and STOCK, D. E. (1977)
"The particle-source-in-cell (PSI-CELL) model for gas-droplet flows".
Dept. of Mech. Eng., Washington State University.

CROWE, C. T. (1974)
"Gas-droplet flow field in the vicinity of an atomiser".
11th JANNAF Comb. Meeting.

DE MARCO, A. G. and LOCKWOOD, F. C. (1975)
"A new flux model for the calculation of radiation in furnaces".
Italian Flame Days, La Rivista dei Combustibili, 29, 184.

DIMOTAKIS, P. E. (1976)
"Single scattering particle laser Doppler measurements of turbulence".
AGARD, C.P. 193, Applications of Non-Intrusive Instrumentation in Fluid Flow Research, Paper 10.

DURST, F., MELLING, A. and WHITELAW, J. H. (1976)
Principles and Practice of Laser-Doppler Anemometry.
Academic Press.

DURÃO, D. F. G. and WHITELAW, J. H. (1975)
"The performance of acousto-optic cells for laser-Doppler anemometry".
J. Phys. E. Sci. Instrum., 8, 776 - 780.

DURÃO, D. F. G., LAKER, J. and WHITELAW, J. H. (1978)
"A micro-processor controlled frequency analyser for laser-Doppler anemometry".
Fluids Section Report FS/78/21, Mech. Eng. Dept., Imperial College, London.

DURÃO, D. F. G. (1976)
"The application of laser anemometry to free jets and flames with and without recirculation".
Ph.D. Thesis, University of London.

DURÃO, D. F. G., LAKER, J. and WHITELAW, J. H. (1979)
"Bias effects in laser-Doppler anemometry".
Fluids Section Report FS/79/5, Mech. Eng. Dept., Imperial College, London.

ELBANHAWY, Y. and WHITELAW, J. H. (1979)
"The calculation of the flow properties of a confined kerosene spray flame".
AIAA Paper 79-7020.

ENGLAND, G. and HOUSEMAN, J. (1973)
"Sampling nitric oxide from combustion gases".
Combustion and Flame, 20, 439 - 442.

EL-SHIRBINI, A. A. (1969)
"Determination of the optimal length of rocket combustion chambers".
Z. Flugwiss, 17, 56 - 63.

FAVRE, A. (1969)
"Problems of hydrodynamics and continuum mechanics".
Soc. Indust. and Appl. Math.

FLETCHER, R. S. and HEYWOOD, J. B. (1971)
"A model for nitric oxide emissions from aircraft gas turbine engines".
AIAA Paper No. 71-123.

FRASER, R. P., EISENKLAM, P. and DOMBROWSKI, N. (1957)
"Liquid atomization in chemical engineering".
British Chemical Engineering.

FRISTROM, R. M. and WESTENBERG, A. A. (1965)
Flame Structure.
McGraw-Hill, New York.

GANESAN, V. and SPALDING, D. B. (1979)
"Numerical modelling of the combustion of fuel sprays in three-dimensional can combustors".
AIAA Paper No. 79-7022.

GANY, A., MANHEIMER-TIMNAT, Y. and WOLFSHTEIN, M. (1976)
"Two-phase flow effects on hybrid combustion".
Acta Astronautica, 3, 241 - 263.

GEORGE, E. G., SIMMONS, F. S. and STICKNEY, T. M. (1956)
"Radiation and recovery corrections and time constants of several chromel-alumel thermocouple probes in high-temperature, high-velocity gas streams".
NACA TN 3766.

GOSMAN, A. D., LI, K. H. and SAMARAWEERA, D. S. A. (1976)
"A numerical calculation procedure for two-phase recirculating flows".
Mech. Eng. Dept., Imperial College, London.

GOSMAN, A. D. and PUN, W. M. (1973)
Lecture notes for course entitled "Calculation of Recirculating Flows".
Imperial College, Mech. Eng. Dept.

GOSMAN, A. D., KHALIL, E. E. and WHITELAW, J. H. (1979)
"The calculation of two-dimensional turbulent recirculating flows".
Turbulent Shear Flows, I, Eds. Durst, F., Launder, B. E., Schmidt, F. W. and Whitelaw, J. H., 237, Springer-Verlag.

GUPTA, H. C. and BRACCO, F. V. (1978)
"Numerical computations of two-dimensional unsteady sprays for application to engines".
AIAA Journal, 16, No. 10, 1053 - 1061.

HABIB, M. A. and WHITELAW, J. H. (1979)
"Velocity characteristics of confined coaxial jets with and without swirl".
To be presented at the Winter Annual Meeting, Fluids Engineering Division of the Americal Society of Mech. Engineers, New York.

HARLOW, F. H. and AMSDEN, A. A. (1975)
"Numerical calculation of multiphase fluid flow".
J. of Computational Physics, 17, 19 - 52.

HINZE, J. O. (1971)
"Turbulent fluid and particle interaction".
Report WTHD No. 32, Mech. Eng. Dept., Delft University of Technology, The Netherlands.

HOTCHKISS, R. S. and HIRT, C. W. (1972)
"Particulate transport in highly distorted three-dimensional flow fields".
Los Alamos Scientific Lab. Report La-DC-72-364.

HOLDERNESS, F. H., TILSTON, J. R. and MACFARLANE, J. (1969)
"Electrical compensation for radiation loss in thermocouples".
N.G.T.E. NT. 758.

HOTTEL, H. C. and SAROFIM, A. F. (1967)
Radiative Transfer.
McGraw-Hill, New York.

HOWELL, J. R. (1968)
"Application of Monte-Carlo to heat transfer problems".
In Advances in Heat Transfer, Eds. Irvine and Hartnett, 5, Academic Press, New York.

HUTCHINSON, P., KHALIL, E. E. and WHITELAW, J. H. (1977)
"The measurements and calculation of furnace-flow properties".
J. Energy, 1, 212.

INGEBO, R. D. (1962)
"Heat transfer and drag coefficients for Ethanol drops in a rocket chamber burning Ethanol and liquid oxygen".
8th Symp. (Int.) on Combustion, 1104 - 1113.

IOANNIDES, E. and GOSMAN, A. D. (1978)
"A survey of the literature relating to oil spray combustion".
UKAEA Report HTFS RS 254.

JOHNSON, T. R., LOWES, T. M. and BEER, J. M. (1974)
"Comparison of calculated and measured temperatures and heat flux distributions in the IJmuiden furnace".
J. Inst. Fuel, 47, 39 - 55.

JONES, A. R. (1976)
"A review of oil droplet size measurement".
Report R/M/N920, Central Electricity Generating Board, Marchwood Laboratories, England.

JONES, W. P. and LAUNDER, B. E. (1973)
"Prediction of low Reynolds number phenomena with a two-equation model of turbulence".
Int. J. of Heat and Mass Transfer, 16.

JONES, W. P. and WHITELAW, J. H. (1978)
"Coupling of turbulence and chemical reaction".
Fluids Section Report FS/78/13, Mech. Eng. Dept., Imperial College, London.

JONES, W. P. (1979)
"Models for turbulent flows with variable density and combustion".
Von Karman Institute for Fluid Dynamics, Lecture Series 1979-2, Prediction Methods for Turbulent Flows.

KENT, J. H. and BILGER, R. W. (1973)
"Measured techniques in turbulent diffusion flames".
First Australasian Conference on Heat and Mass Transfer, Monash University, Melbourne, Sec. 4.4, 39 - 46.

KHALIL, M. B. (1975)
"Analysis of the different factors affecting the accuracy of temperature measurements in flames".
M.Sc. Thesis, Mech. Eng. Dept., Faculty of Engineering, Cairo University.

KHALIL, K. H., EL MAHALLAWY, F. M. and MONEIB, H. A. (1977)
"Effect of combustion air swirl on the flow pattern in a cylindrical oil-fired furnace".
16th Symp. (Int.) on Combustion, The Combustion Institute, 135 - 143.

KHALIL, E. E. (1976)
"Flow and combustion in axisymmetric furnaces".
Ph.D. Thesis, University of London.

KHALIL, E. E. and TRUELOVE, J. S. (1977)
"Calculation of heat transfer in a large gas fired furnace".
UKAEA Report AERE-R 8747 (HTFS RS 225).

KHALIL, E. E. and WHITELAW, J. H. (1977)
"Aerodynamic and thermodynamic characteristics of kerosene spray flames".
16th Symp. (Int.) on Combustion, The Combustion Institute.

KOMIYAMA, K., FLAGAN, R. C. and HEYWOOD, J. B. (1977)
"The influence of droplet evaporation on fuel-air mixing rate in a burner".
16th Symp. (Int.) on Combustion, The Combustion Institute, 549 - 560.

KORN, G. A. and KORN, M. (1961)
Mathematical Handbook for Scientists and Engineers.
McGraw-Hill, New York.

LAMBIRIS, S., COMBS, L. P. and LEVINE, R. S. (1962)
"Stable combustion processes in liquid propellant rocket engines".
5th AGARD Colloqium, Combustion and Propulsion, 569 - 636.

LAND, T. and BARBER, R. (1956)
"Suction pyrometers in theory and practice".
J. of the Iron and Steel Institute, 269 - 273.

LAUNDER, B. E. (1973)
"Two-equation turbulence models".
Report HTS/73/17, Mech. Eng. Dept., Imperial College, London.

LAUNDER, B. E. and SPALDING, D. B. (1972)
Mathematical Models of Turbulence.
Academic Press.

LAW, C. K. (1976)
"Unsteady droplet combustion with droplet heating".
Comb. and Flame, 26, 17 - 22.

LOCKWOOD, F. C. and NAGUIB, A. S. (1975)
"The prediction of the fluctuations in the properties of free, round-jet, turbulent, diffusion flames".
Comb. and Flame, 24, 109 - 124.

LOCKWOOD, F. C. and SHAH, N. G. (1976)
"An improved flux model for the calculation of radiation heat transfer in combustion chambers".
ASME Paper 76-HT-55.

LOCKWOOD, F. C. and SYED, S. A. (1977)
"Prediction of coal fired furnaces".
Mech. Eng. Report, Imperial College, London.

MACFARLANE, J. J. and COLBOURN, A. J. (1969)
"A study of the performance of rotary atomizers".
N.G.T.E. Report No. R.310, Ministry of Defence, Pyestock.

MAGNUSSEN, B. F. and HJERTAGER, B. H. (1977)
"On mathematical modelling of turbulent combustion with special emphasis on soot formation and combustion".
16th Symp. (Int.) on Combustion, The Combustion Institute, 719 - 729.

MAGNUSSEN, B. F., HJERTAGER, B. H., OLSEN, J. G. and BHADURI, D. (1978)
"Effects of turbulent structure and local concentrations on soot formation and combustion in C_2H_2 diffusion flames".
17th Symp. (Int.) on Combustion.

McGUIRK, J. J. and RODI, W. (1978)
"A depth-averaged mathematical model for the near field of side discharges into open-channel flow".
J. Fluid Mech., 86, Part 4, 761 - 781.

McLAUGHLIN, D. K. and TIEDERMAN, W. G. (1973)
"Biasing correction for individual realization of laser anemometer measurements in turbulent flows".
Phys. Fluids, 16, 2082.

MELLOR, A. M. (1973)
"Simplified physical model of spray combustion in a gas turbine engine".
Comb. Sci. and Tech., 8, 101 - 109.

MELLOR, A. M. (1976)
"Gas turbine engine pollution".
Prog. Energy Combust. Sci., 1, 111 - 133.

MELLING, A. (1975)
"Investigation of flow in non-circular ducts and other configurations by laser Doppler anemometry".
Ph.D. Thesis, University of London.

MOSIER, S. A., ROBERTS, R. and HENDERSON, R. E. (1973)
"Development and verification of an analytical model for predicting emissions from gas turbine engine combustors during low-power operation".
Atmospheric Pollution by Aircraft Engines, AGARD CP No. 125.

MOFFAT, R. J. (1962)
"Gas temperature measurement. Temperature : Its measurement and control".
In Sci. and Ind., 3, Part 2, Reinhold Publishing Co., Paper 52, 553 - 571.

MONEIB, H. A. (1979)
Private Communication.
Mech. Eng. Dept., Imperial College, London.

NATARAJAN, R. and GHOSH, A. K. (1975)
"Velocity histories of vaporizing fuel drops moving through stagnant gas".
Fuel, 54, 153 - 161.

OHTA, Y., SHIMOYAMA, K. and OHIGASHI, S. (1975)
"Vaporization and combustion of single liquid fuel droplets in a turbulent environment".
JSME, 18, No. 115.

ONUMA, Y., OGASAWARA, M. and INOUE, T. (1977)
"Further experiments on the structure of a spray combustion flame".
16th Symp. (Int.) on Combustion, The Combustion Institute, 561 - 567.

ONUMA, Y. and OGASAWARA, M. (1975)
"Studies on the structure of a spray combustion flame".
15th Symp. (Int.) on Combustion, The Combustion Institute, 453 - 465.

OWEN, F. K. (1977)
"Laser velocimeter measurements of the structure of turbulent spray flames".
AIAA 15th Aerospace Sciences Meeting, Paper 77-215, Los Angeles, California. Also in Turbulent Combustion, Ed. Kennedy, L. A., Progress in Astronautics and Aeronautics, 58.

ODIDI, A.O.O. (1974)
"The influence of turbulence on the time-mean rate of chemical reactions". Ph.D. Thesis, University of London.

PATANKAR, S. V. and SPALDING, D. B. (1970)
Heat and Mass Transfer in Boundary Layers.
2nd Edition, Intertext Books, London.

POPE, S. B. (1976)
"The probability approach to the modelling of turbulent reacting flows".
Combustion and Flame, 27, 299.

PRIOR, D. S., SWITHENBANK, J. and FELTON, P. G. (1978)
"Stirred reactor modelling of a low-pollution liquid-fuelled combustor".
AIAA Paper No. 77-51, Turbulent Combustion, Ed. Kennedy, L. A., Progress in Astronautics and Aeronautics, 58.

PRATT, D. T. (1976)
"Mixing and chemical reaction in continuous combustion".
Prog. Energy Combust. Sci., 1, 73 - 86.

RAMSHAW, C. (1968)
"Notes on the measurement of gas composition and mixture ratio in a rocket combustion chamber".
J. Inst. Fuel, 455 - 460.

REYNOLDS, A. J. (1974)
Turbulent Flows in Engineering.
John Wiley & Sons, London.

ROACHE, P. J. (1976)
Computational Fluid Mechanics.
Hermosa Publishers.

ROSE, J.W. and COOPER, J.R. (1977) Technical Data on Fuel.
Scottish Academic Press, United Kingdom.

RUDINGER, G. (1975)
"Effect of velocity slip on the burning rate of fuel particles".
J. of Fluids Eng., Transactions of ASME, 321 - 326.

SANGIOVANNI, J. J. and KESTEN, A. S. (1977)
"Effect of droplet interaction on ignition in mono-dispersed droplet streams".
16th Symp. (Int.) on Combustion, The Combustion Institute, Pittsburgh, 577 - 592.

SAMSON, R., BEDEAUX, D., SAXTON, M. J. and DEUTCH, J. M. (1978a)
"A simple model of fuel spray burning. I : Random sprays".
Combustion and Flame, 31, 215 - 222.

SAMSON, R., BEDEAUX, D. and DEUTCH, J. M. (1978b)
"A simple model of fuel spray burning. II : Linear droplet stream".
Combustion and Flame, 31, 223 - 230.

SALOOJA, A. P. (1978)
"Mathematical modelling of, and experimental studies in axisymmetrical combustors".
Ph.D. Thesis, University of London.

SATO, A., HASHIBA, K., HASATANI, M., SUGIYAMA, S. and KIMURA, J. (1975)
"A correctional calculation method for thermocouple measurements of temperature in flames".
Combustion and Flame, 24, 35 - 41.

SAMUELSON, G. S. and HARMON, J. N. (1977)
"Chemical transformation of nitrogen oxides while sampling combustion products".
APCA J. 27 No 7.

SERAG-ELDIN, M. A. S. (1977)
"The numerical prediction of the flow and combustion processes in a three-dimensional can combustor".
Ph.D. Thesis, University of London.

SHARMA, M. P. (1977)
"Numerical and experimental study of gas-particle flows in orifices and venturis".
Ph.D. Thesis, Washington State University.

SPALDING, D. B. (1976)
"Development of the eddy-break-up model of turbulent combustion".
Imperial College, Mech. Eng. Dept., Report HTS/76/1.

SPALDING, D. B. (1953)
"The combustion of liquid fuels".
4th Symp. (Int.) on Combustion, Williams and Wilkins, Baltimore, Maryland, 847 - 864.

SPALDING, D. B. (1955)
Some Fundamentals of Combustion.
Butterworths, London.

SPALDING, D. B. (1970)
"Notes on PARMIX program".
Report BL/TN/A/35, Mech. Eng. Dept., Imperial College, London.

SPALDING, D. B. (1971)
"Concentration fluctuations in a round free jet".
Chem. Eng. Sci., 26, 95.

SPALDING, D. B. (1976)
"Mathematical models of turbulent flames. A review".
Comb. Sci. and Tech., 13, 1 - 25.

SPALDING, D. B. (1977)
"The calculation of free-convection phenomena in gas-liquid mixtures".
Lecture at Mech. Eng. Dept., Imperial College, London.

SPALDING, D. B. (1972)
"A novel finite-difference formulation for differential expressions involving both first and second derivatives".
Int. J. Num. Methods in Eng., 4, 551 - 559.

STYLES, A. C. and CHIGIER, N. A. (1977)
"Combustion of air blast atomized spray flames".
16th Symp. (Int.) on Combustion, The Combustion Institute, 619 - 630.

SYED, S. A. (1977)
"Experimental and theoretical investigation of a horizontal free turbulent diffusion flame".
Ph.D. Thesis, University of London.

TATCHELL, D. G. (1975)
"Convection processes in confined, three-dimensional boundary layers".
Ph.D. Thesis, University of London.

TAYLOR, A. P. (1979)
Private Communication.
Mech. Eng. Dept., Imperial College, London.

TERBUSH, R. K. (1963)
"Improved sonic pyrometer. Temperature : its measurements and control
In Science and Industry, 3, Part 2, Reinhold Publishing Co., 595 - 600.

TINE, G. (1961)
Gas Sampling and Chemical Analysis in Combustion Processes.
AGARDograph 47, Pergamon Press.

TRUELOVE, J. S. (1976)
"A mixed grey gas model for flame radiation".
UKAEA Report AERE-R 8494.

TRUELOVE, J. S. (1976)
"Differential equation models of radiative transfer".
UKAEA Report AERE-R 8364.

TRIBUS, M. (1961)
Thermostatics and Thermodynamics.
Van Nostrand, London.

TUTTLE, J. H., ALTENKIRCH, R. A. and MELLOR, A. M. (1973)
"Emissions from and within an Allison J-33 combustor. II : The effect of inlet air temperature".
Comb. Sci. and Tech., 7, 125 - 134.

TUTTLE, J. H., SHISLER, R. A. and MELLOR, A. M. (1976)
"Investigation of liquid fuelled turbulent diffusion flames".
Comb. Sci. and Tech., 14, 229 - 241.

TUTTLE, J. H., COLKET, M. B., BILGER, R. W. and MELLOR, A. M. (1977)
"Characteristic times for combustion and pollutant formation in spray combustion".
16th Symp. (Int.) on Combustion, the Combustion Institute.

TWARDUS, E. M. and BRZUSTOWSKI, T. A. (1978)
"An experimental study of flame spread and burning in arrays of monosize hydrocarbon droplets".
Comb. Sci. and Tech., 17, 215 - 226.

VRANOS, A., FAUCHER, J. E. and CURTIS, W. E. (1969)
"Turbulent mass transfer and rates of reaction in a confined hydrogen-air diffusion flame".
12th Symp. (Int.) on Combustion, 1051 - 1058.

VISKANTA, R. (1966)
"Radiation transfer and interaction of convection with radiation heat transfer".
Advances in Heat Transfer, 3, 175 - 252.

WESTBROOK, C. K. (1977)
"Three-dimensional numerical modelling of liquid fuel sprays".
16th Symp. (Int.) on Combustion, The Combustion Institute, 1517 - 1526.

WILLIAMS, F. A. (1962)
"Progress in spray-combustion analysis".
8th Symp. (Int.) on Combustion, Williams and Wilkins Co., Baltimore, 50 - 59.

WILLIAMS, F. A. (1965)
Combustion Theory.
Addison-Wesley Publishing Company Inc., London.

WILLIAMS, A. (1973)
"Combustion of droplets of liquid fuels; a review".
Comb. and Flame, 21, 1 - 31.

YANTA, W. J. (1973)
"Turbulence measurements with Laser-Doppler velocimeter".
Naval Ordnance Laboratory, Silver Spring, Maryland, NOLTR-73-94.

YANAGI, T. (1977)
"Effects of probe sampling rates on sample composition".
Combustion and Flame, 28, 33 - 44.

YANAGI, T. (1972)
"Effect of concentration gradient on composition of sampled gas. II : Experimental verification".
Combustion and Flame, 19, 1 - 9.

YANAGI, T. and MIMURA, Y. (1972)
"Effect of concentration gradient on composition of sampled gas. I : Theoretical analysis".
Combustion and Flame, 18, 347 - 355.

YOSHIDA, A. and TSUJI, H. (1978)
"Measurements of fluctuating temperature and velocity in a turbulent premixed flame".
17th Symp. (Int.) on Combustion.

YULE, A. J., CHIGIER, N. A., ATAKAN, S. and UNGUT, A. (1977)
"Particle size and velocity measurements by laser anemometry".
AIAA Paper No. 77-214, 15th Aerospace Sciences Meeting.

APPENDIX I

DETAILS AND CHARACTERISTICS OF FUEL NOZZLES

I.1 The Twin-Fluid Atomizer (unconfined flame experiments)

I.1.1 Geometry

Fig. AI.1 shows the geometrical details of the twin-fluid atomizer which has been used in the unconfined flame experiments described previously in Chapter 2. The kerosene fuel enters the pre-atomization chamber through two tangential slots located in a plane perpendicular to the atomizer axis. At exit from the atomizer nozzle, 0.5 mm diameter, the swirling fuel jet interacts with the surrounding atomization air issuing from 12 small slots of 0.5 mm inclined 45^{o} to the plane normal to the atomizer axis. The fuel and atomization air flow rates are controlled independently and metering devices were provided to allow monitoring and recording of their values. Fig. AI.2 shows a plot of the fuel flow rate against the pressure drop across the fuel nozzle.

I.1.2 Drop Formation and Size Distribution

The method of atomization for the twin-fluid atomizer depends upon the high shearing forces caused by friction between the fuel liquid surface and the high-velocity air stream surrounding it. Ligaments or threads of liquid are first formed by air friction which then break down into drops. The swirling motion in both the fuel and air streams was applied in the present atomizer to enhance mixing and, therefore, the atomization process. The sauter mean diameter of the initial droplet-size distribution at the fuel nozzle is related to the amount of atomization air per unit liquid fuel and

the relative fluid speeds. Fig. AI.3 represents a correlation, reported by Fraser et al (1957), for the sauter-mean diameter obtained for a range of twin-fluid atomizers. This correlation has been used in the present study to estimate the spray mean droplet diameter as indicated in Table 2.3.

I.2 The Rotating-Cup Atomizer (confined flame experiments)

I.2.1 Geometry

The details of the rotating-cup atomizer used in the present work are shown in Fig. AI.4. The kerosene fuel is supplied to the rotating cup, 25.4 mm diameter, at point A through a hypodermic stainless steel tube of 1.0 mm diameter fixed to the atomizer body. As a result of the high centrifugal forces a liquid fuel film is formed at the bottom walls of the cup and flows through the 10 holes indicated by B. The process of atomization, described in the next subsection, occurs at the edge of the cup, point C. The disc, D, is fixed to the rotating cup to prevent blockage of the holes B by carbon deposition from the flame. The driving variable-speed motor of the atomizer (Oberg Machine Company) provided high rotational speeds which range between 5,000 to 100,000 rpm. The driving motor has an internal air cooling passage. To control the cooling air flow and to prevent damaging the motor bearings by direct contact with the flame, the rotating cup was enclosed in the casing E as indicated in Fig. AI.4. The relation between the fuel flow rate and the pressure drop across the hypodermic tube is shown in Fig. AI.5 for the present atomizer.

I.2.2 Drop Formation and Size Distribution

The process of drop formation can be described as follows.

The liquid fuel arrives at the rotating cup edge as a thin, circumferentially uniform sheet. The atomization process is shown in Fig. AI.6 which is reproduced from the reported results of Macfarlane et al (1969). The figure shows a view looking vertically downwards across the edge of the cup. Drops form on the edge and as they reach a critical size, determined by the balance of the opposed surface tension and centrifugal forces, the drop elongates to form a thread with a spherical droplet at its forward end. This system then fragments to form a main droplet of closely reproducible size and a chain of much smaller satellite droplets. As indicated by Macfarlane et al (1969) the percentage mass contained in the satellite droplets varies with the rotational speed and the fuel flow rate. In general, it ranges between 6.0 to 40% of the total mass. Fig. AI.7, see Macfarlane et al (1969), shows the variation of the mean diameter of main droplet with the rotational speed for a 25.4 mm diameter spinning disc and spinning cup atomizers. Macfarlane et al (1969) indicated that, for a certain atomizer diameter, the mean droplet diameter depends mainly on the rotational speed but can be slightly modified by the fuel properties. The results of Fig. AI.7 were, therefore, used to estimate the spray mean droplet diameter corresponding to the present operating conditions, see Table 2.4.

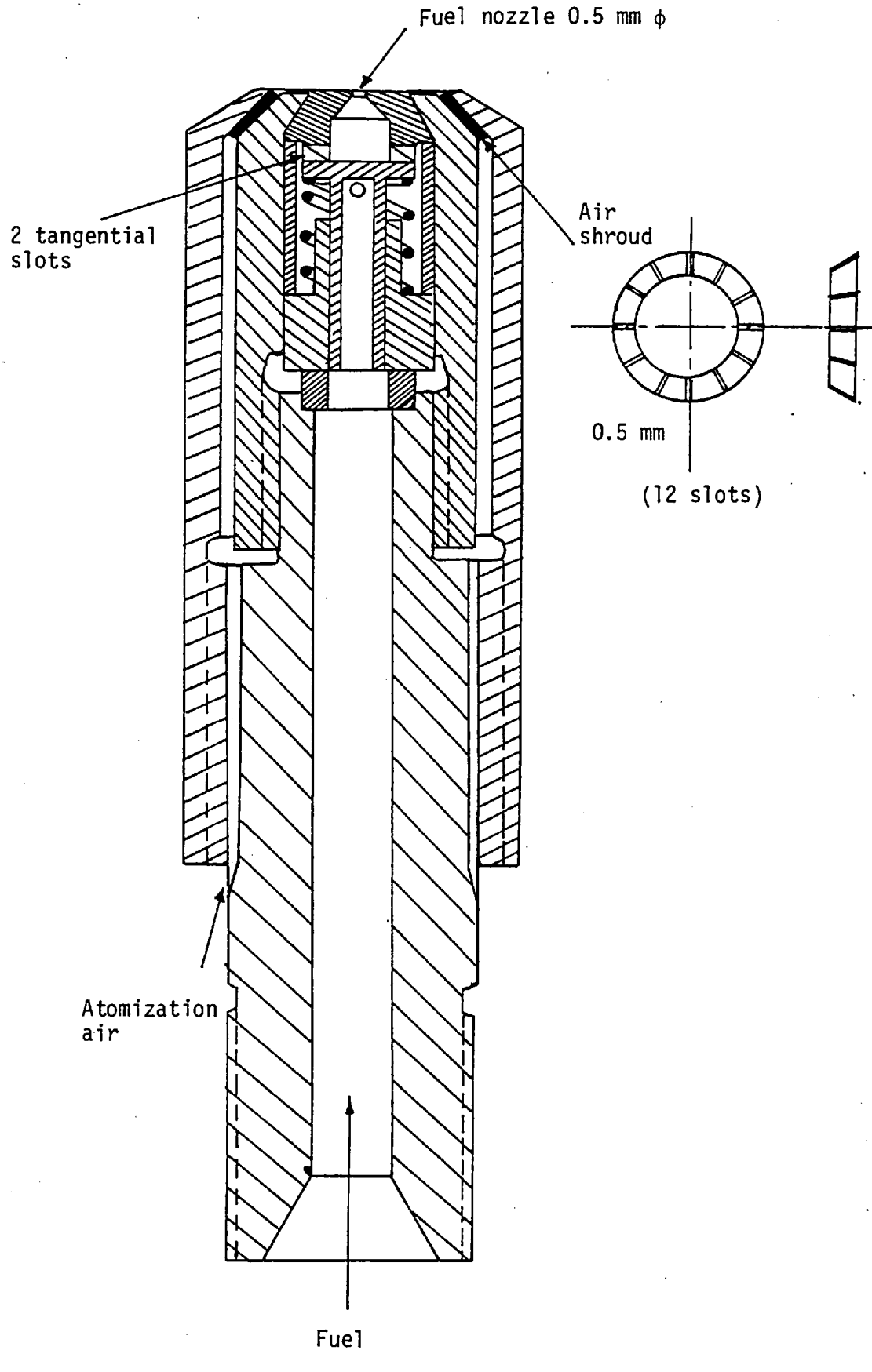

Fig. AI.1 Twin-fluid atomizer, unconfined flame measurements

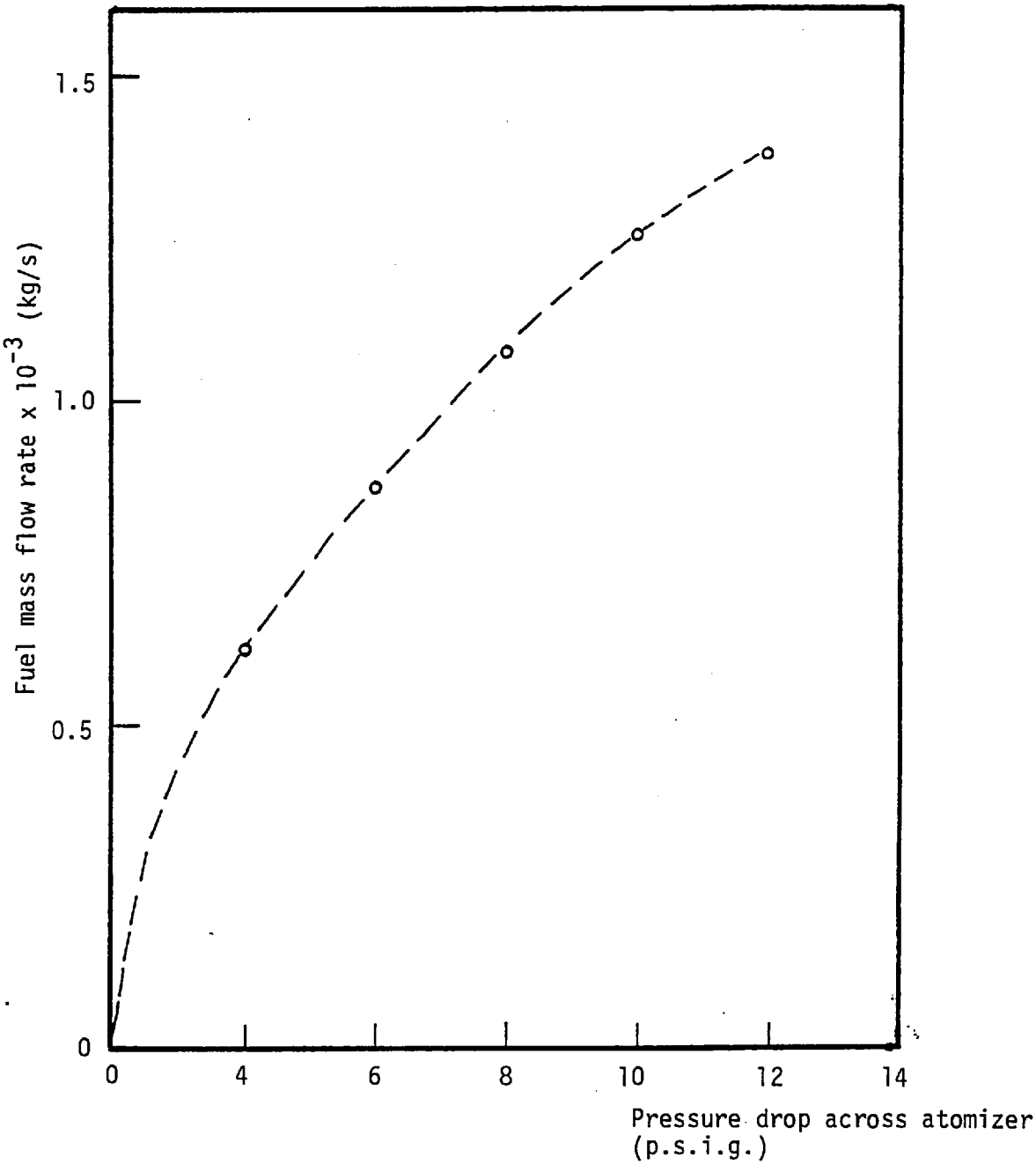

Fig. AI.2 Calibration of the fuel nozzle - unconfined flame burner

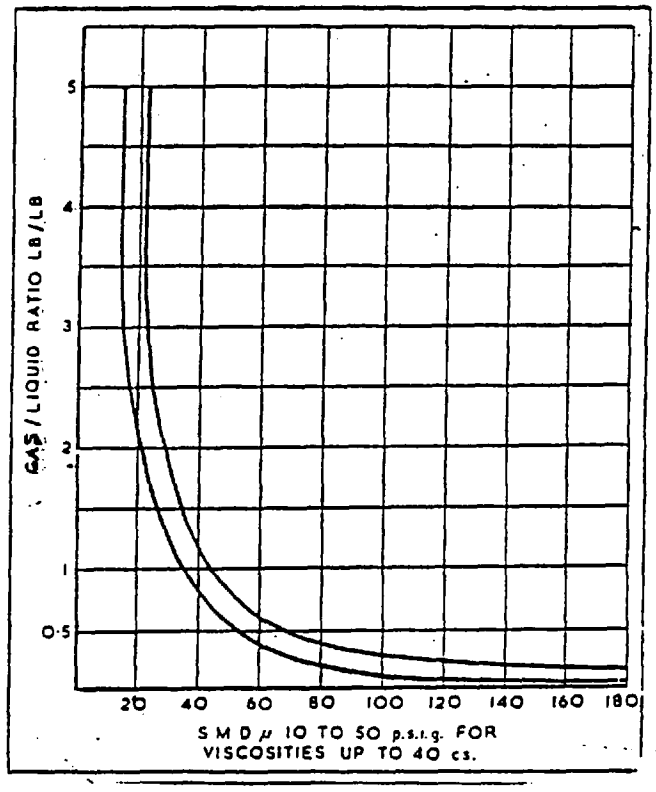

Fig. AI.3 Drop size correlation for twin-fluid atomizers, Fraser et at (1957)

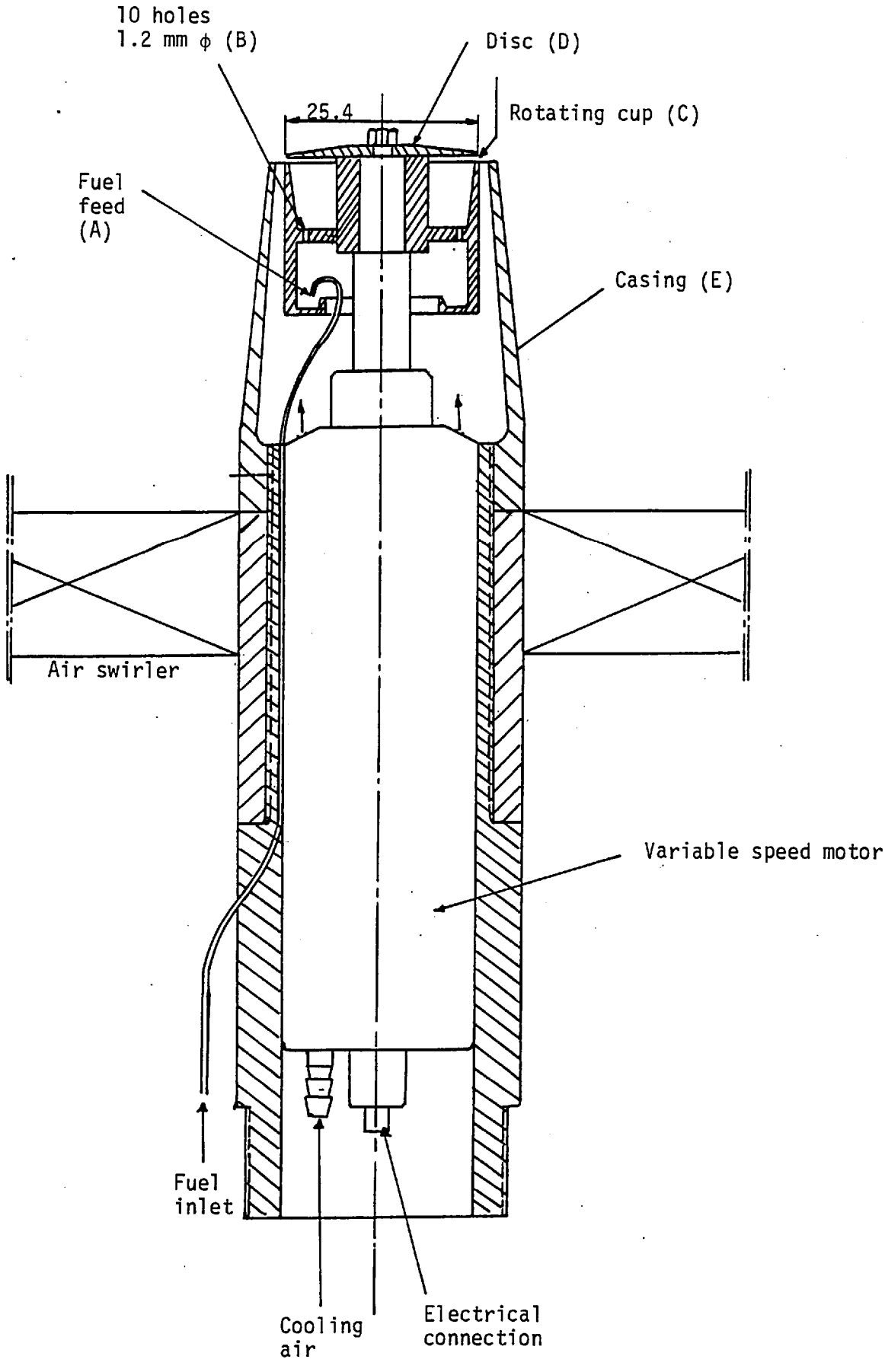

Fig. AI.4 The rotating-cup atomizer

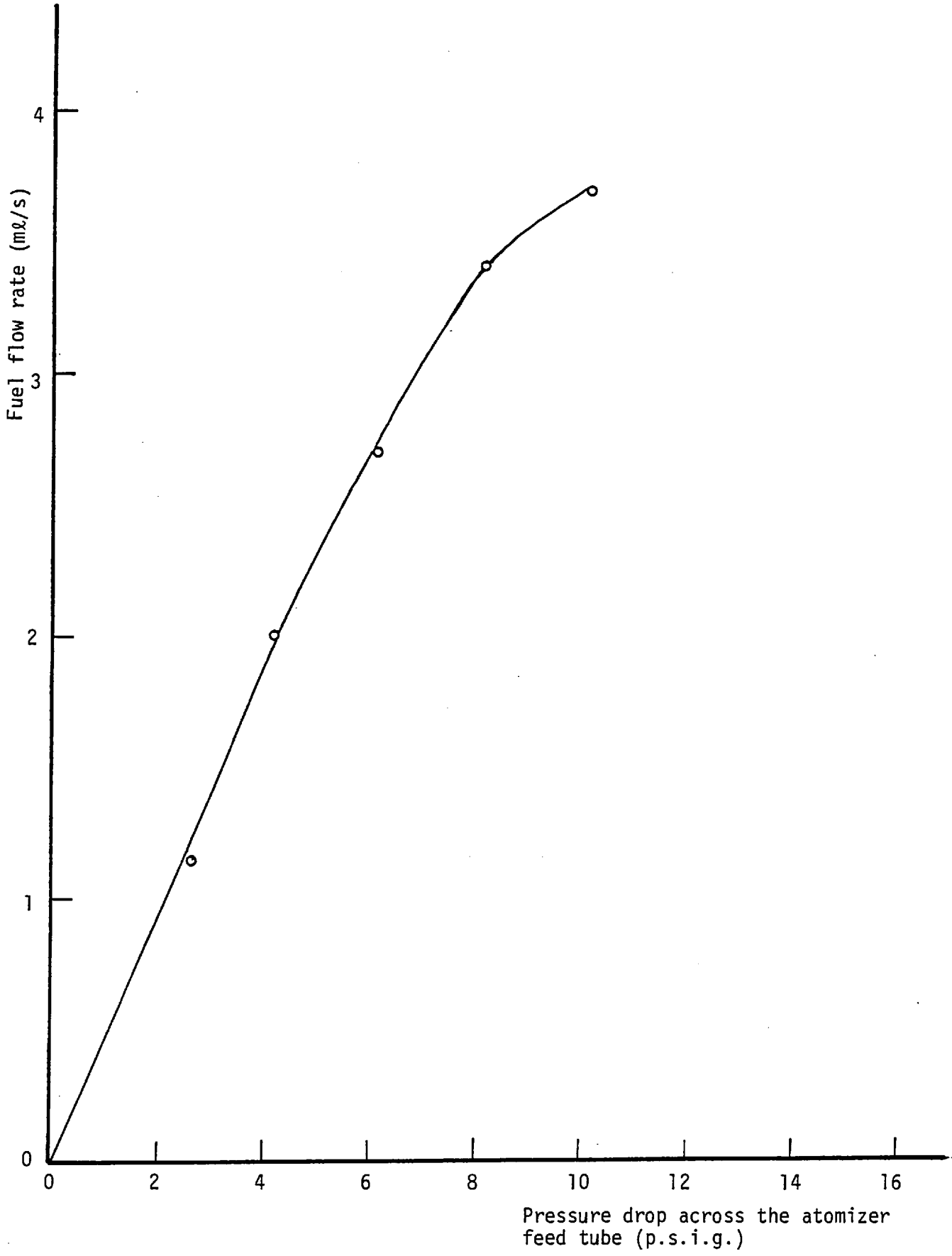

Fig. AI.5 Calibration of the atomizer fuel feed tube - confined flame experiments

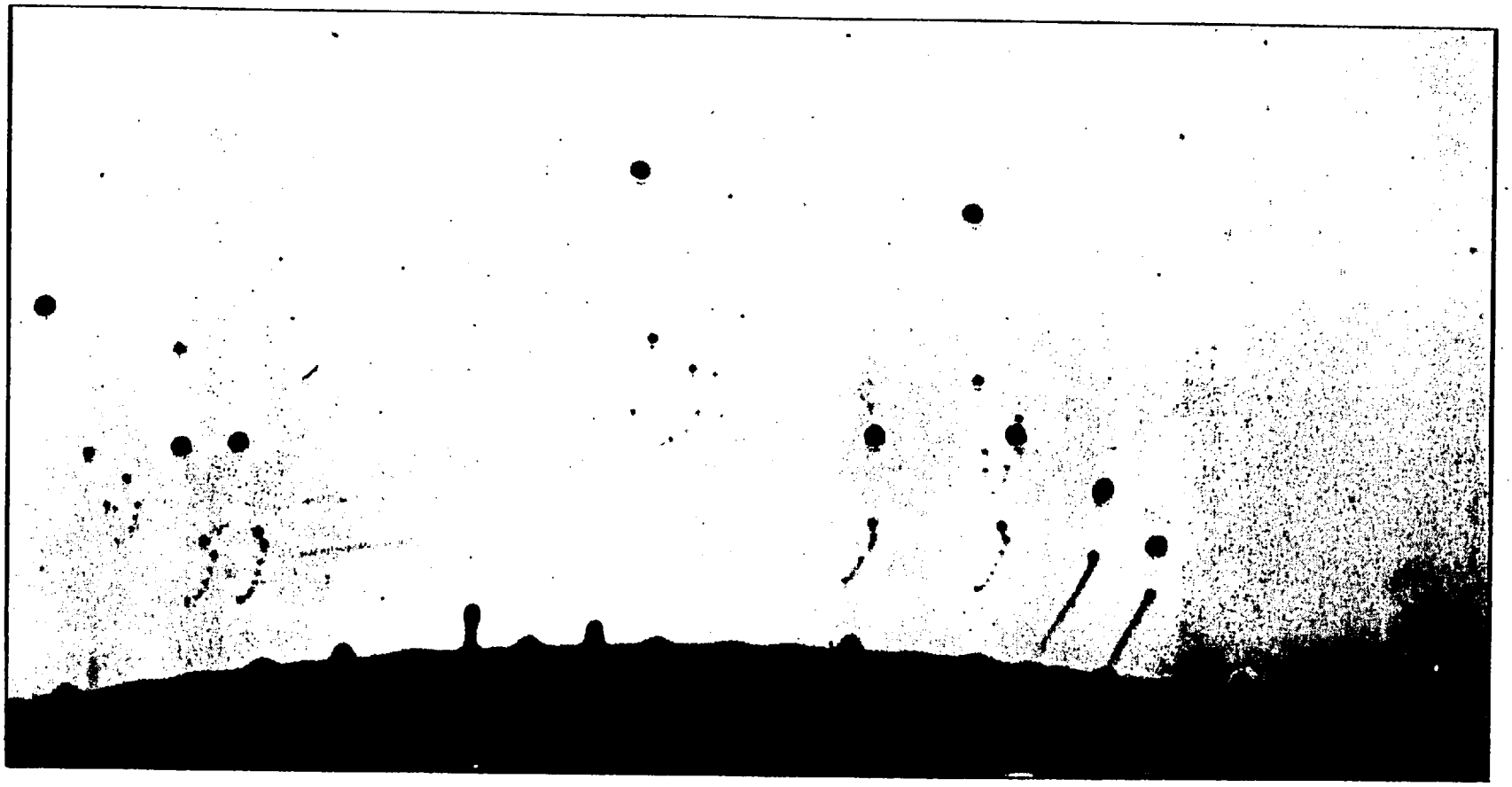

Fig. AI.6 The droplet formation process, Macfarlane et al (1969)

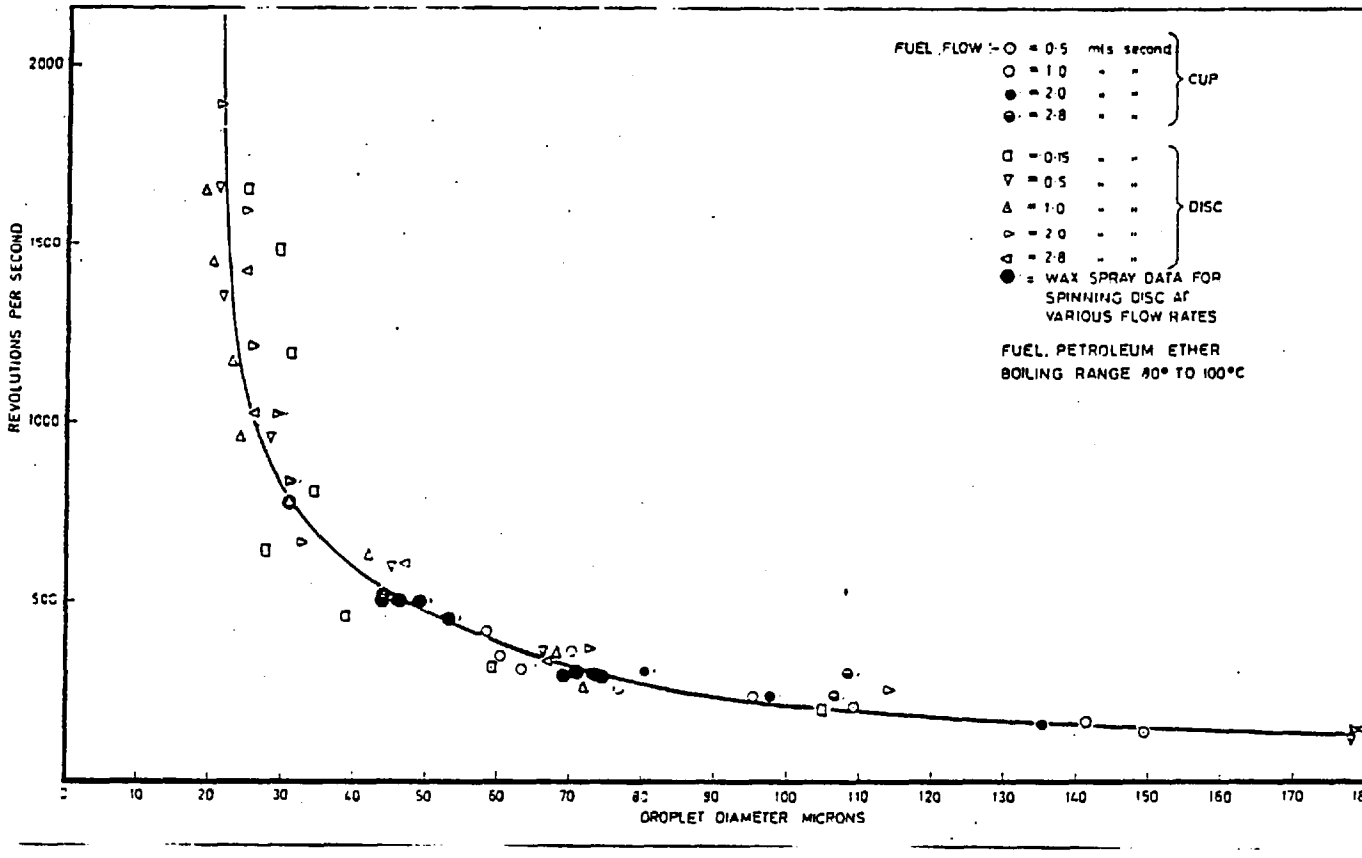

Fig. AI.7 Mean diameter of main droplet - spinning disc and spinning cup atomizer, Macfarlane et al (1969)

APPENDIX II

AIR SWIRLERS AND THE CALCULATION OF SWIRL NUMBERS

Figs. AII.1 and AII.2 show the geometrical details of the five air swirlers used in both the unconfined and confined flames experiments of the present study. All swirlers are of the straight-vane cascade type. The two swirlers shown in Fig. AII.1 have 12 blades of 2 mm thickness which are inclined 45^{o} and 60^{o} to the main direction of the flow. The three swirlers of Fig. AII.2 (confined flame experiments) have 10 blades of 2 mm thickness with three angles of 30^{o}, 45^{o} and 60^{o}. Velocity measurements at exit from the former air swirlers, unconfined flames, were reported by Founti (1979) and a sample of the results is reproduced in Fig. AII.3. Axial velocity measurements for the other three swirlers were performed in the present study and the corresponding radial profiles are shown in Fig. AII.4. The air swirlers are typically characterised by the swirl number defined as the ratio between the angular momentum of the air flow through the swirler and the axial momentum multiplied by a characteristic radius, i.e.:-

$$S_W = \frac{\int_{r_i}^{r_o} \rho\, U \,.\, W \,.\, r \,.\, r \,.\, dr}{\int_{r_i}^{r_o} \rho\, U \,.\, U \,.\, r \,.\, dr \,.\, R}$$

where r_i and r_o are the inner and outer radii of the swirler, U and W are the axial and tangential velocity components and R is a characteristic dimension.

A sample of the radial profiles of the tangential velocity

component is shown in Fig. AII.5. Table AII.1 shows the calculated swirl numbers for the five swirlers used in this study.

TABLE AIV.1

SWIRLER NUMBER FOR DIFFERENT AIR SWIRLERS

Swirler	Swirler vane angle	Swirl number	Remarks
1	60	0.77	Unconfined flame experiments
2	45	0.45	
3	30	0.76	Confined flame experiments
4	45	1.32	
5	60	1.94	

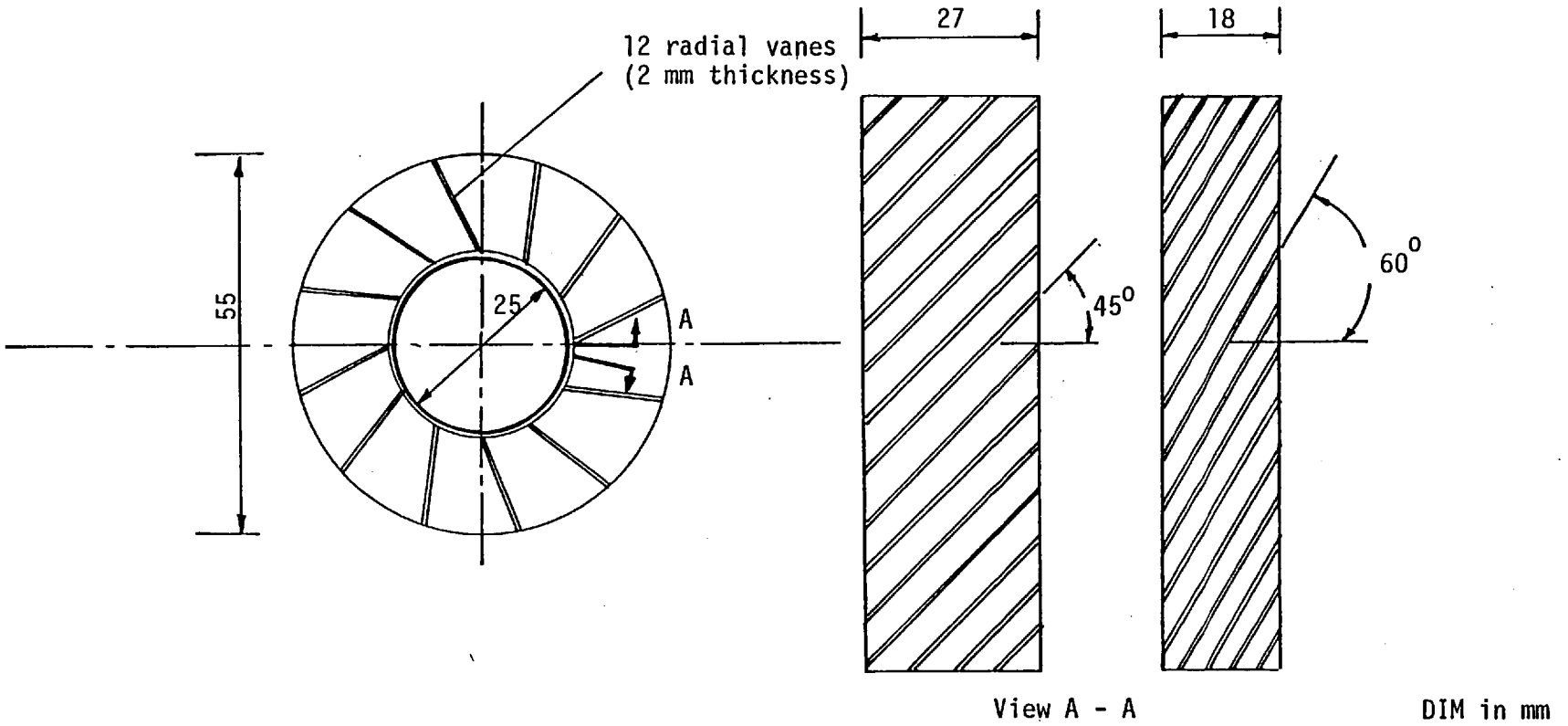

Fig. AII.1 Geometrical details of the two air swirlers used in the unconfined flame experiments

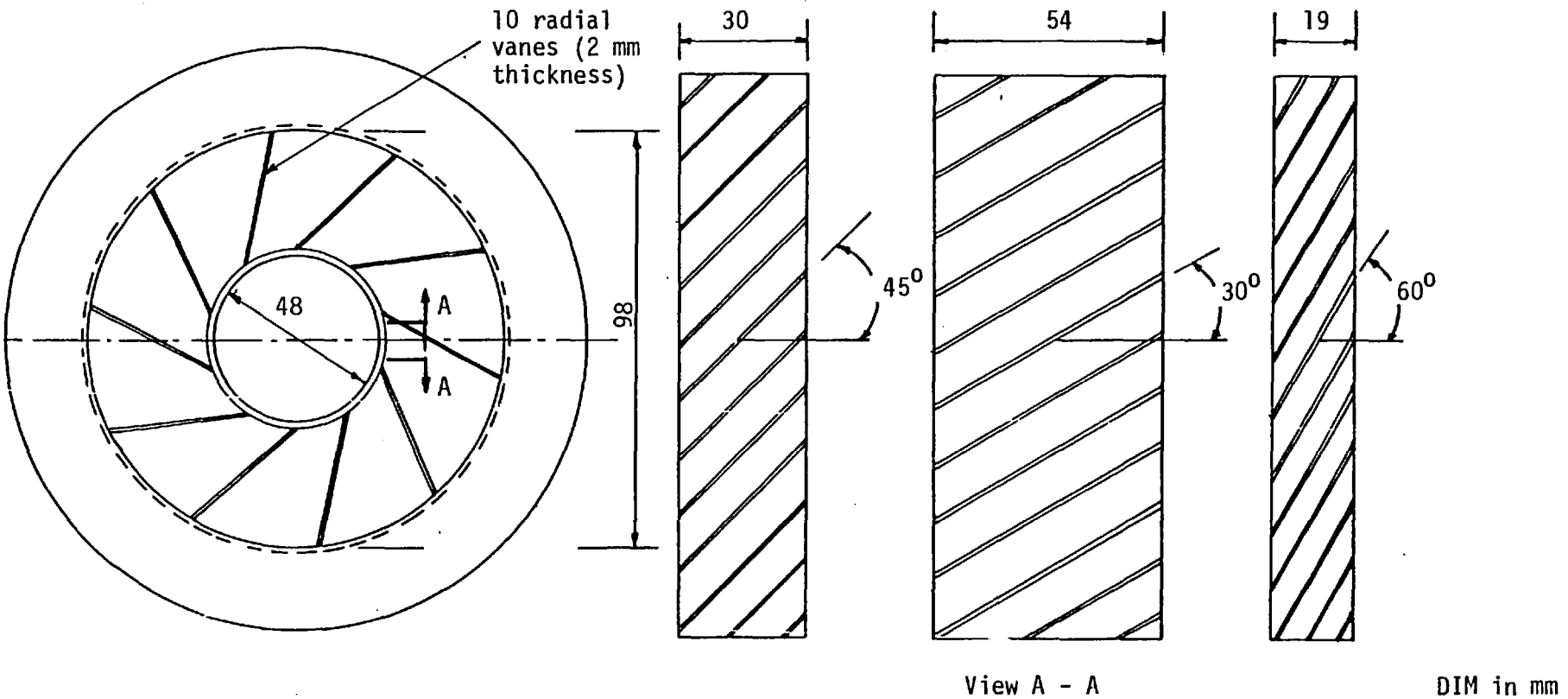

Fig. AII.2 Geometrical details of the 3 air swirlers used in the confined flame experiments

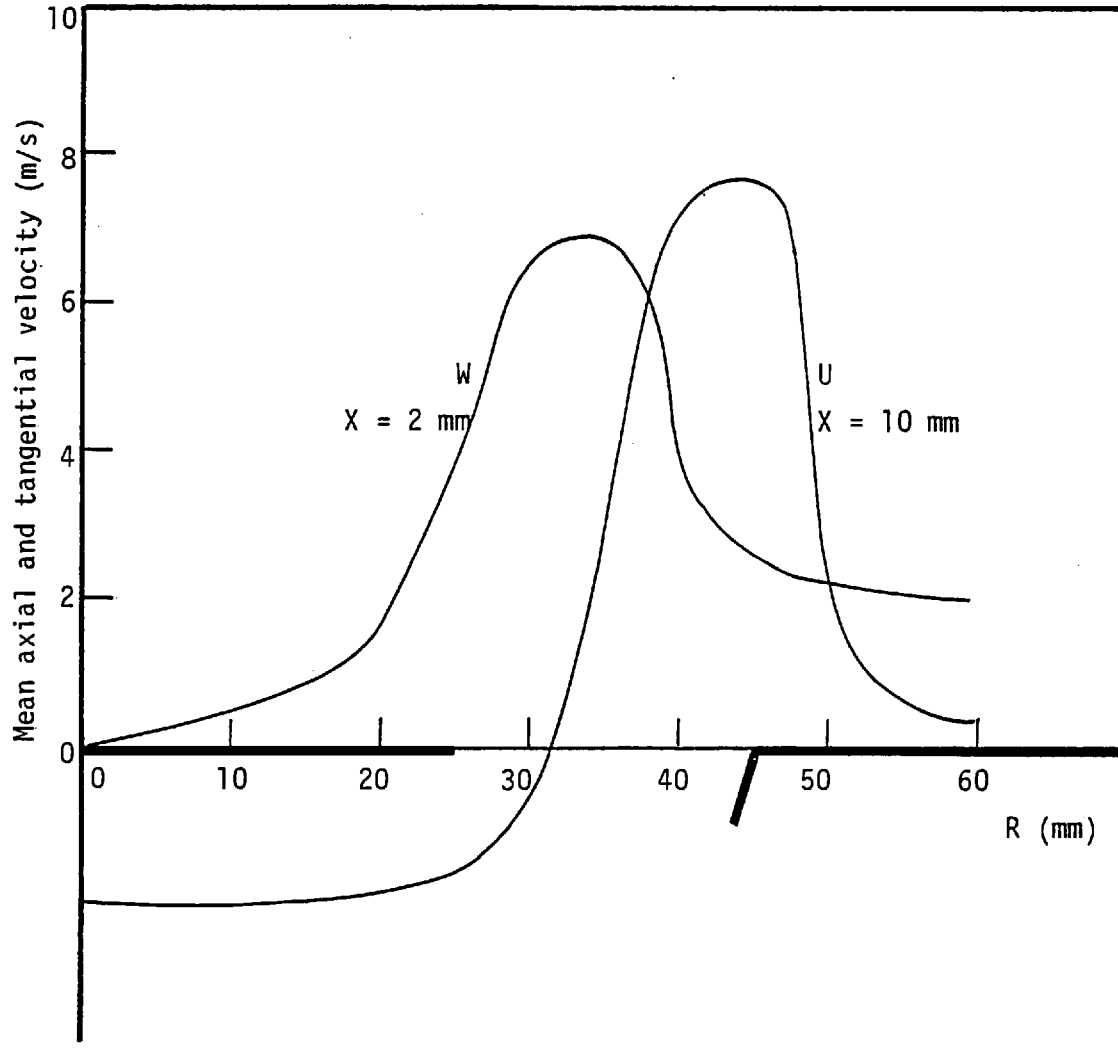

Fig. AII.3 Radial profiles of mean axial and tangential velocity at exit from the unconfined flame burner, Founti (1979)

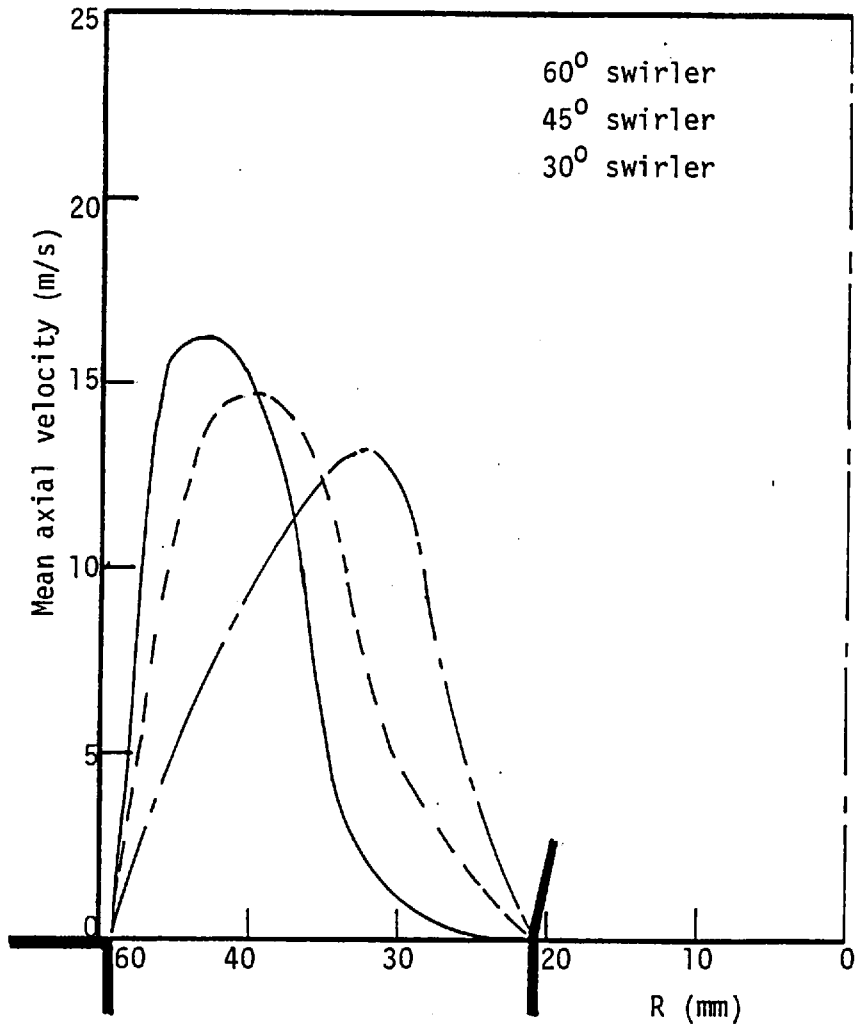

Fig. AII.4 Radial profiles of mean axial velocity component at exit from the 3 air swirlers - confined flame experiments

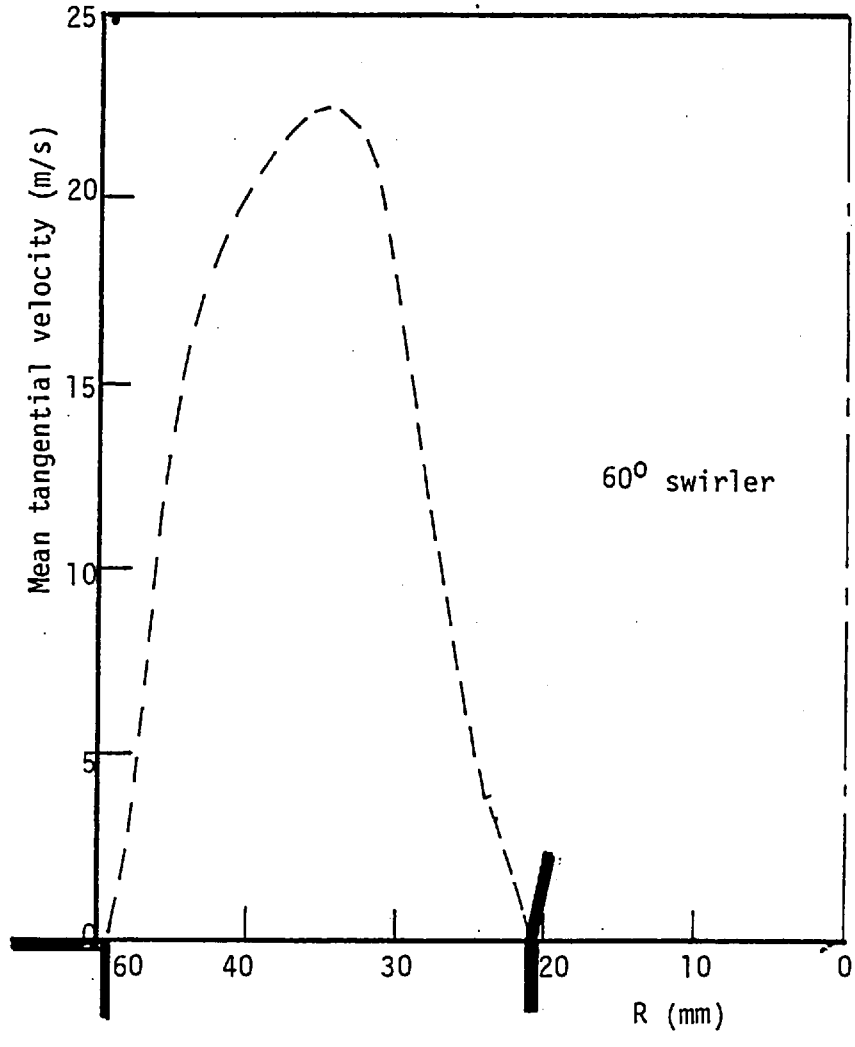

Fig. AII.5 Radial profile of the mean tangential velocity component at exit from the 60° air swirler

APPENDIX III

To demonstrate the extent to which the spread in the droplets size-distribution affects their velocity, the equations representing the motion of an evaporating droplet, along the direction of the flame centreline, were solved numerically for droplets injected with different diameters. This allowed the calculation of the droplet velocity and diameter as a function of the distance from the fuel nozzle.

The momentum balance equation for the droplet, Hinze (1971), can be written as:-

$$\left(\frac{\pi}{6} \cdot \rho_p \cdot D_p^3\right) \frac{dU_p}{dt} = \frac{\pi}{8} C_D \cdot Re_\ell \cdot D_p \cdot \mu_g \, (U_f - U_p) - \frac{\pi}{6} \cdot \rho_p \cdot D_p^3 \cdot g \qquad (1)$$

where:-

ρ_p : droplet density
D_p : droplet diameter
U_p : droplet axial velocity
μ_g : gas viscosity
U_g : gas velocity
g : gravitational acceleration

Re_ℓ is the droplet Reynolds number based on the relative velocity $|U_f - U_p|$. The drag coefficient C_D is calculated from the following expressions, see Williams (1973):-

$$C_D = 27 \, Re_\ell^{-0.84} \qquad 0 < Re < 80$$

$$C_D = 0.271\ Re_{\ell}^{0.217} \qquad 80 < Re < 10^4$$

$$C_D = 2.0 \qquad Re > 10^4$$

The rate of change of droplet diameter with time, dD_p/dt, is calculated from:-

$$\frac{dD_p}{dt} = \left[\frac{-\ 2\ K_f}{\rho_p \cdot cp_f}\ (2 + 0.56\ Re_{\ell}^{0.5})\ \ell n\ (1 + B)\right] \cdot \frac{1}{D} \qquad (2)$$

where K_f and cp_f are the gases thermal conductivity and specific heat and B is the transfer number, Spalding (1953), i.e.:-

$$B = c_{p_v}\ (T_f - T_{sat})\ L$$

c_{p_v}, T_f, T_{sat} and L are the constant pressure specific heat of the fuel vapour, the gas mean temperature, saturation temperature of the liquid fuel and the fuel latent heat of vapourization respectively.

Equations 1 and 2 were solved for a presumed droplet injection velocity and fluid properties which are relevant to the present measurements. The effect of the high velocity atomization air on the droplet motion was taken into account by assuming a high gas velocity close to the fuel nozzle. Fig. AIII.1 shows the calculated droplet velocity along the flame centreline for different diameters. The results of run 3 are plotted on the same figure for reference purposes. It is clear from Fig. AIII.1 that the spread in the droplet size distribution, especially at the near-nozzle locations, is associated with a corresponding large spread in velocity. However, droplet collisions and break-up, as well as the difference in injection velocity for different diameters and the

turbulent flow, are likely to modify the spread in velocity associated with different diameters. For example, the velocity probability distributions corresponding to centreline points in run 3, at x/D = 0.6, 1.0 and 2.2, which are shown in Fig. AIII.2 indicate a larger spread in velocity compared to that shown in Fig. AIII.1. This indicates that the high velocity fluctuations observed during the measurements, at regions close to the burner, can be attributed, in part, to the spread in droplet velocity associated within the size range. It is also clear from Fig. AIII.1 that both the influence of the size distribution on the rms velocity decrease with downstream distance and is likely to be negligible for x/D > 2.

The increase in the mean velocity due to combustion at downstream regions of the flame (approximately x/D > 1.4) is demonstrated in Fig. AIII.3 where the droplet velocity is shown to increase with the mean temperature of the gases.

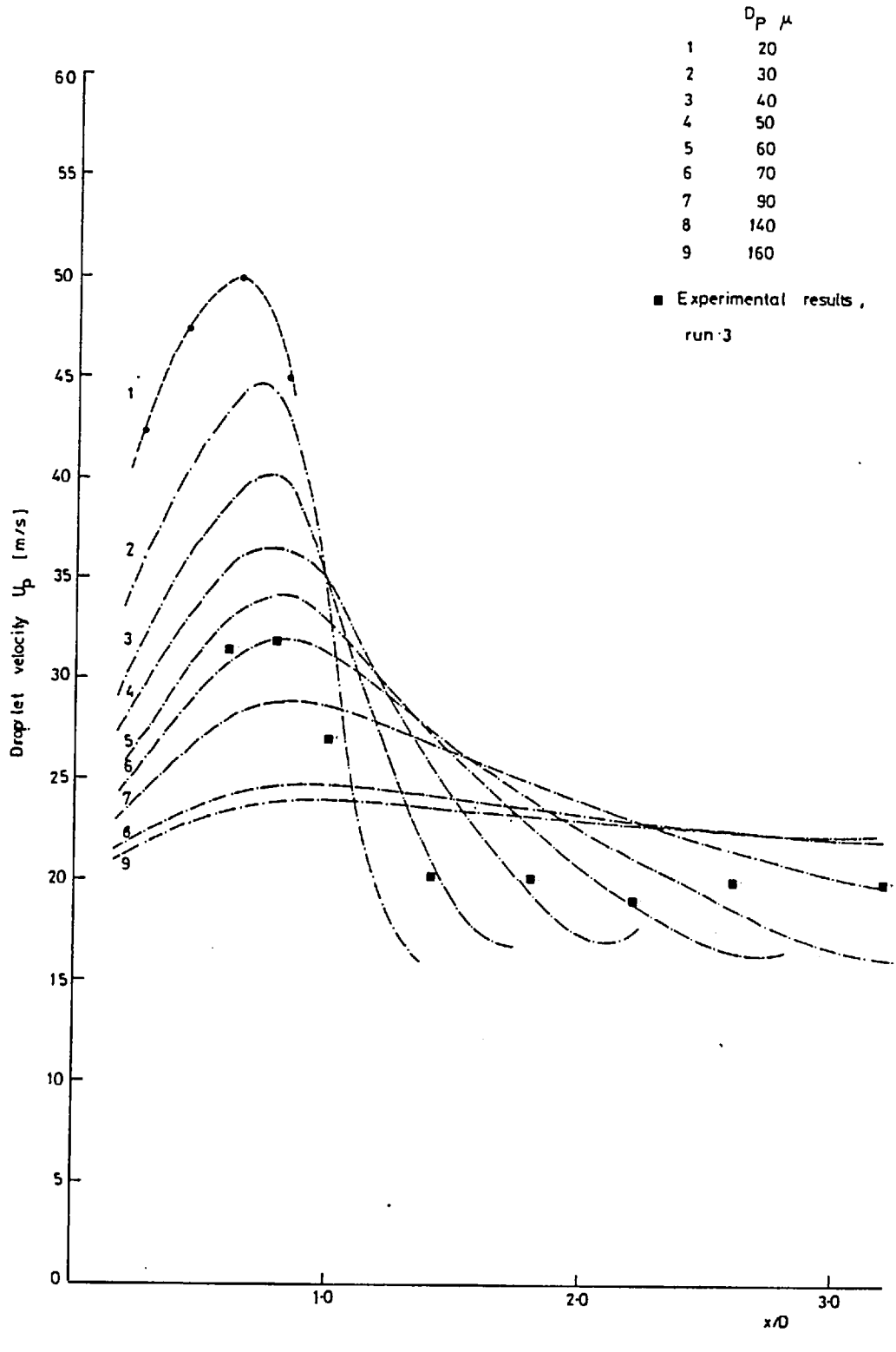

Fig. AIII.1 Calculated droplet velocity along the flame centreline for different initial diameters

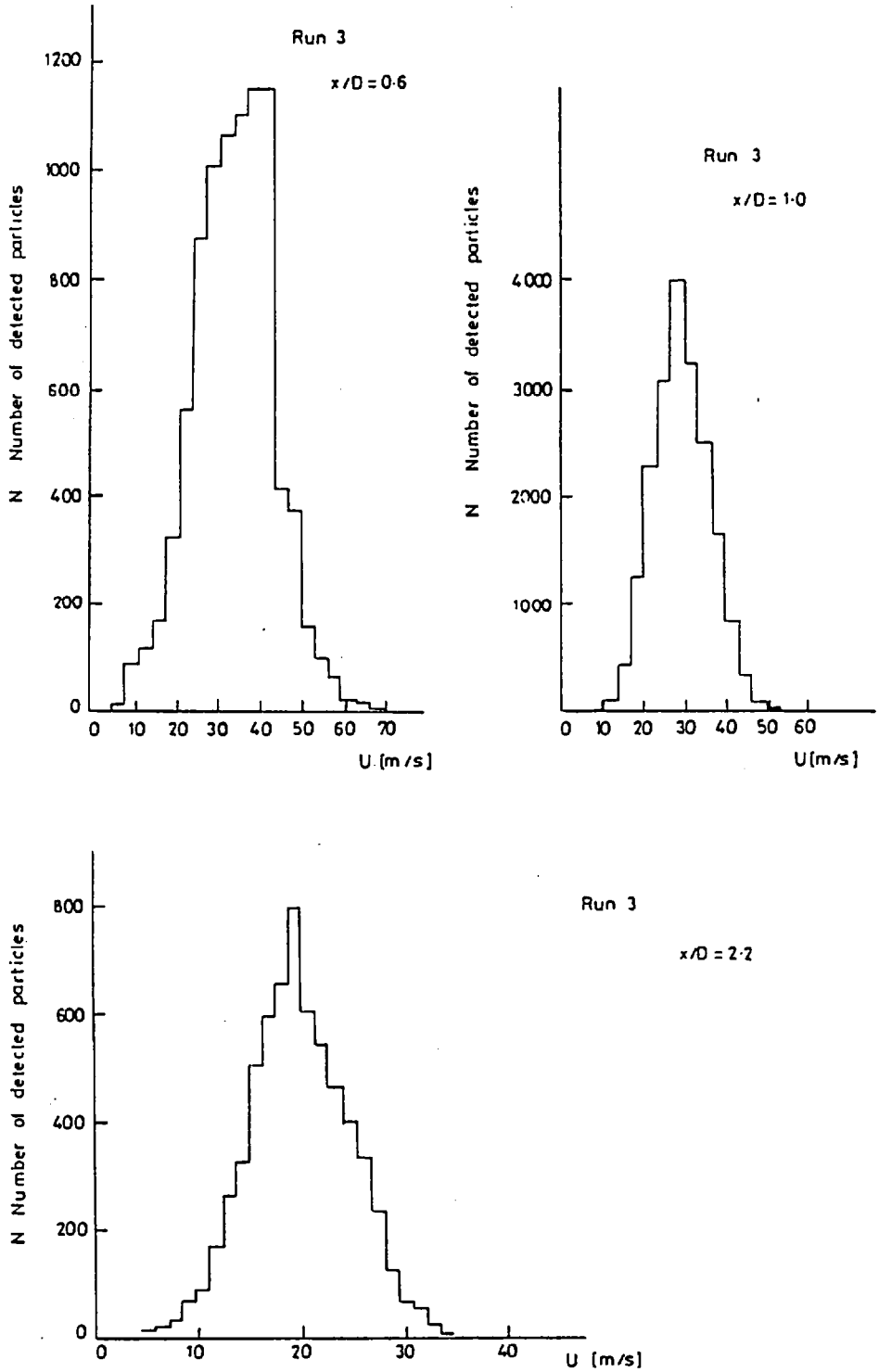

Fig. AIII.2 Velocity-probability distributions - run 3

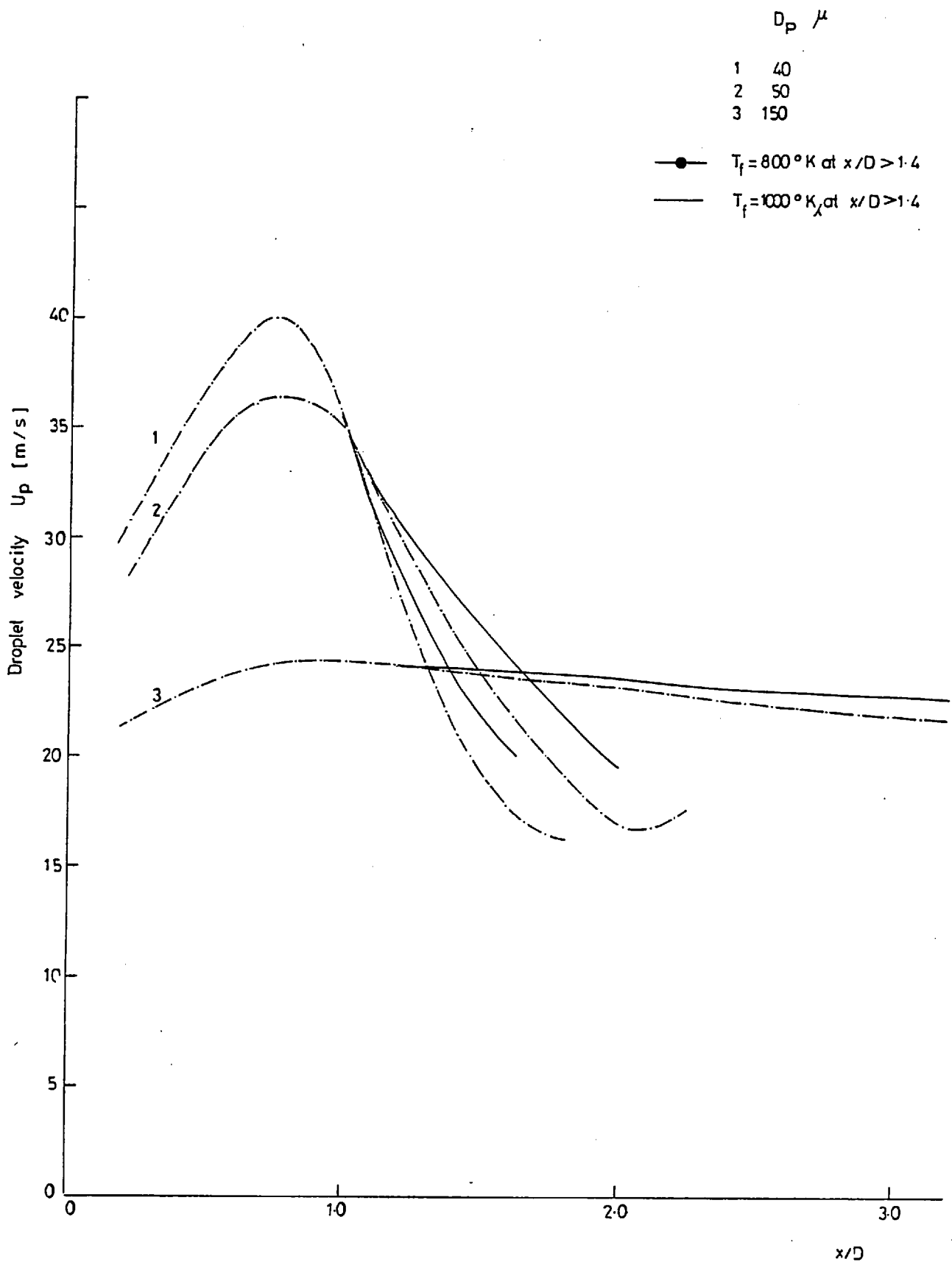

Fig. AIII.3 Calculated droplet velocity along the flame centreline for different initial diameters and gases mean-temperature

APPENDIX IV

REFERENCE EXPERIMENTAL DATA - CONFINED FLAME EXPERIMENTS

The results of temperature and species concentration measurements obtained for the confined flame experiments of Chapter 2 are presented in this appendix in the form of radial profiles at different axial locations within the flame. These serve as a reference to the contour plots presented in Chapter 2 and allow the reader to extract the experimental data of interest with much ease. The radial profiles of temperature, O_2, CO_2 and CO corresponding to runs 1, 2, 3, 4 and 5, see Table 2.3, are shown in Figs. AIV.1 through AIV.20 respectively and the temperature profiles of run 6 are shown in Fig. AIV.21.

A sample of the symmetry checks for the temperature measurements, see Section 2.2.2, are presented in Fig. AIV.22 and the results correspond to those of run 1, see Table 2.3. Also shown in Figs. AIV.23 to AIV.25 are samples of symmetry and repeatability checks for the species concentration measurements of O_2, CO_2 and CO, see Section 2.2.4. The results correspond to those of run 2, see Table 2.3.

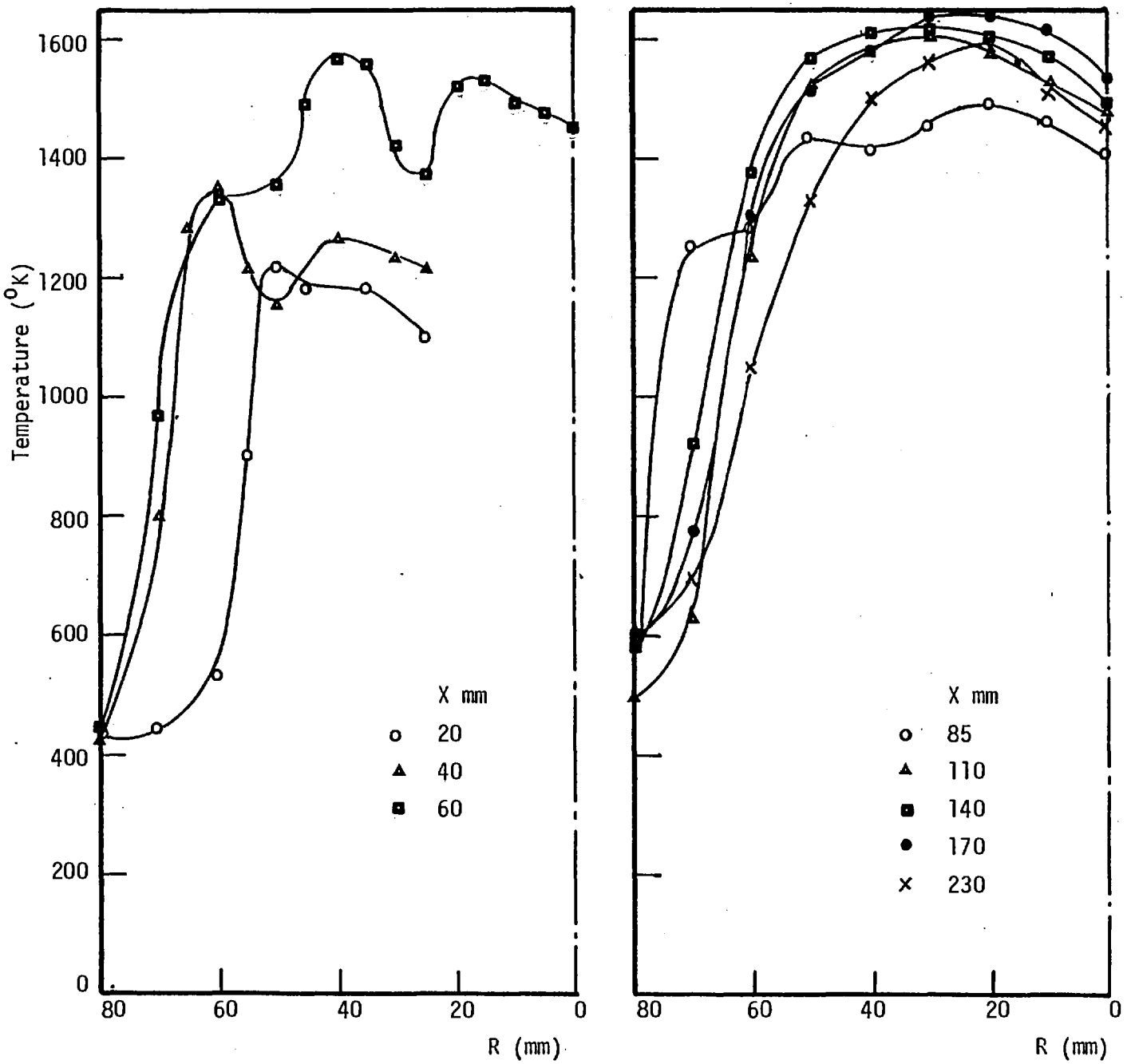

Fig. AIV.1 Radial profiles of mean gas temperature, run 1

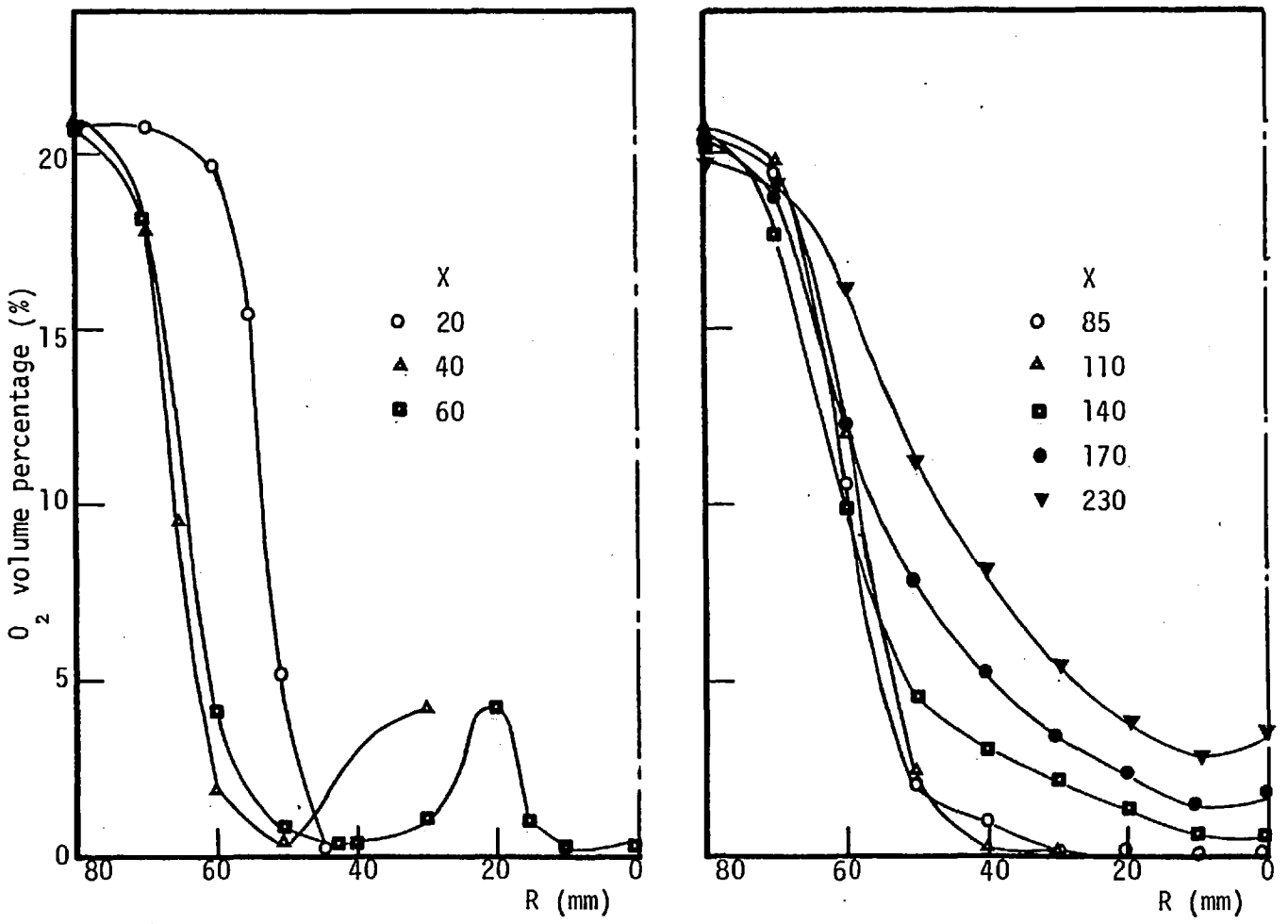

Fig. AIV.2 Radial profiles of O_2 volume percentage - run 1

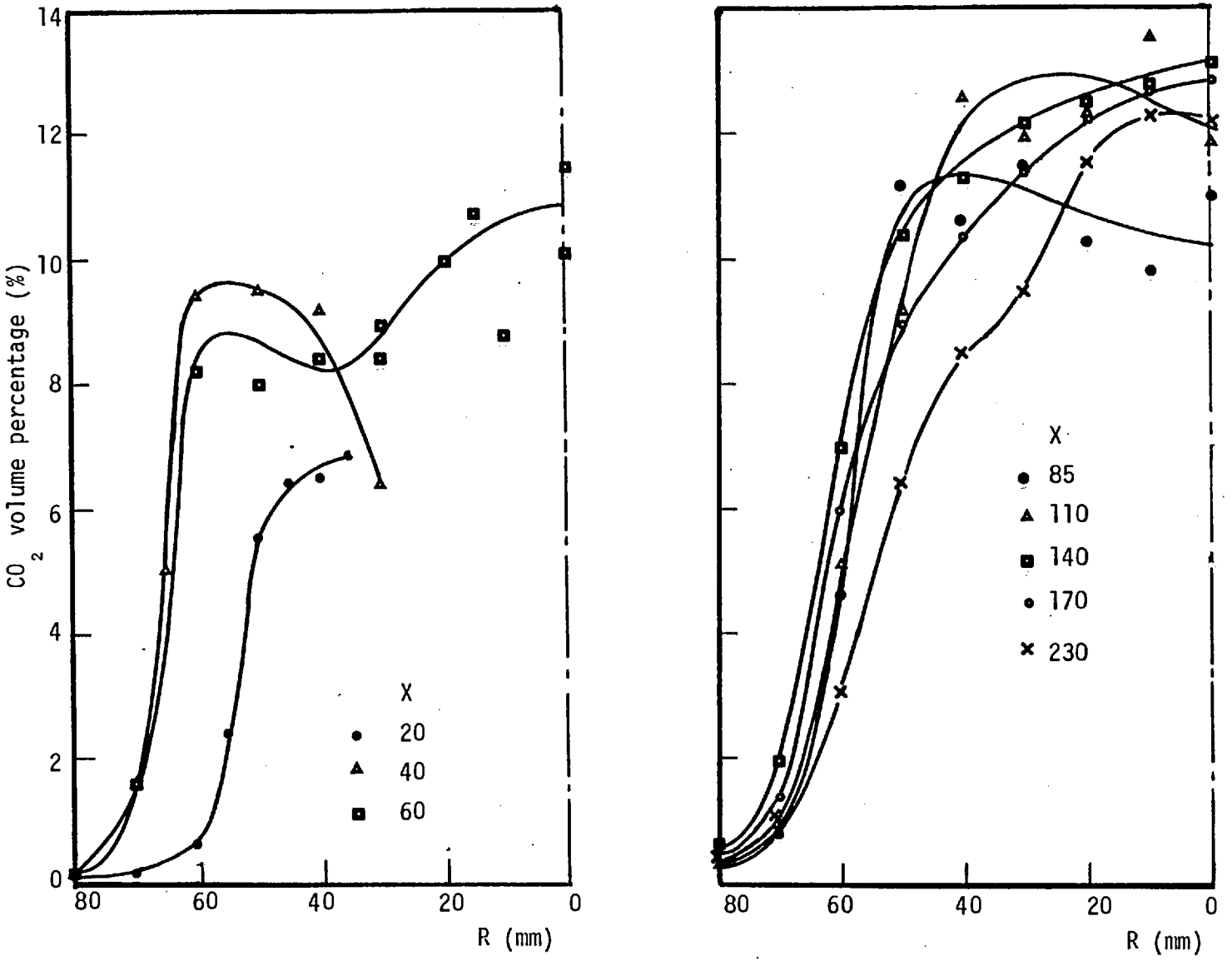

Fig. AIV.3 Radial profiles of CO_2 volume percentage - run 1

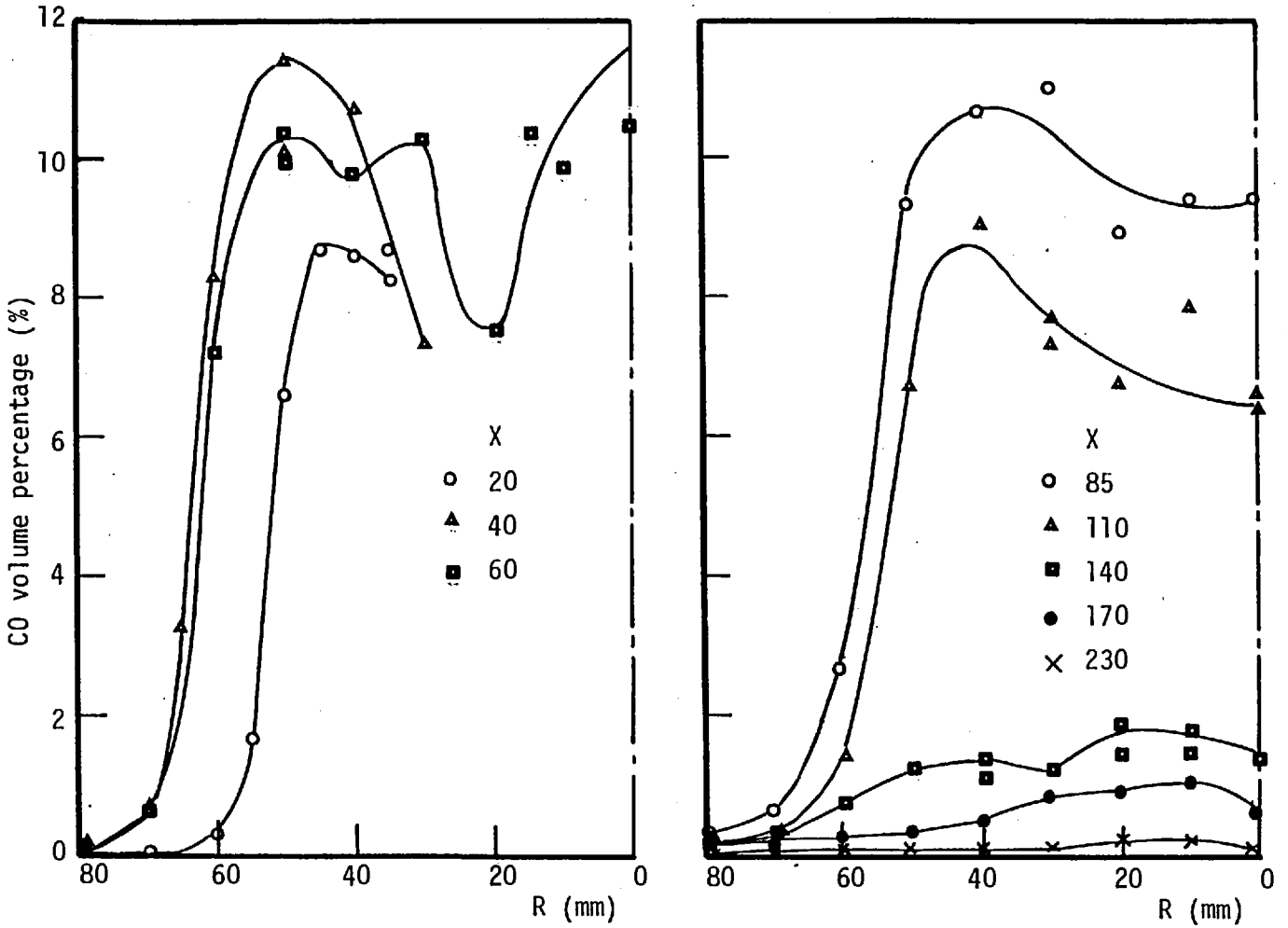

Fig. AIV.4 Radial profiles of CO volume percentage - run 1

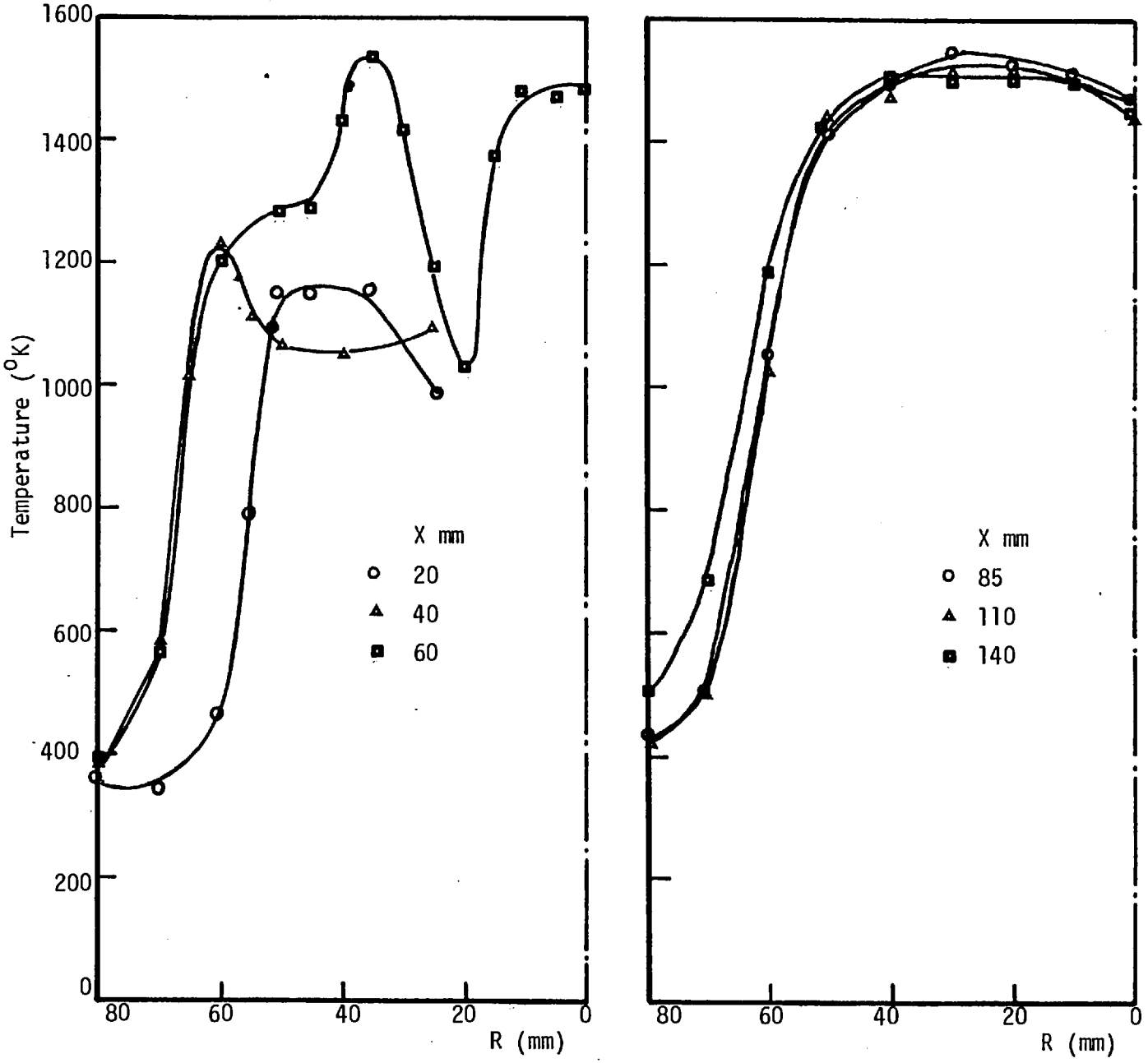

Fig. AIV.5 Radial profiles of mean gas temperature - run 2

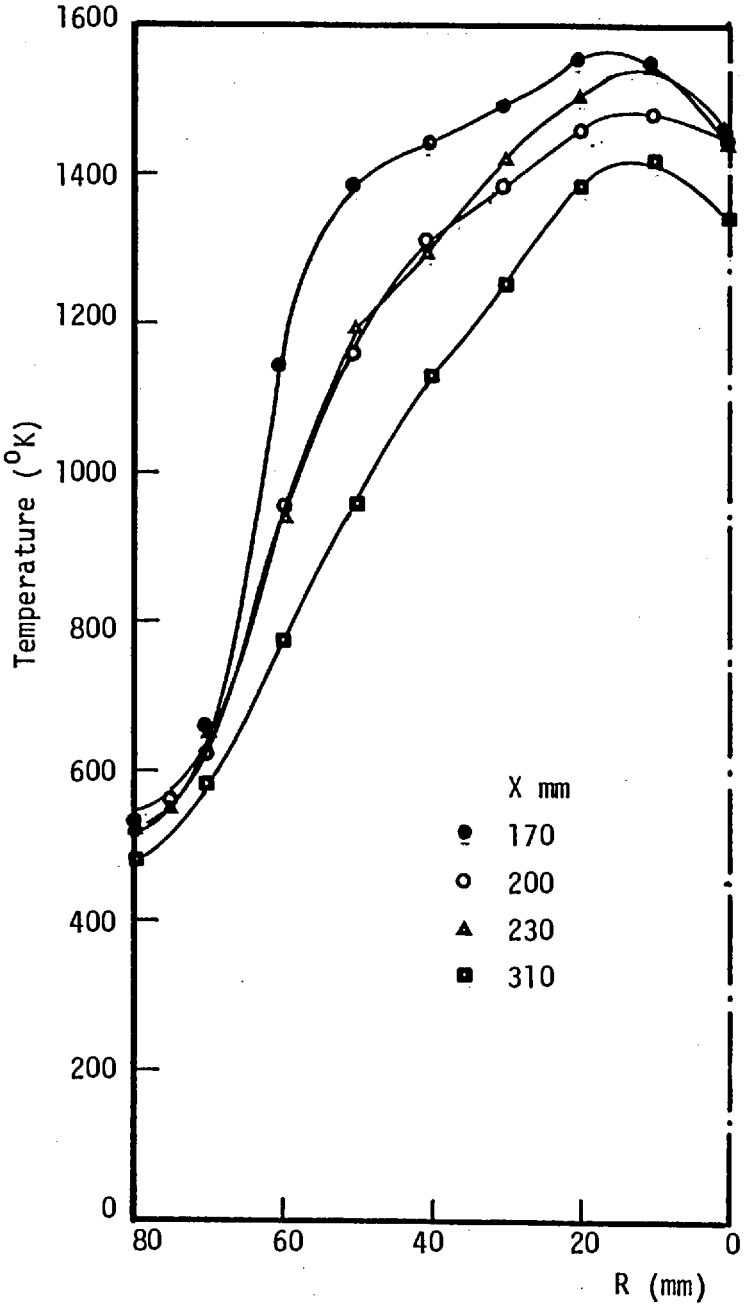

Fig. AIV.5 Continued

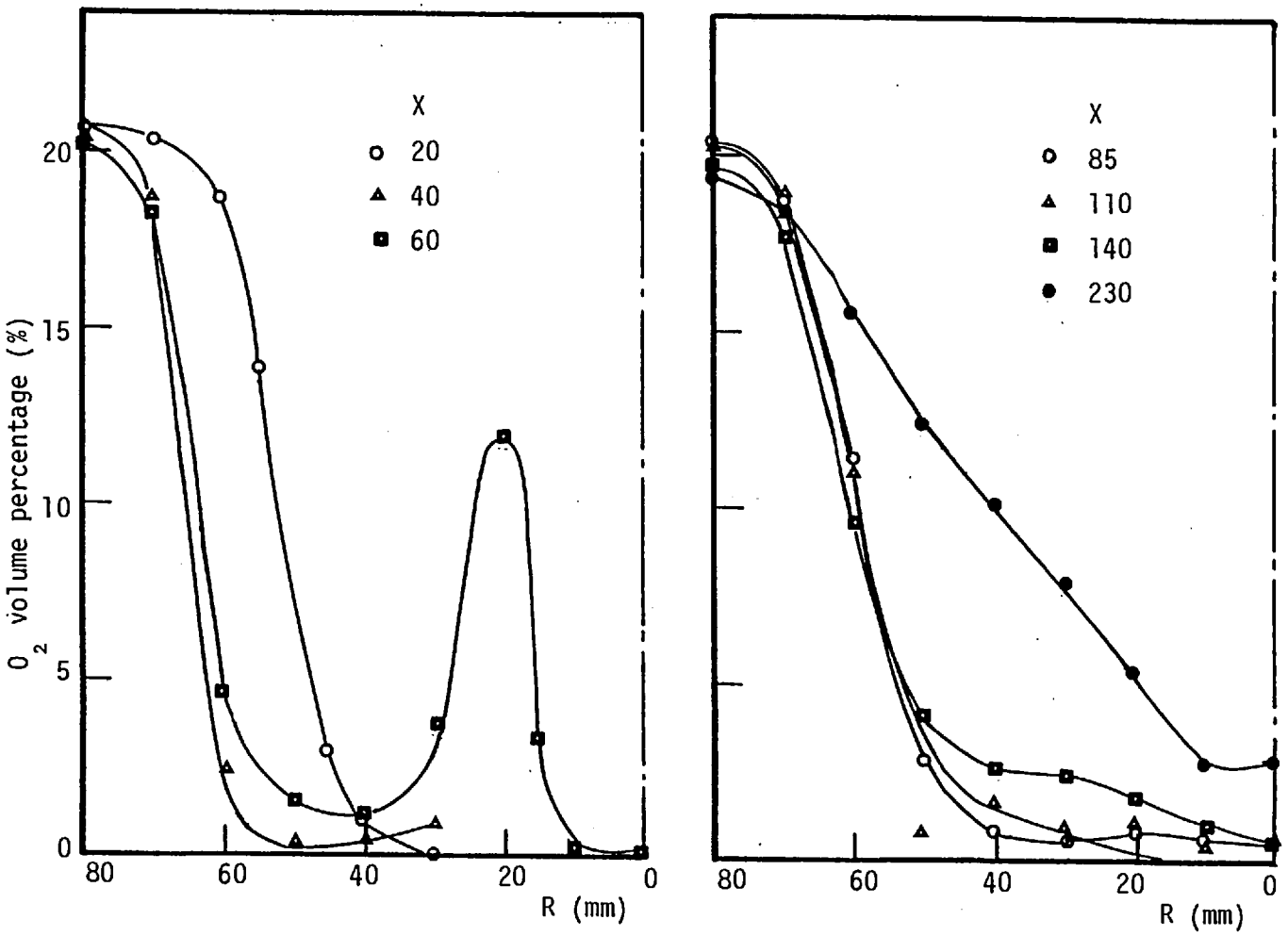

Fig. AIV.6 Radial profiles of O_2 volume percentage - run 2

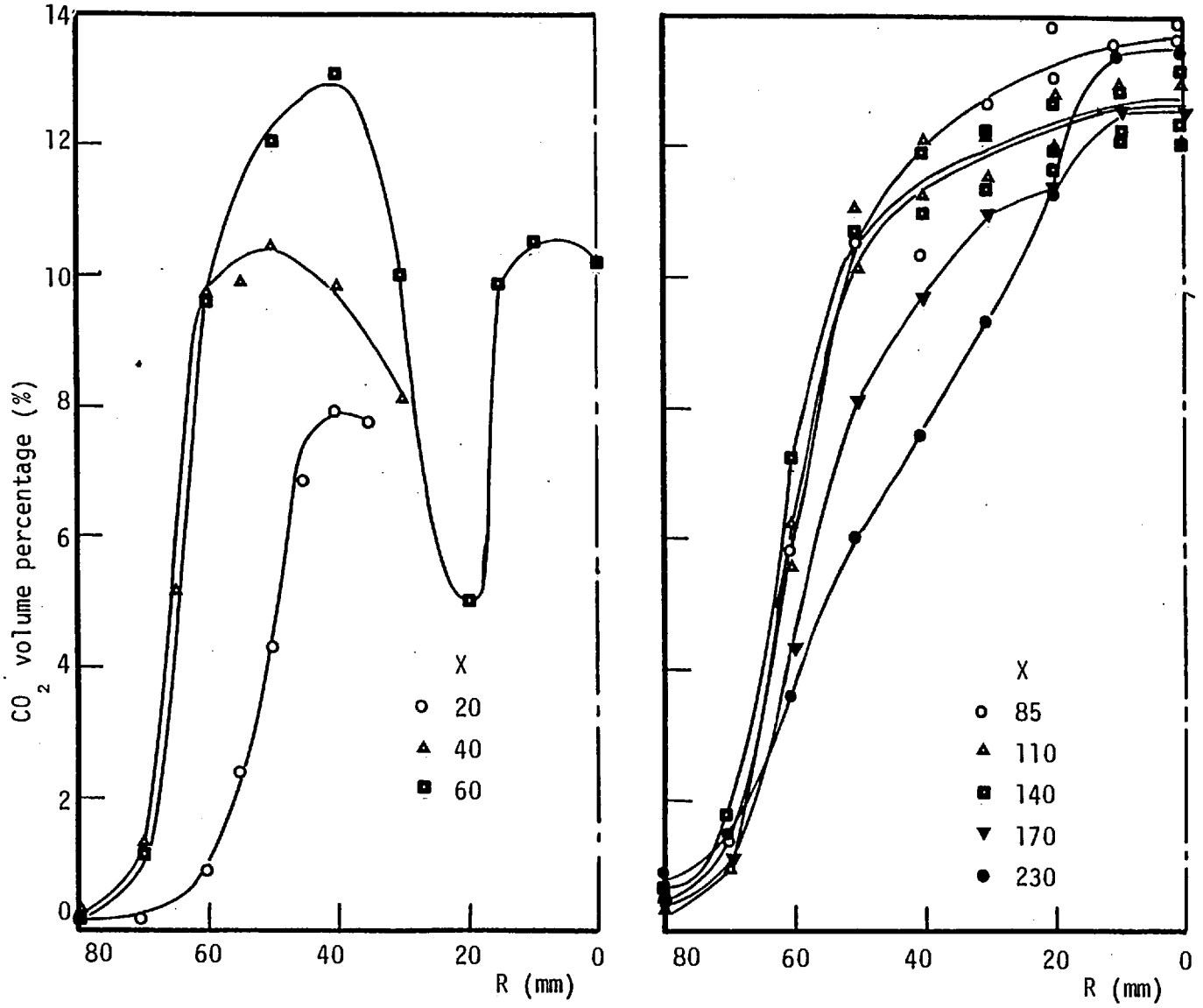

Fig. AIV.7 Radial profiles of CO_2 volume percentage - run 2

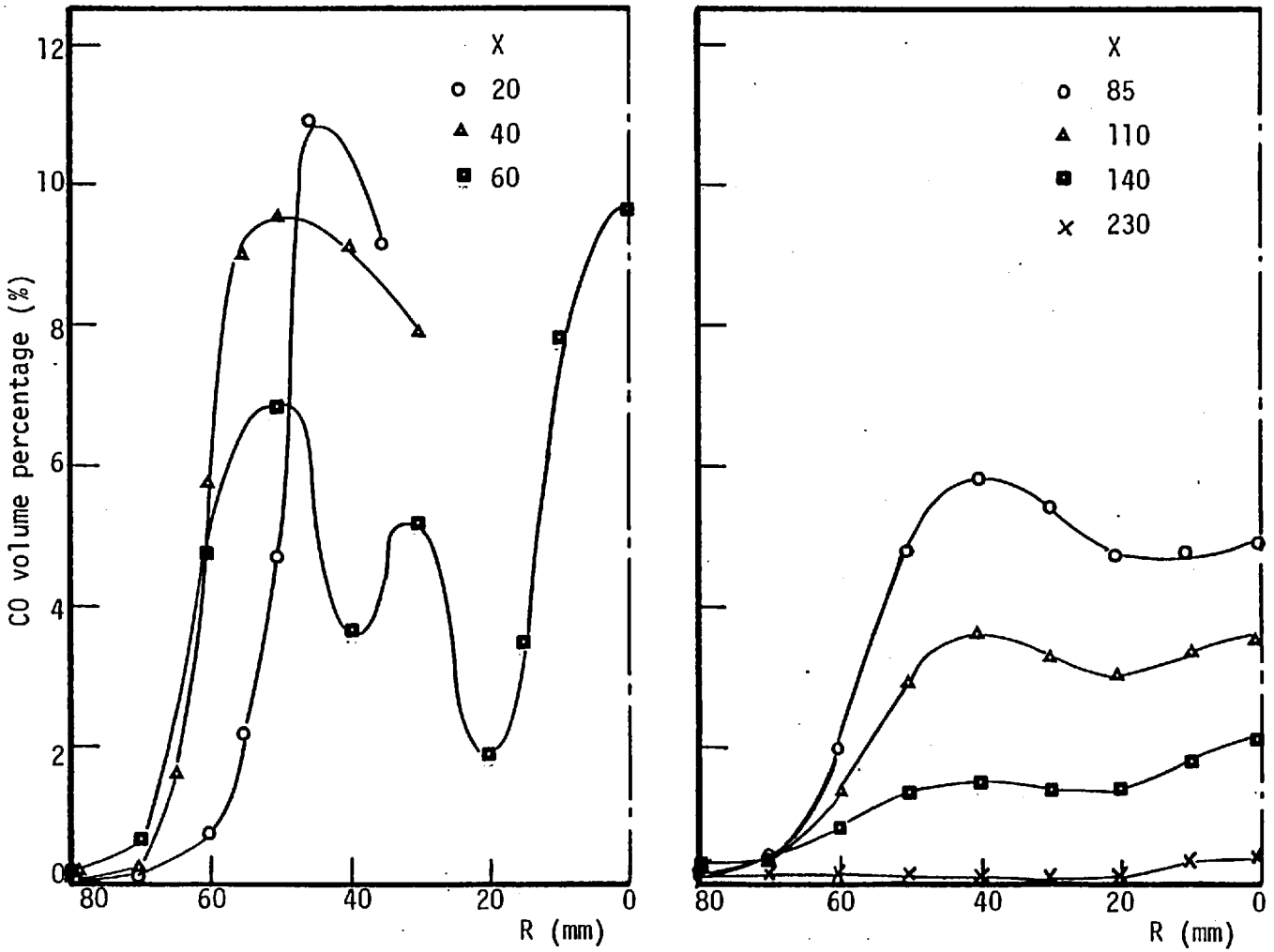

Fig. AIV.8 Radial profiles of CO volume percentage - run 2

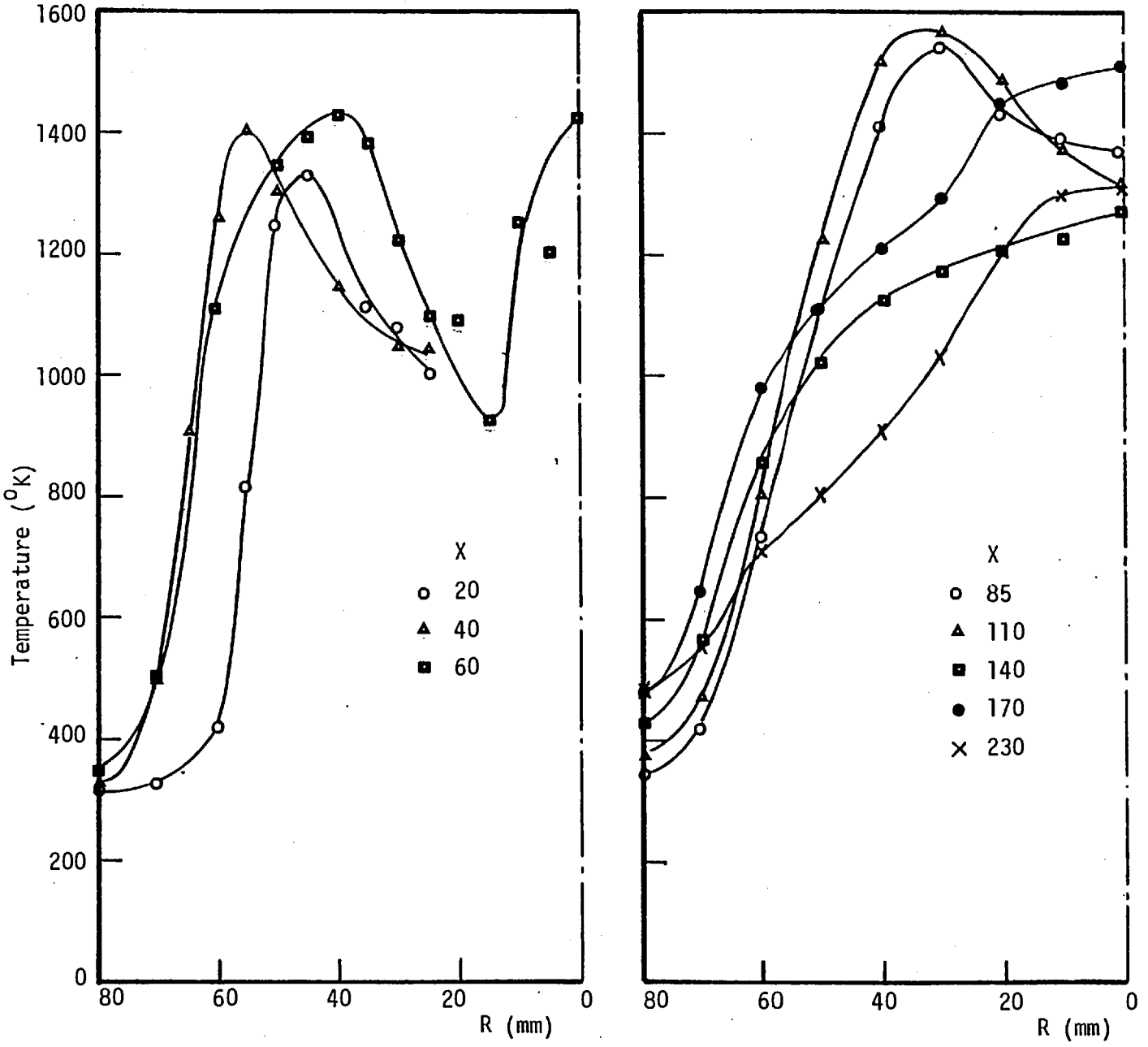

Fig. AIV.9 Radial profiles of mean gas temperature - run 3

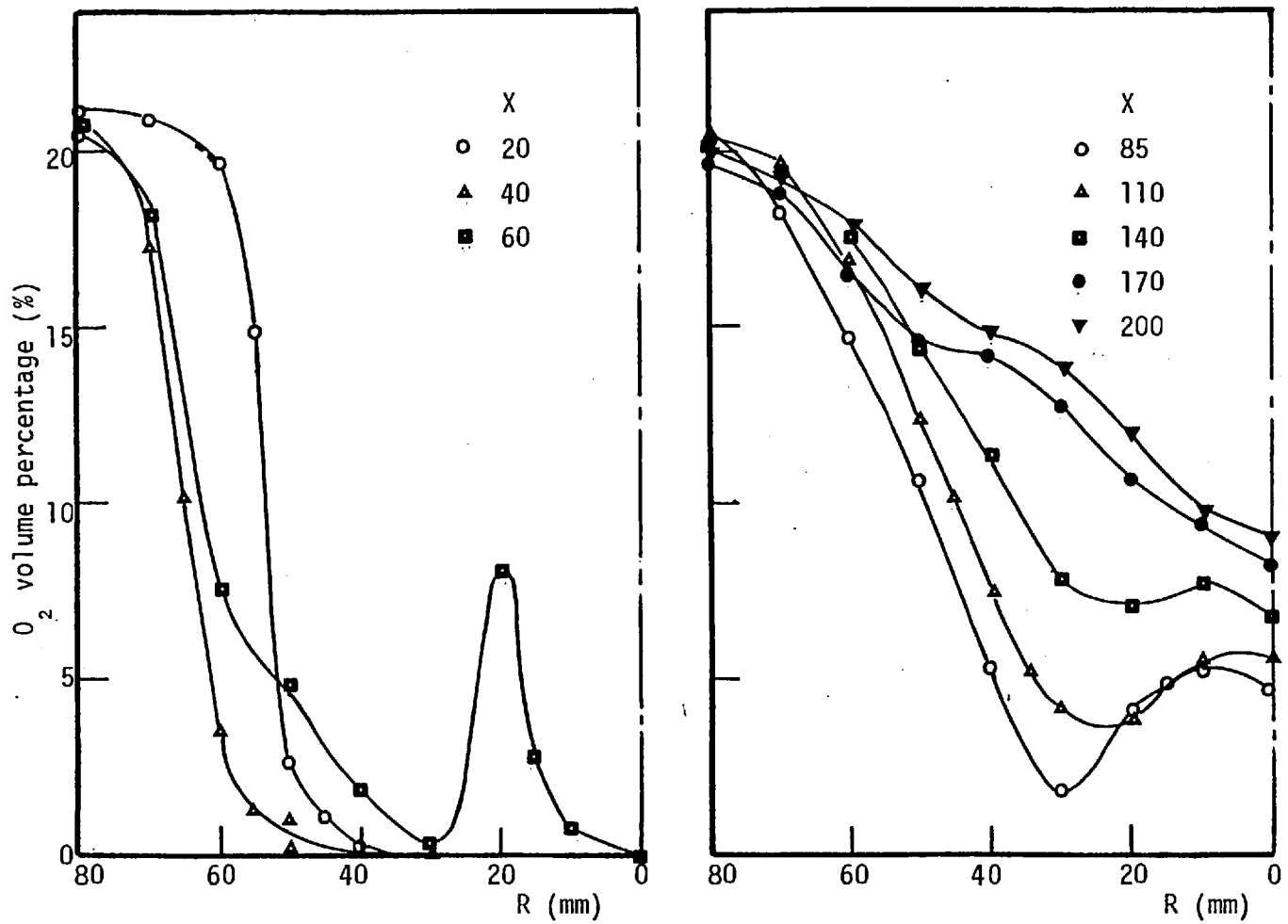

Fig. AIV.10 Radial profiles of O_2 volume percentage - run 3

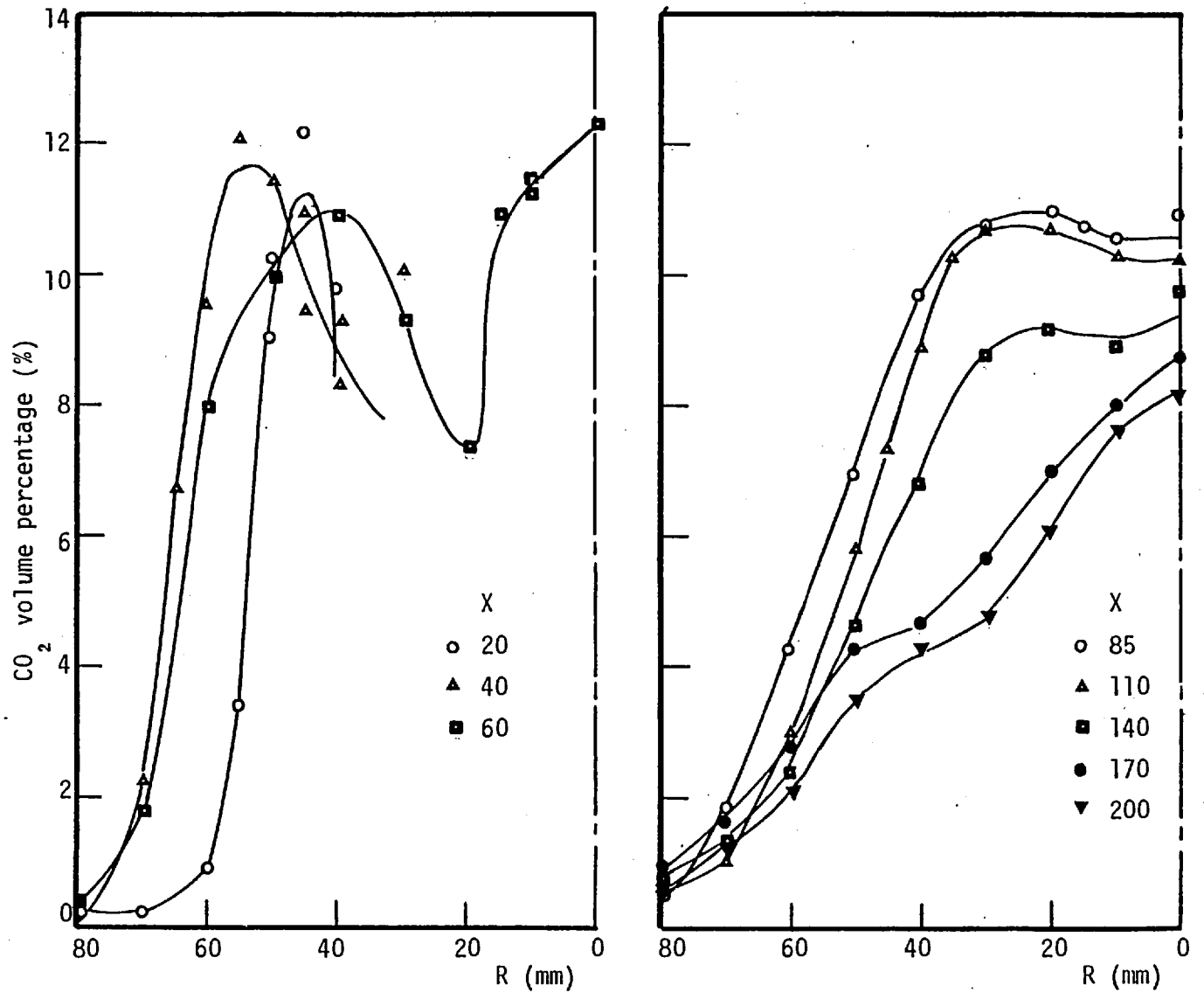

Fig. AIV.11 Radial profiles of CO_2 volume percentage - run 3

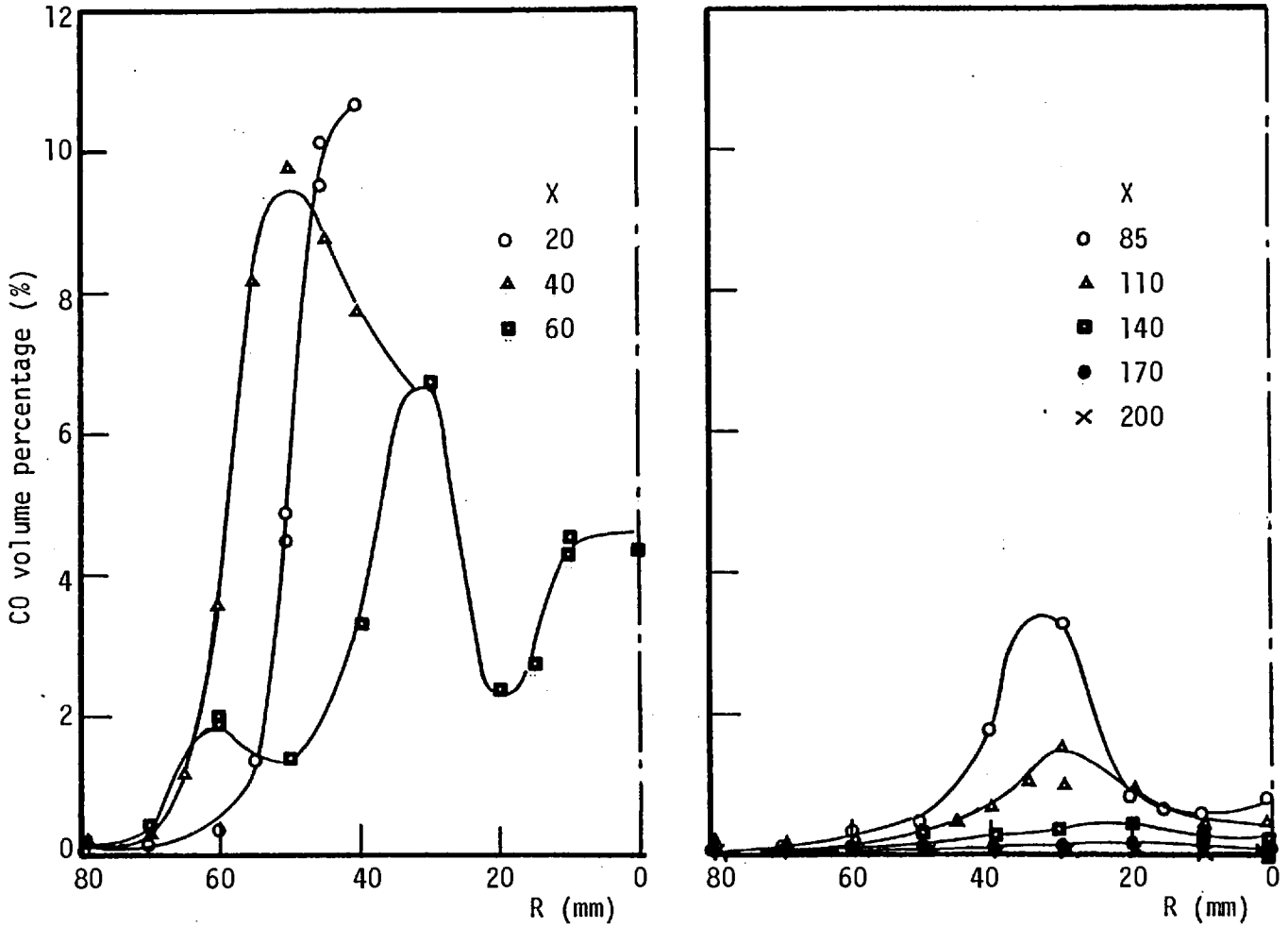

Fig. AIV.12 Radial profiles of CO volume percentage - run 3

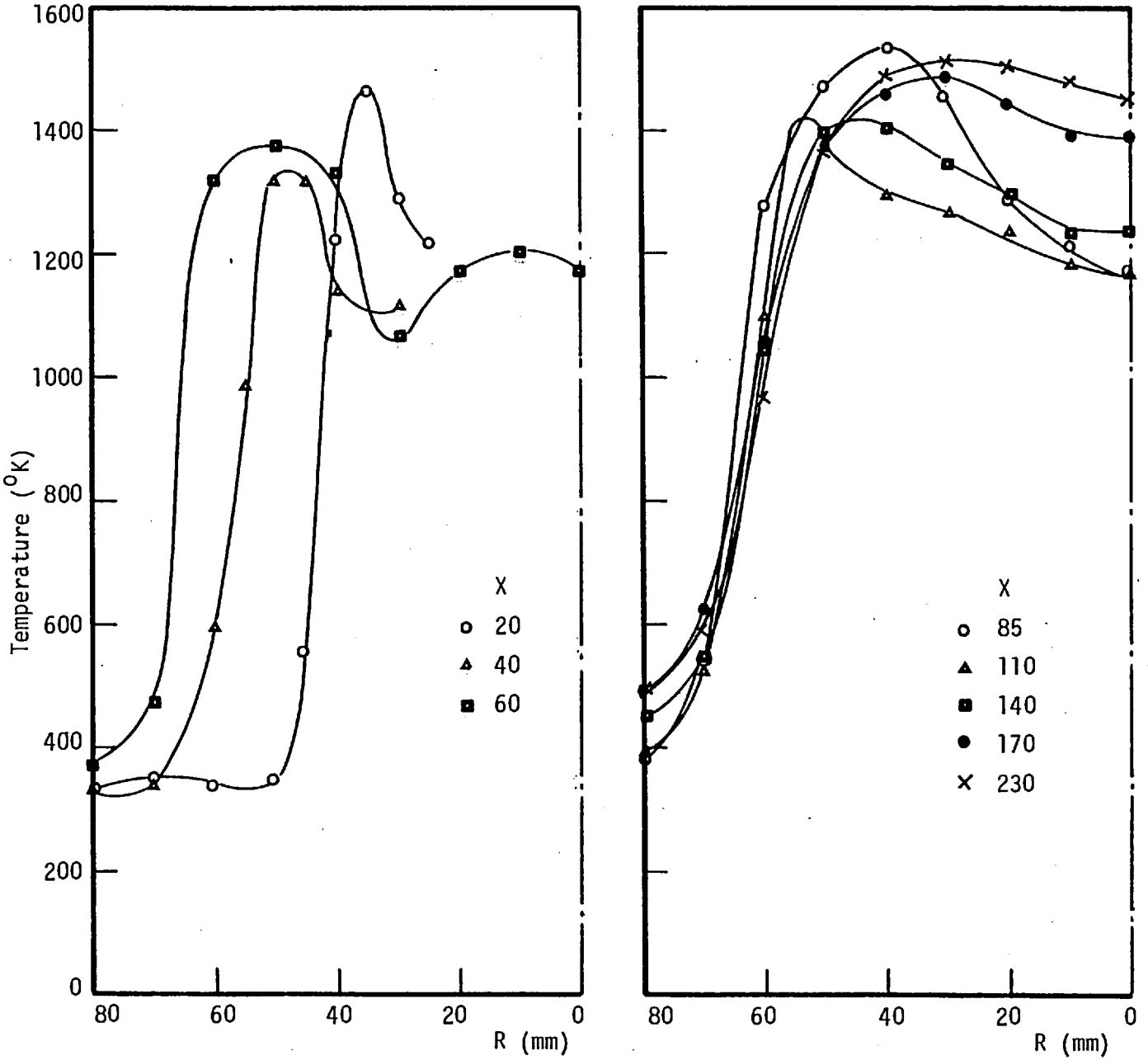

Fig. AIV.13 Radial profiles of gas mean temperature - run 4

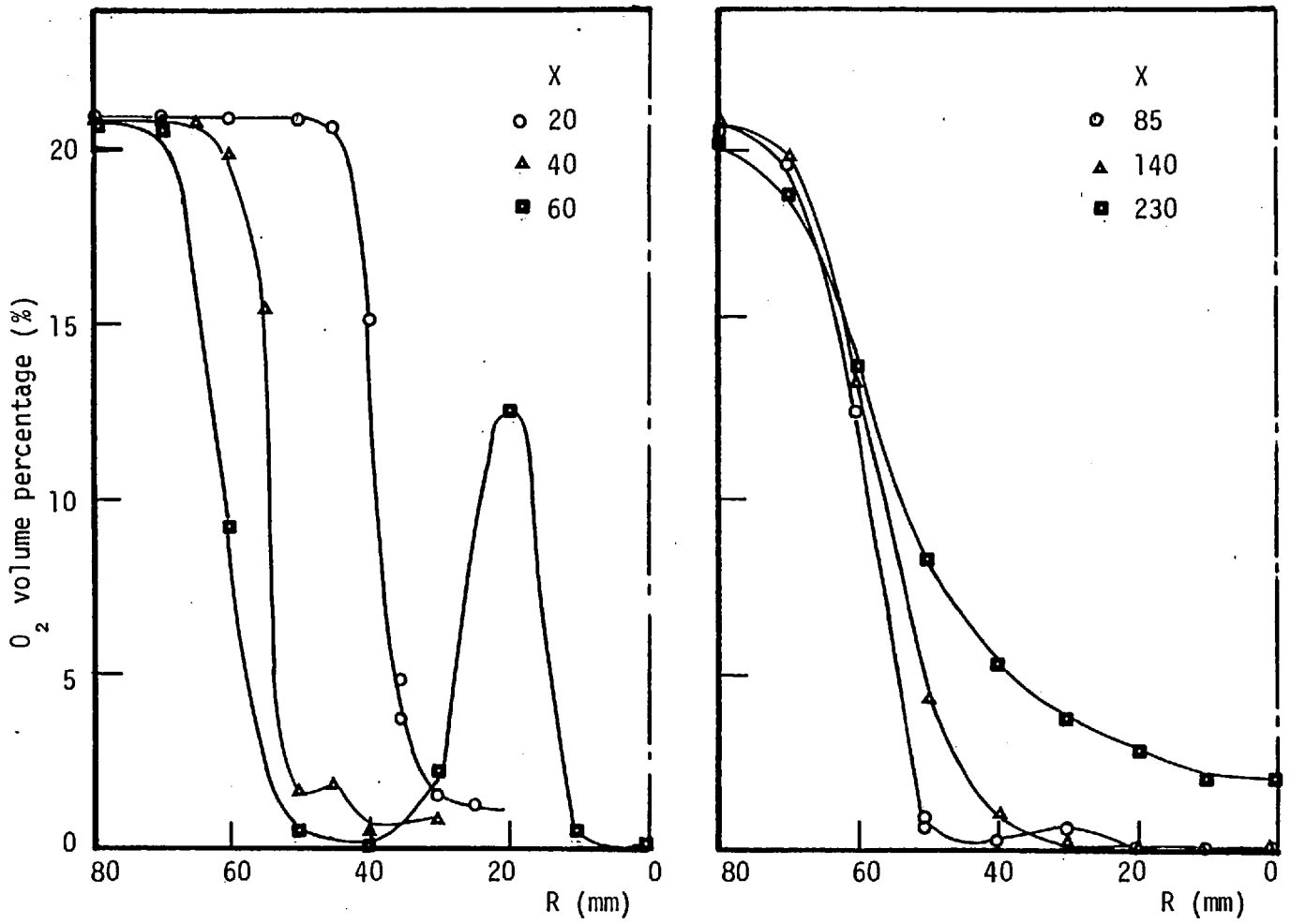

Fig. AIV.14 Radial profiles of O_2 volume percentage - run 4

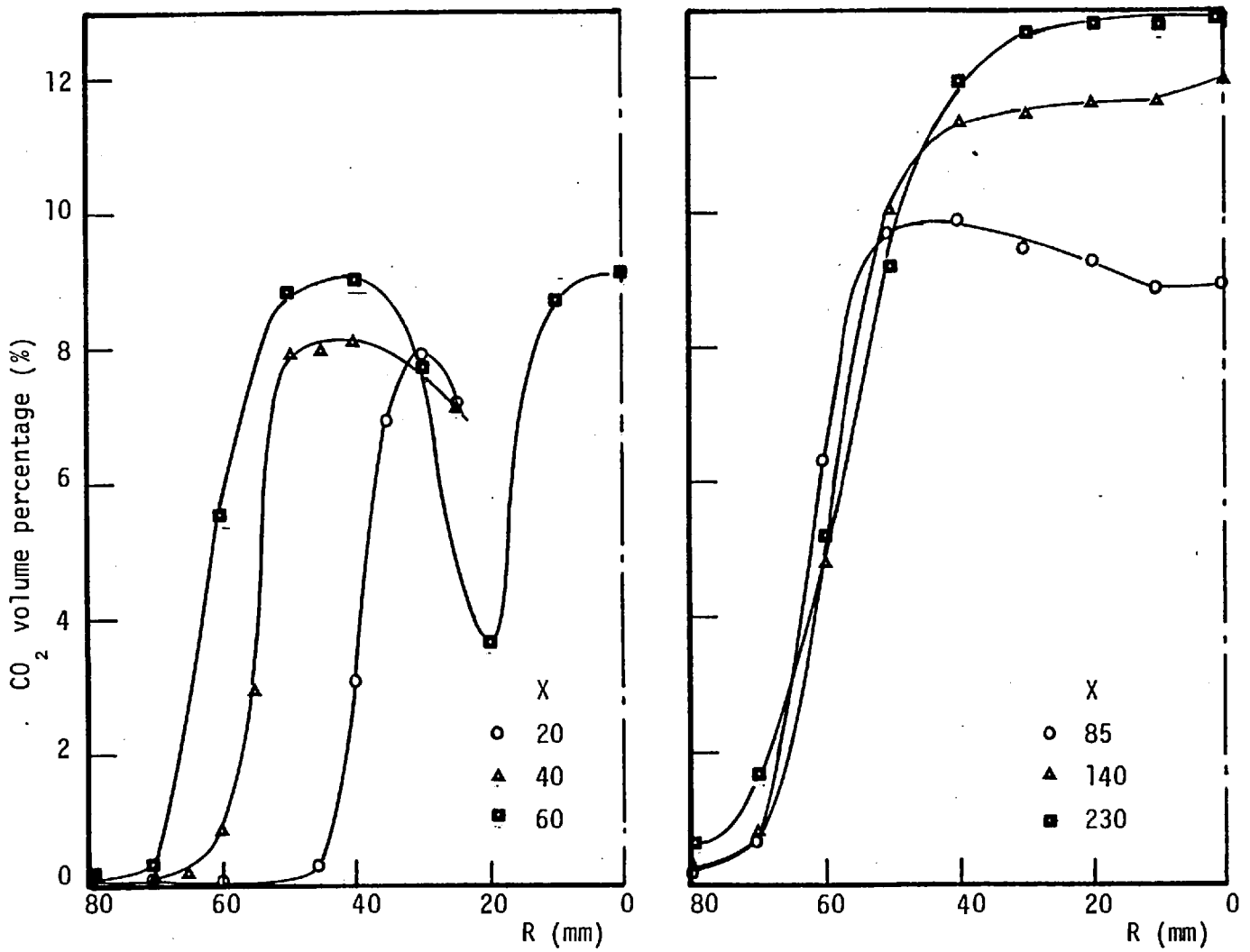

Fig. AIV.15 Radial profiles of CO_2 volume percentage - run 4

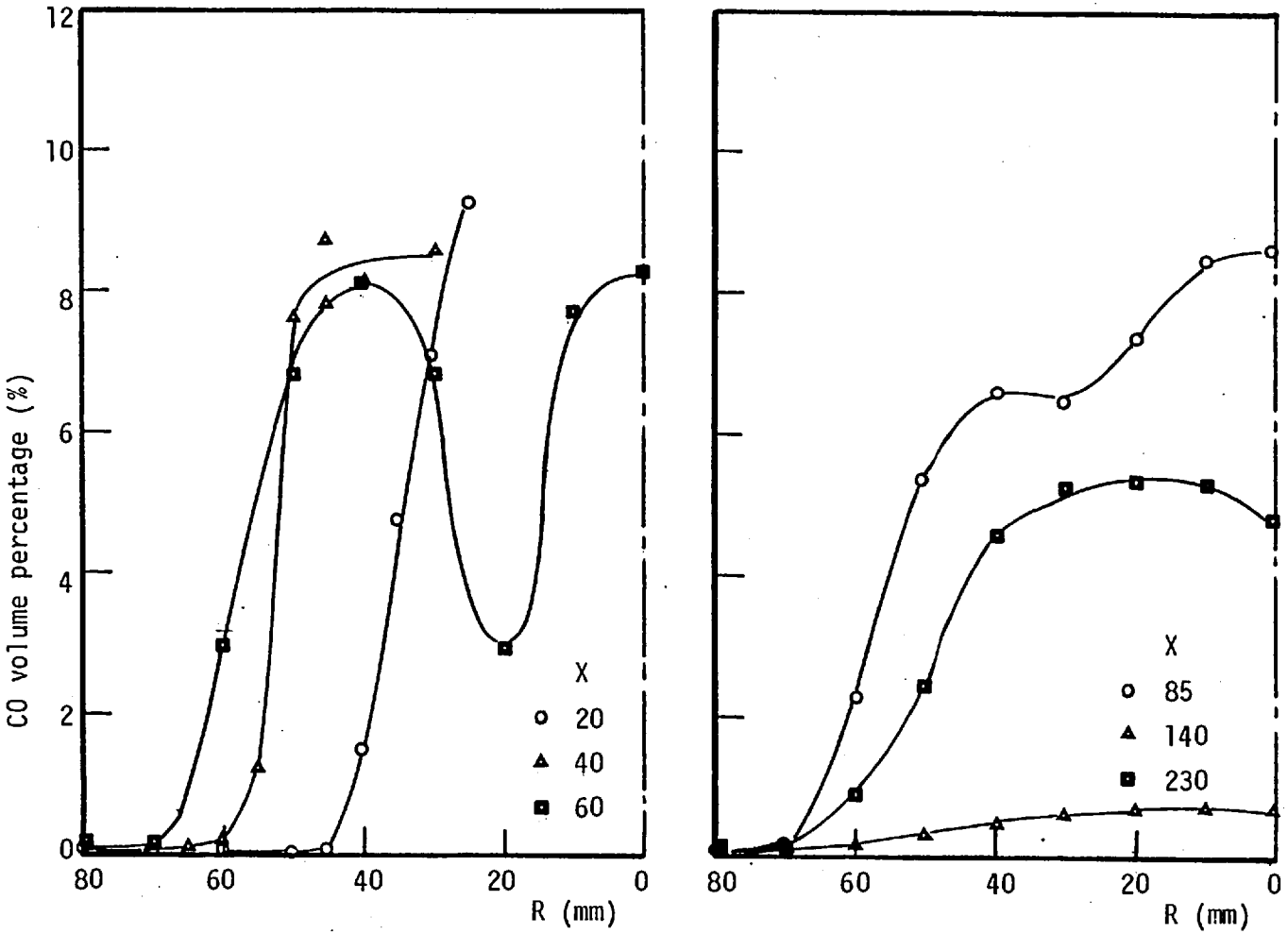

Fig. AIV.16 Radial profiles of CO volume percentage - run 4

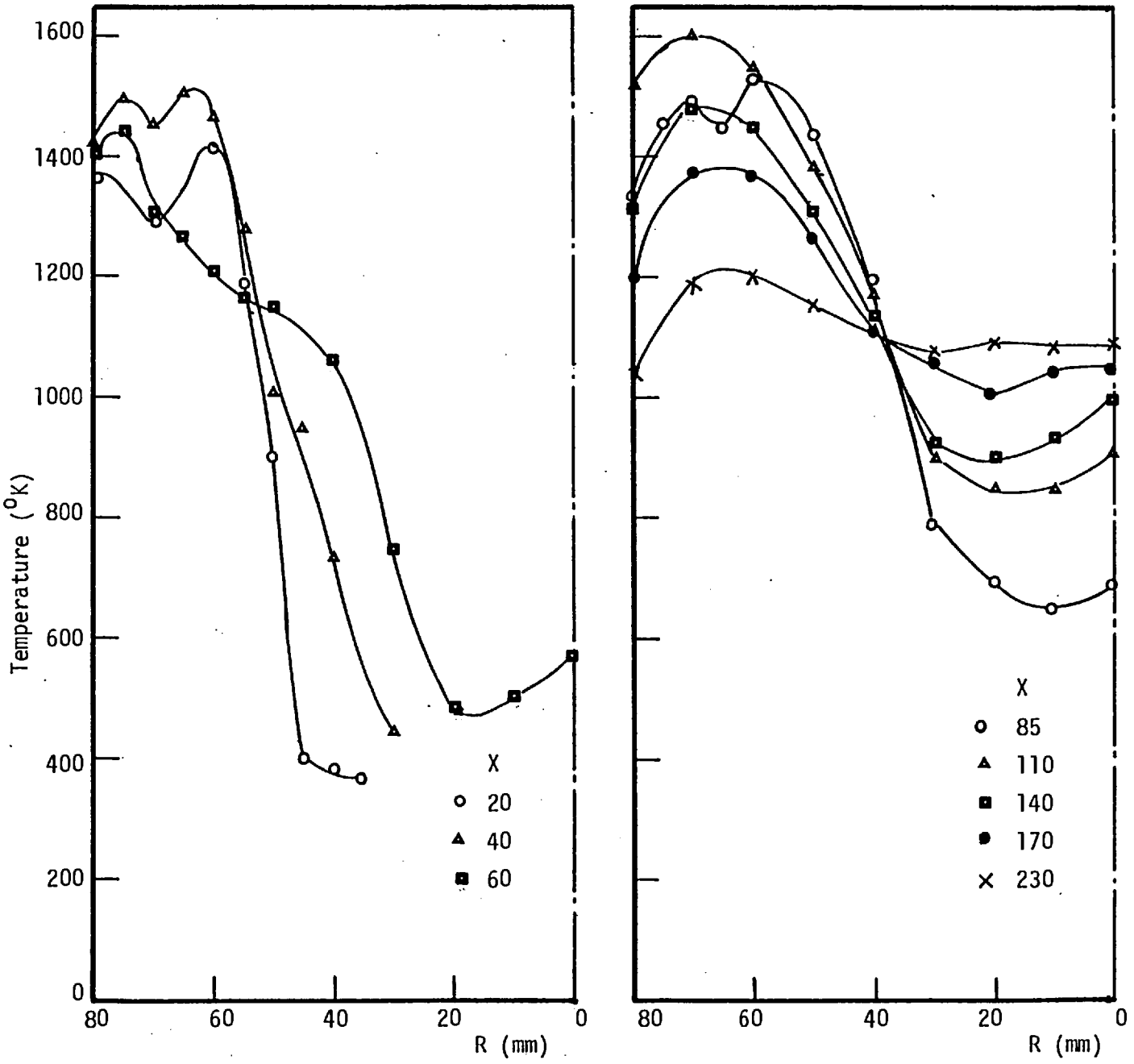

Fig. AIV.17 Radial profiles of mean gas temperature - run 5

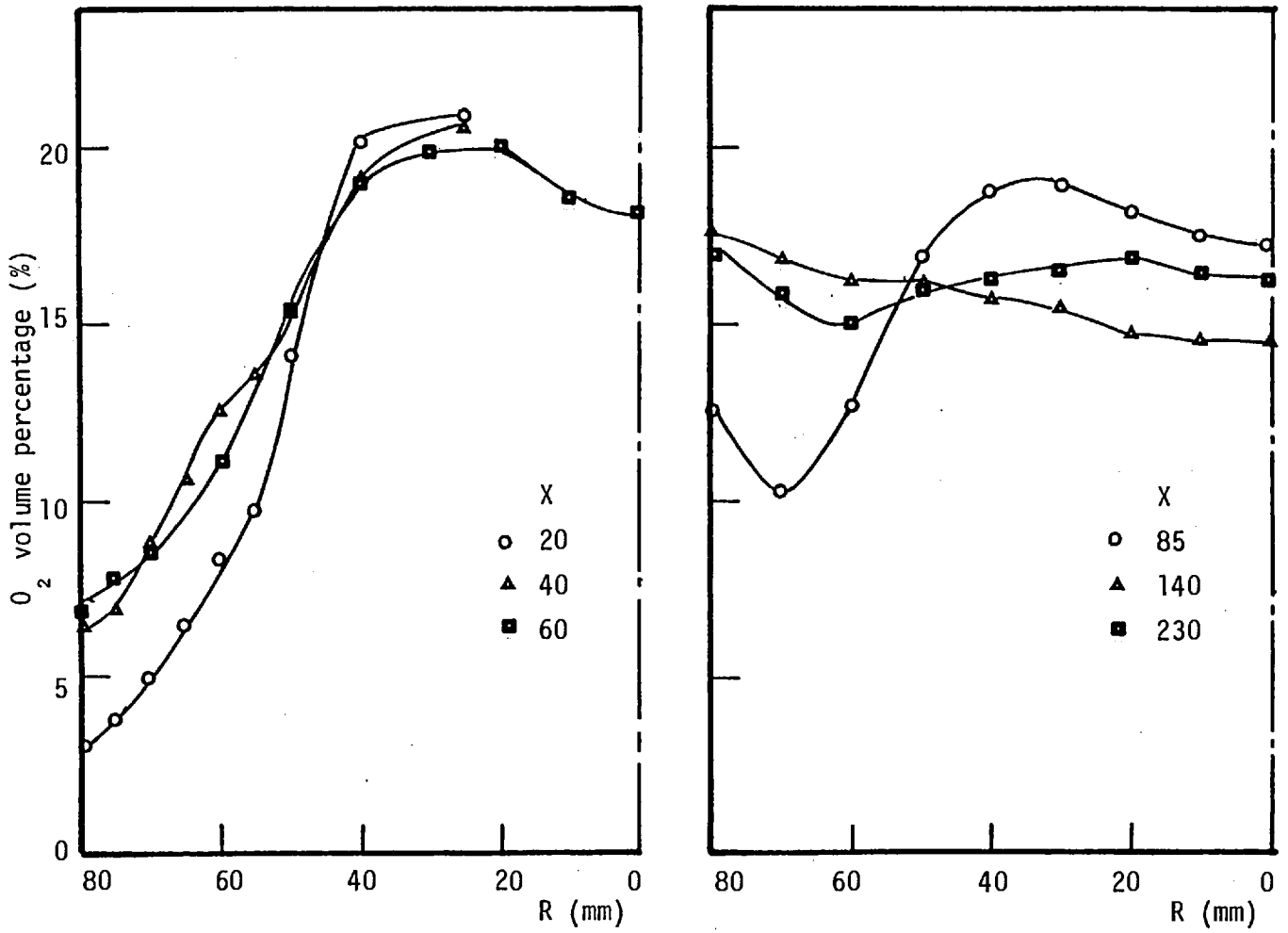

Fig. AIV.18 Radial profiles of O_2 volume percentage - run 5

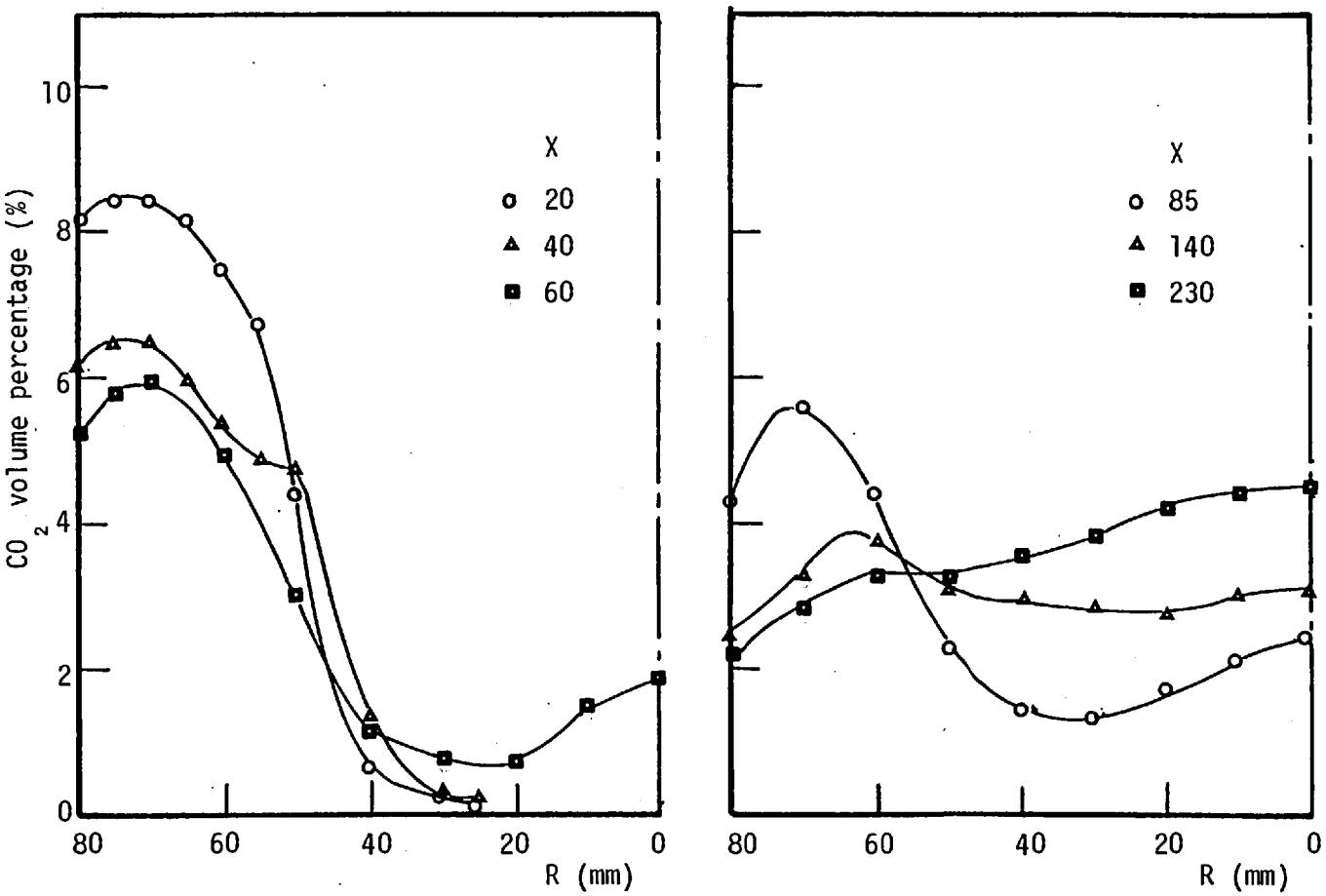

Fig. AIV.19 Radial profiles of CO_2 volume percentage - run 5

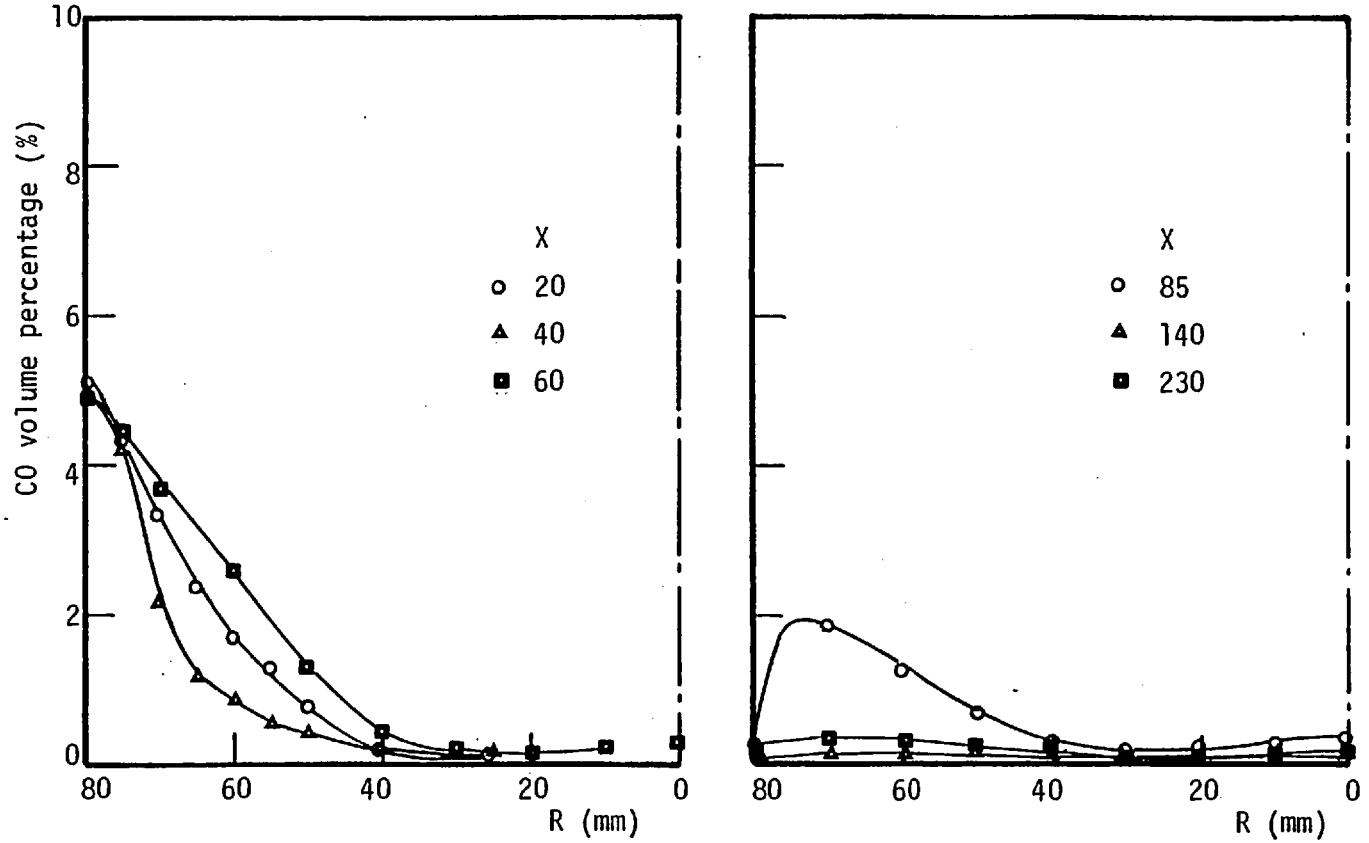

Fig. AIV.20 Radial profiles of CO volume percentage - run 5

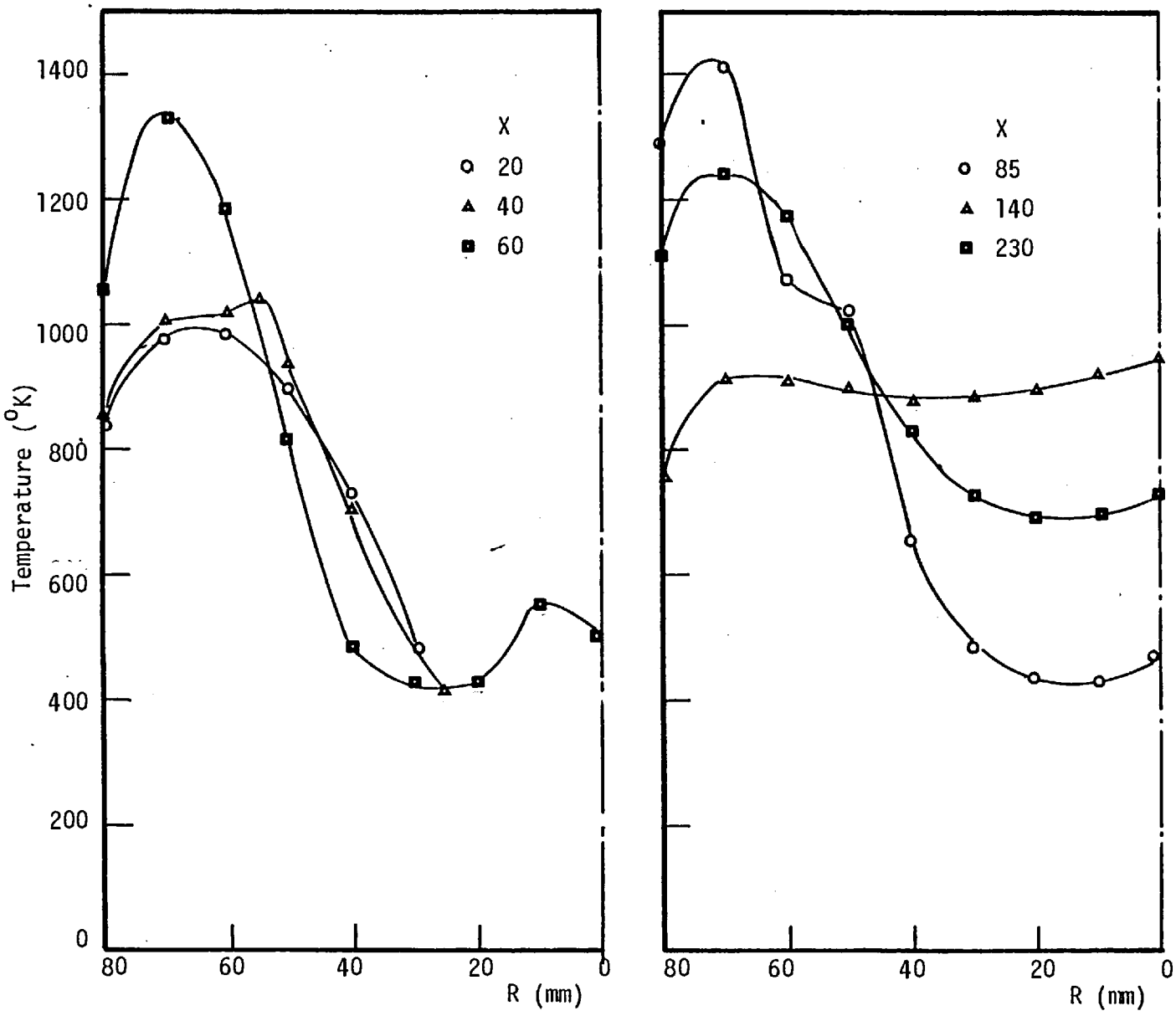

Fig. AIV.21 Radial profiles of mean gas temperature - run 6

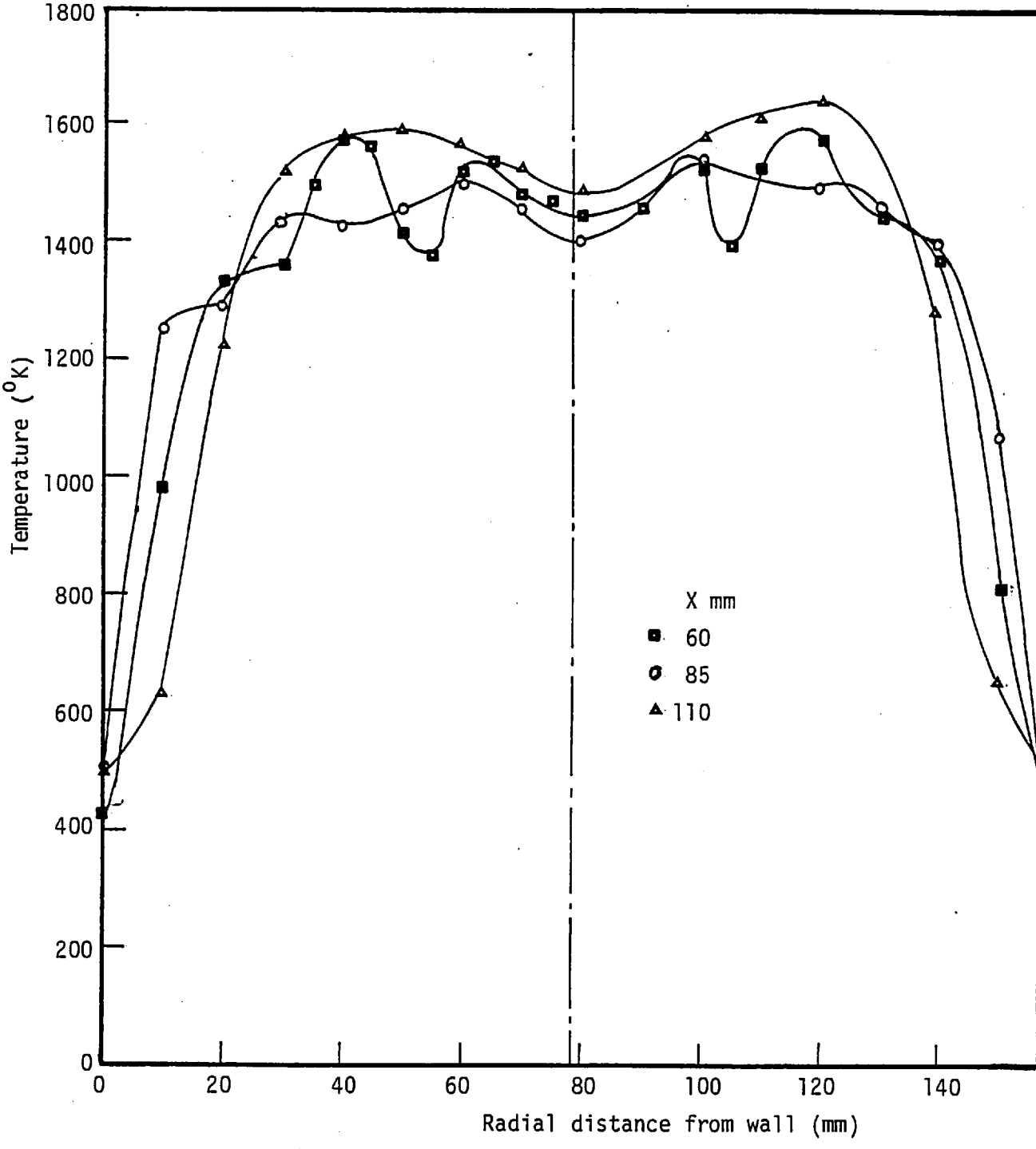

Fig. AIV.22 A sample of the symmetry checks for the temperature measurements, run 1 (Table 2.3)

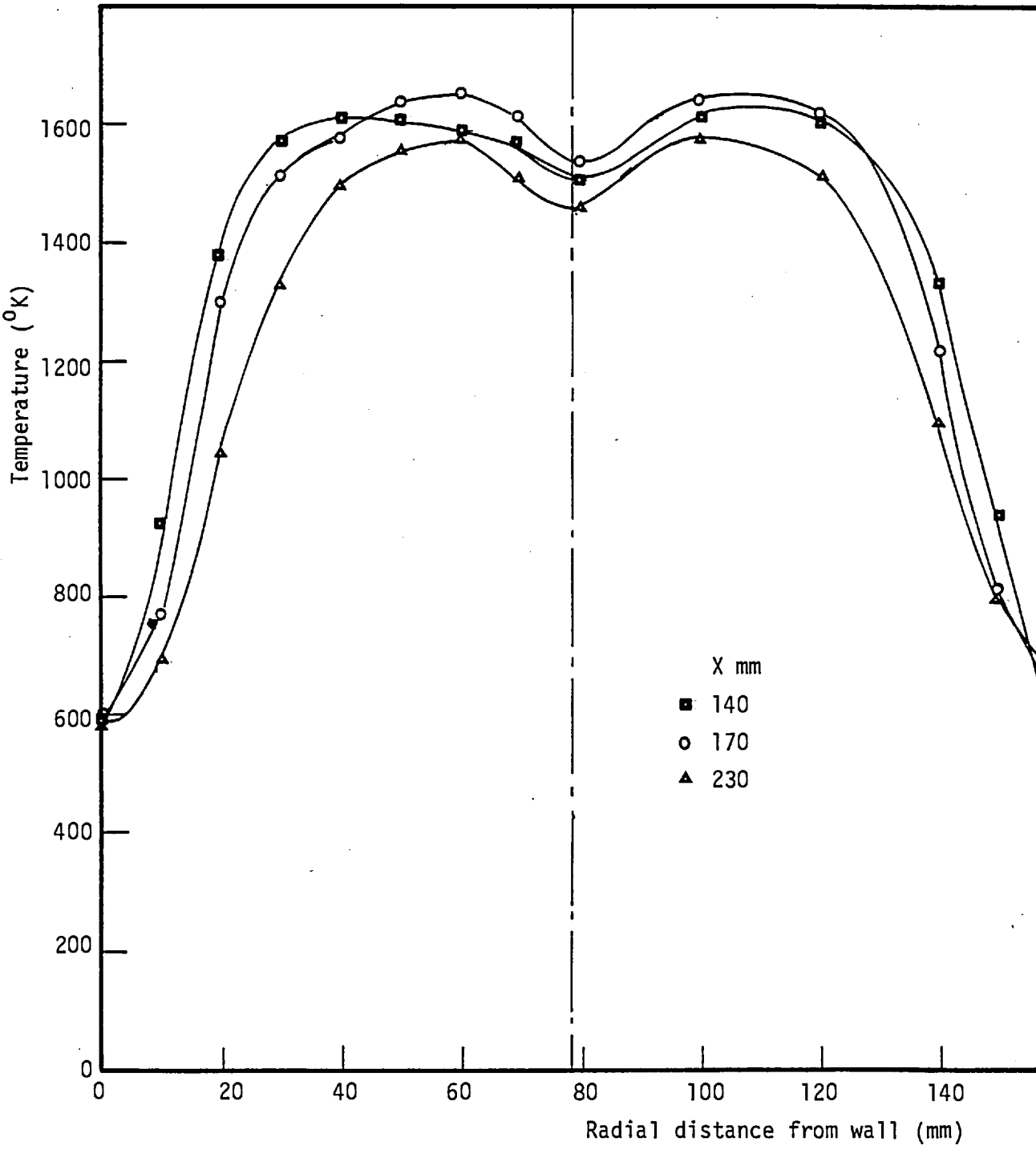

Fig. AIV.22 (Continues)

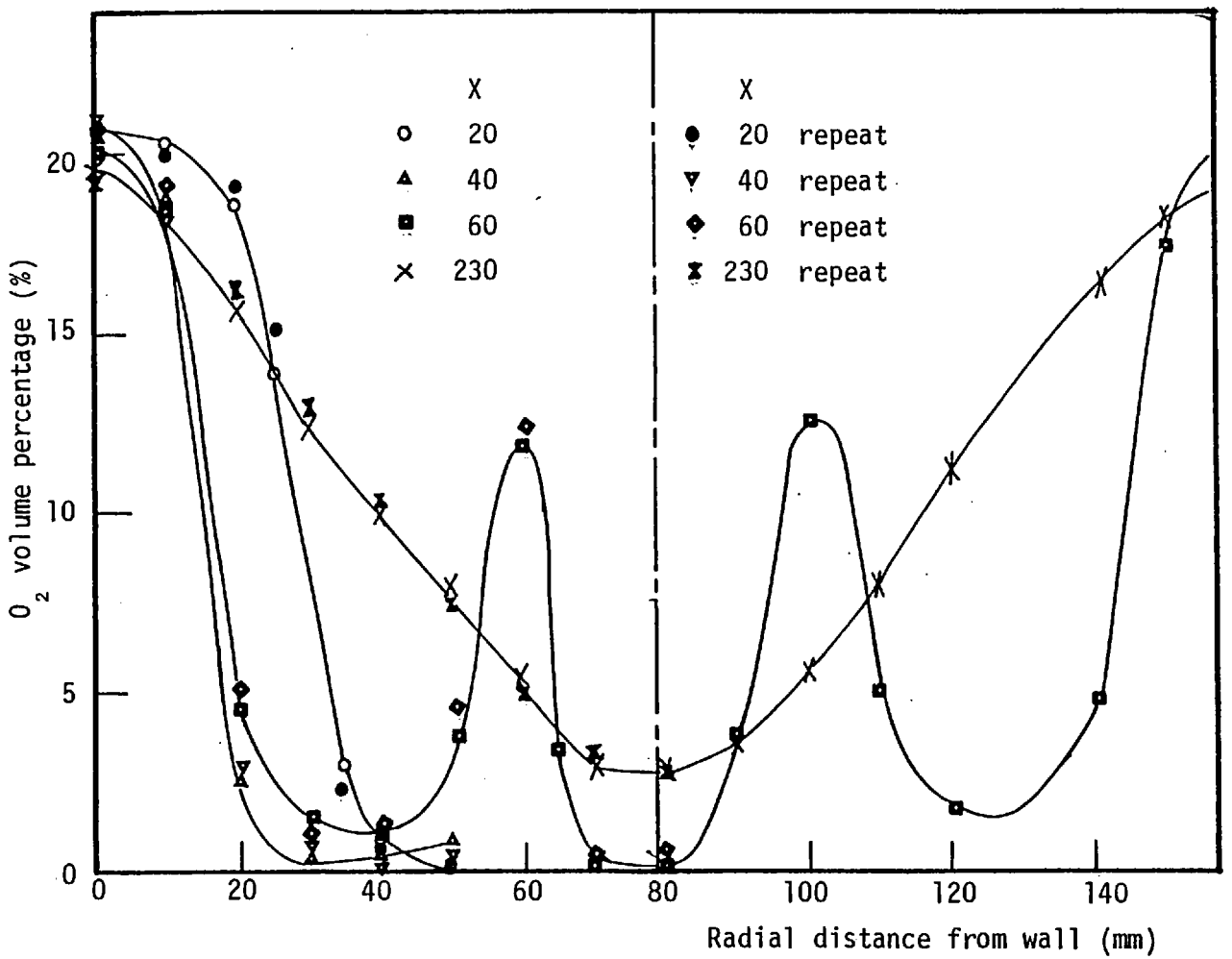

Fig. AIV.23 A sample of symmetry and repeatability checks for O_2 volume concentrations, run 2 (Table 2.3)

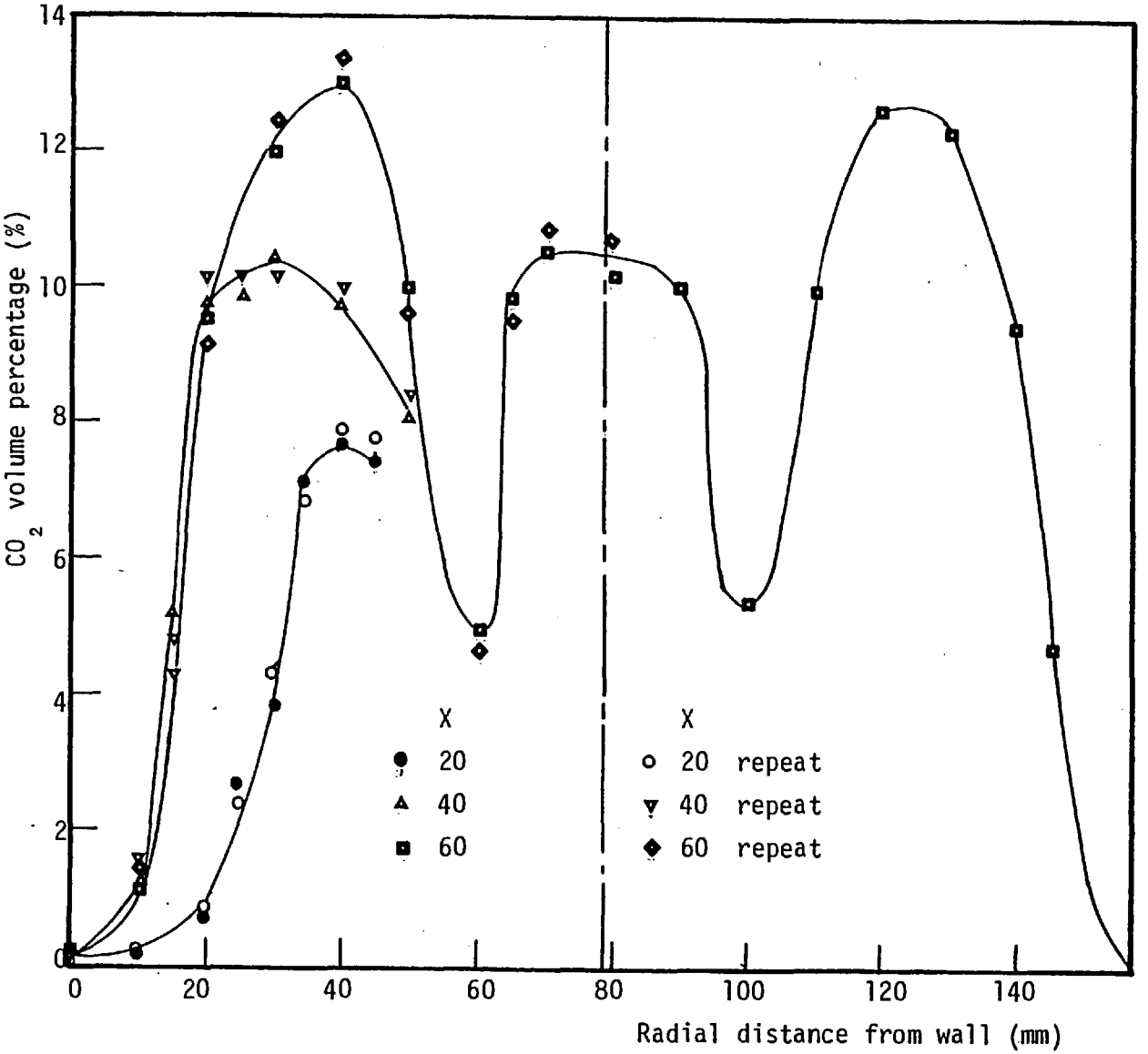

Fig. AIV.24 A sample of the symmetry and repeatability checks for CO_2 volume concentrations, run 2 (Table 2.3)

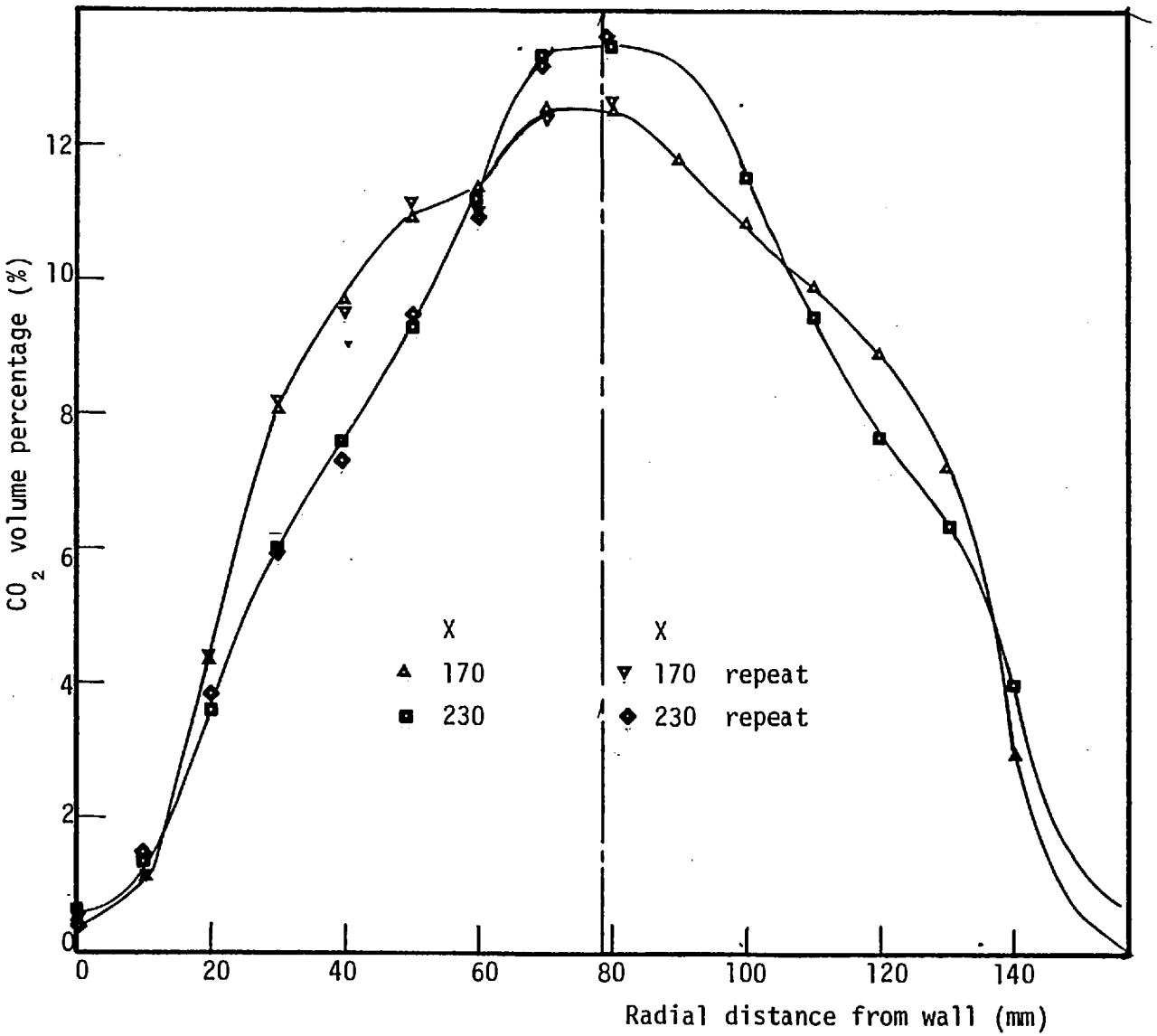

Fig. AIV.24 (Continued)

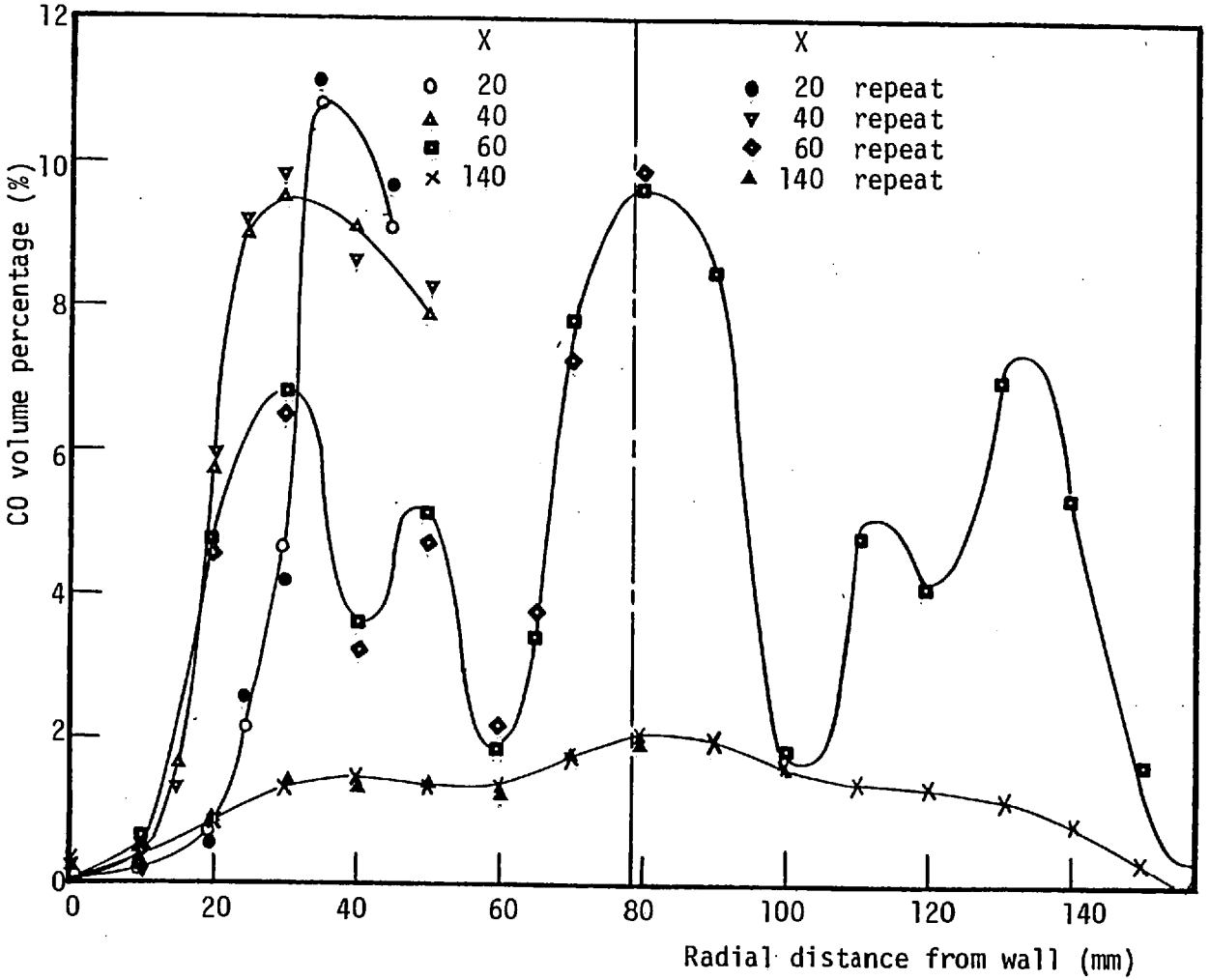

Fig. AIV.25 A sample of the symmetry and repeatability checks for CO volume concentration, run 2 (Table 2.3)

COMBUSTION AND FLAME 33, 281-290 (1978)

Combustion-Driven Oscillations in a Small Tube

Y. EL BANHAWY, A. MELLING and J. H. WHITELAW

Imperial College of Science and Technology, Department of Mechanical Engineering, Fluids Section, London SW7 2BX, England

Velocity and noise characteristics have been measured in the flow in a model combustor, which allows the simulation of combustion oscillations similar to those observed in afterburners. Local values of the mean axial velocity and the rms of the corresponding fluctuations have been obtained by laser-Doppler anemometry for a range of operating conditions resulting in flames with and without discrete-frequency oscillations. The mean velocities and normal stress distributions, but not the turbulence intensity distributions, are shown to increase considerably with combustion. The intensity and frequency of the sound pressure were also measured as a function of equivalence ratio, velocity, and added gas. The results showed, for example, that velocity and sound pressure fields are related and that the intensity of the oscillations could be suppressed by injection of helium gas downstream of the stabilising ring. This suppression led to a small decrease in the corresponding normal stress; to a first approximation, the resulting thrust was not altered.

1. INTRODUCTION

The existence of combustion-driven oscillations, at discrete frequencies, has been observed in turbulent combusting flows, see for example, references 1-4, and can limit the performance of heat transfer and power generation. The present investigation was motivated by the related problem in afterburners, where combustion-driven oscillations often exist if the equivalence ratio of the burning mixture exceeds a limit that depends on geometry and flow boundary conditions. Measurements of the axial velocity component and the rms of the corresponding fluctuations have been obtained downstream of an annular flame stabilizer located in a round pipe of 23 mm diameter; related measurements of sound pressure intensity and frequency are also reported. The flames were formed by air-propane mixtures at equivalence ratios corresponding to combusting flows with and without detectable discrete frequencies; isothermal air measurements were also carried out for reference purposes. It was demonstrated by Hakluytt et al. [2] that the addition of helium to the gas mixture could modify the intensity of combustion oscillations, and this possibility is investigated.

In afterburner arrangements, a mixture of gas turbine exhaust products and fuel is burned in a short duct. The flame is usually stabilized on a bluff-body annular ring, and the resulting products exhaust to atmosphere through a nozzle; the flow may be further complicated by the engine by-pass air. The geometrical configuration of the afterburner corresponds to a tube with upstream and down-stream boundary conditions that allow the reflection of a pressure wave, and the method of burning corresponds to a distributed and large source of energy. For tubes of length-to-diameter ratio significantly greater than unity, and for the arrangements with an open and a closed end, the resonant frequency corresponds to a wave length four times greater than the duct length. The details of the open and closed ends may imply impedance characteristics that can modify the reflection process. Combustion-driven oscillations at a discrete frequency of about 550 Hz have been observed in the present investigation, and this

0010-2180/78/0033-0281$01.25

corresponds closely to the resonance frequency of the combustor tube, calculated as a quarter-wave tube to be $F_R = 520$ Hz.

The available evidence [1, 6] suggests that the oscillation frequency is determined by the acoustic characteristics of the combustor, and its amplitude depends, according to Rayleigh (see reference 6), on the extent to which the available energy overcomes and exceeds the acoustic energy damping, and on the phase between the acoustic pressure and heat release rate fluctuations. The fluctuations in heat release can be influenced, for example, by vorticies passing through the flame front, see references 1-4, or by intermittent burning of the inlet combustible mixture due to the ignition time lag, see references 7 and 8. The influence of the available energy and the injection of helium into the reaction zone on the oscillation amplitude is considered here, and the amplitude of the combustion-driven oscillations is shown to increase with available energy and decrease with injection of helium.

One difficulty associated with the investigation of combusting flows, especially with oscillations, is the limited range of instruments that can be used successfully. Reported work on combustion-driven oscillations in the literature shows that, while information of the intensity and frequency distribution of the pressure field are available (for example, references 4 and 5), local velocity measurements are very few (1, 3, 4). In the present case, the sound intensity and frequency were measured and provide quantitative measures of the intensity and frequency distribution of the flow-generated pressure field. The measurements are, however, based on an interpretation of the noise characteristics of the entire flow field and provide no information of local properties and of the generated thrust. Thus a laser Doppler anemometer was used to allow the mean axial velocity and the rms of the corresponding fluctuations to be measured. The spectrum of the fluctuating energy can, in principle, be measured with laser-Doppler anemometry equipment [9] but was not attempted here; probability distributions, corresponding to each local velocity measurement are, however, discussed. The instrumentation used here allowed the experiments to be carried out in a small-diameter tube with consequently increased safety and small cost.

2. EQUIPMENT AND EXPERIMENTAL PROGRAM

Figure 1 shows the flow configuration, the air and fuel (propane) supply systems, a cooling arrangement for the test section, and a solid particle (titanium dioxide) generator for seeding the flow [10]. Details of the stabilising orifice and the test section are also shown. The suppression of combustion oscillations was achieved by injection of helium through six holes equally distributed around the stabilising orifice. Further details are provided in reference 11.

Velocity measurements were carried out with a laser Doppler anemometer operating in the fringe mode with an acousto-optic (Bragg) cell for frequency shifting. An argon-ion laser (Spectra Physics model 164) was used at a wave length of 488 nm with approximately 100 mw power. The acousto-optic cell provided both beam splitting and frequency shifting of 30 MHz between the two beams [12]. A 200-mm focal length lens was used to focus and cross the beams at the half angle, Φ, of 8.36. Forward scattered light was collected and focussed on to a photomultiplier with a lens of 150 mm focal length.

The signal from the photo-multiplier was supplied to an oscilloscope for observation and to a spectrum analyser (Hewlett Packard model 8553B/9552A/141T). The spectrum analyser was connected to a sweep generator and a digital counter with an electronic typewriter. The probability density distribution of velocity and hence the mean velocity and associated rms of velocity fluctuations were obtained from the digital output of this arrangement as described in references 1 and 9. This signal-processing arrangement does not provide the real-time information necessary to allow the frequency of any flow oscillation to be detected. In principle, information of this type could be obtained by the use of a frequency-tracking demodulator or counter, with appropriate logic. The quality and noncontinuous nature of the signals obtained here precluded the use of instrumentation of this type.

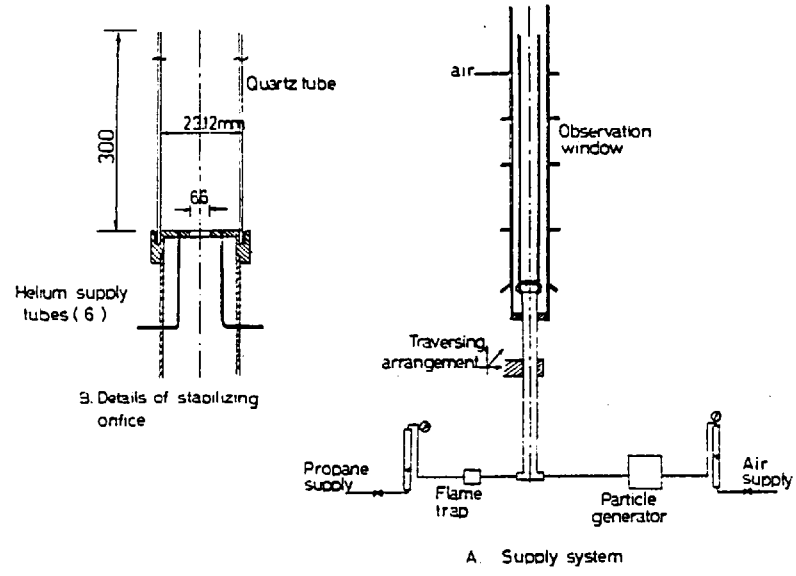

Fig. 1. Flow configuration.

The velocity measurements are subject to position uncertainty of up to 0.5 mm, to instrumentation errors of up to ±2% in mean velocity and up to ±5% in normal stress. The instrumentation errors were due mainly to the finite values of frequency interval of the spectrum analyser. The number of signals considered in the evaluation of each velocity and velocity correlation depended on the turbulence intensity and on the nature of the flow. Table 1 presents a sample of turbulence information. The values of e_μ and e_σ corresponding to the errors in mean and rms frequency due to the number of individual velocities considered are shown to be negligibly small. The errors in the values of skewness and flatness will be larger but are unlikely to alter the conclusion that they are similar to those associated with near-Gaussian probability-density distributions.

Sound pressure level and frequency of oscillation were measured with a microphone located 40 cm from the combustor. The pressure signal was input to a frequency analyser to determine the oscillation frequency and the rms amplitude of the sound pressure.

The experimental program comprised two main sets of measurements. Velocity measurements were carried out in combusting flow along the tube centreline for two values of the input equivalence ratio ϕ with identifiable oscillations. The two equivalence ratios corresponded to two mass flow rates of the fuel (propane) as indicated in Table 2. Suppression of the combustion-driven

TABLE 1

Sample of Turbulence Properties and Errors in Doppler Spectra

Point in Run No.	$\bar{\nu}_D$ MHz	$\tilde{\nu}_D$ MHz	Skewness $\overline{u^3}/(\overline{u^2})^{3/2}$	Flatness $\overline{u^4}/(\overline{u^2})^2$	e_μ	e_σ	N	Remarks
14	69.48	13.79	0.066	2.9	0.0095	0.0192	5405	Buzz
107	58.93	5.74	0.089	2.8	0.0075	0.0267	2805	No buzz

TABLE 2

Working Conditions for Velocity Measurements

Run No.	m_a (g/s)	m_f (g/s)	ϕ	F (Hz)	A (db)	Remarks
13, 14, 15	1.25	0.077	0.965	570	109	comb. flow "Buzz"
17	1.25	0.086	1.077	580	112	comb. flow "Buzz"

oscillations was investigated by injecting air and helium into the stabilization region of the flow and measuring the frequency and sound pressure level for different injection rates. Velocity measurements, for two runs with and without helium injection, were also obtained, Table 2.

3. DISCUSSION OF EXPERIMENTAL RESULTS

3.1 Velocity Measurements in Combusting Flow with Oscillations

The distribution of the mean axial velocity component and the rms of the corresponding fluctuations along the tube, for two values of ϕ, are shown in Fig. 2. At x/D of 0.5 the velocity values are already well above the average inlet velocity; at higher values of x/D the velocity increases gradually to a maximum at about x/D of 1.75 for $\phi = 0.966$ and x/D of 1.5 for $\phi = 1.077$. Further downstream, the velocity decreases but at a slower rate than the corresponding isothermal results of reference 11, which are plotted on the same figure. The higher velocities attained in the combusting flows and the slower decay rate are due to the additional energy supplied by the combustion.

The distribution of the rms of the velocity fluctuations is also significantly higher than the corresponding isothermal flow results. The turbulence intensity ranges from 0.35, in the upstream region, to 0.25; these higher values are probably associated with the superposition of regular oscillations, made significant by the energy of combustion. Close inspection of the combusting results of Fig. 2 indicates a tendency for the maximum mean velocity and rms value to increase with equivalence ratio, particularly in the upstream region. In addition to the tendency for velocity to increase with equivalence ratio, the maxima in the mean and rms quantities are shifted slightly towards the stabilising orifice; this suggests that the combustion is completed within a shorter length of the tube.

As indicated in Tables 1 and 2, sound-pressure intensity measurements corresponding to the velocity results of Fig. 2, indicated predominant frequencies and high amplitude (buzz). The measured spectra indicated that almost all the fluctuating energy existed at the predominant frequency, and although the velocity characteristics of Table 1 for Run 14 suggest that the velocity-probability density distribution was near Gaussian, the measured distribution indicated two peaks. The peaks were not, however, close to delta functions, but rather part of wide distributions. This indicates that, although the velocity and pressure signals possessed predominant frequencies, the former also had turbulent fluctuations.

3.2 Helium and Air Injection

The measured frequency and amplitude of the sound pressure level are plotted against the ratio of M_{inj}/M and shown in Fig. 3 (see also Table 3) for two runs with helium injection and two for air injection. The measurements indicated insignificant fluctuation energy at frequencies other than those shown on the figure. Frequency values, at the maximum amplitude of oscillations, are shown to be around 550 Hz, which corresponds closely to the calculated average combustor natural frequency of 520 Hz; this natural frequency, F_R, was calculated for an average gas mean-temperature and based on excitation of a quarter-wave mode of standing oscillations within the com-

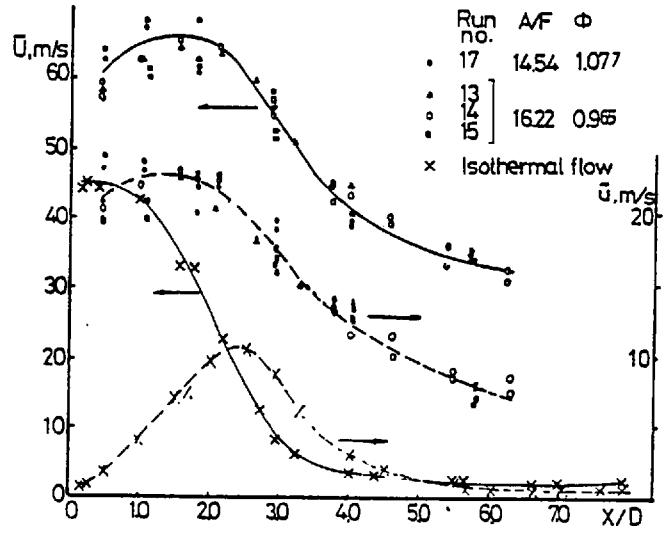

Fig. 2. Centre line mean axial velocity and the rms of the corresponding fluctuations.

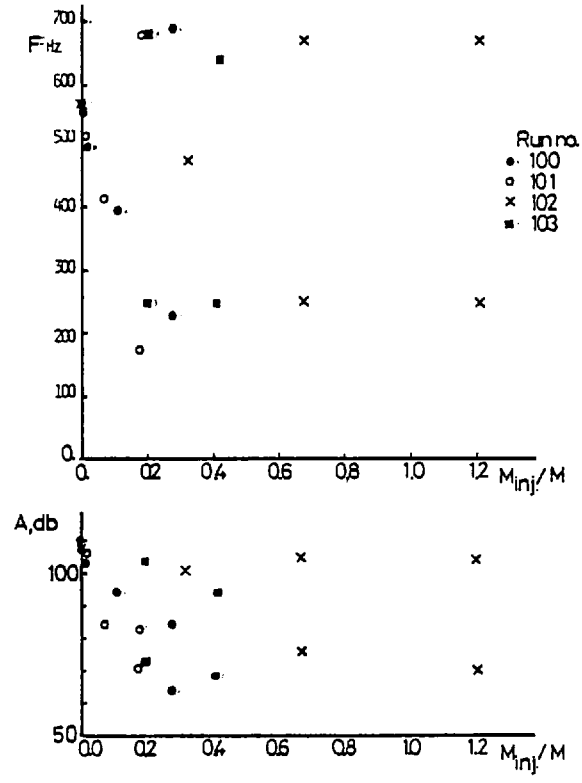

Fig. 3. Measured frequency and rms of the sound pressure level at different M_{inj}/M values.

TABLE 3
Working Conditions for Measurements Concerned with the Suppression of Oscillations

Run No.	m_a (g/s)	m_f (g/s)	$m_{He,inj}$ (g/s)	$m_{a,inj}$ (g/s)	ϕ	F (Hz)	A (db)
100	1.25	0.077	–	–	0.965	570	109
100	1.25	0.077	0.017	–	0.965	500	103
100	1.25	0.077	0.049	–	0.965	400	94
100	1.25	0.077	0.83	–	0.965	{690 230}	{84.5 64}
101	1.60	0.086	0.017	–	0.842	520	{107 84.5}
101	1.60	0.086	0.049	–	0.842	420	
101	1.60	0.086	0.083	–	0.842	{680 175}	{83.5 71.0}
102[a]	1.25	0.077	–	0.22	0.82	480	101
102[a]	1.25	0.077	–	0.32	0.768	{670 255}	{105 76}
102[a]	1.25	0.077	–	0.43	0.718	{670 250}	{104.5 70.0}
102[a]	1.25	0.077	–	0.50	0.689	630	81
103[a]	1.60	0.086	–	0.22	0.74	{680 250}	{104 73}
103[a]	1.60	0.086	–	0.32	0.703	{635 250}	{94 69}
104	0.98	0.067	–	–	1.07	520	101
104	1.14	0.067	–	–	0.92	520	104
104	1.24	0.067	–	–	0.846	465	97
105	1.25	0.077	–	–	0.965	570	110
105	1.42	0.077	–	–	0.85	515	106.5
105	1.52	0.077	–	–	0.795	460	97
105	1.60	0.077	–	–	0.764	{680 250}	{103 72}
106	1.42	0.086	–	–	0.95	580	112
106	1.60	0.086	–	–	0.842	540	109
106	1.71	0.086	–	–	0.789	470	103.5
106	1.79	0.086	–	–	0.754	{680 250}	{103 72}
107	1.20	0.077	0.06	–	1.01	410	88
108	1.20	0.077	–	–	1.01	576	112

[a] ϕ calculated on the basis of total mass of air in the combustor.

bustor. An increase in M_{inj}/M led to a reduction of both the frequency and amplitude of oscillation. However, for values of M_{inj}/M of more than around 0.2, two measured values were obtained for the frequency and are associated with different amplitudes of oscillation with average values lower than that without injected mass (≅25 db reduction).

The change of frequency with air and helium injection is due mainly to changes in the temperature field within the combustion tube. The injection of helium into the reaction zone of the tube caused a reduction in the local fuel and air concentrations, and due to the higher heat capacity, mean temperature of the reactants decreased. The overall result is a reduction in the local heat-release

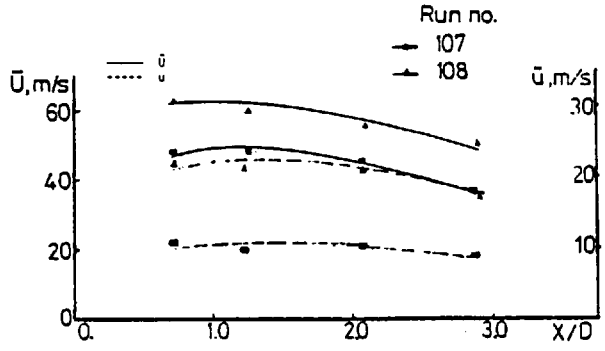

Fig. 4. Centre line distribution of mean axial velocity and the rms of the corresponding fluctuations: combusting flow.

rate with consequently lower amplitude of oscillations.

The reduction of the oscillation amplitude with air injection is less for the same injected mass (or momentum) flow and also for mean flows of similar total injection, Table 3. This indicates that the oscillation amplitude reduction is not related to the aerodynamics of the injection jets. The same conclusion was reached by Hakluytt et al. [2] by altering the injection position. However, the amplitude variations associated with air injection probably results from the decrease in the overall equivalence ratio with consequently lower available energy to drive the oscillations. It can be seen from Table 3 (runs 100 to 103) that suppression of oscillations can be obtained at a lower value of M_{inj}/M for the flame with the lower equivalence ratio.

Measured values of the centre-line mean velocity and the rms of the corresponding fluctuations are shown in Fig. 4 for a combusting flow with oscillations (run 108) and a combusting flow with helium injection (run 107) to decrease the amplitude of oscillations. The mean and fluctuating velocity components are both decreased with helium injection; this is again related to the reduction in the mean temperature. While the decrease in the mean velocity is about 21.5%, that for the fluctuating component is about 51%. The more pronounced decrease in the latter results from the suppression of the discrete-frequency oscillations; inspection of the measured probability density distributions suggested that the random fluctuations associated with turbulence are probably unaffected. This confirms that the velocity fluctuations and the noise amplitude are coupled and that velocity measurements provide relevant information.

The ability of helium injection to suppress the buzz phenomenon in practical combustors is limited by the amount of helium necessary for sufficient amplitude reduction and the resulting thrust. The maximum amount of helium used in the present work was about 5% of the total mass of reactants (≅30% by volume), which provided a reduction in the sound pressure level of about 30 db. Provided that the combustion tube is long enough to allow the completion of the initially retarded chemical reaction, the axial velocity at the tube exit will not be significantly affected by helium injection. Hence, to a first approximation, the thrust will remain the same.

3.3. Effect of Equivalence Ratio and Fuel Mass Flow Rate

The measured values of frequency and amplitude of oscillations corresponding to runs 104, 105, and 106 are plotted against equivalence ratio on Fig. 5. The results show an increase in both the amplitude and frequency of oscillations with equivalence ratio and fuel flow rate, see also Table 2. The increase in frequency is related to the temperature effects on the acoustic characteristics of the combustion tube. The increase in amplitude stems mainly from the increase in the available energy.

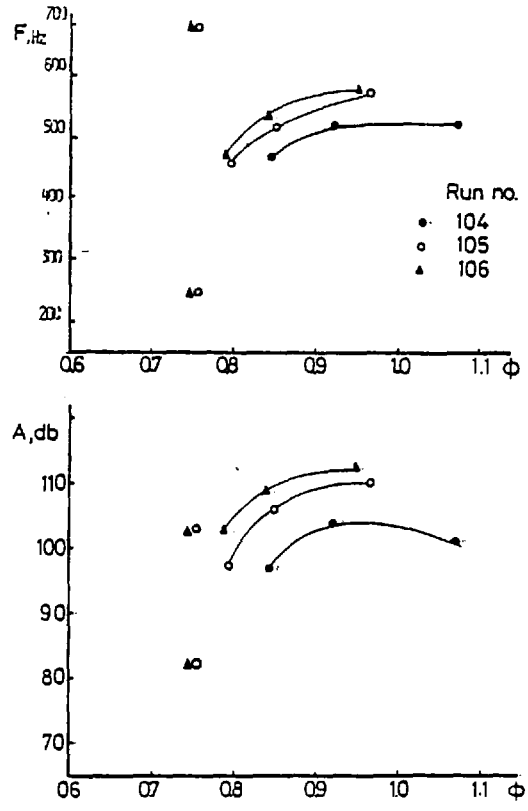

Fig. 5. Measured frequency and rms of the sound pressure level at different equivalence ratios.

4. DISCUSSION

The results presented in the previous section, in addition to their direct practical relevance, provide clues which assist understanding of the physical processes involved in oscillating combustion systems. Previous papers, for example reference 7 and 8, have hypothesised that there is a lag time associated with combustion and that this gives rise to variations in heat release; these variations, if in phase with the natural oscillation of the pressure wave, give rise to combustion oscillations. An alternative approach (see for example reference 2), appropriate to afterburner systems with stabilisers that give rise to vortex shedding, suggests that the natural pipe oscillation and that due to the shedding may be in phase and again give rise to combustion oscillations.

The present results were obtained with a geometrical configuration that is unlikely to give rise to strong vortex shedding, and this is borne out by the near-Gaussian nature of the probability density distributions measured with isothermal flow and with the lower equivalence ratios. Weak shedding is possible, of course, and could rise from mechanisms such as those observed by Crow and Champagne [13], Hill and Greene [14], and Cherdron et al. [15]. It is unlikely, however, that weak shedding of this type would have a significant influence on the present flow characteristics. It is more likely that the natural frequency of the cavity gives rise to a weak pressure wave which influences the velocity field and, particularly in upstream regions, results in the combustion of fuel in a periodic manner and at a phase and frequency identical to that of the pressure wave that causes it. As a consequence, the heat release variations are also in phase with the natural frequency. In situations where vortex shedding from a bluff body is possible and likely to be strong, it may well be possible to dampen the pressure oscillation at the natural frequency and, therefore, the combustion oscillations.

The addition of helium or air to the present flow has the effect of lowering the overall temperature and, therefore, of reducing the natural frequency and the corresponding amplitude. This does not explain the separation of the pressure energy into two frequencies with almost equally divided intensity, which occured with the higher injection rates. The higher frequency is clearly, however, a harmonic of the lower, and it is probable that, as the available energy decreases, the ordered structure breaksdown first into two frequencies before further disintegration to greater disorder and finally to a turbulent-like spectrum.

5. CONCLUSIONS

The following conclusions may be extracted from the results of the present work.

1. Low-frequency high-amplitude (550 Hz, 105 db) combustion oscillations have been observed in a model combustor, and the results suggest that the driving mechanism involves fluctuations in the rate of heat release, due to discrete frequencies in

the power spectrum of velocity, and pressure oscillations in the enclosure.

2. A reduction in the noise amplitude was achieved by:

(a) Injection of an inert gas with high heat capacity into the tube to act as a dilutant and heat sink. However, the mass of helium required to reduce the amplitude by 30 db was around 5% of the total mass of reactants (30% by volume).

(b) Reducing the equivalence ratio or fuel mass flow rate. Both reduce the available energy and possibly change the reaction rate.

3. Changing from isothermal to combustion oscillation conditions led to an increase in the mean axial velocity and a much higher increase in the corresponding rms of fluctuations. The large rms values, observed with combusting flow, involve the superposition of regular fluctuations on the turbulent flow field, at least for the higher equivalence ratios.

4. The expected link between velocity fluctuations and the rms of sound pressure level, which has been confirmed here, indicates the importance of local velocity measurements under buzz conditions where local amplitudes of oscillation are required.

The authors gratefully acknowledge financial support from the Ministry of Defence. The quartz burner tube was kindly lent by J. P. D. Hakluytt, who also assisted by discussion, particularly in the early stages of the investigation.

NOMENCLATURE

A rms sound pressure level in dB
A/F air-fuel ratio
C velocity of sound m/s
D combustor inner diameter, mm
e_μ relative error in mean Doppler frequency
e_σ relative error in rms Doppler frequency
F measured frequency of oscillations Hz
F_R system acoustic frequency as a quarter wave resonator $F_R = C/4L = 520$ Hz in the present case
L combustor length, mm
M axial momentum of mixture at exit from the orifice
M_{inj} axial momentum of injected helium or air at exit from injection holes
m_a mass flow rate of air g/s
m_f mass flow rate of fuel (propane) g/s
$m_{a_{inj}}$ mass flow rate of injected air g/s
$m_{He,\,inj}$ mass flow rate of injected helium g/s
N total number of particles detected by spectrum analyser
$\bar{U}$ mean axial velocity component m/s
$\tilde{u}$ rms of the fluctuating axial velocity component m/s
x axial distance, mm
μ the mean value of a Gaussian pdf
$\bar{\nu}_D$ mean Doppler frequency MHz
$\tilde{\nu}_D$ rms Doppler frequency MHz
σ the rms value of a Gaussian pdf
ϕ equivalence ratio; in this case $\phi = (1/0.063)\cdot(m_f/m_a)$
Φ half angle between the two laser beams in degrees

REFERENCES

1. Clare, H., Durão, D. F. G., Melling, A., and Whitelaw, J. H., Investigation of a V-gutter stabilized flame by laser anemometry and Schlieren photography. AGARD, C.P. 193, *Applications of Non-Intrusive Instrumentation in Fluid Flow Research*, 1976.
2. Hakluytt, J. P. D., Tilston, J. R., Hussey, M. E. Private communication.
3. Durst, F., Melling, A., and Whitelaw, J. H. Laser anemometry measurements in a square duct with and without combustion oscillations. Imperial College, Mech. Eng. Dept. report EHT/TN/A/40, 1972.
4. Durão, D. F. G., Melling, A., Pope, S. B., and Whitelaw, J. H. Laser anemometry measurements in the vicinity of a gutter-stabilized flame. Imperial College, Mech. Eng. Dept. Report EHT/TN/A/41, 1973.
5. Speich, C. F., and Putnam, A. A., Pulsations in single-portgas-fired residential heating equipment. *Heating, Piping and Air Conditioning* 30, 139 (1958).
6. Markstein, G. H. (Ed.), *Non-Steady Flame Propagation*. Pergamon, New York, 1964.
7. Howland, A. H., and Simmonds, W. A., Combustion inside refractory tubes. *4th Symp. (Int.) on Combustion*, Williams and Wilkins, Baltimore, Maryland, 1953, p. 592.
8. Ross, P. A. Some observations of flame stabilization in sudden expansion. *Jet Propulsion* 28, 123 (1958).

9. Durst, F., Melling, A., and Whitelaw, J. H. *Principles and Practice of Laser-Doppler Anemometry.* Academic Press, New York, 1976.
10. Asalor, J. O., and Whitelaw, J. H. The design and performance of a cross-flow particle generator for use in laser-Doppler anemometry. *DISA Inf.* 19, 5 (1976).
11. El Banhawy, Y. H., Melling, A., and Whitelaw, J. H., Combustion driven oscillations in a small tube. Imperial College, Mech. Eng. Dept. Report CHT/77/5, 1977.
12. Durão, D. F. G., and Whitelaw, J. H., The performance of acousto-optic cells for laser-Doppler anemometry. *J. Phys. E: Sci. Instrum.* 8, 776 (1975).
13. Crow, S. C., and Champagne, F. H., Orderly structure in jet turbulence. *J. Fluid Mech.* 48, 547 (1971).
14. Hill, W. G., and Greene, P. R., Self-excited superturbulence: The Whistler nozzle. Grumman Research Department, Report RE-488.
15. Cherdron, W., Durst, F., and Whitelaw, J. H., Asymmetric flows and instabilities in symmetric ducts with sudden expansion. *J. Fluid Mech.* 84, 13 (1978).

Received 6 September 1977; revised 22 February 1978